Renato Paulo
dos Santos Mendes

Pluma estuarina do Rio Douro: deteção, processos e dinâmica

The Douro estuarine plume: detection, processes and dynamics

Universidade de Aveiro Departamento de Física
2016

Universidade do Porto Faculdade de Ciências

Universidade do Minho Departamento de Física

Renato Paulo
dos Santos Mendes

Pluma estuarina do Rio Douro: deteção, processos e dinâmica

The Douro estuarine plume: detection, processes and dynamics

Dissertação apresentada à Universidade de Aveiro para cumprimento dos requisitos necessários à obtenção do grau de Doutor em Física, realizada sob a orientação científica do Doutor João Miguel Sequeira Silva Dias, Professor do Departamento de Física da Universidade de Aveiro, da Doutora María Teresa de Castro Rodríguez, Professora do Departamento de Física Aplicada da Faculdade de Ciências de Ourense, Universidade de Vigo e do Doutor Nuno Alexandre Firmino Vaz, estagiário de pós-doutoramento da Universidade de Aveiro.

O autor foi financiado pela Fundação para a Ciência e Tecnologia (FCT), através da bolsa de doutoramento com a referência SFRH/BD/79555/2011, no âmbito do Quadro de Referência Estratégico Nacional (QREN) e do Programa Operacional de Potencial Humano (POPH), comparticipado pelo Fundo Europeu e por fundos nacionais do Ministério da Educação e Ciência (MEC).

o júri

presidente

António Manuel Melo de Sousa Pereira
Professor Catedrático do Departamento de Eletrónica, Telecomunicações e Informática da Universidade de Aveiro

vogais

José Carlos Pinto Bastos Teixeira da Silva
Professor Associado do Departamento de Geociências, Ambiente e Ordenamento do Território, Faculdade de Ciências da Universidade do Porto

Ramiro Joaquim de Jesus Neves
Professor Associado do Departamento de Engenharia Mecânica, Instituto Superior Técnico da Universidade de Lisboa

Rámon Gómez-Gesteira
Professor Catedrático do Departamento de Física Aplicada da Faculdade de Ciências de Ourense, Universidade de Vigo, Ourense, Espanha

Jesus Manuel Pedreira Dubert
Professor Auxiliar do Departamento de Física da Universidade de Aveiro

João Miguel Sequeira Silva Dias
Professor Auxiliar com Agregação do Departamento de Física da Universidade de Aveiro (orientador)

agradecimentos / acknowledgements

I would like to thank many people who supported and participated actively during my journey as a PhD student. Thank you for the help, encouragement and friendship.

Firstly, a special thanks to my three supervisors. To Prof. João Miguel Dias for guidance and all the good advices during this 4 year journey. I hope next year *our* Sporting will give us more reasons to celebrate. To Prof. Maite de Castro for the patience, trust and for such a warming welcome in Ourense. To Nuno Vaz for the daily assistance and constant brainstorming in the NMEC lab.

To the NMEC working group, in particular to Magda Sousa and João Rodrigues for the hard work during the implementation of MOHID and WRF models, also to Ana Picado and Carina Lopes for sharing solutions during our PhD journey.

To all colleagues and professors in EPhysLAB at Ourense (University of Vigo). I would like to give special thanks to Moncho Gómez-Gesteira for his guidance and advice. This work would not be the same without his suggestions. To Diego for the constant sharing of ideas, problems and solutions during our work on MODIS datasets.

To Prof. José Carlos da Silva (FCUP) for his availability, for allowing my presence in his remote sensing classes, and for his important help in my first steps in detection of river plumes using ocean-colour data.
To Carlos Rocha (UNSW) for the indispensable help at the beginning of MODIS images processing in UNIX environment.
To Gonzalo Saldías (College of Earth, Ocean, and Atmospheric Sciences, OSU) for all suggestions and collaboration in our studies related to turbid plumes.
To Paulo Leitão (Hidromod) for the support with MOHID solutions, in particular with problems related to MPI and OpenMP implementations.
To Prof. Fátima Sousa (FCUL), Antonina dos Santos and Miguel Santos (IPMA) for providing *in situ* coastal measurements. Although they are not used in this thesis, it would be certainly helpful for future researches.
To Instituto Hidrográfico for providing important *in situ* observations from ECOIS and NICC projects.
To Prof. Tim Oswald (UA) for his availability to revise the english of one of the scientific papers that support this dissertation. It would be very difficult to publish it without his corrections.

To my family and friends, whose support I could always count on.

To Ju for the unconditional support, understanding and loads of patience in these last years.

palavras-chave Rio Douro, plumas estuarinas, modelação numérica, MOHID, deteção remota, cor do oceano, MODIS

Resumo O Douro é um dos maiores rios da Península Ibérica, constituindo a maior descarga de água doce para o Oceano Atlântico na costa noroeste portuguesa. A sua pluma estuarina tem particular relevância na dinâmica costeira e na modulação de fenómenos biogeoquímicos. São objetivos desta dissertação contribuir para a compreensão dos processos físicos associados à geração e propagação da pluma estuarina do Rio Douro no oceano, assim como para o conhecimento dos seus padrões de dispersão e da forma como estes alteram a hidrologia e a circulação costeira, considerando os agentes forçadores típicos deste fenómeno (caudal fluvial, vento e maré) e índices climáticos relevantes. Para concretização destes objetivos foram desenvolvidas e aplicadas metodologias inovadoras de processamento de dados de deteção remota, assim como novas implementações estuarinas e costeiras de modelos numéricos. Através de imagens MODIS, otimizadas para o estudo de fenómenos costeiros, efetuou-se uma deteção rigorosa da pluma. Identificou-se uma relação entre o sinal túrbido $nLw555$ e o caudal, demonstrando-se este produto como um bom *proxy* para a observação da pluma no oceano. As escalas temporais e espaciais da pluma foram caraterizadas através destas imagens, combinadas com dados de caudal fluvial, maré, vento e precipitação, e também com índices climáticos relevantes. Para compreender a propagação da pluma e caracterizar a sua dinâmica e impacto na circulação costeira, foi desenvolvida uma aplicação 3D de modelos estuarinos e costeiros com malhas aninhadas de resolução variável. Definiram-se e analisaram-se diferentes cenários de vento e descarga fluvial. A interação da pluma do Rio Douro e do Minho foi ainda analisada através dos resultados de simulações baseadas num evento de inverno. Os compósitos túrbidos mostraram que a pluma é facilmente detetada quando o caudal é maior que $\sim$500 m^3 s^{-1}. A descarga fluvial e o vento são os principais forçadores da sua propagação, enquanto a maré é apenas importante na região próxima à embocadura do estuário. Observaram-se relações a uma escala interanual entre a turbidez da pluma e os índices climáticos East Atlantic e NAO, com uma correlação máxima identificada com 1 e 3 meses de desfasamento, respetivamente. Com base nos resultados das simulações efetuadas, a pluma é classificada como de larga escala e de adveção superficial, apresentando características de uma pluma prototípica. Em condições de caudal moderado a elevado, a descarga estuarina é suficiente para gerar uma corrente costeira para norte sem ação do vento. Em eventos de ventos leste, a propagação da pluma é similar ao caso sem vento, com um aumento da velocidade da corrente. Uma corrente costeira para sul é unicamente identificada sob condições de forte vento de oeste. Ventos de norte tendem a estender a pluma para o largo, com uma inclinação na direção sudoeste, enquanto ventos de sul intensificam a corrente para norte, sendo a mistura das plumas do Douro e do Minho uma consequência possível. A análise desta interação apontou a contribuição do Douro como importante na estabilização da WIBP e nas trocas de água entre o oceano e as Rias Baixas. A interação da pluma do Douro com estuários localizados a sul da sua foz e a confirmação *in situ* da recirculação observada nos resultados numéricos afiguram-se como temas relevantes para investigações futuras.

keywords Douro River, estuarine plumes, numerical modelling, MOHID, remote sensing, ocean-colour, MODIS

Abstract The Douro is one of the largest rivers of the Iberian Peninsula, representing the most important freshwater input into the Atlantic Ocean (on the northwestern Portuguese coast). Its estuarine plume has particular relevance on coastal dynamics and biogeochemistry. The main goal of this dissertation is to contribute to increase knowledge on physical processes associated with the generation and propagation of the Douro estuarine plume. The general patterns of dispersion in the ocean and how the plume change hydrography and coastal circulation were also evaluated, considering the typical drivers involved (river discharge, wind and tide) and relevant climate indices. Innovative methodologies to process remote sensing data, as well as new implementations of high-resolution estuarine and coastal numerical models have been developed and applied. The plume was detected through MODIS images, optimized for coastal studies. The relation between the turbid $nLw555$ signal and river discharge was identified, demonstrating that this product is a good proxy for the observation of the Douro estuarine plume in the coastal ocean. An interconnected approach, combining these images, river discharge, tide, wind and precipitation data, as well as relevant climate indices, was used to study the temporal and spatial scales of the plume. The implementation of estuarine and coastal models with nested domains of variable resolution was developed to understand the plume propagation and characterize its dynamics and impact on coastal circulation. Using these applications, different scenarios of wind and river discharge were defined and analysed. The interaction of the Douro and the Minho estuarine plumes was further evaluated through simulations based on a winter event. Turbid composites showed that the plume is easily detected when river discharge is greater than $\sim$500 m^3 s^{-1}. River discharge and wind are the main driver acting on the plume propagation, whilst tidal effect is only important near the estuary mouth. A relation between turbid plume and climate indices East Atlantic (EA) and North Atlantic Oscillation (NAO) was observed at inter-annual scale, with a maximum correlation identified at 1 and 3-month lags, respectively. The Douro estuarine plume is classified as large-scale and surface-advected, presenting characteristics of a prototypical plume, based on the results of the numerical simulations. The estuarine outflow is sufficient to generate a northward coastal current without wind action under moderate-to-high river discharge conditions. Under easterly winds, the propagation pattern is similar to the case without wind forcing, with a slight increase in the northward current. A southward coastal current is only generated by strong westerly winds. Under upwelling-favourable winds, the plume extends offshore with tilting towards southwest. Southerly winds increase the velocity of the northward current, being the merging of the Douro and Minho estuarine plumes a likely consequence. The analysis of this interaction pointed out the Douro as an important contributor to the WIBP stabilization and in the water exchange between ocean and Rias Baixas. The interaction of the Douro estuarine plume with estuaries located south of its inlet and the *in situ* confirmation of the re-circulation bulge observed in numerical results seem as relevant for future research topics.

Publications and communications in the context of this dissertation

Several publications in peer-reviewed journals and presentations at international and national conferences resulted from the research developed in this thesis. Some publications were used as basis for several chapters of this thesis (marked in bold in the list below).

Papers in international journals indexed in Web of Science:

- Mendes R., Vaz N., Fernández-Nóvoa D., da Silva J., deCastro M., Gómez-Gesteira M. and Dias J. (2014). Observation of a turbid plume using MODIS imagery: The case of Douro estuary (Portugal). *Remote Sensing of Environment*, 154:127–38. (**Chapter 2**)

- Mendes R., Saldías G.S., Vaz N., deCastro M., Gómez-Gesteira M., Dias J.M. (*under review*). Douro turbid river plume seasonal and interannual variability: relation with atmospheric teleconnection patterns. *Remote Sensing of Environment.* (**Chapter 3**)

- Mendes R., Vaz N. and Dias J.M. (2013). Potential impacts of the mean sea level rise on the hydrodynamics of the Douro river estuary. *Journal of Coastal Research*, (SI65):1951–6. (**Chapter 4**)

- Mendes R., Sousa M.C., deCastro M., Gómez-Gesteira M. and Dias J.M. (2016). New insights into the Western Iberian Buoyant Plume: Interaction between the Douro and

Minho River plumes under winter conditions. *Progress in Oceanography*, 141:30–43. (**Chapter 6**)

Papers in international journals indexed in Web of Science that have minor contributions but related with the aim of this dissertation:

- Sousa M.C., Mendes R., Álvarez I., Vaz N., Gómez-Gesteira M. and Dias J.M. (2014). Unusual circulation patterns of the Rias Baixas induced by Minho freshwater intrusion (NW of the Iberian Peninsula). *PLoS ONE*, 9(11):e112587.

- Fernandéz-Nóvoa D., Mendes R., deCastro M., Dias J.M., Sanchez-Arcilla A., Gómez-Gesteira M. (2015). Analysis of the influence of river discharge and wind on the Ebro turbid plume using MODIS-Aqua and MODIS-Terra data. *Journal of Marine Systems*. 142:40-46.

- Saldías G.S., Largier J., Mendes R., Pérez-Santos I., Vargas S.A., Sobarzo M. (*under review*). Satellite-measured interannual variability of turbid river plumes off central-southern Chile: Spatial patterns and the influence of climate variability. *Progress in Oceanography*.

- Fernandéz-Nóvoa D., deCastro M., Des M., Mendes R., Gómez-Gesteira M. (*under review*). Characterization of Iberian river plumes by means of synoptic patterns obtained through MODIS imagery. *Progress in Oceanography*.

- Marta-Almeida M., Mendes R., Amorim F.N., Cirano M., Dias J.M. (*under review*). Oceanic dispersion of River Doce after the greatest Brazilian environmental accident. *Marine Pollution Bulletin*.

Other publications:

- Mendes R., Gómez-Gesteira M., deCastro M., Vaz N., Dias J.M. (2013). Observação da pluma estuarina do Douro através de imagens MODIS de alta resolução. *Revista*

Avances en Ciencias de la Tierra (ACT), 4:11-22.

Presentations at international and national conferences:

- Vaz N., Sousa M.C., Mendes R., Picado A., Plecha S., Dias J.M. (2012). Estudo do impacto das plumas estuarinas na costa oeste de Portugal continental: uso de malhas tridimensionais encaixadas. *V Congresso Brasileiro de Oceanografia*. 13-16 November. Rio de Janeiro, Brazil.

- Mendes R., Rocha C., da Silva J.C.B., Gómez-Gesteira M., deCastro M., Vaz N., Dias J.M. (2013). Observação da pluma estuarina do Douro através de imagens MODIS de alta resolução (Observation of the Douro Estuary turbid plume using high-resolution MODIS ocean colour images). *8º Simpósio de Meteorologia e Geofísica da APMG*. 18-20 March. Ericeira, Portugal.

- Mendes R., Rocha C., da Silva J.C.B., Gómez-Gesteira M., deCastro M., Vaz N., Dias J.M. (2013). Observation of the Douro estuary turbid plume using high-resolution MODIS ocean color images. *6th Workshop on Remote Sensing of the Coastal Zone*. 6-7 June. University of Basilicata, Matera, Italy.

- Mendes R., Vaz N., Dias J.M. (2013). Potential impacts of the mean sea level rise on the hydrodynamics of the Douro River estuary. *12th International Coastal Symposium (ICS 2013)*. 8-12 April. Plymouth University, Plymouth, UK.

- Mendes R., Vaz N., Fernández-Nóvoa D., da Silva J.C.B., deCastro M., Gómez-Gesteira M., Dias J.M. (2014). Observação da pluma túrbida do Estuário do Douro através de imagens MODIS-Aqua. *Encontro de Oceanografia*. 21-22 March 2014. Nazaré, Portugal.

- Fernández-Nóvoa, D., Mendes R., M. deCastro M., Dias J.M., Gómez-Gesteira M. (2014). Analysis of the most important River Plumes in the Atlantic and

Mediterranean Iberian coast by means of Satellite imagery. *International Meeting on Marine Research*. 10-11 July. Peniche, Portugal.

- Mendes, R. (2014). Aplicacação de produtos de sensores multiespectrais no oceano costeiro: Pluma túrbida do Rio Douro. *Mega Censos da Ria de Aveiro: Detecção Remota na Prática*. 3 December. University of Aveiro, Aveiro, Portugal.

- Fernández-Nóvoa, D., Gómez-Gesteira M., deCastro M., Mendes R., Des M., Dias J.M.(2015). Characterization, analysis and comparative of the most important Atlantic Iberian river plumes using MODIS imagery. *VIII Symposium on the Iberian Atlantic Margin*. 21-23 September. Málaga, Spain.

- Fernández-Nóvoa, D., Gómez-Gesteira M., Mendes R., deCastro M., Vaz N., Dias J.M. (2015). Satellite imagery to evaluate the main drivers influencing the Tagus turbid plume development. *ECSA 55*. 6-9 September. London, UK.

Contents

List of figures

List of tables

List of acronyms

ADCP	Acoustic Doppler Current Profiler
ADI	Alternate Direction Implicit
API	Application Programming Interface
CDOM	Coloured Dissolved Organic Material
CFSR	Climate Forecast System Reanalysis
CMAP	Merged Analysis of Precipitation
CZCS	Coastal Zone Color Scanner
CPC	Climate Prediction Center
CTD	Conductivity, Temperature, and Depth
DTM	Digital Terrain Model
EA	Eastern Atlantic
ECOIS	Estuarine COntributions to Inner Shelf dynamics
EOF	Empirical Orthogonal Functions
ESA	European Space Agency
ESRL	Earth System Research Laboratory
FES2004	Finite Element Solution 2004
FES2012	Finite Element Solution 2012
GEBCO	GEneral Bathymetric Chart of the Oceans
GFS	Global Forecast System
GOTM	General Ocean Turbulence Model

HF	High Frequency
IH	*Instituto Hidrográfico*
IPCC	Intergovernmental Panel on Climate Change
MERIS	MEdium Resolution Imaging Spectrometer
MODIS	MODerate resolution Imaging Spectroradiometer
MOHID	Water Modelling System
NAO	North Atlantic Oscillation
NASA	National Aeronautics and Space Administration
NCAR	National Center of Atmospheric Research
NCDC	National Climatic Data Center
NCEP	National Centers for Environmental Prediction
NICC	Northwest Iberian Coastal Current
NIR	Near InfraRed
NOAA	National Oceanic and Atmospheric Administration
NOMADS	National Operational Model Archive and Distribution System
OAR	Office of Oceanic and Atmospheric Research
OBPG	Ocean Biology Processing Group
OpenMP	Open Multi-Processing
PCOMS	Portuguese Coast Operational Modelling System
PC	Principal Component
PIC	Particulate Inorganic Carbon
PSD	Physical Sciences Division
ROFI	Region Of Freshwater Influence
SAR	Synthetic Aperture Radar
SeaDAS	SeaWIFS Data Analysis System
SeaWiFS	Sea-Viewing Wide Field-of-View Sensor

SMOS	Soil Moisture and Ocean Salinity
SNIRH	*Sistema Nacional de Informações sobre Recursos Hídricos*
SSE	Sea Surface Elevation
SST	Sea Surface Temperature
SVD	Singular Value Decomposition
SWIR	ShortWave InfraRed
TSM	Total Suspended Matter
TVD	Total Variation Diminishing
UNESCO	United Nations Educational, Scientific and Cultural Organization
UTC	Universal Time Coordinates
WIBP	Western Iberian Buoyant Plume
WOA2009	World of Ocean Atlas 2009
WOA2013	World of Ocean Atlas 2013
WRF	Weather Research and Forecasting model

List of symbols

A_{eddy}	Sum of grid point where $OW \leq OW_0$
A_h	Horizontal turbulent viscosity
AS	Available scenes
A_z	Vertical turbulent viscosity
$Bias$	Bias function
B_i	Outflow Burger number
C_{10}	Surface drag coefficient
C_d	Dimensionless drag coefficient
C_D	Bottom drag coefficient
C_{Da}	Depth averaged drag coefficient
E	Total irradiance
E_d	Downward irradiance
E_{kp}	Plume Ekman number
E_u	Upward irradiance
f	Coriolis frequency
F_0	Extra-terrestrial solar flux
f_a	Annual frequency (1/365.25 days)
FP	Source or sink term
Fr_i	Outflow Froude number
Fr_1	Upper-layer Froude number

Fr_{1m}	Upper-layer Froude number at the mouth
Fr_{1p}	Upper-layer Froude number within the plume
f_s	Semi-annual frequency (2/365.25 days)
F_w	Equivalent depth of freshwater
g	Gravity acceleration
$g_e^{'}$	Reduced gravity determined for estuarine outflow
$g_p^{'}$	Reduced gravity determined for plume
$g_r^{'}$	Reduced gravity determined for river input
h	Bottom depth
h_i	Bottom depth at the estuary mouth
h_p	Plume thickness
K_b	Bulk Kelvin number
k_c	von Karman constant
K_H	Horizontal diffusion coefficient
K_m	Mouth Kelvin number
K_V	Vertical diffusion coefficient
L_a	Upward radiance contributions due to aerosol scattering (Mie diffusion)
L_g	Upward radiance contributions due to *sun glint*
L_r	Upward radiance contributions due to molecular Rayleigh scattering
L_{ra}	Upward radiance contributions due to Rayleigh-aerosol scattering
L_u	Total upward radiance
L_w	Water-leaving radiance
L_{wc}	Upward radiance contributions due to the *white*-capping phenomena
$MD - AS$	Mean river discharge for available scenes
N	Number of records
nLw	Normalized water-leaving radiance

N_P	Number of valid pixels
$\overline{OC}$	Mean value of the ocean-colour variable
OC_a	Amplitude of annual harmonic
$OC_{ns(t)}$	Non-seasonal anomaly
OC_s	Amplitude of semi-annual harmonic
$OC_{sh(t)}$	Seasonal harmonic time series for the ocean-colour variable at each pixel
OC_t	Original series of the ocean colour variable
OW	Okubo-Weiss parameter
OW_0	Okubo-Weiss threshold
p	Pressure
P	Fraction of particles
P_{AP}	Percentage of available pixels
p_{atm}	Atmospheric pressure
P_i	Number of particles inside each Ria
P_m	Number of particles in the adjacent area of each Ria's mouth
p_v	p-value
Q_E	Estuarine outflow
Q_f	River discharge
Q_x	Zonal component of the Ekman transport
r	Correlation coefficient
R_{ep}	Reynolds number
R_{Di}	Internal Rossby radius of the estuarine outflow
R_{Di}	Internal Rossby radius of the plume
$Rich$	Richardson number
R_i	Outflow Rossby number

Ri_E	Estuary Richardson number
Ri_{E-Mean}	Estuary Richardson number during neap-tides
Ri_{E-Neap}	Estuary Richardson number during mean tides
$Ri_{E-Sring}$	Estuary Richardson number during spring-tides
RH	Relative humidity
$RMSE$	Root mean square error
R_p	Plume Rossby number
Rr	Irradiance reflectance
Rrs	Remote sensing reflectance
S_A	Area of surface
S_a	Reference salinity - 35.6
SE	Standard error
SD	Standard deviation
$SKILL$	Skill parameter
s_n	Normal component of strain
SR	Solar radiation
s_s	Shear component of strain
$S(z)$	Salinity of the water column
t	Time
T_{air}	Air temperature
T_i	Diffuse transmittance of the atmosphere
u	Zonal velocity component
u_c	Velocity of the flow
u_{dis}	Contribution of discharge to W_S calculation
u_F	Random fluctuation of particle velocity
U_i	Mean velocity of the estuarine outflow

u_M	Mean flow velocity
u_{plu}	Velocity of the flow in the plume (surface layer)
u_P	Particle velocity
u_s	Velocity normal to the section
u_{tidal}	Tidal velocity
u_{wind}	Contribution of wind to W_S determination
v	Meridional velocity component
V_{F_w}	Freshwater volume
$V_{F_w}(SecN)$	Freshwater volume transported through section N
VP	Average of valid pixels for each cell
w	Vertical velocity component
W	Wind velocity
W_{10}	Wind velocity at 10 m height
W_E	Width of the estuary
$Wflux$	Advective flux
W_m	Width of the estuary mouth
W_p	Extent of the plume across-shelf
W_S	Wind strength index
W_x	Zonal wind component
W_y	Meridional wind component
x	Longitude in Cartesian coordinates
x_i	Particle position in Cartesian coordinates
X_{obs}	Observed data
X_{model}	Predicted data
x_s	Horizontal distance across section
y	Latitude in Cartesian coordinates

z	Depth
z_0^b	Bottom roughness length
η	Free surface elevation
λ	Wave length
ρ	Density
ρ'	Density anomaly
ρ_0	Reference density
ρ_a	Air density
ρ_{amb}	Ambient seawater density
ρ_r	River input density
σ_{OW}	Spatial standard deviation of OW
$\vec{\tau}_W$	Wind surface stress
$\vec{\tau}_{Wx}$	Zonal component of wind surface stress
$\vec{\tau}_{Wy}$	Meridional component of wind surface stress
Φ	Radiant flux
ϕ_a	Annual phase
ϕ_s	Semi-annual phase
ω_r	relative vorticity

Chapter 1

Introduction

1.1 Motivation

Estuarine discharges originate coastal water masses of lower density carrying several dissolved and suspended riverine materials, and consequently with distinct properties from surrounding ocean waters. This outflow to the coast can be commonly observed near the estuaries mouth by the different colour between riverine and ocean waters. The area of propagation of these water masses in ambient coastal ocean, identified by riverine/estuarine properties (salinity, temperature, density, colour, etc.), is defined as the river or estuarine plume.

River plumes are the major gateways of materials transfer from land to coastal ocean, e.g. nutrients, biological species, sediments and contaminants (Morris et al., 1995; Demaster and Pope, 1996; Smith and Demaster, 1996; Le Pape et al., 2003; Bruland et al., 2008). The impact and dispersion of riverine material along coast strongly depends on physical processes, which determine the plume fate over shelf (Horner-Devine et al., 2015). Thus, the evaluation of river plume's dispersion and dynamics has particular relevance since, for example, transported dissolved materials can largely affect the primary production and, consequently, the economy of local communities. With the growth of the world's coastal population combined with future expected climate change impacts in these regions, an

extra pressure will be placed on coastal areas. Consequently, a good understanding of the river plumes dynamics and processes, necessary to predict their propagation in the ocean, is essential in terms of both scientific research and socio-economic purposes.

The characteristics and processes related with generation and propagation of estuarine plumes are rather difficult to generalize, since each coastal system presents particular features. Additionally, *in situ* monitoring of these coastal features is often very difficult due to great spatial and temporal variability of its dominant drivers. Thus, coastal circulation models and remote sensing imagery have started to be used recently to fill the gaps on the understanding of plume's dynamics and to predict and study in detail their patterns and physical processes (Chao and Boicourt, 1986; Fong and Geyer, 2002; García Berdeal et al., 2002; Robinson, 2004; Choi and Wilkin, 2007; Guo and Valle-Levinson, 2007; Otero et al., 2008; Palacios et al., 2009; Horner-Devine et al., 2009; Valente and da Silva, 2009; Jurisa and Chant, 2012; Saldías et al., 2012). These tools are particularly relevant to examine and compare how different buoyant plumes propagate under different forcing drivers and regional settings (e.g. river discharge, tide, wind magnitude and direction, ocean currents, coastal bathymetry and morphology, etc.).

Regarding the northern Portuguese and Galician shelf, some studies highlighted the importance of the river runoff, and consequently of estuarine plumes, in the coastal circulation (Peliz et al., 2002; Santos et al., 2004; Relvas et al., 2007; Torres and Barton, 2007). In this region, buoyancy discharge from the Douro River among others, combined with a warmer and saltier poleward current, determines the circulation during the autumn. Studies by Peliz et al. (2002) and Otero et al. (2008, 2009, 2013) revealed the role of the alongshore winds in the confinement (downwelling-favourable conditions) or exportation (upwelling-favourable conditions) of the buoyant outflow. In these studies they found the accumulation of a less dense water mass originated from all river outflowing along northern Portuguese coast as one large buoyant plume: the Western Iberian Buoyant Plume (WIBP).

The dynamics of one of the main WIBP contributors (the Minho River) was previously assessed in detail by Sousa (2013), revealing a rapid response of the plume to wind variations. Here, the Minho plume flows northwards under downwelling-favourable

conditions, propagating into Rias Baixas where may reverses the local circulation patterns and affects biological productivity (deCastro et al., 2004; Álvarez et al., 2008; Sousa et al., 2014c,b).

Despite the numerous studies, addressing coastal upwelling and WIBP dynamics under several scenarios (Peliz et al., 2002; Otero et al., 2008, 2009, 2013), reduced attention has been given to the individual study of the freshwater output from the Douro Estuary, a system that can be considered the most important freshwater contributor and sediment and nutrient supplier to the Atlantic Ocean in the Northwestern Iberian coast. Thus, the study of the Douro estuarine plume dynamics is crucial for a deeper understanding of the inner-shelf physical processes in the region.

1.2 Objectives

This dissertation aims to understand the physical processes associated with the generation and propagation of the Douro estuarine plume in the adjacent coastal ocean taking into account the effects of typical drivers of this phenomenon (river discharge, wind and tide) as well as of relevant climate indexes. Particularly, it intends to know in detail the Douro estuarine plume dynamics and how its physical properties change the adjacent coastal hydrography and circulation. Innovative remote sensing data processing methodologies and new coastal and estuarine numerical models implementations were used to achieve these objectives, in combination with prior available *in situ* observations. This work has the following specific goals:

- develop a methodology to detect and characterize the mean-state of the Douro estuarine plume under different conditions using remote sensing imagery;
- study the inter-annual and seasonal variability of the Douro estuarine plume using long-term remote sensing imagery;
- characterize the Douro river discharge and the estuary hydrography;

- implement a 2D numerical model for the Douro Estuary;
- develop a 3D nested model application to study the propagation of the Douro estuarine plume and its impact on the adjacent coastal hydrography and circulation;
- characterize the Douro estuarine plume dynamics under different conditions of river discharge and wind forcing;
- study the interaction between the Douro and Minho estuarine plumes and its effect on the WIBP dynamics.

1.3 Background

1.3.1 Douro River and coastal region

In the northern Portuguese coast, one of the most important buoyancy sources is the Douro River estuary. The Douro River is located in a granitic drowned valley flowing to the Northwestern coast of Portugal (Figure 1.1).

The Douro is an international watershed, shared between Spain (80%) and Portugal (20%). It is the the largest drainage basin in the Iberian Peninsula, with an area of 97 682 km^2 (Figure 1.1a). The Douro River has its source at Los Picos de Urbion (La Rioja, Spain) at an altitude of 1700 m, flowing to the coast across a total distance of 927 km. The Douro basin is heavily dammed, mostly for hydroelectric generation (Ferreira et al., 2003), with 51 large dams regulating the flow within the watershed. The large dams retain more than 1100 hm^3 (13%) of water in Portuguese reservoirs and 7500 hm^3 (87%) on the Spanish side of the watershed (Bordalo et al., 2006).

The estuary itself is located near the second largest city of Portugal, Porto, with an estimated population of 1.8 million people in the Porto Metropolitan Area.

The Douro Estuary plays an important role in the regional and Portuguese national economy, being a navigable channel for many commercial, fishing and tourism ships. It is upstream limited by a dam (Crestuma-Lever dam), built in 1985 at a distance of 21.6 km

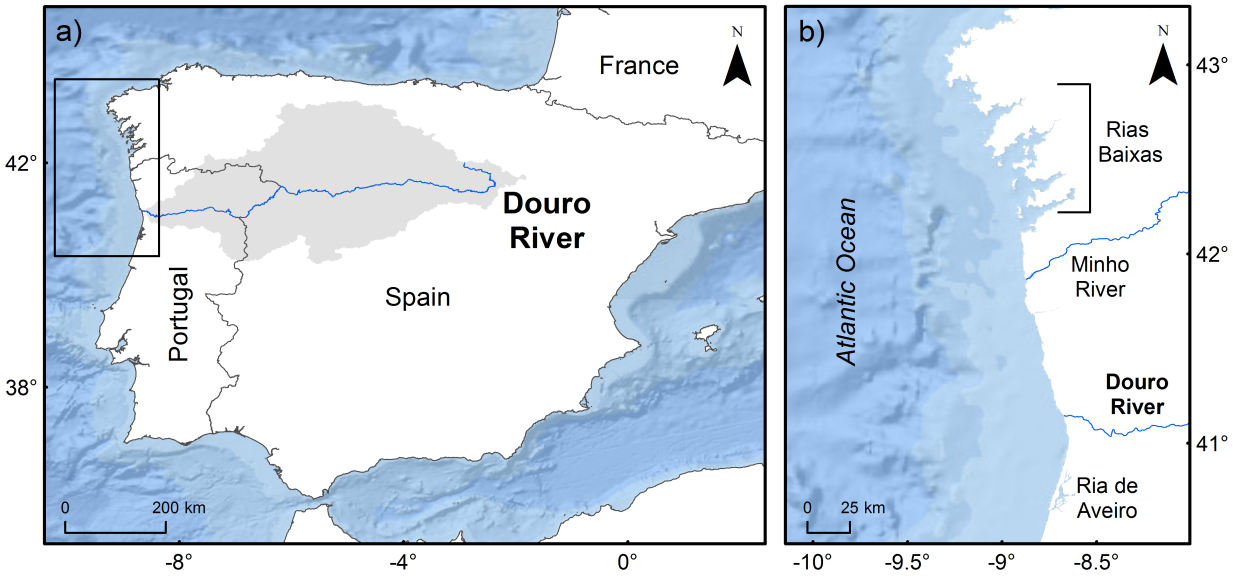

Figure 1.1: Douro River and its drainage basin (a). Northwestern Iberian coast and location of the Ria de Aveiro Lagoon, Douro and Minho estuaries, and Rias Baixas (b).

from the mouth, for electric power generation purposes. The total estuarine area and water volume are about 9.8 $\times$ 10^6 m^2 and 58.8 $\times$ 10^6 m^3, respectively (Ferreira et al., 2003). From literature, the annual mean river flow ranges from 455 m^3 s^{-1} to 708 m^3 s^{-1} (Ferreira et al. (2003), Bordalo et al. (2006), Azevedo et al. (2010) and from `http://www.ospar.org`). The river discharge is characterized by high short-term variability, ranging between zero flow and >1000 m^3 s^{-1}, in a temporal scale of hours (Azevedo et al., 2008). Tide is majority represented by semi-diurnal components with an average tidal range of 2.8 m at the mouth and 2.6 m at the head of the estuary (Vieira and Bordalo, 2000). The maximum tidal range, during spring tides, is 3.8 m (Ferreira et al., 2003) and the average tidal prism is about 20.9 $\times$ 10^6 m^3 (Ferreira et al., 2003). The residence time of the estuary ranges from 8 hours, during winter, to more than two weeks, during summer (Vieira and Bordalo, 2000; Ferreira et al., 2003). The estuary is highly dependent on river discharge with strong vertical salinity stratification under conditions of low runoff, whereas during high river flows the whole estuary became a river (Vieira and Bordalo, 2000). The Local Natural Reserve of Douro Estuary, located on the left margin of the estuary mouth, is composed by several important biotopes, being one of the main areas in Portugal that offers good condition of shelter and

feeding for migratory wintering shorebirds (Carvalho et al., 2013).

Rainfall episodes enhance river plume outflow, promoting a significant supply of suspended and dissolved matter to the continental shelf (e.g. sediments and nutrients) (Saraiva et al., 2007; Reis et al., 2012). The Douro River delivers about 87% of the fluvial sediments discharged into the Northwestern Iberian coast (Dias, 1987) and the actual deficit of sediments discharged by its estuary is commonly referred as the primary reason for severe erosion along southward beaches (Oliveira et al., 1982; Dias, 1990; Veloso-Gomes et al., 2004).

The Douro estuarine plume, combined with the WIBP itself, also poses a particular relevance on the coastal biogeochemistry features under winter conditions, in particular during upwelling events (Santos et al., 2004; Ribeiro et al., 2005; Prego et al., 2007; Picado et al., 2014). Vertical stratification, enhanced by the plume, plays a key role in larvae retention (Santos et al., 2004). In these events, buoyant water rich in nutrients stimulates phytoplankton growth (Chícharo et al., 2003; Santos et al., 2004; Prego et al., 2007), contributing to an increase of primary production

The Douro River is the main freshwater contributor to the WIBP (Peliz et al., 2002), which is a low-salinity water lens ($<$35.7) expanding over the shelf with 30-40 km wide and about 20 m depth. Mesoscale studies showed that current velocities at the WIBP, during extremely high discharges, could reach more than 1 m s^{-1} under strong downwelling-favourable winds (Marta-Almeida et al., 2002; Ruiz Villarreal et al., 2005). Otero et al. (2008, 2013) have identified three characteristic situations of the WIBP response to wind events: a) a plume confinement to the coast during downwelling-southerly-winds, b) a plume expansion during the declining phase of the downwelling event by relaxation of wind and c) a plume expansion by upwelling-northerly-winds.

There are other freshwater sources along the Northwestern Iberian Peninsula coast, which can influence the Douro estuarine plume dynamics or be influenced by its buoyancy and properties (Figure 1.1). The Minho River is the second most important freshwater source flowing to the Atlantic Ocean in the region. There are other small freshwater sources (the Ave, Cávado and Lima rivers, Figure 1.1), but have insignificant discharges when

compared to the two rivers referred. Two other far estuarine systems are potentially located in the area of the Douro estuarine plume influence: the Rias Baixas, four flooded tectonic valleys (Ria de Vigo, Ria de Pontevedra, Ria de Arousa, and Ria de Muros) located 110 km north of the Douro River (Figure 1.1); and the Ria de Aveiro coastal lagoon, mainly a tidal driven system and highly dynamic in terms of physical and biogeochemical processes, located 60 km south of the Douro Estuary (Figure 1.1).

1.3.2 Estuarine plumes

The first studies concerning estuarine/river plumes and its dynamic were present by Takano in the fifties years (Takano, 1954, 1955). These studies describe the steady state theory of a river plume entering the sea off a straight coast. From sixties to eighties, extensive field observational studies of the plume dynamics had been undertaken around the world. There were studies in the Columbia River estuary (Stefánsson and Richards, 1963; Park, 1966) and Connecticut Estuary (Garvine, 1974) in the U.S.A.; in the Fraser River (Royer and Emery, 1982) in Canada; in the Rhine River estuary (van Alphen et al., 1988) in the Netherlands; and in the Rhone River estuary (Szekielda and Kupferman, 1973) in France.

Typical features characterize most of river plume systems: near the mouth of an estuary, the freshwater outflow frequently forms an anticyclonic bulge, and a buoyancy-driven coastal-attached current transports a large portion of the freshwater along the coast. This is the classical view in the absence of wind, tidal and wave forcing (Figure 1.2) described in Yankovsky and Chapman (1997), Yankovsky (2000), Fong and Geyer (2002) and Hetland (2005), among others.

Several authors divided the plume morphology in many forms. Garvine (1982) has proposed a scheme that divides the buoyant surface plumes into three contiguous spatial fields: source, near and far-field regions. The source field is the region comprising the river/estuary mouth. The near-field is where the initial expansion of the plume occurs and the contrast between plume and ambient waters is still large. Usually its outer boundary is

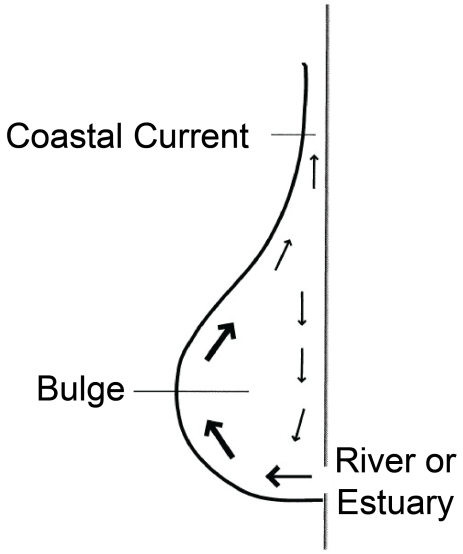

Figure 1.2: Plume circulation scheme (bulge and coastal current). The flow along the seaward side of the bulge transports water that supplies both the coastal current and the continually growing recirculation within the bulge (adapted from Fong and Geyer (2002)).

marked by a sharp frontal region. The far-field region is where the final merge of source water with the ambient water occurs.

Later, Hetland (2005) decomposed the system estuary-river plume into three interacting components: the estuary, the near and far-field plumes. The estuary and the near-field plumes are characterized by intense mixing of fresh and salt water. The far-field region refers to the area outside the influence of the river mouth. Essentially, the river-runoff control is more effective in the near-field region. Once the inertia momentum from the river discharge ends or weakens, the wind forcing becomes one of the key factors controlling the plume structure and buoyant plume dispersion (Warrick, 2004; Hetland, 2005). Moreover, Horner-Devine et al. (2009) proposed a modification in the Garvine classification, decomposing the near-field plume into the pulsed tidal plume and the residual recirculating plume for studies in estuaries or rivers with with large tidal influence, such as the Columbia River in the USA.

Recently in a review regarding river plumes (Horner-Devine et al., 2015), all these schemes were combined and summarized. The most important processes in a river/estuarine plume are determined by the scale, geometry and different forcings of the plume. Thus,

several different plume shapes are observed in the field based on the geometry of the coast, on the magnitude of the discharge and on other external forcing such as wind. Based on that, Horner-Devine et al. (2015) presents the six plume morphologies most observed around the world (Figure 1.3): the prototypal; the nonrotational; the wide estuary; the angled inflow; the delta; and the Region Of Freshwater Influence (ROFI).

The anatomy of a prototypal plume (Figure 1.3a) is composed by four dynamical regions: 1- the source region, where the buoyancy and inertial momentum determined by estuarine processes are responsible for the initial transformation of river discharge; 2- the near-field region, where the river momentum exceeds the buoyancy of the plume layer. In coasts where tides are important, this region is strongly time dependent, specially because of the ebb-flood cycle, and is common referred as the tidal plume (Horner-Devine et al., 2009; Nash et al., 2009; Kilcher and Nash, 2010; Kilcher et al., 2012); 3- the mid-field region, where the inflow tends to decrease its influence in the plume fate. It marks the transition from the inertial near-field jet to the geostrophic and/or wind-dominated far-field plume; 4- the far-field region, where the river discharge has no influence in the plume and its dynamic

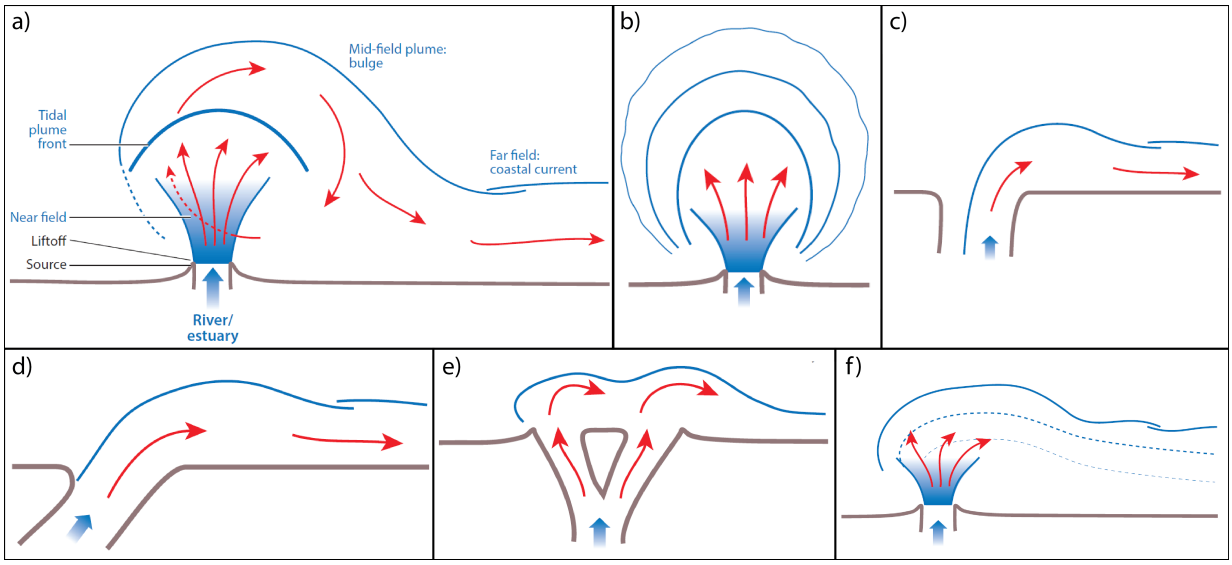

Figure 1.3: River plume morphologies: prototypical (a), nonrotational (b), wide estuary (c), angled inflow (d), delta plume (e), and ROFI (f) (adapted from Horner-Devine et al. (2015)).

is determined by Coriolis, buoyancy, wind, and, in some occasions, bottom stress. If wind magnitude and direction do not favour the offshore plume transport, a coastal current is created along shelf. The Columbia (Hickey et al., 1998; Horner-Devine, 2009; Hickey et al., 2010), Merrimack (MacDonald et al., 2007; Hetland and MacDonald, 2008), the Niagara (Masse and Murthy, 1992; Horner-Devine et al., 2008), and the Hudson rivers plumes (Kohut et al., 2005; Chant et al., 2008a; Jurisa and Chant, 2012) are recognized examples of prototypal plumes.

The nonrotational plumes (Figure 1.3b) are only slightly affected the Earth's rotation, because the rivers mouths are located close to the equator or the discharge is very small. The Teign and the Amazon rivers plumes are examples of this type of plumes (Geyer et al., 1991; Lentz and Limeburner, 1995; Pritchard and Huntley, 2006; Molleri et al., 2010).

Wide estuary plumes (Figure 1.3c) do not have either near field region and re-circulating bulge. The rivers mouth are sufficiently wide to separate freshwater to one side of the estuary due to Earth's rotation. These type of plume just present the coastal current (far-field region). Examples include the Chesapeake and Delaware Bay plumes (Marmorino et al., 2000; Houghton et al., 2004; Dzwonkowski and Yan, 2005; Whitney and Garvine, 2005).

In the angled inflow plumes (Figure 1.3d) the inflow occurs with a small exit angle to the coast, affecting significantly the direction of the plume propagation. Thus, these plumes typically have no bulge. The Eel River plume is a classic example (Geyer et al., 2000).

The delta plumes (Figure 1.3e) are common formations from many of the world's largest river systems, such as Mississippi (Walker, 1996; Schiller et al., 2011), Changjiang (Lu and Shi, 2007; Wu et al., 2014), Nile and Mekong deltas. The freshwater enters the ocean by several river channels, creating many outflows, which interact with each other in the coastal sea.

In ROFI's, the plumes have a strong interaction with the bottom and the bottom friction controls its offshore length scale (Figure 1.3f). This type of plume is characteristic from shallow marginal seas like the coast of United Kingdom, Belgium and Netherlands. The Rhine (de Kok, 1996; de Ruijter et al., 1997; Hessner et al., 2001) and Liverpool bay

(Verspecht et al., 2009; Palmer and Polton, 2011) are typical examples.

A large number of dynamical classifications for the plumes had been proposed and applied along the time.

Chao (1988a) suggested a classification scheme based upon an internal Froude number and a dissipation parameter. The coastal current evolution was divided in four dynamical groups: subcritical, supercritical, diffusive-subcritical and diffusive-supercritical.

Garvine (1995) proposed a classification where Kelvin number evaluates the relative importance of inertia and rotation. The two limiting cases are the small and large-scale discharges.

Yankovsky and Chapman (1997) developed a simple theory that predicts the vertical structure and offshore spreading of a localized buoyant inflow onto a continental shelf. From a formulation based on the barotropic Rossby radius and on the Burger number, they identify three different types of plumes in terms of their vertical structures: a bottom-advected plume; a surface-advected plume and an intermediate plume.

More classifications in terms of external plume forcings, e.g. wind, can be found in literature. For example, the wind index purposed by Whitney and Garvine (2005) assesses the relative importance between the river discharge and wind intensity in the plume propagation.

The structure of the plume can be quite different from the simplistic view of a prototypal plume. The spatial and temporal variability of plume events will be affected by a number of factors, including storms and rainfall seasonal cycles, magnitude and direction of wind stress, bathymetry, discharge strength and exit angle (Lihan et al., 2008). Since plumes are very dynamic systems (changing in a time-scale of the order of hours), it is very difficult to monitor events using traditional methods, such as mooring arrays and shipboard surveys (Otero and Siegel, 2004). Thus, the implementation of numerical models and the use of remote sensing observations are essential to fully assess and understand the estuarine plume dynamics (Chao and Boicourt, 1986; Chao, 1988b; Ruddick et al., 1994; Kourafalou et al., 1996; Xing and Davies, 1999; Fong and Geyer, 2001; García Berdeal et al., 2002; Otero et al., 2008; MacCready et al., 2009; Hetland, 2010).

1.3.3 Remote sensing

With the fast growing and development of the satellite technology, remote sensing has become one of the most popular methods to detect river plumes in recent years. Remote sensors can distinguish most river plumes from oceanic water because they differ in colour, turbidity, salinity and/or temperature. Salinity is traditionally the natural tracer of freshwater plumes. Although remotely sensed surface salinity both by Soil Moisture and Ocean Salinity (SMOS) (Font et al., 2010) and Aquarius satellite missions (Le Vine et al., 2007) from European Space Agency (ESA) and National Aeronautics and Space Administration (NASA) respectively, was already used to study river plumes (i.e. Amazon River plume, Korosov et al. (2015)), the spatial and temporal resolution are not enough for mapping smaller plumes, which can present fine-scale spatial structure that changes rapidly, like the Douro.

Due to these limitations, ocean-colour satellite images have been historically used with considerable success to track the behaviour and main scales of riverine plumes because of the optical differences and significant correlation between turbidity and surface salinity (Robinson, 2004; Dzwonkowski and Yan, 2005; Thomas and Weatherbee, 2006; Palacios et al., 2009; Shi and Wang, 2009b; Valente and da Silva, 2009; Saldías et al., 2012). The turbidity concept is associated with the measurement of water *cloudiness* (Davies-Colley and Smith, 2001). It is usually linked to the presence of suspended and dissolved matter, such as clay, silt, finely divided organic matter, plankton and other microscopic organisms, organic acids and dyes, which decreases the water transparency (ASTM-International, 2003; Petus et al., 2010; Güttler et al., 2013). River plumes often present strong suspended sediment signals, affecting that water *cloudiness*, especially in the green and red light wavebands in the visible region of electromagnetic spectrum (Loisel et al., 2013).

The most widely used colour sensors in ocean studies are the Sea-Viewing Wide Field-of-View Sensor (SeaWiFS) onboard of the SEASTAR (or OrbView2), the MEdium Resolution Imaging Spectrometer (MERIS) aboard of the Envisat satellite or the MODerate resolution Imaging Spectroradiometer (MODIS) sensors onboard both Terra and Aqua

satellites. The spatial resolution of these sensors is higher than 1 km (can be 250 m), depending on the bands used (Nezlin et al., 2005; Nezlin and DiGiacomo, 2005). Nowadays, only the MODIS-Terra and MODIS-Aqua are fully operational with free access to all images collected since February 2000 (MODIS-Terra).

MODIS instruments (Figure 1.4a) are designed to take measurements in spectral regions that have been used by previous satellite sensors, i.e. SeaWiFS and Coastal Zone Color Scanner (CZCS). MODIS extended that environmental data sets and promoted the continuity of data collection essential for understanding both long and short-term change in the global environment. Instruments capture data in 36 spectral bands with wavelengths ranging from 0.4 μm to 14.4 μm and at different spatial resolutions. Two bands are imaged at a nominal resolution of 250 m at nadir, with five bands at 500 m, and the remaining at 1 km (Table 1.1). Both satellites with MODIS sensor are set at a sun-synchronous orbit at 705 km of altitude with a 10:30 a.m. descending node (Terra) and 1:30 p.m. ascending node (Aqua)(Figure 1.4b), achieving a 2330 km swath and providing a global coverage every one to two days. MODIS sensors aboard Aqua and Terra satellites were designed to provide measurements in large-scale global dynamics, including changes in Earth's cloud cover, radiation budget and processes occurring in the oceans.

MODIS imagery can be found in the NASA OceanColor website (`http://oceancolor.`

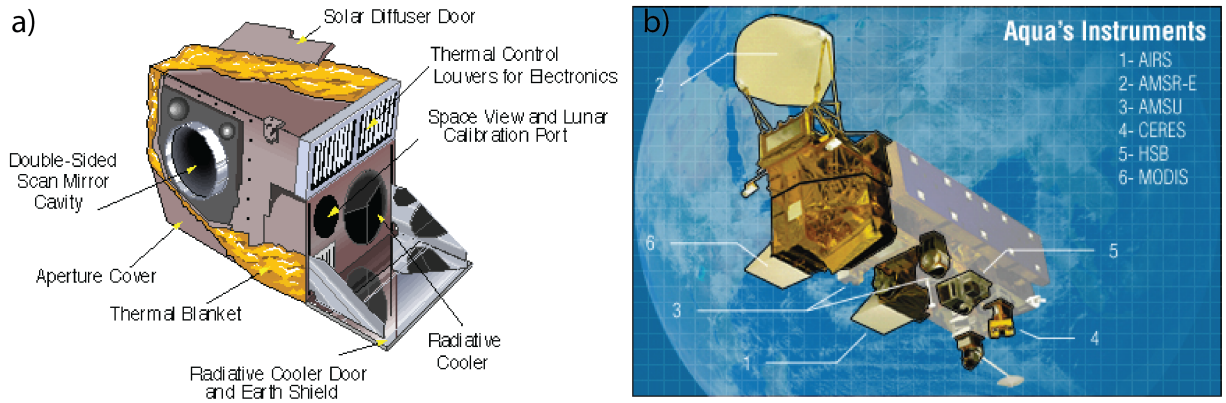

Figure 1.4: The MODIS instrument (`http://mcst.gsfc.nasa.gov/`)(a) and Aqua satellite (`http://aqua.nasa.gov`)(b)

Table 1.1: The 36 spectral band captured by the MODIS instrument (adapted from `http://modis.gsfc.nasa.gov/`).

Primary Use	Band	Bandwidth (nm)	Resolution (m)
Land	1	620–670	250
Cloud / Aerosols	2	841–876	250
	3	459–479	500
Land	4	545–565	500
Cloud	5	1230–1250	500
Aerosols properties	6	1628–1652	500
	7	2105–2155	500
	8	405–420	1000
	9	438–448	1000
Ocean-colour	10	483–493	1000
	11	526–536	1000
Phytoplankton	12	546–556	1000
	13	662–672	1000
Biogeochemistry	14	673–683	1000
	15	743–753	1000
	16	862–877	1000
	17	890–920	1000
Atmospheric	18	931–941	1000
Water Vapour	19	915–965	1000

Primary Use	Band	Bandwidth (μm)	Resolution (m)
	20	3.660–3.840	1000
Surface and cloud	21	3.929–3.989	1000
temperatures	22	3.929–3.989	1000
	23	4.020–4.080	1000
Atmospheric	24	4.433–4.498	1000
pressure	25	4.482–4.549	1000
	26	1.360–1.390	1000
Cirrus clouds	27	6.535–6.895	1000
water vapour	28	7.175–7.475	1000
Cloud properties	29	8.400–8.700	1000
Ozone	30	9.580–9.880	1000
Surface and cloud	31	10.780–11.280	1000
temperatures	32	11.770–12.270	1000
	33	13.185–13.485	1000
Cloud top	34	13.485–13.785	1000
altitude	35	13.785–14.085	1000
	36	14.085–14.385	1000

`gsfc.nasa.gov`), which is supported by the Ocean Biology Processing Group (OBPG) at NASA's Goddard Space Flight Center at different levels of information: Level 0 (L0) - data that are unprocessed at full resolution; Level 1A (L1A) - data that are reconstructed, unprocessed at full resolution, time-referenced and annotated with ancillary information including radiometric and geometric calibration coefficients and georeferencing parameters computed and appended but not applied to the Level 0 data; Level 1B (L1B) - L1A data that have instrument/radiometric calibrations applied; Level 2 (L2) - data of derived geophysical variables at the same resolution as the source L1 data; Level 3 (L3) - data derived from geophysical variables that have been aggregated/projected onto a defined spatial grid over a defined time period; and Level 4 (L4) - data that are model outputs or results from analyses of lower level data.

Ocean-colour images from MODIS has been successfully used to track the behaviour

and principal scales of variability of river plumes in coastal areas around the globe. As examples: the Danube delta, Romania (Güttler et al., 2013), several rivers in Mediterranean Sea (Arnau et al., 2004; Fernández-Nóvoa et al., 2015), the Tagus Estuary, Portugal (Valente and da Silva, 2009), rivers in the Bay of Biscay, France (Doxaran et al., 2009; Petus et al., 2010, 2014; Costoya et al., 2015), the Mississippi River (Miller and McKee, 2004; Shi and Wang, 2009b), the Columbia River (Palacios et al., 2009; Horner-Devine et al., 2009), the Chesapeak Bay (Dzwonkowski and Yan, 2005), the coastal region southern California coast (Nezlin et al., 2007; Warrick et al., 2007; Nezlin et al., 2008; Lahet and Stramski, 2010), the Delaware Bay (Jiang et al., 2009) and the Hudson River (Chant et al., 2008a) in USA, the Amazon River, Brazil (Kilham and Roberts, 2011; Aurin et al., 2013), the La Plata River, Argentina/Uruguay (Dogliotti et al., 2011), small rivers off central Chilean coast, Chile (Saldías et al., 2012), the Congo River, Republic Democratic of the Congo/Angola (Hopkins et al., 2013), the Tokachi River, Japan (Lihan et al., 2008), the Yellow River (Qiao et al., 2008) among other rivers that flow into East China Sea in China (Ahn et al., 2008) and the Brisbane River (Yu et al., 2011) and the rivers in Mackay–Whitsunday region of Queensland (Brodie et al., 2010) in Australia.

Ocean-colour radiometry is the measurement of spectral distribution of radiance (or reflectance) upwelling from the ocean in the visible regime of the electromagnetic spectrum (Figure 1.5). It is a passive remote sensing method where the sensor *simply* observes the light (in this case irradiated from the Sun) that is emitted or reflected by the water mass.

Reflectances are the most commonly used apparent optical properties in scientific works about the ocean behaviour. In the early days of ocean-colour remote sensing, algorithms to relate the irradiance reflectance, Rr, with quantities such as chlorophyll concentrations were developed (Gordon and Morel, 1983; Loisel and Morel, 1998). Recently, Rrs (remote sensing reflectance) and nLw (normalized waterleaving radiance) became the apparent optical properties of choice for remote sensing of ocean properties and the basis for many other algorithms (O'Reilly et al., 1998; Gordon and Voss, 1999; O'Reilly et al., 2000).

Rrs is defined as the light incident onto the water surface that is eventually scattered back to the sensor through the surface (IOCCG (2011) and `http://www.oceanopticsbook.`

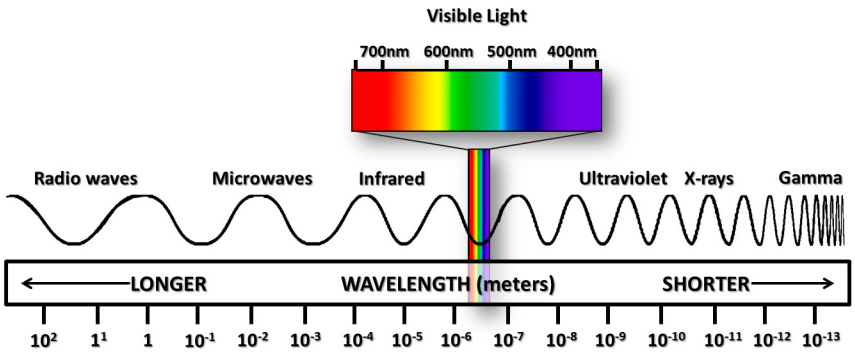

Figure 1.5: Electromagnetic spectrum from `www.ces.fau.edu/nasa`.

`info`). The total downward irradiance at sea level, E_d, with the upwelling irradiance light, E_u, represents the total irradiance, E, of a horizontal surface (Figure 1.6, IOCCG (2011)). The irradiance, E, in a wavelength, λ, at a given depth, z, can be defined as the radiant flux, Φ, per unit area of surface, S_A (Kirk, 1994):

$$E(z,\lambda) = \frac{d\Phi}{dS_A} \tag{1.1}$$

Rrs is then defined as:

$$Rrs = \frac{L_w}{E_d} \tag{1.2}$$

where water leaving radiance, L_w, is the radiance leaving the sea at nadir and quantified *just*

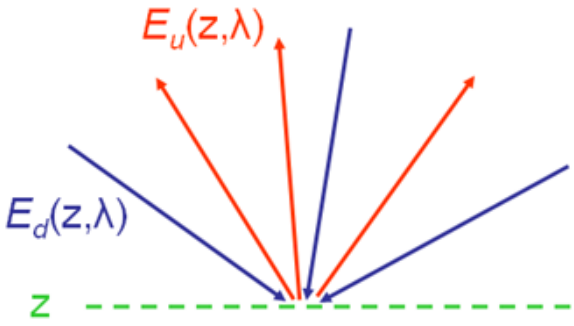

Figure 1.6: Light rays contributing to the irradiance reflectance, Rr, from `http://www.oceanopticsbook.info`.

above surface, taking into account refraction and reflection at the interface. L_w is a part of the total upwelling radiance, L_u (Figure 1.7, Equation 1.3) detected by the sensor. L_u is the linear sum of L_w, which is not directly measured, with contributions by molecular Rayleigh scattering, L_r (can be accurately computed), by aerosol and Rayleigh-aerosol scattering, L_a and L_{ra}, respectively (estimated in Near InfraRed (NIR) bands from measured radiances and extrapolated to visible using aerosol models), by the *white*-capping phenomena, L_{wc} (estimated from statistical relationships with wind speed) and by the direct solar radiation specularly reflected from the ocean surface (*sun glint*), L_g (Gordon and Wang, 1992). T_i is the diffuse transmittance of the atmosphere, which depends mainly on Rayleigh scattering and gaseous absorption. This parameter can be well computed (Gordon and Morel, 1983).

$$L_u = L_r + (L_a + L_{ra}) + T_i.L_{wc} + L_g + T_i.L_w \tag{1.3}$$

The process of retrieving L_w is typically referred as atmospheric correction (Equation 1.3).

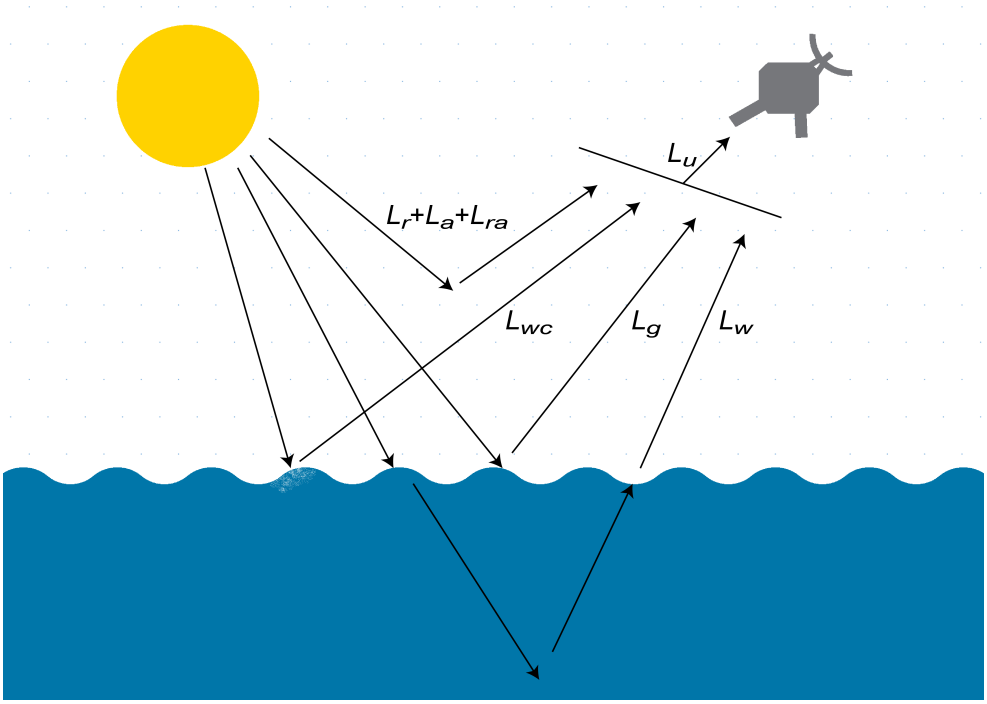

Figure 1.7: Simplified scheme of light rays path contributing to L_u measured by the satellite.

Classic methods for atmospheric correction exploit the high absorption by seawater in the red and NIR spectral regions. In the open ocean, water can be considered to absorb all the light in the NIR. Thus, the captured signal is assumed to be due to the atmospheric path radiance and sea surface reflectance. This is not always the case when considering turbid waters, e.g. coastal regions (Loisel et al., 2013), and frequently other atmospheric corrections approaches and methods, e.g. using information from ShortWave InfraRed (SWIR) bands, had been performed to generate more accurate images in moderate and high turbid regions (Ruddick et al., 2000; Wang and Shi, 2007; Shi and Wang, 2009a; Wang et al., 2009; Aurin et al., 2013).

After successfully atmospheric correction, L_w is the estimate result given by the ocean-colour measurements coming from an angle and azimuth defined by the viewing angle and position of the satellite sensor and not nadir. The L_w normalization process reduces the dependence on the Sun's elevation and the viewing incidence angle (Robinson, 2010; IOCCG, 2011):

$$nLw = L_w \frac{F_0}{E_d} \tag{1.4}$$

where F_0 is the extra-terrestrial solar flux. Since F_0 is a constant, nLw, at any wavelength, is always function of Rrs (see Equation 1.2).

nLw represents what a sensor would measure if looking straight down from an orbit just above the sea surface at the bottom of the atmosphere. This is what our eyes would detect as the colour and brightness of the sea, ignoring any light reflected from the surface (Robinson, 2010)

This is one of the standard products of the ocean-colour sensors and will be used throughout this thesis.

1.3.4 Numerical modelling

Numerical modelling studies performed in various regions around the world have proven to be useful tools for analysing plume dynamics in coastal zones affected by river

outflows (Fong and Geyer, 2001; García Berdeal et al., 2002; Choi and Wilkin, 2007; Guo and Valle-Levinson, 2007; Otero et al., 2008; Horner-Devine et al., 2009; Jurisa and Chant, 2012).

Chao and Boicourt (1986) were the first to model estuarine plumes with a 3D numerical model, in contrast to previous analytic plume studies (Kao, 1981). The effect of the wind in river plumes was studied a few years later by Chao (1988b), for a wide theoretical estuary. In the mid-1990s and at the beginning of the 21^{th} century, realistic modelling studies have gained great popularity in the scientific community. For example, Ruddick et al. (1995) reported on a 3D modelling study of Rhine River estuarine plume and de Kok (1996, 1997) developed a two-layer model for the same river plume in the Netherlands. The investigation of this topic was progressively extended onto the shelf (Kourafalou et al., 1996; Xing and Davies, 1999; Fong and Geyer, 2001; García Berdeal et al., 2002). Since the beginning of the 21^{th} century, several ocean models have been developed and used to study the plume dynamics in tidal estuaries and coastal waters (de Kok et al., 2001; Liu et al., 2002; Arnoux-Chiavassa et al., 2003; Otero et al., 2008; Jurisa and Chant, 2012; Otero et al., 2013).

Regarding wind influence, all studies confirm the primary conclusion of Chao (1988b): the plume response to wind can be described by the Ekman drift, even when the propagation area is shallow and frictional. During upwelling-favourable alongshore winds, the plume is advected offshore and becomes thinner. In contrast, during downwelling-favourable winds, the coastal jet is strengthened, leading to an alongshore acceleration of the plume.

Tidal forcing is also an important constraint factor of the plume dynamics, depending on the different tidal prism and river discharge conditions in the estuary (Vaz et al., 2009a). For example, numerical modelling simulations show that the spring-neap cycle can contribute to a partially-detached anticyclonic bulge formation near the mouth (Yankovsky et al., 2001), a propagation of isolated low salinity patches over ocean (Rong and Li, 2012), and a stabilization of the plume bulge growth (Isobe, 2005).

In the northern Portuguese coast, apart from the full description of shelf circulation and WIBP behaviour, presented by Otero et al. (2013), no other studies of the Douro

adjacent coastal circulation were found. In the Otero et al. (2013) study, the coarse resolution (∼1.3 km) of the model used did not allow an adequate analysis of the inner-shelf circulation, as were note captured pulses from river plumes associated with the tidal phase of estuary mouths.

In this work the numerical model Water Modelling System (MOHID) was the choice to simulate estuarine and coastal dynamics of Douro. MOHID (`www.mohid.com`) is a 3D baroclinic finite volume marine model, designed for coastal and estuarine shallow water applications. It has been applied to different coastal and estuarine areas, showing its ability to simulate complex flows features. In Portugal, several estuarine systems have been studied: Douro (Silva, 1996) and Mondego rivers (Saraiva et al., 2007); Ria de Aveiro (Trancoso et al., 2005; Vaz et al., 2005, 2007, 2009b; Mendes, 2010), Óbidos (Malhadas et al., 2009) and Ria Formosa (Silva et al., 2002) coastal lagoons; and Tagus (Braunschweig et al., 2003; Vaz et al., 2011), Sado (Martins et al., 2001), and Guadiana estuaries (Saraiva et al., 2007). Furthermore, MOHID has been implemented in other parts of the Iberian Peninsula: for example in the Galician Rias (Minho-Rias Baixas region (Sousa, 2013), Ria de Pontevedra (Ruiz-Villarreal et al., 2002), and Ria de Vigo (Taboada et al., 1998; Montero and Pérez-Villar, 1999). Other works in open and coastal ocean regions were performed, as an operational model implementation for the Iberian coast (Portuguese Coast Operational Modelling System (PCOMS), Mateus et al. (2012)), studies about portuguese coastal circulation (Coelho et al., 2002), the Algarve region (Leitão et al., 2005), and the North Sea (Bernardes, 2007).

All this extensive number of studies in several coastal environments, with different resolutions, allows showing that MOHID has total capabilities to simulate the dynamics of the Douro estuarine plume in the Northwestern Iberian coast.

1.4 Structure

This dissertation is divided in 7 chapters. After this introductory chapter, Chapter 2 presents a method to observe and characterize the mean-state of the Douro plume using

ocean-colour satellite data, evaluating the role of the main drivers (river discharge, wind, and tide).

In Chapter 3, an assessment of the seasonal and inter-annual variability of the Douro plume is carried out, using long-term MODIS images. Additionally, possible connections between the turbid signal and the most representative regional patterns of atmospheric variation (Eastern Atlantic (EA) and North Atlantic Oscillation (NAO)) were examined.

Chapter 4 presents a general overview of MOHID numerical model and the set-up of coastal and estuarine models. This chapter also includes the analysis of model accuracy in reproducing the Douro estuarine plume. The characterization of the estuarine plume under different wind and river discharge scenarios can be found in Chapter 5. In Chapter 6, an integrated analysis of the interaction between the Douro and Minho estuarine plume was performed, as well as their individual influence on the WIBP behaviour under winter conditions. Finally, in Chapter 7, the general conclusions of the dissertation are drawn and suggestions for further work are presented.

Chapter 2

Detection of the Douro plume using MODIS imagery

2.1 Introduction

The aim of this Chapter is to present an ad-hoc methodology to observe and characterize the Douro plume and its spatial and temporal variability by using long-term ocean-colour satellite data (2003-2011) and concurrent *in situ* wind, tidal and river discharge data. Additionally, the role of the main drivers (river discharge, wind and tide) in Douro turbid plume surface features was evaluated.

Since the Douro River is the main contributor of sediments to the Northwestern Iberian coast (Figure 2.1), its load often generates high levels of turbidity with distinctive optical properties from the offshore ocean, which are visible in ocean-colour images such as MODIS.

In the Northwestern Iberian coast remote sensing has only occasionally been used to perform qualitative comparisons with model results (Otero et al., 2008, 2009, 2013). In these studies the Sea Surface Temperature (SST) and Chlorophyll-a concentration were used as plume tracers in coastal waters, which can induce erroneous assumptions, as mentioned by those authors.

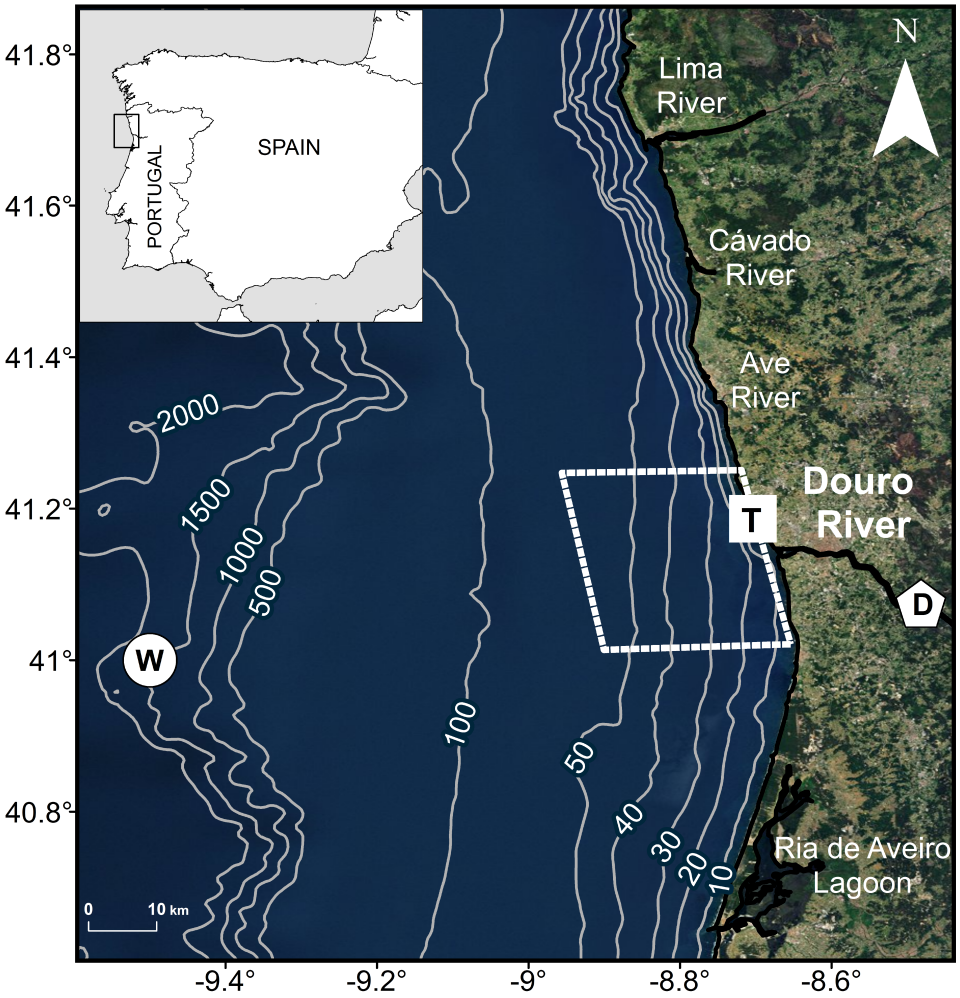

Figure 2.1: Location of the study area. Northwestern Portuguese coast off Douro Estuary with the location of the main rivers outflows near the interest point (Lima, Cávado, and Ave rivers and Ria de Aveiro Lagoon). The wind data station is marked with a circle (W). The dam and the tide gauge at Leixões harbour are marked with a pentagon (D) and square (T), respectively. The box near the river mouth represents the near-field area of influence of the Douro River (white double dashed line). The bathymetry, from GEneral Bathymetric Chart of the Oceans (GEBCO), is shown with white lines (contours in meters).

Despite the numerous studies addressing coastal upwelling and the dynamics of the WIBP under several scenarios (Peliz et al., 2002; Otero et al., 2008, 2009, 2013), little attention has been given to the influence of the Douro Estuary input into the coastal adjacent areas. The exceptions are the studies presented by Teodoro et al. (2009) and Gonçalves et al. (2012), in which a complex methodology to infer the Douro-river plume

size based on the concentration of Total Suspended Matter (TSM) was elaborated, using images from MERIS. Results indicate that the plume is generated only when the river outflow exceeds about 400 m^3 s^{-1} at the dam (see Figure 1 in Teodoro et al. (2009)).

This Chapter is organized as follows. In Section 2.2, the methodology and data used are described. Section 2.3 presents the main results of ocean-colour satellite images in the area of the Douro turbid plume based on the period from 2003 to 2011. In Section 2.4, the river discharge, wind direction and tide amplitude influence on Douro turbid signal are analysed and discussed. The paper ends in Section 2.5 where the main findings are summarized.

2.2 Data and methods

Daily high-resolution ocean-colour data and concurrent wind, tidal and river discharge *in situ* data from 2003 to 2011 were obtained and used to study the seasonal and spatial variability of the Douro Estuary turbid plume and the relative importance of the main drivers on its dynamic.

2.2.1 River discharge, wind and tidal data

Daily mean Douro River outflow data, at the Crestuma-Lever dam (Figure 2.1), were obtained from the *Sistema Nacional de Informações sobre Recursos Hídricos* (SNIRH) database (`www.snirh.pt`). During the study period (2003-2011), the Douro River flow presents a traditional seasonal variation for high discharges (Figure 2.2a). A strong deviation between the lowest (about 0 m^3 s^{-1}) and the highest (over 2500 m^3 s^{-1}) daily discharges is visible in the winter months. Values higher than 4000 m^3 s^{-1} were occasionally registered. The mean value is always lower than 1000 m^3 s^{-1}; and the meanly maximum was observed in January (942 m^3 s^{-1}).

According to Peel et al. (2007), the Douro region presents Mediterranean climate features under the Köppen climate classification. As a result, the river basin receives most

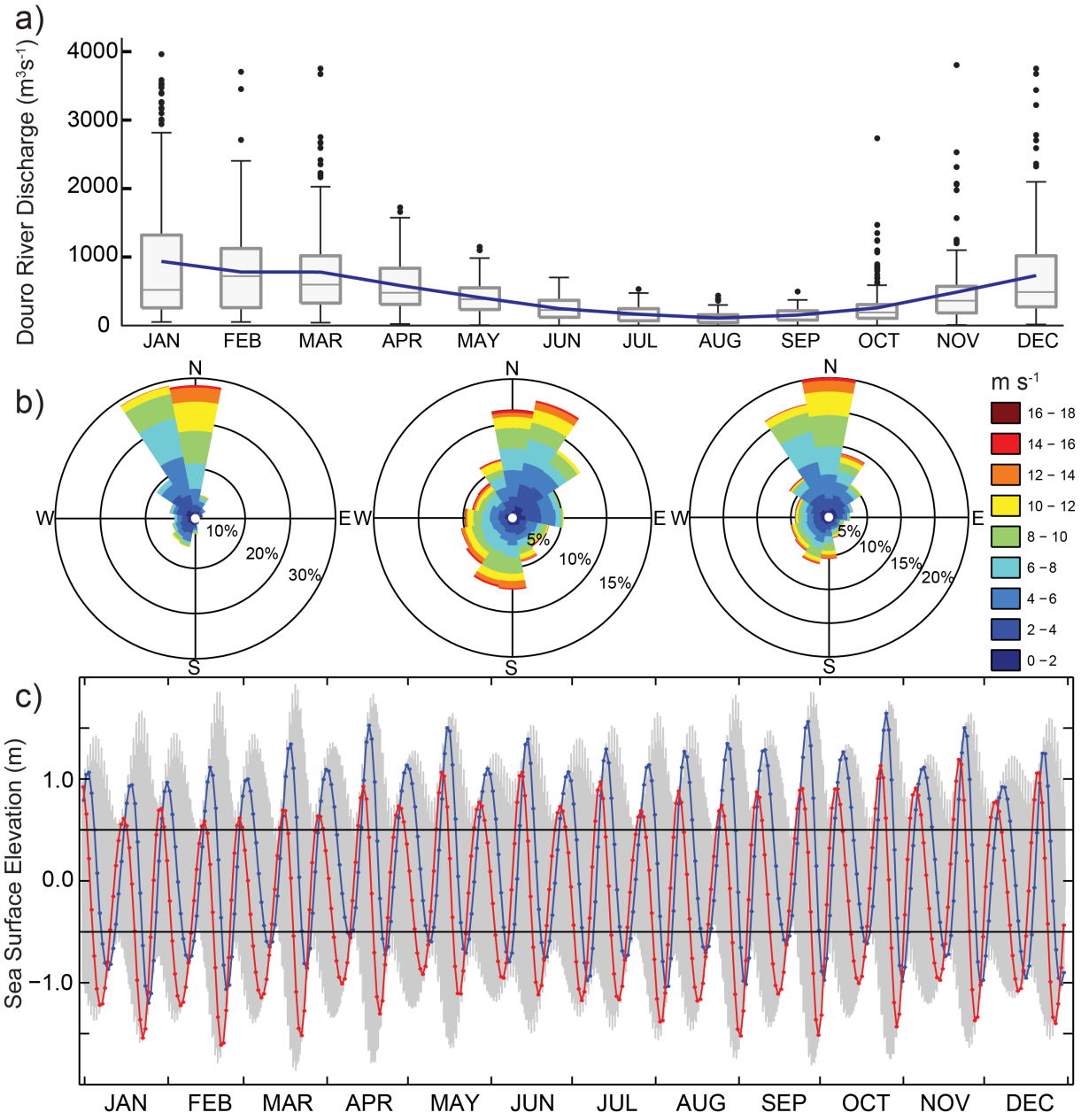

Figure 2.2: Douro River discharge at Crestuma dam during 2003-2011 (a). Curve: monthly average; line inside box: median; lower and upper box limits: first and third quartiles, respectively; lower and upper whiskers: minimum and maximum river discharges, respectively; dots: outliers. Wind rose diagrams calculated for the same period (b), during summer (left), winter (centre) and at annual scale (right). SSE at Leixões tidal gauge during 2007 (grey line), tidal situation at 11:30 and 13:30 Universal Time Coordinates (UTC) for each day (red and blue thick lines marked with solid points) (c).

of the precipitation during winter season, not receiving significant precipitation during summer. Thus, the river inflow at Crestuma dam from June to September is very low, with a mean flow of only about 150 m^3 s^{-1}.

Wind data were obtained from National Oceanic and Atmospheric Administration (NOAA)'s National Operational Model Archive and Distribution System (NOMADS), which is maintained at NOAA's National Climatic Data Center (NCDC) (Saha et al., 2010). The Climate Forecast System Reanalysis (CFSR) was developed by NOAA's National Centers for Environmental Prediction (NCEP) (`http://rda.ucar.edu/pub/cfsr.html`). Wind data with a spatial resolution of 0.5-0.5° and a 6-hourly time resolution from January 1979 to December 2011, covering the atmosphere, ocean, sea ice and land were used for the wind data, at a 10 m reference height. The wind components were processed for the closest available site near the Douro Estuary mouth (41°N, -9.5°E, see Figure 2.1). Previous research carried out along the Iberian Peninsula coast has proved that CFSR data are accurate compared with buoy measurements (Álvarez et al., 2014).

In the Western Iberian ocean region, wind tends to be aligned with the coastal orientation (Figure 2.2b) (Gómez-Gesteira et al., 2006; Álvarez et al., 2008, 2011; Sousa et al., 2013). Note that wind is defined with the direction from which the wind is blowing (according with the meteorological convention). The wind characterization indicates strong upwelling-favourable conditions, especially during summer (Figure 2.2b, left). These conditions also occur during winter (Figure 2.2b, centre) but with lower intensity and predominance. Strong southwesterly winds during winter season (Figure 2.2b, centre) are linked to cyclogenetic processes, which generate frequent rainfall episodes (Trigo and DaCamara, 2000; Lorenzo et al., 2008).

Synthetic tidal data were calculated for a location near the mouth of the estuary for the period 2003 - 2011, using the T_Tide package (Pawlowicz et al., 2002), based on the major local tidal constituents. These were determined from hourly sea surface elevation data measured at a tidal gauge located at Leixões harbour during 2007 (Figure 2.1). A strong semi-diurnal signature - M_2 (Amplitude=1.05 m; Phase=76.5°), S_2 (0.37 m; 104.8°), N_2 (0.22 m; 58.4°), and K_2 (0.10 m; 101.5°) - with non-negligible diurnal amplitude

- K_1 (0.07 m; 60.6°), and O_1 (0.05 m; 318.4°) - is noticeable in the data (Figure 2.2c). Semi-diurnal harmonic constituents represent more than 87% of total tidal wave energy. The average tidal range is 2.8 m with a maximum of about 3.8 m during equinoctial spring tides. Results agree with information described in the literature (Vieira and Bordalo, 2000; Marta-Almeida and Dubert, 2006).

2.2.2 Ocean-colour data

Available full-resolution L1A files from MODIS-Aqua and MODIS-Terra covering the Douro Estuary region (swaths inside the box 40°−43°N; 11°−7.5°W) were used. L1A files were processed to L1B using the SeaWIFS Data Analysis System (SeaDAS) software (version 6.4, Baith et al. (2001)), following standard procedures for processing raw data files. However, some customize steps were performed in order to obtain improved L2 ocean-colour images in turbid zones, as the Douro coastal area. The methodology adopted in this work is based on the Aurin et al. (2013) approach to obtain high-resolution images from MODIS, which provides a clearer turbid signal from Douro estuarine outflow and it assesses better results, especially near coast, where the band saturation and stray light misassumption are critical (Saldías et al., 2012; Aurin et al., 2013). Instead of using merged images with SWIR and NIR band atmospheric correction based on turbidity boundary, only the SeaDAS standard correction was applied (Bailey et al., 2010) to quantify the NIR contribution with the iterative bio-optical optimization. Regarding local turbid levels, it was chose not to employ SWIR bands during the atmospheric correction procedure. Moreover, the 2130 nm SWIR band was also used to mask clouds with a threshold albedo of 0.018 and the high light masks were disabled. The stray light masks were set to a 3 × 3 array around land and clouds and the unrealistic Rrs values were discarded.

Several water leaving radiances (nLw) at 412 nm, 443 nm, 469 nm, 488 nm, 531 nm, 555 nm, 645 nm, 667 nm, 678 nm, and 748 nm were computed to study the spectral signatures of the coastal zone under different river discharge conditions. The swaths were interpolated into a regular lat-lon grid (0.005° × 0.005°) and daily averaged images were

generated when more than one existed for the same day. The strongest turbid signal is observed at green bands ($nLw547$ and $nLw555$), as it was previously reported for other locations (e.g. Nezlin et al. (2005), Nezlin and DiGiacomo (2005), Thomas and Weatherbee (2006) and Saldías et al. (2012)). In addition, a comparison among all nLw of the visible spectrum (Terra and Aqua) and river discharge time series was performed. Firstly, only daily images with more than 70% of valid pixels in a region near the mouth of river (Figure 2.1) were considered in this evaluation. The difference of valid days for each nLw was also analysed. The linear Pearson correlation coefficients between the mean radiance value in the chosen region and the Douro River discharge were calculated (Table 2.1). As expected, the maximum coefficient correlation was observed at red bands ($nLw645$, $nLw667$, and $nLw678$) and the next one at $nLw555$ band. But, taking into account the percentage of used days, the confidence on the results for the red bands is considerably lower when compared

Table 2.1: Average percentage of available days (more than 70% of cloud-free pixels within the box, Figure 2.1) (P_{AP}) and the coefficient of correlation between nLw time series and daily river discharge (r) for images from MODIS Aqua and Terra.

		Aqua		Terra	
Wave length (nm)	Spatial resolution (m)	P_{AP} (%)	r	P_{AP} (%)	r
412	1000	24.3	0.30	30.9	0.22
443	1000	33.4	0.39	35.7	0.35
469	500	36.1	0.43	36.3	0.38
488	1000	35.0	0.47	37.8	0.43
531	1000	32.0	0.55	37.7	0.51
547	1000	32.3	0.57	37.5	0.54
555	500	38.0	0.60	38.0	0.56
645	250	28.0	0.71	33.3	0.64
667	1000	27.5	0.70	30.8	0.62
678	1000	30.1	0.69	34.0	0.59

with $nLw555$. For instance, there is a difference of 10% of valid days between $nLw555$ and $nLw645$ band for MODIS-Aqua sensor. As the objective of this study is to evaluate the turbid plume mean state under different conditions, the number of valid images becomes crucial to increase the robustness and accuracy of results. Concerning the resolution, Aurin et al. (2013) in their studies of the Mississippi River, Yangtze River, Amazon River and Chesapeake Bay pointed out that more than 90% of the optical variability is explained with 500 m resolution within plume regions. Allowing for correlation coefficient (Aqua – 0.60; Terra – 0.56), excellent imagery coverage (38%), and sufficient native nominal resolution (500 m), the $nLw555$ band offers the best compromise to study this turbid feature (Table 2.1). Additionally, the small differences between Aqua and Terra data for green channels (Franz et al., 2007) allow the merging of both sensors $nLw555$ images. For the region of interest, the signal-to-noise ratio of $nLw555$ images is $<$11% considering the relative differences between Terra and Aqua and their daily average. After merging MODIS-Aqua and Terra $nLw555$ images, the results of robustness significantly increase (48.3% of possible days were valid) and the correlation coefficient maintains its significance (0.60) compared when only MODIS-Aqua was used.

2.2.3 Evaluating plume signal and its drivers

The Douro estuarine plume propagation is forced and influenced by the river discharge, tide and wind. Most of the previous studies using ocean-colour images usually focus on particular events. Here an ad-hoc method was developed to ascertain the contribution of individual drivers on plume propagation. This method intends to group together different synoptic situations according to the main driving mechanism to describe the mean state feature of the plume.

Wind intensity and direction play a key role in the plume pathway and are linked to the river input: low-pressure conditions, which are characterized by southwesterly winds, are connected to precipitation and therefore high river discharge. Due to this relation, it is very difficult to isolate a single estuarine plume forcing and compare, individually, their

time series correlations with $nLw555$ data. Thus, to study the wind effect, the average of turbid fields under different wind conditions was used.

When the plume covers a larger area and reaches far-field locations due to extreme freshwater inflow, the wind increases its relevance in the plume pathway (Hetland, 2005). Hence, the impact of wind from the main directions on the Douro plume motion was studied exclusively during high river discharges. A $nLw555$ daily composite will be then considered as the average pixel calculation if the following three conditions are fulfilled: the river discharge has to be above of the 75^{th} percentile (570 m^3 s^{-1}) computed for the 9 years, the average wind intensity in the preceding two days must be higher than 2 m s^{-1} in order to avoid the calms and a deviation of $\pm$ 45° is allowed for each major quadrants.

The Douro estuarine plume variability was examined under high and low tide periods. To highlight the difference in the turbid pattern, a method similar to the approach defined for assessing the wind influence on plume has been followed: only $nLw555$ images with daily river discharge above the 75^{th} percentile (570 m^3 s^{-1}) were taking into account. MODIS-Terra and MODIS-Aqua overpass the Douro Estuary region at approximately 11:30 and 13:30 UTC, respectively. Then, $nLw555$ composites for high (higher than 0.5 m) and low (lower than -0.5 m) tides were created, considering the computed sea surface elevation at 11:30 and 13:30 UTC for each day. These representative ocean property maps are used in order to characterize the effect of each tidal phase in the Douro estuarine plume propagation. The tidal aliasing effect, explained by the sun-synchronism of the Aqua and Terra satellite orbits and the local tides, must be included in the discussion of tidal effects on turbid coastal patterns (see e.g. Valente and da Silva (2009)). Due to this aliasing effect, all images during low tides (below -0.5 m) were obtained after spring tide periods (between spring and neap tides). On the other hand, the images corresponding to high tides (above 0.5 m), only cover periods before spring tides (between neap and spring tides) (Figure 2.2c). However, the use of two imagery sources (Terra and Aqua) with different overpass times decreases the aliasing importance, allowing a better balance among the possible scenes during high and low tides (Table 2.2).

Table 2.2: Available scenes (AS), average of valid pixels used for each cell calculation (VP), average standard error (SE, mW cm$^{-2}\mu$m^{-1} sr^{-1}), and mean river discharge for the available scenes ($MD-AS$, m^3 s^{-1}). The results are presented to all composites calculated: low and high river discharges (<25%, >75%), predominant wind directions (North, South, East, and West), and minimum and maximum tidal times (low and high water).

	River discharge		Wind				Tide	
	<25%	>75%	N	S	E	W	Lo	Hi
AS	822	822	265	208	89	190	446	622
VP	461	301	145	38	50	44	124	171
SE	0.02	0.05	0.03	0.04	0.04	0.05	0.03	0.03
$MD-AS$	76	1292	972	1230	1087	1376	1276	1139

2.3 Results

2.3.1 River discharge driven plume propagation

Figure 2.3 depicts the distribution of $nLw555$ values over the river discharge percentile ranges in the box area (Figure 2.1). The $nLw555$ mean field during low river discharge conditions (lower than 148 m^3 s^{-1}, percentile 25%) and high river discharges (higher than 570 m^3 s^{-1} - percentile 75%) are calculated from average pixel value over these days. Strong relationship between the Douro River discharge and $nLw555$ data is noticeable.

Higher values represent coastal turbid water and lower values define ocean clear waters. The highly coherent turbid structure and its size are recognized by $nLw555$ composites, supporting the choice of this measure to ascertain the Douro turbid plume variability. Under low discharge conditions, a negligible turbid signal is detected. In situations of river discharges lower than the 25$^{\text{th}}$ percentile (148 m^3 s^{-1}), there is no plume (Figure 2.3a). The pixel distribution is almost unimodal with most of the values below 0.8 mW cm$^{-2}\mu$m^{-1} sr^{-1}.

Under high river flow, the pixel distribution of $nLw555$ composite images is markedly

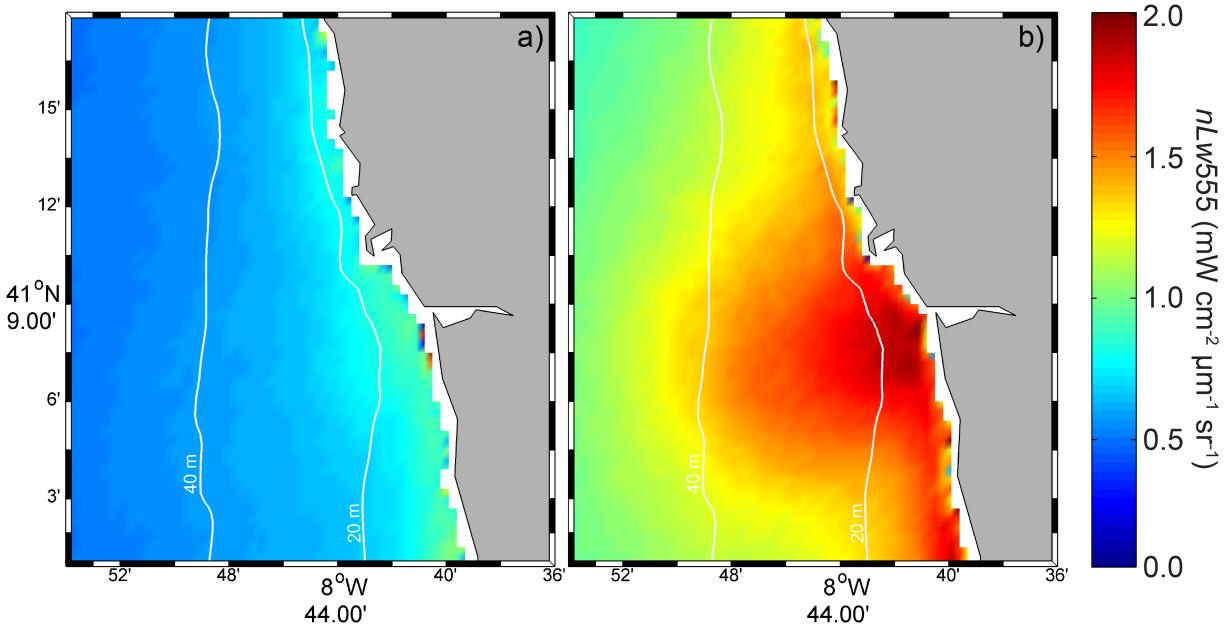

Figure 2.3: $nLw555$ composites for low (a) and high (b) discharges calculated from daily scenes when river input is below 25$^{\text{th}}$ percentile and above 75$^{\text{th}}$ percentile, respectively.

bimodal with a clear difference between ocean (values below 0.8 mW cm$^{-2}\mu$m^{-1} sr^{-1}) and coastal turbid waters (Figure 2.3b). A bulge is visible near the Douro Estuary mouth with an offshore extension of approximately 10 km. Note that definition of bulge in literature can be quite ambiguous. Here it was considered a jet-like bulge when there is a radially turbid coherent structure extending offshore from the estuary mouth, which is wider than the alongshore coastal turbid band, and with high turbid values. The definition of a turbid value to identify the plume front is usually very subjective, as it often depends on the terrestrial characteristics and sediment loads from different rivers. Nezlin et al. (2005) present a methodology to define this limit through the comparison of the precipitation rates in the river basin and in the plume area. As the precipitation rate for Douro watershed is not directly correlated with the plume area due to the dam in the river previously referred, a comparison between the accumulated $nLw555$ values for both 25$^{\text{th}}$ and 75 $^{\text{th}}$ percentile composites was performed (Figure 2.4). This analysis warrants that under low river discharges it is very unlikely to find pixels with values higher than 1.1 mW cm$^{-2}\mu$m^{-1} sr^{-1}. More than 99% of the pixels in the low river discharge composite are lower than this

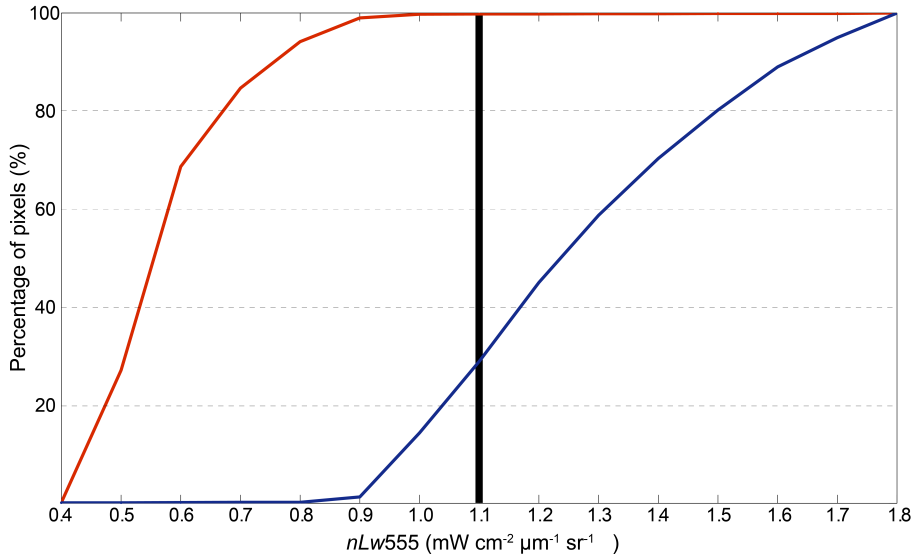

Figure 2.4: The accumulative percentage of pixels below different turbid limit for the $nLw555$ composite for low (red line) and high (blue line) river discharge. The vertical line represents the turbid threshold (1.1 mW $cm^{-2}\mu m^{-1}$ sr^{-1}).

value. On the contrary, the high river discharge composite shows that more than 70% of pixels are higher than 1.1 mW $cm^{-2}\mu m^{-1}$ sr^{-1}. From this method, it is assured that the source of pixels with values higher than 1.1 mW $cm^{-2}\mu m^{-1}$ sr^{-1} are most likely related with freshwater input than other turbid sources, such as phytoplankton blooms and wind-wave resuspension. Despite the subjectivity of this threshold, hereafter this value is considered as the most suitable to identify the Douro estuarine plume front.

The possible scenes, average of the number of valid pixels, average standard error for each pixel and mean river discharge for the possible scenes are presented in Table 2.2 in order to discuss the results robustness. The standard error was calculated following $SE = SD/\sqrt{N_P}$, where SD is the standard deviation and N_P is the number of valid pixels used in the mean state calculation for each cell.

2.3.2 Wind driven plume propagation

Daily composites, which fulfil the requirements (see Chapter 2.2.3) to be selected for average turbid plume field, under different wind regimes (North, South, East, and

West) are depicted in Figures 2.5 and 2.6. Upwelling-favourable winds induce an offshore expansion of the Douro estuarine outflow plume (Figure 2.5b). The plume structure has a slight inclination southwestward. Two turbid coastal bands are detectable in opposite directions from the Douro Estuary mouth. Up north, a coastal plume is visible. Cávado River (see Figure 2.1) appears to have a non-negligible contribution for this coastal turbid band. Turbid pixels greater than 1.6 mW $cm^{-2}\mu m^{-1}$ sr^{-1} are found nearby the river mouth. The southward turbid band has stronger signal intensity with values greater than 1.6 mW

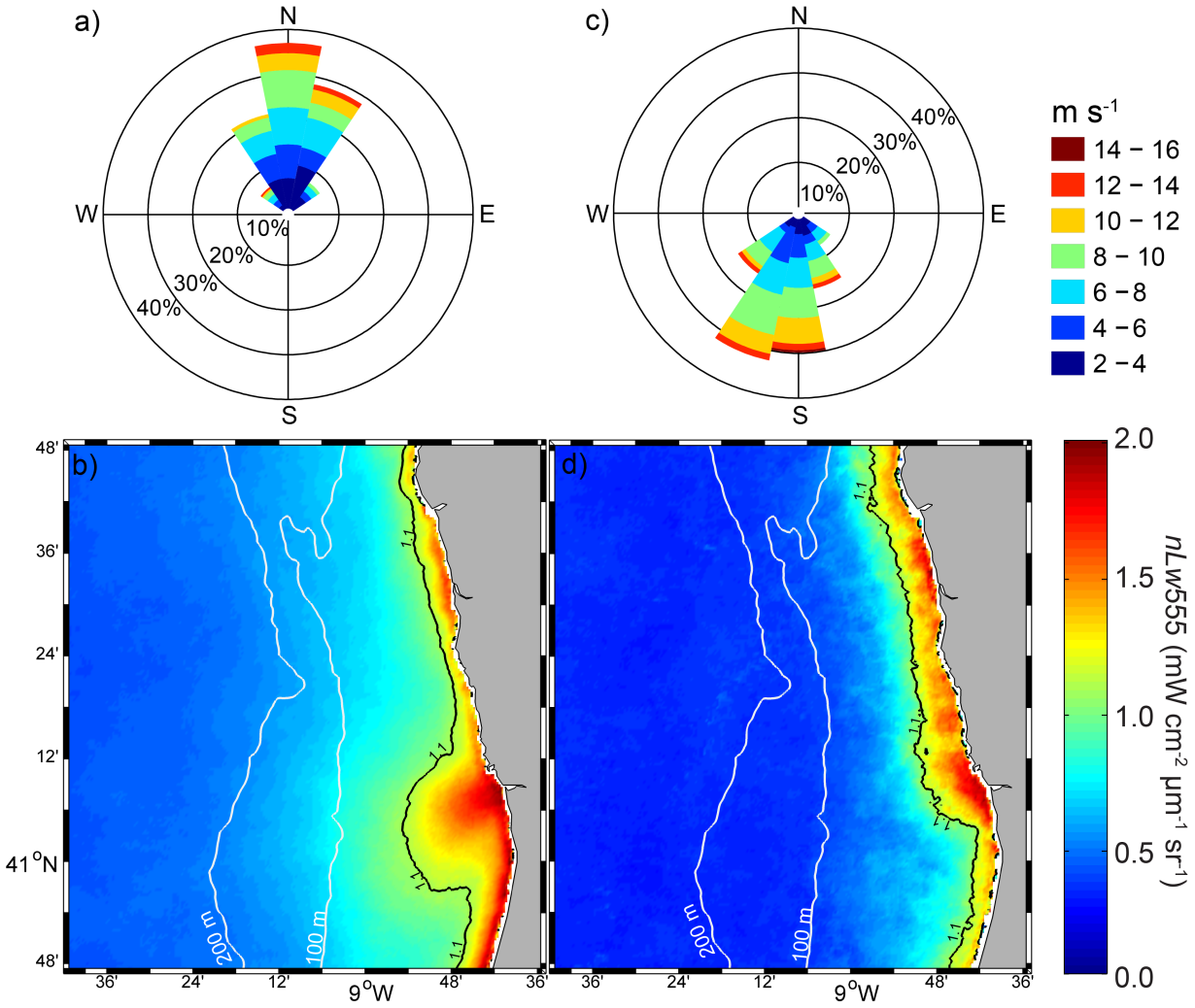

Figure 2.5: Wind rose diagrams and the corresponding $nLw555$ composites of Douro estuarine plume under northerly (a, b) and southerly (c, d) wind conditions. The black line represents the contour value of 1.1 mW $cm^{-2}\mu m^{-1}$ sr^{-1}.

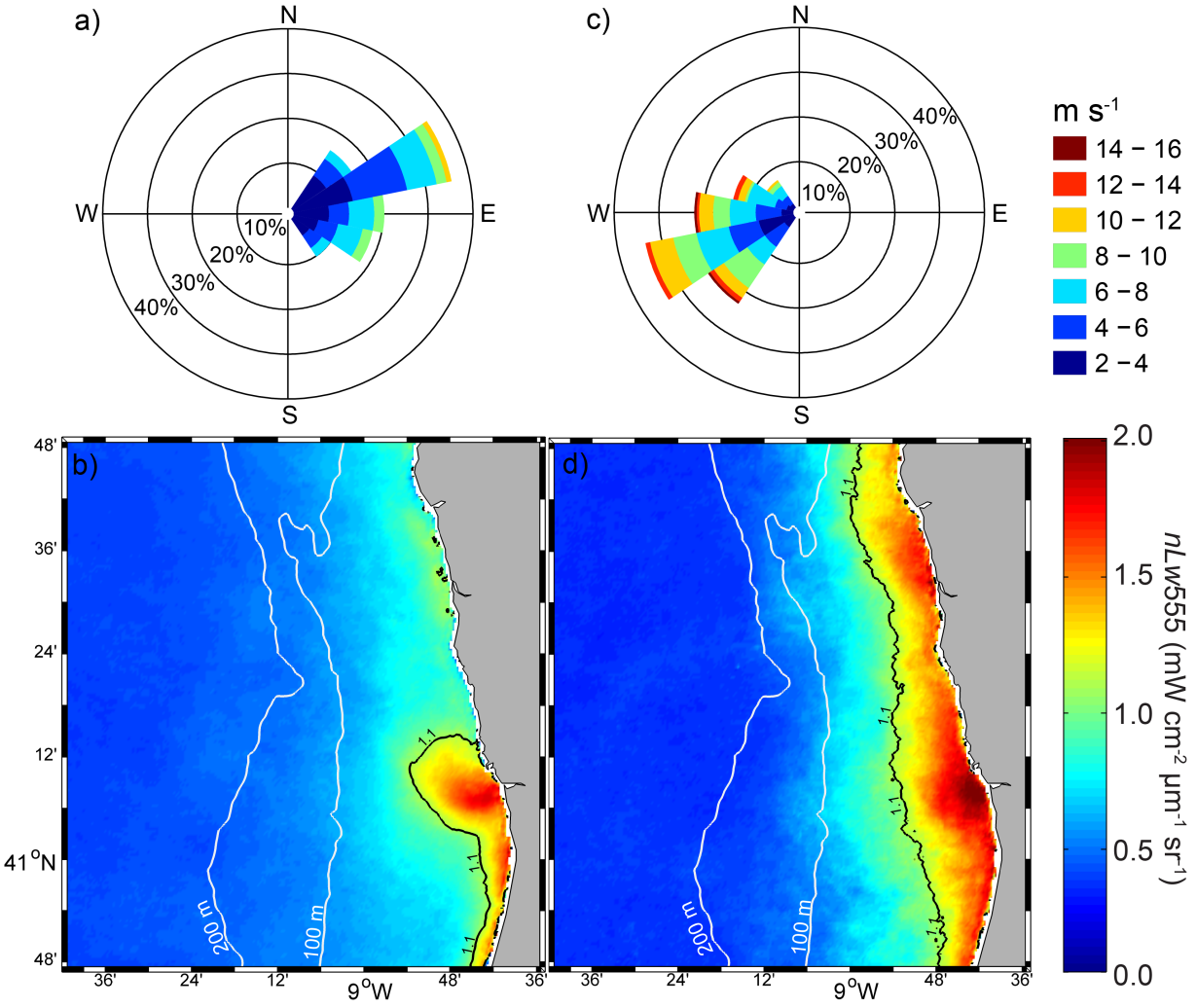

Figure 2.6: Wind rose diagrams and the corresponding $nLw555$ composites of Douro estuarine plume under easterly (a, b) and westerly (c, d) wind conditions. The black line represents the contour value of 1.1 mW $cm^{-2}\mu m^{-1}$ sr^{-1}.

$cm^{-2}\mu m^{-1}$ sr^{-1}.

The Douro turbid plume mean-state under downwelling-favourable wind is highlighted in Figure 2.5d. Despite the plume cannot be so clearly identified as in the counter case, there is an alongshore plume confinement to the coast along the north direction. This coastal buoyancy body of water has about 10 km width and the bulge formation is not perceptible. Southward, there is an irregular and weak turbid signal (1.1 – 1.4 mW $cm^{-2}\mu m^{-1}$ sr^{-1}). This turbid band is about 2-3 km wide.

Concerning wind direction, the pixel distribution shows a predominance of strong winds blowing from north, north-northeast and south-southwest in upwelling and downwelling-favourable conditions, respectively (Figures 2.5a and 2.5c). Results present a similar pattern for both cases in terms of wind intensity and percentage of occurrence. It should be noticed that the average wind magnitude, during 2 days before the day of image acquisition, could reach 14 m s^{-1}.

The impact of cross-shore winds on the shape of the plume is shown in Figure 2.6. The average turbid plume is mapped during easterly and westerly wind events. When the wind blows from the land (Figure 2.6b), a bulge is identified near the estuary mouth. The bulge has a northwestern direction with a clear detachment from coast at the north side. A short turbid coastal band is identified south of the bulge. The average turbid pattern under westerly winds shows an expected plume confinement to the coast in both alongshore directions (Figure 2.6d). There is a continuous coastal turbid band of about 25 km width. The bulge delimitation is unclear; however, higher turbid values (>1.8 mW $cm^{-2}\mu m^{-1}$ sr^{-1}) are found flattened near the Douro Estuary mouth, presenting a semi-circular shape.

Concerning the pixel distribution on magnitude and wind directions, some differences must be taken into account in the analysis of cross-shore wind influence (Figures 2.6a and 2.6c). The westerly winds predominant directions are from west-southwest (Figures 2.6c). However, strong winds (over 12 m s^{-1}) can be found from all directions in this quadrant. Otherwise, all easterly winds are weaker (lower than 12 m s^{-1}) with a major predominance from east-northeast and east directions (Figures 2.6a).

Differences between Figures 2.5b and 2.5d and Figures 2.6b and 2.6d are depicted in Figure 2.7a and 2.7b, respectively. The southerly winds persistence causes a coastal negative anomaly region, which is visible in the turbid field towards the north from the estuary mouth (Figure 2.7a). This region of influence is a very regular structure about 15 km wide. The bulge region and the southward short coastal band present the major turbid differences (higher than 0.4 mW $cm^{-2}\mu m^{-1}$ sr^{-1}). This positive anomaly, caused by the wind blowing from the north quadrant, reaches an extension of about 60 km. A region with low positive values of about 0.2 mW $cm^{-2}\mu m^{-1}$ sr^{-1} divides the bulge and the southward

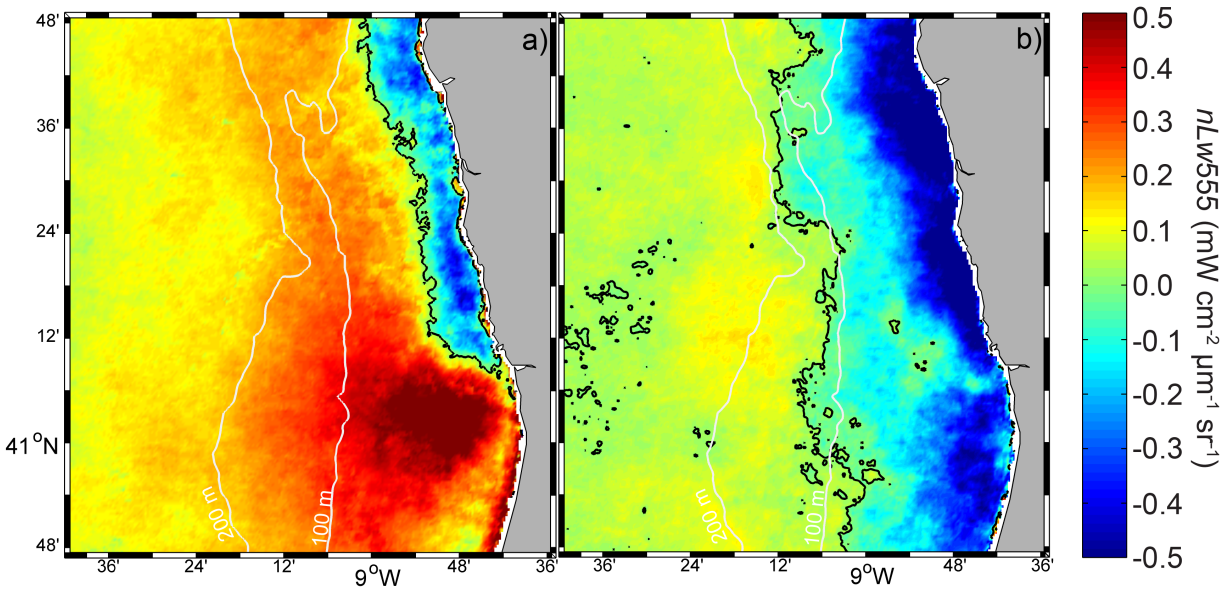

Figure 2.7: (a) Douro estuarine plume under northerly wind conditions (Figure 2.5c) minus under southerly wind conditions (Figure 2.5d). (b) Douro estuarine plume under easterly wind conditions (Figure 2.6c) minus under westerly wind conditions (Figure 2.6d).

turbid coastal area (Figure 2.7a). It is important to note that even in the northern part of the area (>15 km from the coast), there is a remarkable influence of the northerly winds.

Differences on the turbid field caused by easterly and westerly winds show strong negative anomalies (lower than -0.4 mW $cm^{-2}\mu m^{-1}$ sr^{-1}) in regions north and south from the estuary mouth (Figure 2.7b). These areas of influence of westerly winds present an offshore decreasing until 20-25 km from the coast, when positive values became dominant. Inside the negative influenced area, some differences in the intensity should be noted. For instance, there are small areas in front of the estuary mouth where the differences are close to 0 or even slightly positive.

Obviously, there are important differences concerning the results robustness for the wind mean states (Table 2.2). North, south, and westerly winds have a larger number of possible scenes (Figure 2.2b). However, the average of valid pixels in each mean state presents some differences. Since the south and westerly are linked to precipitation in the region, their scenes are more contaminated by clouds. This fact also explains that under these wind regimes the mean Douro river discharge for the possible scenes is higher. The

lower standard error (0.03 mW cm$^{-2}\mu$m^{-1} sr^{-1}) when wind blows from the north is expected regarding the number of possible scenes and the average of valid pixels.

2.3.3 Tidal influence on the plume

Turbid mean fields during high and low tides are shown in Figures 2.8a and 2.8b, respectively, and are described below. In general, no significant differences can be found between composites during high and low tide periods. During low tides, turbid coastal bands (north and southward) are visible with some pixels over 1.8 mW cm$^{-2}\mu$m^{-1} sr^{-1}.

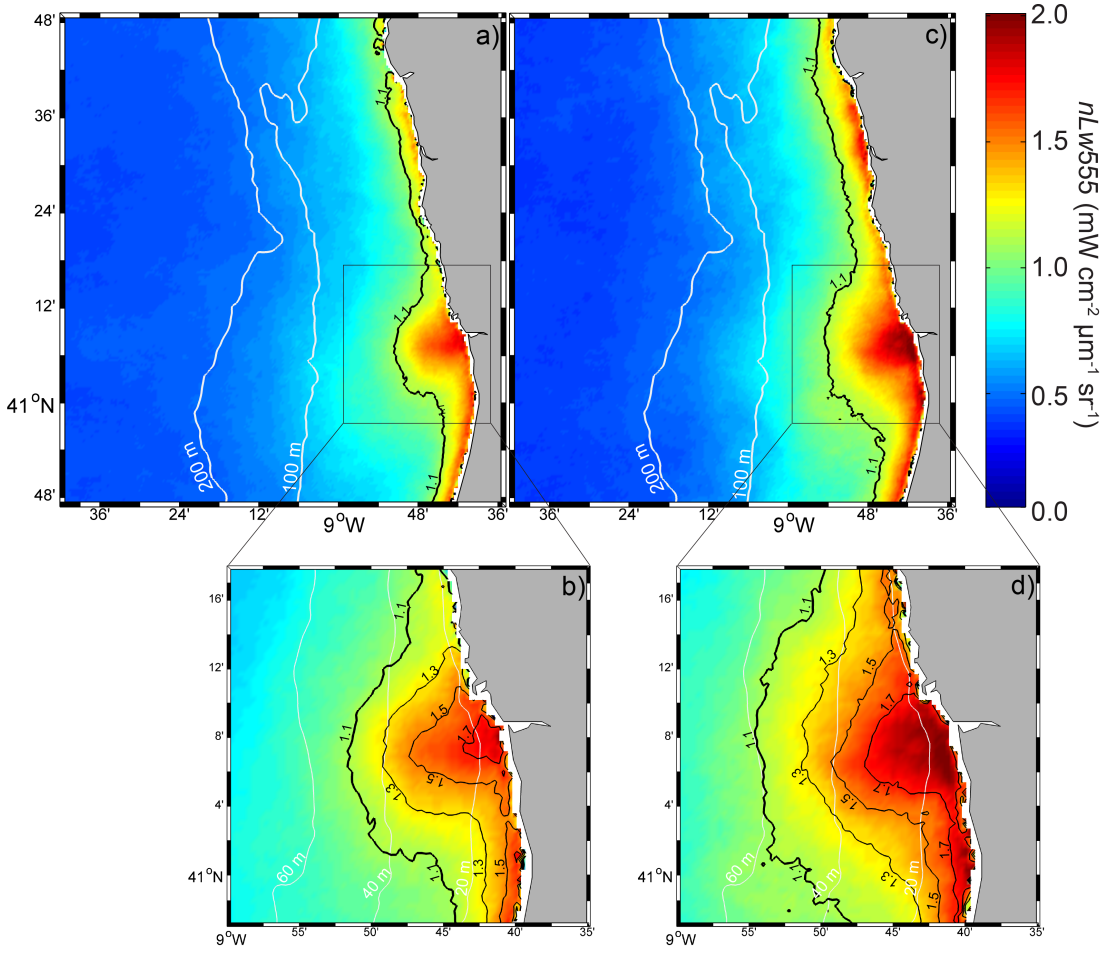

Figure 2.8: Composites during high (a) and low tide periods (b). The black line represents the contour value of 1.1 mW cm$^{-2}\mu$m^{-1} sr^{-1}. The corresponding zoom images are presented below (c, d). The thicker black line represents the contour value of 1.1 mW cm$^{-2}\mu$m^{-1} sr^{-1} and the thin lines represent the contour values of 1.5, 1.3, and 1.1 mW cm$^{-2}\mu$m^{-1} sr^{-1}.

The offshore expansion of the turbid limit (1.1 mW $cm^{-2}\mu m^{-1}$ sr^{-1}) is very regular and about 10-15 km wide under low tide conditions. During high tide, north and south coastal bands present an irregular pattern less than 5 km wide. However, stronger changes are observed close to Douro and Cávado estuary mouths. During high tides a clear retraction of the Douro bulge is detected (Figure 2.8a). On the other hand, under low tides, an offshore expansion of the Douro bulge is noticeable, presenting a semi-circular shape (Figure 2.8b).

The distinct shapes related to the tidal phase become more evident in zoom images (Figure 2.8c and 2.8d). During high tides, the 1.7 mW $cm^{-2}\mu m^{-1}$ sr^{-1} contour line is confined to the Douro Estuary adjacent coast (Figure 2.8c). In the opposite case, i.e. for low tides, higher turbid values (above 1.7 mW $cm^{-2}\mu m^{-1}$ sr^{-1}) reaches a 10 km offshore extension (Figure 2.8d). The same pattern is observed for lower turbid contour lines (1.5, 1.3, and 1.1 mW $cm^{-2}\mu m^{-1}$ sr^{-1}). However, this difference fades at distances larger than 25 km offshore. At this limit, no differences are found between both tidal cases (Figure 2.8a and 2.8b).

The robustness and image balance between two tidal phases are very satisfactory. The number of possible scenes is different because of the MODIS images match up with sea surface elevation. There is a better representation of high tides than of lower ones. However, the ratio between the average valid pixels and the possible cases are almost equal (about 28%). The standard error and the mean river discharge for the possible cases are broadly the same, which further increases the results significance.

2.4 Discussion

The present study showed a marked influence of river input on turbid patterns in the Douro river coastal zone. There is a consistent relation between the spatial distribution of $nLw555$ and the daily river discharge. The number of pixels with high turbid values, and consequently the plume area, is enhanced with the increase of the river inflow measured at the dam (Figure 2.3). During low river discharge it is very unlikely to find pixel values above 1.1 mW $cm^{-2}\mu m^{-1}$ sr^{-1}. Despite some subjectivity associated with the methodology

to find the turbid plume limit, during high river discharge the 1.1 mW $cm^{-2}\mu m^{-1}$ sr^{-1} contour line is considered good representative of the plume front. Conversely, medium turbid values between 0.5 and 1.0 mW $cm^{-2}\mu m^{-1}$ sr^{-1} were observed under low river discharges (Figure 2.4a). These medium turbid plumes may be related to phytoplankton blooms, typical of upwelling regions (Saldías et al., 2012), and/or wind-wave resuspension. Rusu and Soares (2013) discuss wave contribution to higher turbid patterns in the near shore regions. Although the river discharge threshold to plume appearance is arguable, a circular turbid pattern is well observed off Douro River when the flow exceeds 500 $m^3 s^{-1}$. This result is consistent with the values discussed in previous works by Mourato (2008) and Teodoro et al. (2009).

The role of alongshore winds on the Douro plume dynamics is crucial to define the estuarine water fate during high river discharge conditions (higher than 570 m^3 s^{-1}). Under upwelling-favourable winds, an offshore expansion of the bulge is observed. Northerly winds cause, indeed, an offshore displacement of the plume. The plume extension and its southwestward advection by surface currents agree with modelling results presented in previous works (Otero et al., 2008, 2013), representing a common feature along the Portuguese coast as studied by Vaz et al. (2009a) for the Tagus Estuarine plume. However, the southward turbid band attached to the coast was not described in those studies. Due to the Coriolis deflection, a plume movement to right of the estuary mouth is expected in the Northern hemisphere. This could be explained as the result of southward wind-driven surface currents. In shallow waters the surface cross-shore transport decreases and the transport is entirely in the direction of the wind-driven circulation in regions shallower than the surface boundary layer (Lentz and Fewings, 2012). This southward turbid band is also observed under south, east (weak but visible) and west wind regimes. These features were also observed in numerical models, when an ambient flow (10 cm s^{-1}) is imposed in the opposite direction of the Kelvin wave propagation (García Berdeal et al., 2002). The northwest dominant wave direction, representing about 72% of the occurrences (Rusu and Lisboa, 2007), induces a surface current in the North-South direction - littoral drift - (Veloso-Gomes et al., 2004) that could represent this ambient flow. Based on wave energy,

the littoral drift could play an important role in sediment transport up to 3-4 km off the coast (12 – 16 m depth, Coelho and Veloso-Gomes (2006)) transporting sediments southwards (Dias et al., 2002). This near coastal flux could also be related with the spatial orientation of the estuary axis (direction of the discharge relative to the coast)(Yankovsky et al., 2000; Garvine, 2001). The direction of the Douro Estuary inlet has an alongshore component. The angle between coastline and inlet orientation is approximately 45°, in the opposite direction of Coriolis deflection, which can promote a southward flux near the estuary mouth.

Turbid patterns show a confinement of the estuarine plume in the near coastal region (towards the north) under downwelling-favourable winds and high-river discharge. This is due to the combined effect of the wind and the Coriolis force on the northern hemisphere, which tends to push the plume towards coast. The dimensions of this turbid coastal feature (10 km width) agree with the numerical modelling results of Otero et al. (2008) for the WIBP dimensions. The southerly wind forces an onshore current, which confines the Douro plume coastward. The formation of the bulge is not clear and increases the chance of the freshwater from the Douro Estuary to merge with water from smaller rivers located further north (i.e. from Ave, Cávado and Lima rivers). Thus, a continuous coastal-attached turbid band is generated to the north. Important biogeochemical consequences would take place, since water from these smaller rivers spreads their constituents over a much larger area, amplified by the Douro Estuary input from the south (Warrick, 2004; Saldías et al., 2012).

The influence of cross-shelf winds on plume dynamics has been usually ignored in previous studies. However, as pointed out by Lentz and Fewings (2012), in waters shallower than 30 m the cross-shelf wind stress is a non-negligible term in the cross-shelf momentum balance. Nevertheless, although the offshore winds in the Douro Estuary region are often weak some differences in the turbid composites could be attributed to wind stress influence. Moreover, estuarine water is flushed into the ocean generating a bulge in front of the estuary mouth. In the case of easterly winds there is a clear plume offshore detachment from the coast with a deflection to the right. Despite the same direction of wind stress and estuarine flux, the offshore advection is significantly higher under upwelling-favourable winds cases.

This can be explained in terms of wind magnitude, which is important in both cases. However, offshore surface transport seems to reach a stationary location (25 km), then turning to an alongshore direction, while during northerly winds offshore spreading occurs until the plume waters are no longer distinguishable from the ocean waters. These results are consistent with those presented by Chao (1988b), Choi and Wilkin (2007) and Jurisa and Chant (2012). Westerly winds tend to accumulate freshwater along the coastline and to decrease the cross-shore transport. The bulge is squeezed towards the coast generating an alongshore turbid band both in northward and southward directions. A similar pattern can be found in numerical simulations carried out by Chao (1988b).

Tides were found to influence the near-field turbid plume close to the coast and estuary mouth. Between high and low tide periods, no significant differences were found regarding the offshore maximum advection. The major discrepancies were observed in the near-field bulge, where tidal currents are important. This area of influence seems to be representative of a pulsed tidal plume zone. In this case, the tidal pulse is generally energetic, strongly stratified, and typically bounded on its outer edge by sharp fronts with a semi-circular formation (Horner-Devine et al., 2009). The region of tidal influence for the Douro estuarine plume only extends 20 km offshore, radially from the estuary mouth.

Interpretation of the observed turbid area difference between high and low tides must be cautious because of tidal aliasing (Valente and da Silva, 2009). As all images obtained during low tides correspond to periods after spring tides, this could enhance turbid coastal values and mask the *real* differences between low and high tides, as pointed out by Valente and da Silva (2009) for the Tagus turbid plume. However, as no significant differences were found regarding the offshore maximum advection between the high and low tide turbid composites (see Figure 2.8), the fortnightly tidal cycle seems to be less important in the case of the Douro turbid plume compared to the Tagus one. Possibly, this is due to the water residence time inside the Douro Estuary, which is too short to enhance turbidity during spring tides, when compared e.g. to the Tagus Estuary (Braunschweig et al., 2003).

2.5 Conclusion

Remote sensing images were found to be useful in order to understand the Douro plume behaviour. Merged $nLw555$ images from MODIS sensors aboard of Aqua and Terra satellites showed results of significant robustness to detect turbid plume signals. An ad-hoc method groups together different synoptic situations according to the main driving mechanisms (river discharge, wind and tide) in order to describe the mean state feature of this turbid plume. The main conclusions of this Chapter are the following:

- A strong relationship was found between the Douro River discharge and $nLw555$ data. A circular turbid pattern is well observed when the flow exceeds 500 m^3 s^{-1}. There is no plume evidence under low-discharge regime (lower than 148 m^3 s^{-1});

- An offshore plume expansion is observed under upwelling-favourable winds and high river discharges. Under southerly winds, there is a plume confinement to the coast in the northward direction. The bulge formation is not clear and the possibility of the plume to merge with water from smaller rivers increases;

- Under easterly winds, the turbid maps show a bulge generation with an offshore detachment from the coast. A smaller offshore spreading is observed in comparison with upwelling-favourable wind situations. Westerly winds tend to accumulate freshwater near shore and consequently to decrease cross-shore advection. The bulge is confined to the coast producing a continuous turbid band in the alongshore directions;

- No significant offshore differences are found in turbid patterns between high and low tide periods. Major discrepancies were observed in the near-field area. During low tide, a representative tidal plume with a semi-circular formation is observed. The region of high turbid values was spread about 10 km from the coast.

The seasonal and inter-annual variability of the Douro estuarine plume, showing the impact of long-term atmospheric variation in its length scales using the MODIS composites

here developed will be addressed in the Chapter 3.

Chapter 3

Douro turbid river plume seasonal and inter-annual variability: relation with atmospheric teleconnection patterns

3.1 Introduction

In Chapter 2 were described the mean characteristics of the Douro River plume through ocean-colour imagery, highlighting that the turbid plume is well observed when the river flow exceeds 500 m^3 s^{-1}. In addition, an important wind influence on the offshore transport and fate of the plume was also revealed, showing typical features described above for along shore winds. The shape of the near-field plume was found to be strongly influenced by the ebb-flood cycle.

This Chapter aims to evaluate the seasonal and inter-annual variability of the Douro turbid plume (Figure 3.1) through the use of long-term ocean-colour satellite data (2000-2014), highlighting its relation with the river discharge, precipitation rates and wind anomalies during contrasting NAO and EA phases. The NAO and EA are two of the most representative regional patterns of atmospheric variation in the Northern Hemisphere, influencing the local precipitation and river discharges, with higher amplitude during

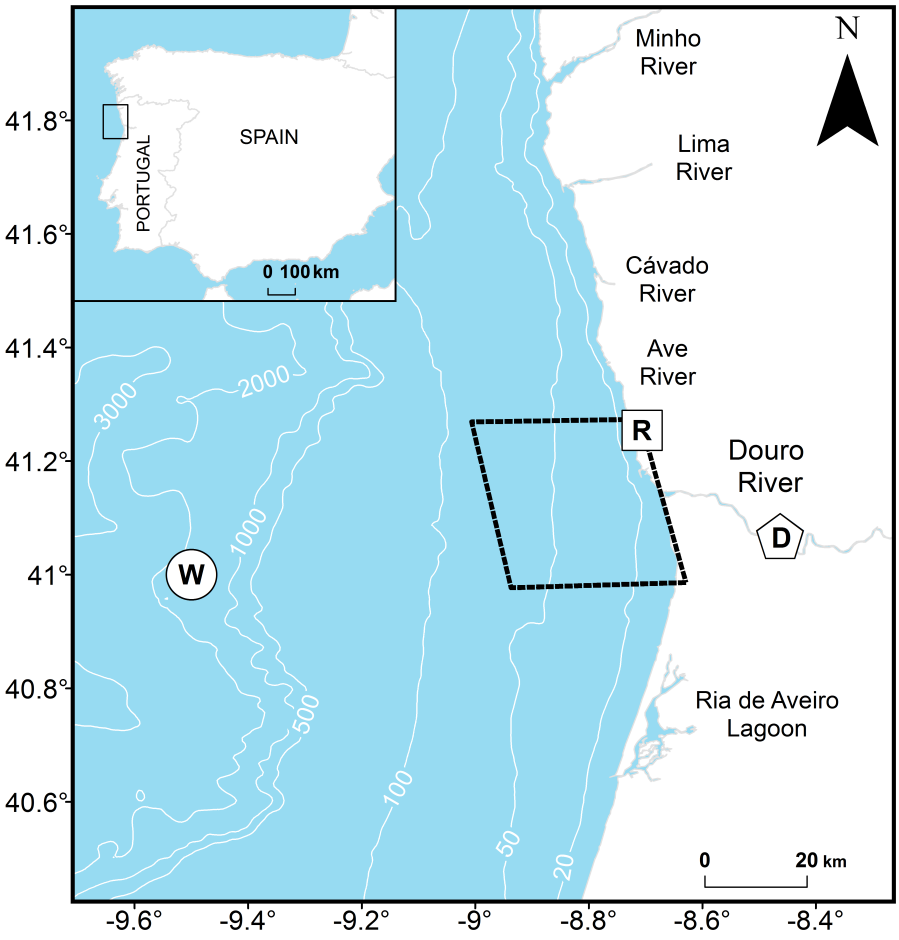

Figure 3.1: Study Area with location of the main rivers near the interest point. Wind and precipitation data stations are marked with a circle and square, respectively. The pentagon represents the location of the downstream Douro River dam. The dashed black box near the river mouth represents the near-field area. Bathymetry, from GEBCO, is shown with white lines (contours in meters).

winter (Zorita et al., 1992; Trigo et al., 2004; Lorenzo and Taboada, 2005; deCastro et al., 2006, 2008). Several works have shown a significant correlation between NAO index and precipitation in Galicia during winter (northwest of Iberian Peninsula) (Zorita et al., 1992; Esteban-Parra et al., 1998; Lorenzo and Taboada, 2005). Trigo et al. (2004) found that winter discharge of the main Iberian rivers are significantly correlated with the (DJF) NAO index for the period 1973-1998 with a 1-month lag peak (-0.76 for Douro, -0.77 for the Tagus and -0.79 for the Guadiana river). Furthermore, deCastro et al. (2006) found

significant correlations between Minho river discharge and (DJF) NAO index for the period 1970-2005 with a 2-month lag peak, showing a decreased correlation in the last years, in agreement with the decreased trend in spatial correlation found by Trigo et al. (2004). Regarding EA variability, Rodriguez-Puebla et al. (1998) found correlation with the annual precipitation for Iberian Peninsula for April EA, while deCastro et al. (2006) showed a negative correlation between Minho River discharge and (DJF) EA with a peak at 1-month lag.

Data and methods followed to reach the objectives of this Chapter are described in Section 3.2. The results and discussion are presented in Section 3.3, highlighting the dominant spatio-temporal plume patterns along the coast and their connection to wind and climate indices at inter-annual scale. Finally, the principal conclusions of this Chapter are shown in Section 3.4.

3.2 Data and methods

3.2.1 Ocean-colour imagery

Following the method for the characterization of the Douro turbid plume presented in Chapter 2, daily composites of $nLw555$ from MODIS-Aqua and MODIS-Terra were obtained. The processing generates high-resolution (500 m) daily images from February 2000 to December 2014. Swaths were mapped into a regular lat-lon grid ($0.005^{\circ}\times0.005^{\circ}$) and daily averaged images were generated when more than one existed for the same day.

Moreover, small differences between Aqua and Terra data for green channels (Franz et al., 2006) allow merging the $nLw555$ images from both platforms in this region (Mendes et al. (2014), Chapter 2). These minor discrepancies were also statistical stated in Section 2.2.2 of the previous Chapter. The average and standard deviation of $nLw555$ in the Douro region from Aqua, Terra, and merged data from both satellites are depicted in Figure 3.2. Differences in long-term averages and standard deviation are practically unnoticeable between platforms and the merged product. High standard deviation values are restricted

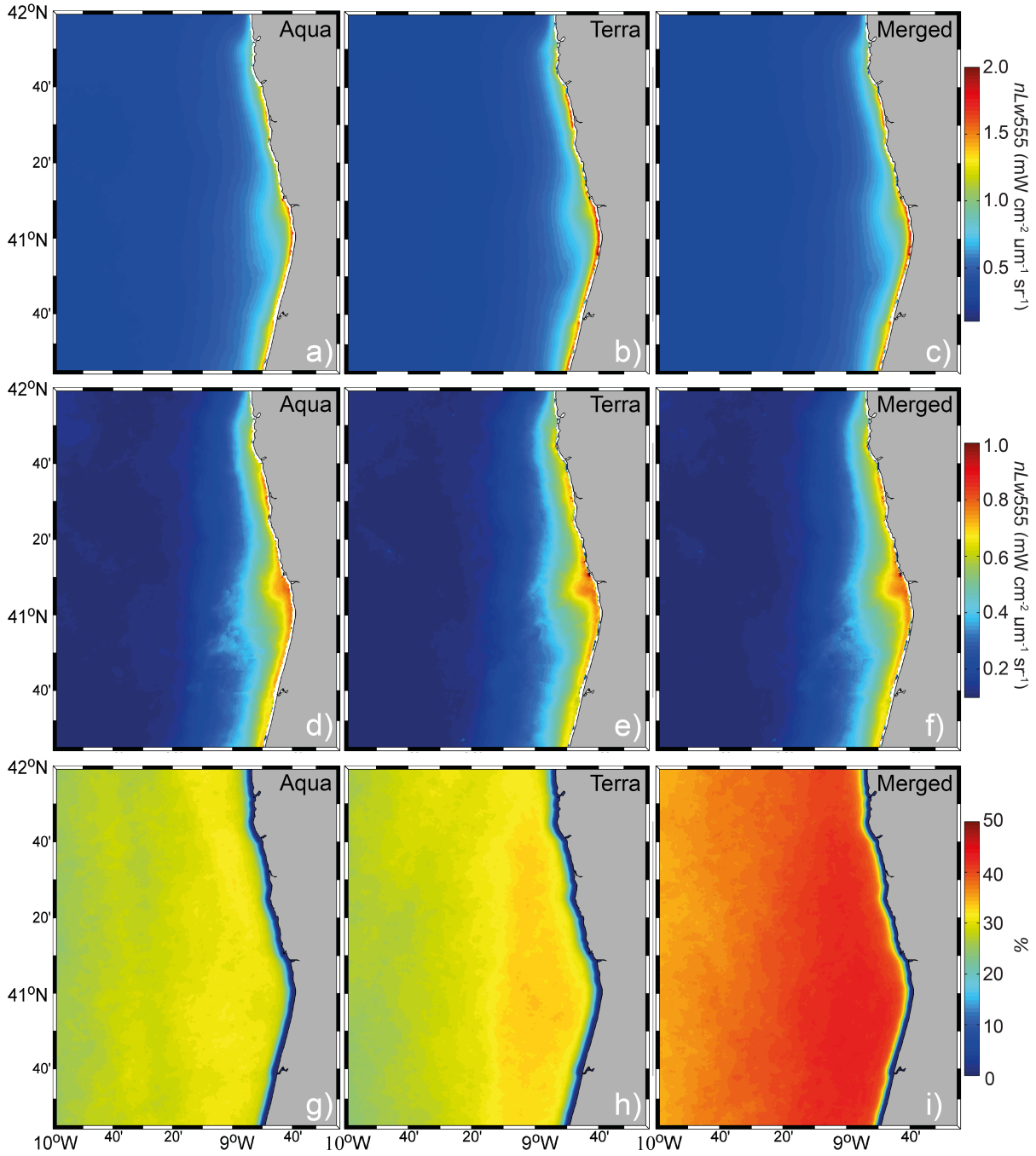

Figure 3.2: (upper panels) Averages, (middle panels in the vertical direction) standard deviations, and (lower panels) percentage of daily cloud-free data of $nLw555$ from (left panels) MODIS-Aqua, (middle panels in the horizontal direction) MODIS-Terra, and (right panels) the merged MODIS-Aqua-Terra composites.

to the pixels near the Douro River mouth where the turbid plume has a major impact (Figure 3.2d, 3.2e, 3.2f). Merged data, however, presents a considerable increase of daily available pixels (Figure 3.2i). Using $nLw555$ merged data results in a maximum of 40-45% of cloud-free data coast-wide, whereas the available data is greatly reduced to 25-35% in the other cases (Figures 3.2g and 3.2h). Then, $nLw555$ merged composites were monthly averaged to guarantee >99% of good data in the entire study area and, at the same time, to study the inter-annual variability of the Douro turbid river plume.

3.2.2 River discharge, wind, and precipitation rate

As in Chapter 2, daily mean Douro River outflow data, at the Crestuma-Lever dam (D in Figure 3.1), were obtained from the SNIRH database (`www.snirh.pt`) and wind data were retrieved from NOAA's NOMADS, which is maintained at NOAA's NCDC (Saha et al., 2010) for an ocean location close to the Douro Estuary mouth (41°N, -9.5°E, W in Figure 3.1).

Along the western coast of the Iberian Peninsula, the practicable upwelling index (UI) can be considered equal to $-Q_x$, the zonal component of the Ekman transport per unit length:

$$Q_x = \frac{\rho_a C_d}{\rho_w f}(W_x^2 + W_y^2)^{1/2} W_y \tag{3.1}$$

where W_x and W_y are the zonal and meridional components of wind data, $\rho_a = 1.22$ kg m^{-3} is the air density, $C_d = 1.4 \times 10^{-3}$ is a dimensionless drag coefficient, $\rho_w = 1025$ kg m^{-3} is the sea water density and f is the local Coriolis frequency (Bakun, 1973; Nykjær and van Camp, 1994; Gómez-Gesteira et al., 2006; Álvarez et al., 2010).

Monthly precipitation data were retrieved from NOAA/Office of Oceanic and Atmospheric Research (OAR)/Earth System Research Laboratory (ESRL) Physical Sciences Division (PSD), Boulder, Colorado, USA (`http://www.esrl.noaa.gov/psd/`). This global dataset has been constructed on a 2.5° latitude-longitude grid from 1979 to present day by merging hydrometric gauge observations, estimates inferred from a variety of satellite

observations, and the NCEP-National Center of Atmospheric Research (NCAR) reanalysis. Climate Prediction Center (CPC) Merged Analysis of Precipitation (CMAP) dataset was used with success to investigate the annual and inter-annual variability in large-scale precipitation, showing a reasonable agreement with long-terms means (Xie and Arkin, 1997). Data were processed and monthly averaged for the closest available site near the Douro Estuary (R in Figure 3.1).

3.2.3 Composites for EOF analysis

Non-seasonal composites of $nLw555$ were computed by subtracting seasonal harmonic cycles at each pixel in order to study the dominant patterns of inter-annual variability in turbid river plumes. By doing this, the stationary contribution of the seasonal cycle is removed, and consequently, changes in phase and strength of these harmonics are considered in the non-seasonal anomalies. The seasonal harmonics were computed through the following equation:

$$OC_{sh(t)} = \overline{OC} + OC_a cos(2\pi f_a t - \phi_a) + OC_s cos(2\pi f_s t - \phi_s) \tag{3.2}$$

where $OC_{sh(t)}$ is the seasonal harmonic time series for the ocean-colour variable at each pixel, $\overline{OC}$ is the mean value, OC_a and OC_s are the amplitudes of annual and semi-annual harmonics, f_a and f_s are the annual (1/365.25 days) and semi-annual (2/365.25 days) frequencies, ϕ_a and ϕ_s are the annual and semi-annual phases, and t is time. Then, the non-seasonal anomalies ($OC_{ns(t)}$) were computed by subtracting the seasonal harmonics from the original series (OC_t):

$$OC_{ns(t)} = OC_t - OC_{sh(t)} \tag{3.3}$$

non-seasonal composites were used in the Empirical Orthogonal Functions (EOF) analysis for decomposing the dominant modes of variability. The EOF was computed following the Singular Value Decomposition (SVD) approach to avoid the very large

covariance matrix due to the high resolution of images (Thomson and Emery, 2014).

3.2.4 Climate indices

Monthly NAO and EA teleconnection indices were obtained from the CPC at the NCEP (`www.cpc.noaa.gov`) over the period 2000-2014. The NAO consists of a north–south dipole of geopotential anomalies, with one centre located over Greenland and the other one spanning the region between 35° and 40°N in the central North Atlantic, near the Azores archipelago. EA consists of a north–south dipole that spans the entire North Atlantic Ocean. EA dipole is displaced southeastward the NAO with the centres near 55°N, 20-35°W and 25-35°N, 0-10°W. A detailed description of these indices can be found at `http://www.cpc.noaa.gov/data/teledoc/telecontents.shtml`.

3.3 Results and discussion

3.3.1 Seasonal evaluation

The comparison between monthly averaged series of $nLw555$, river discharge and precipitation rate for the period 2000-14 is depicted in Figures 3.3a and 3.3c. $nLw555$ data are the average of values within a box close to river mouth (dashed line in Figure 3.1), where the Douro estuarine outflow has more influence on turbidity patterns. A relation between $nLw555$, river discharge and precipitation is noticeable (Figures 3.3a and 3.3c). Correlation coefficient between the Douro River discharge and $nLw555$ is 0.81 with $p_v<0.01$. All extreme discharge events match $nLw555$ peaks, which indicates the use of high-resolution $nLw555$ composites as important to study this river plume variability at inter-annual scale (Mendes et al. (2014) - Chapter 2). For example, the 2000-01 maximum is one of most extreme events in terms of river discharge, when it was observed a maximum of the Douro River mean daily outflow higher than 8000 $m^3\ s^{-1}$ (Marta-Almeida et al., 2002; Ruiz Villarreal et al., 2005). A similar correlation is observed in terms of annual climatology with very low values during summer months and higher in winter (Figure 3.3b). The turbidity is more

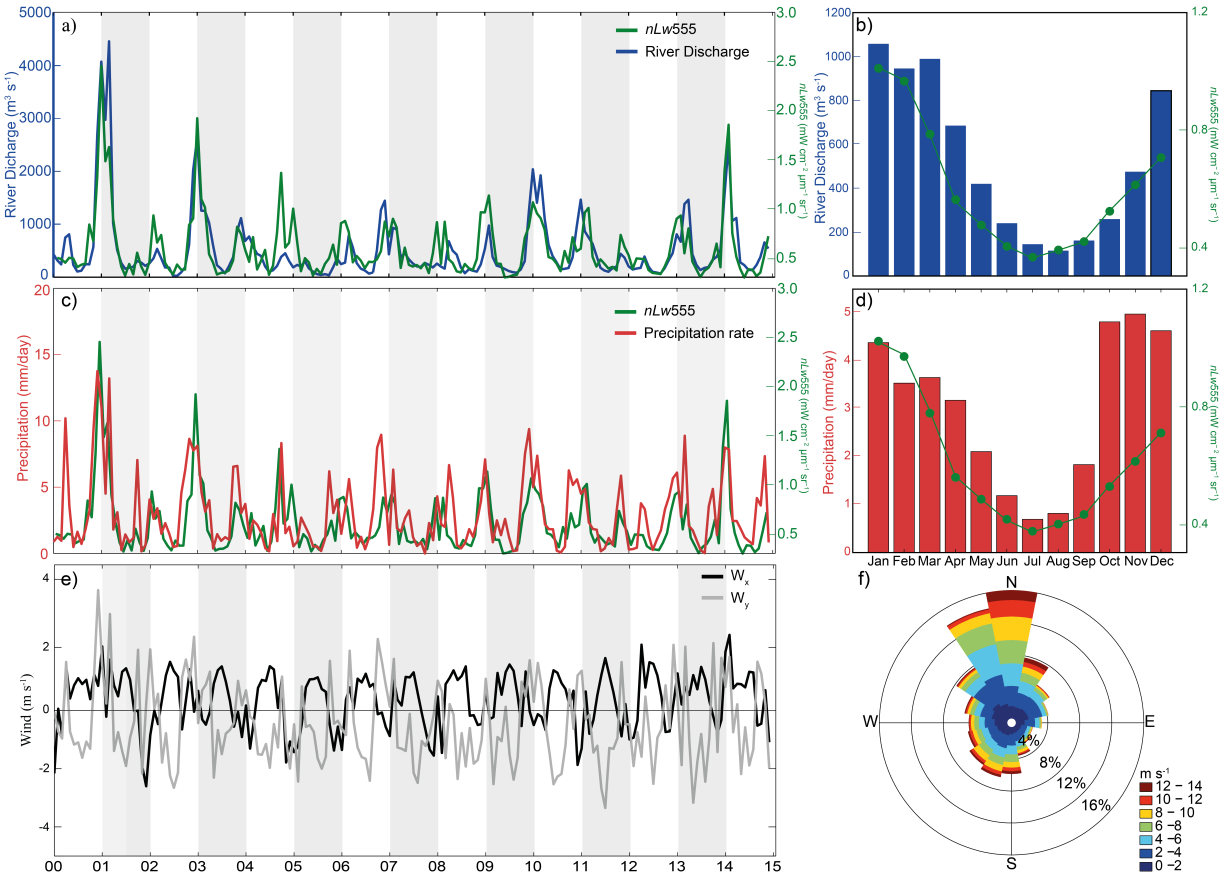

Figure 3.3: (left panels) Temporal evolution and (right panels) mean annual cycles of monthly $nLw555$ data (a, b), monthly river discharge (c, d) and precipitation. (e) Time series and (f) mean annual cycles of meridional (W_y) and zonal (W_u) wind components.

sensitive to the river discharge in early winter, possible due to higher sediments supply after summer, which are then carried by river to the coast.

The correlation coefficient between precipitation and $nLw555$ time series is smaller (r=0.58; p_v<0.01) (Figure 3.3c). However the maxima correlation was found with a 1-month lag ahead (r=0.65; p_v<0.01), which confirms the visual analysis from the annual climatological data (Figure 3.3d). The precipitation is higher during autumn than winter. The non-coincident pattern between precipitation and river discharge can be caused by the outflow regulation by several dams along the river's course.

Two typical patterns are observed regarding wind condition during these 15 years (Figure 3.3e): Northerly and positive zonal winds are persistent during summer, inducing

strong upwelling events (Fraga, 1981; Fiúza et al., 1998; Álvarez et al., 2010, 2011)(Figures 3.3e and 3.3f); During winter, upwelling-favourable winds are no longer prevalent. Strong southwesterly winds during winter season (Figures 3.3e and 3.3f) are linked to precipitation episodes (Trigo and DaCamara, 2000; Lorenzo et al., 2008), which, in turn, are associated with the highest peaks in river discharge (2000-01, 2002-03, and 2013-14 events) (Figures 3.3a and 3.3e).

3.3.2 Wind and river runoff influence on $nLw555$ anomalies

The long term (2000-2014) spatio-temporal variability of the Douro turbid plume was characterized by means of longitudinal monthly anomalies of $nLw555$ averaged for a latitude band coincident with the estuary mouth (41.14° - Figure 3.4a). Monthly anomalies of river discharge and meridional and zonal wind components are also represented in Figures 3.4b, 3.4c, and 3.4d, respectively, to further clarify their relation with anomalous plume patterns. Aqua satellite was launched in July 2002, which partially explains the blank areas (areas without values) observed in 2000 and 2001 (in particular in the winter of 2000/01) – $nLw555$ composites before July 2002 correspond to MODIS-Terra only (Figure 3.4a).

Anomalous high $nLw555$ values are observed during 2000-01, 2002-03, and 2013-14 winters, while 2001-02, 2004-05, 2005-06, 2007-08, and 2011-12 winters appear to be less impacted by the river discharge and, consequently, by the turbid river plume (Figure 3.4a).

Relation between river outflow and $nLw555$ is less important in terms of the turbid plume extent. The wind forcing presents a secondary role in the cross-shore propagation of the Douro estuarine plume (Mendes et al. (2014) - Chapter 2).

Maximum plume extent was found on 2002-03 winter (Figure 3.4a), but higher river discharges and $nLw555$ anomalies were found on 2000-01 winter (Figure 3.3a). Alongshore winds play a key role on the plume confinement and offshore expansion events at inter-annual scale during positive anomalies of river discharge. Downwelling-favourable winds occurred during 2000-01, related to the landwards transport of the plume (Otero et al., 2008; Mendes et al., 2014), were stronger than during 2002-03 winter, which can explain this difference.

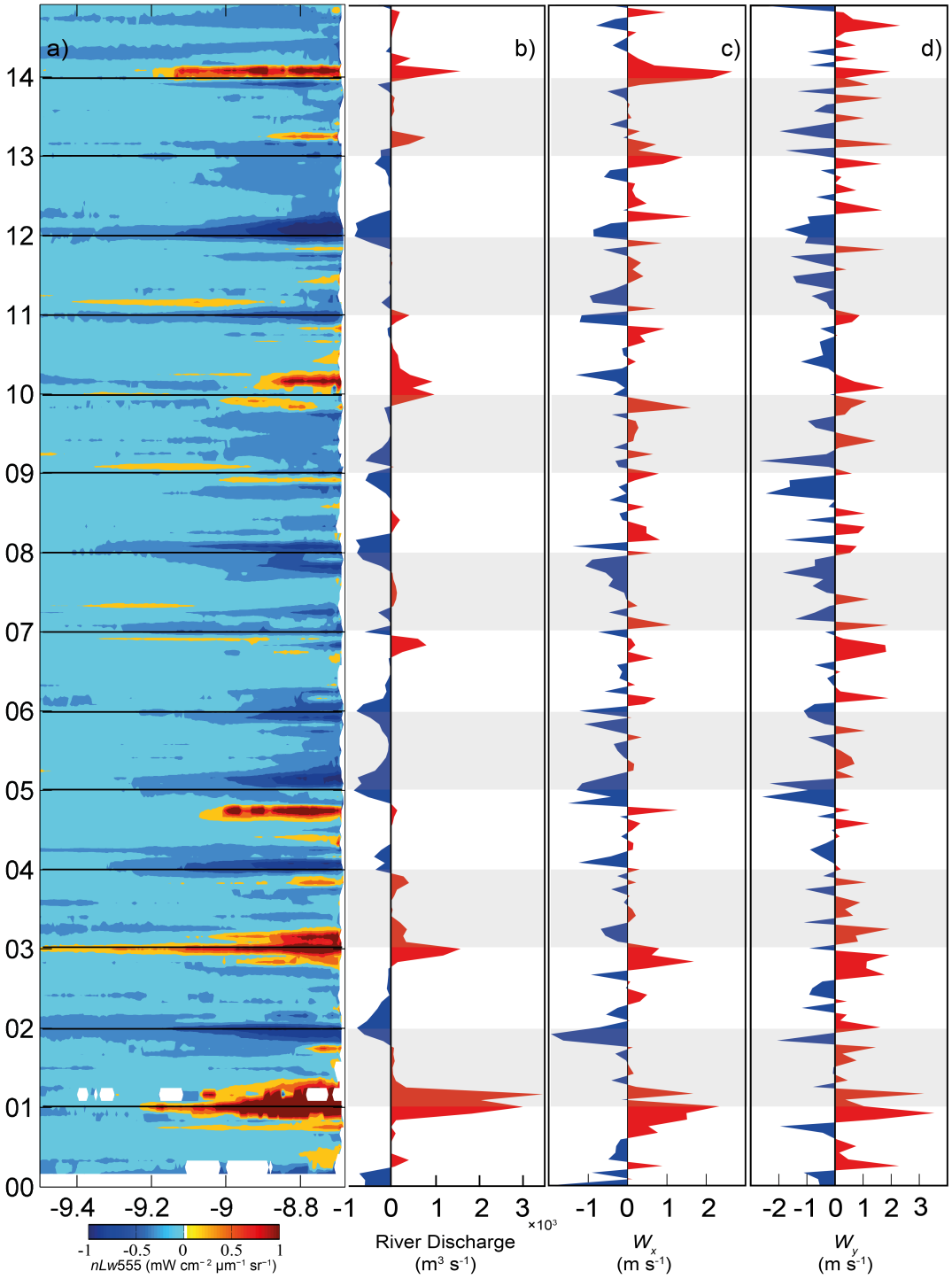

Figure 3.4: (a) Hovmöller diagram of monthly $nLw555$ anomalies for a latitudinal band coincident with Douro River mouth. (b) Douro river discharge and (c) zonal and (d) meridional wind monthly anomalies.

Great negative $nLw555$ anomalies are usually associated with winters with the predominance of upwelling-favourable winds, i.e. 2001-02, 2004-05, 2005-06, 2007-08, and 2011-12 winters (Figures 3.4a, c, d). Persistent northern and northeasterly winds induce winter upwelling events (deCastro et al., 2008; Álvarez et al., 2009), which have similar atmospheric patterns to those observed during summer, when precipitation and river discharge are minimum.

3.3.3 Inter-annual variability of dominant patterns

EOF analysis was carried out to examine dominant non-seasonal plume variability using $nLw555$ images. The first three EOFs and corresponding time series (Principal Component (PC)) are represented in Figure 3.5. The EOF spatial coefficients indicate the spatial extension and the dynamic importance of the processes in the study region, while PCs indicates the importance of the phenomenon (Navarro and Ruiz, 2006). The first EOF represents 59.7% of the total variance (Figure 3.5a). All the spatial coefficients were negative with the maxima found near the river mouth and decreasing offshore. This result represents the major influence of the Douro River discharge on $nLw555$ pattern. The first PC (Figure 3.5d) has a similar pattern to river discharge anomalies (Figure 3.4b), with a significant correlation coefficient of 0.62 (p_v<0.01) – negative PC values represent major plume events. A punctual disagreement was found on the autumn of 2004. The second and third EOF modes represent 9.4% and 6.1% of the total variance, respectively (Figures 3.5b and 3.5c).

Spatial variability of the second EOF enables the identification of two different zones (Figure 3.5b), showing different forcing mechanisms in these regions. Turbidity is enhanced along the coast – positive values in Figure 3.5e correspond to periods with anomalous plumes near shore. Values of EOF are negative in the open ocean and positive near the shoreline.

The PC2 is negatively correlated with UI monthly anomalies (r=0.33, p_v<0.01)(Figure 3.5e), showing that the second EOF spatial variability is influenced by the zonal Ekman

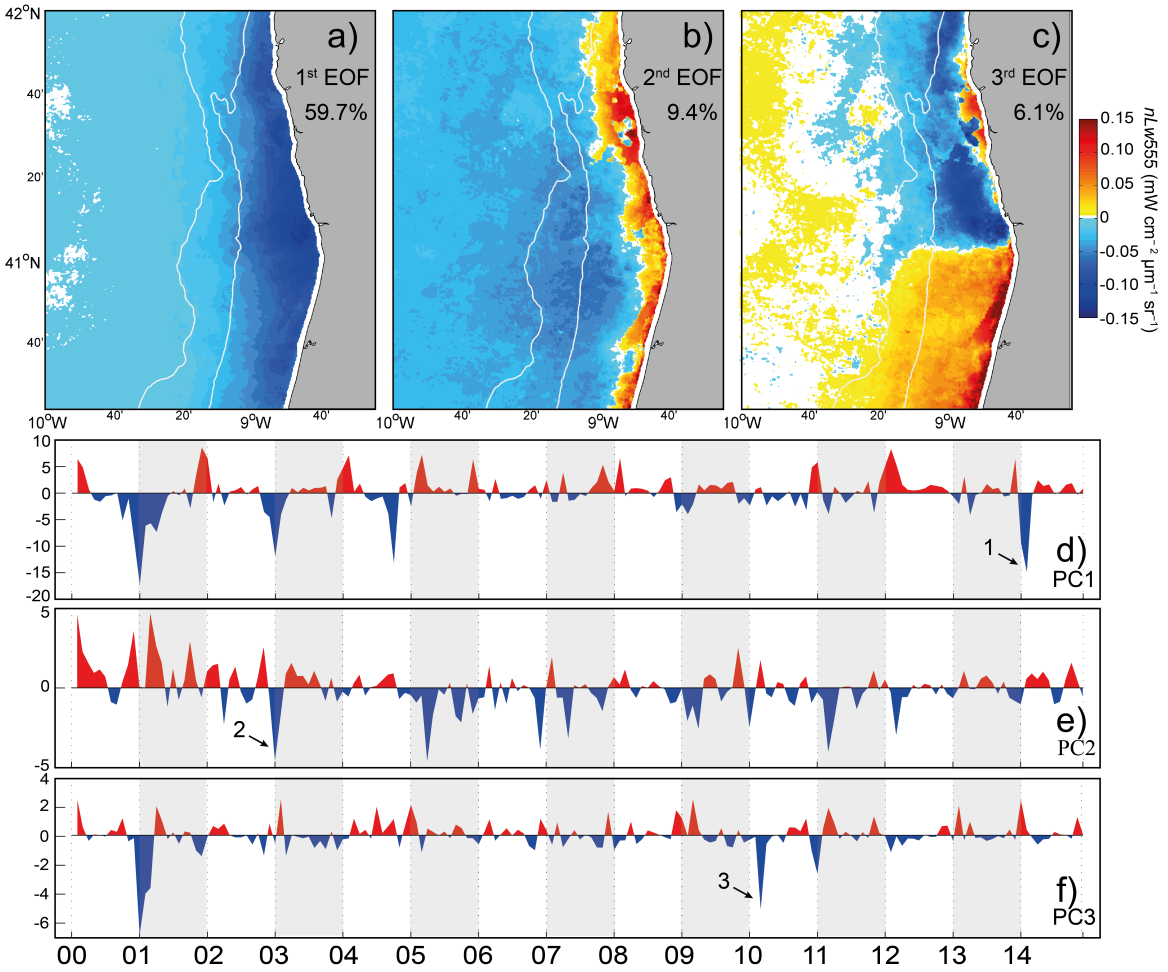

Figure 3.5: First three modes of EOF analysis after removing the annual and semi-annual harmonics of monthly $nLw555$ fields (a, b, and c, respectively). The percent of variance of each mode is also shown. First three PC showing the time evolution of the modes presented above (d, e, and f, respectively).

transport, which is consequently related with offshore transport of the plume (Figure 3.5b).

The third EOF presents two separated groups of plume patterns (Figure 3.5c), located northward and southward of the Douro river mouth. Values are negative at the north, while at the south they are positive with similar amplitude. Values are close to zero at 200 m isobath (Figure 3.5c). The third EOF pattern is similar with the mean-state of the Douro estuarine plume under downwelling-favourable winds shown in Chapter 2 (Mendes et al., 2014). Thus, the meridional wind component seems to influence the third EOF spatial distribution. The correlation between PC3 times series and alongshore wind component

(r=0.22, p_v<0.01)(Figure 3.5f) reveals the secondary importance of meridional winds in the Douro estuarine plume propagation.

$nLw555$ monthly composites corresponding to the extreme negative values described in the principal components (1, 2 and 3 in Figures 3.5d, 3.5e and 3.5f) are depicted in Figures 3.6a, 3.6b and 3.6c. Wind rose diagrams for each situation are also included.

During February 2014 (Figure 3.6a), PC1 presents a high negative amplitude and a smaller influence of PC3 mode. As stated above, the strong positive anomaly of river discharge explained this pattern. In this case, precipitation rate seem to be in phase with river discharge (Figures 3.3a and 3.3c) and southwest and westerly winds are predominant. Westerly winds tend to accumulate freshwater along the coastline and to decrease the cross-shore transport (Chapter 2; Chao (1988b) and Mendes et al. (2014)). The turbid plume is confined to the coast generating a northward and southward alongshore band (Chapter 2, Mendes et al. (2014)). The southward band has stronger intensity (represented by positive PC3 amplitude) with values greater than 2.5 mW cm^{-2}μm^{-1} sr^{-1}. The nearshore region between the Douro and Ria de Aveiro is shallower than the northern coast (Figure 3.1). Thus, wave sediment resuspension may be the cause of high turbid values in this area (12 – 16 m depth, Coelho and Veloso-Gomes (2006)).

During January 2003 (Figure 3.6b), PC2 shows a maximum amplitude with an

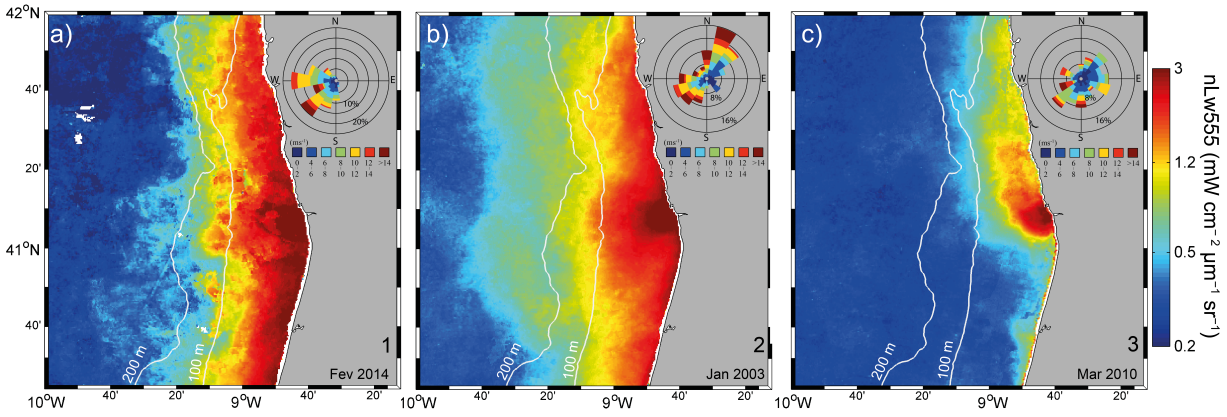

Figure 3.6: (a, b, c) $nLw555$ monthly fields for extreme negative peaks in EOF time series (1, 2, and 3 in Figures 3.5d, 3.5e and 3.5f). Wind roses are included for the same months with the direction indicating where the wind is blowing from (meteorological convention).

important influence of PC1 (Figure 3.5e). High turbid values are found along both northward and southward directions, which are explained by PC1 amplitude. However, as precipitation peaks as well as southwesterly winds are not in phase with river discharge (Figure 3.3 and Figure 3.4), the plume shows a characteristic pattern when compared with previous case. Northerly winds were predominant along this month (negative zonal component of Ekman transport), causing winter upwelling events, which control the turbid plume fate. High turbid values (3 mW $cm^{-2}\mu m^{-1}$ sr^{-1}) are found in the bulge area, close to the river mouth, and an offshore expansion of the bulge is observed (Chapter 2; Otero et al. (2008, 2013) and Mendes et al. (2014)). Moreover, the plume structure has a slight southwestward inclination, and two turbid coastal bands are detectable in opposite directions from the Douro Estuary in agreement with plume mean-state during upwelling events described in Chapter 2. Medium turbid values (0.5-1.0 mW $cm^{-2}\mu m^{-1}$ sr^{-1}) covered a large offshore area, indicating an increase of cross-shore transport caused by upwelling-favourable winds.

The spatial distribution of a PC3 negative extreme is depicted in Figure 3.6c. A high river discharge anomaly was observed on March 2010 (Figure 3.4b), with an intense $nLw555$ anomaly limited nearshore (Figure 3.4a). Southerly winds associated with a negative NAO phase (Vicente-Serrano et al., 2011), pushed the Douro turbid plume against the coast (Chapter 2; Otero et al. (2008) and Mendes et al. (2014)) generating a continuous coast-attached turbid band to the north, and increasing the possibility of the Douro plume to merge with water from smaller rivers discharging from the coast. The buoyant coastal plume originated from this mixture (WIBP) often generates a strong northward surface current that has substantial biological implications on surrounding area, namely in the Minho River region and in the Rias Baixas (western coast of Galicia, Spain) (Marta-Almeida et al., 2002; Sousa et al., 2013, 2014a; Mendes et al., 2016).

3.3.4 Climate influence

The correlation between variables presented in Figure 3.3 ($nLw555$, river discharge, and precipitation rate) and the teleconnection indices (NAO and EA) were calculated

during winter months (DJF) from 2000 to 2014. In addition, time lags between the variables were also considered: Lag 1 represents JFM values of $nLw555$, Douro River discharge and precipitation rate; Lag 2 corresponds to FMA and so on. The correlation coefficients between DJF atmospheric patterns and the referred variables (with different lags) are depicted in Figure 3.7.

The EA index shows to be directly correlated with the three variables. A positive EA pattern represents low pressure dominating the study area during winter months. Under this situation, more cold fronts reach the Northwestern Iberian coast resulting in a precipitation increase (Lorenzo and Taboada, 2005; deCastro et al., 2006). Precipitation has a high significant correlation with EA index (r=0.64) when no lag is considered. Then, this correlation coefficient decreased continuously until no significant values were observed with lags of 2, 3, and 4 months (Figure 3.7). This result is in agreement with a previous study carried out by Lorenzo and Taboada (2005), in the southern part of Galicia and in the

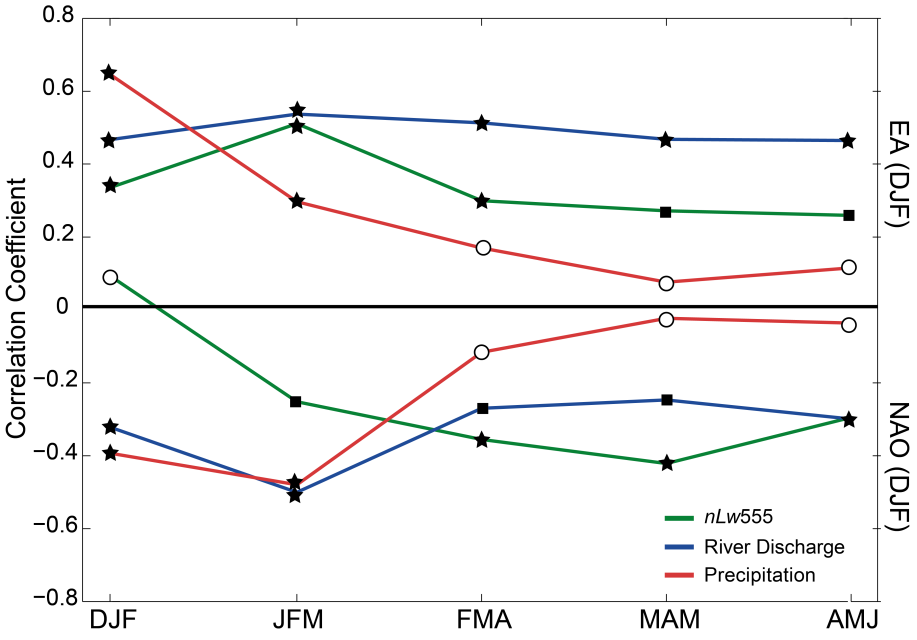

Figure 3.7: DJF atmospheric correlation patterns (EA – above; NAO – bellow) with $nLw555$, river flow, and precipitation from 2000 to 2014. A 0 lag corresponds to the DJF period, 1 to JFM period, and so on. Results with a significance level greater than 95% are represented by stars, greater than 90% by squares, and less than 90% by empty circles.

Atlantic coast (about 80 km north of the Douro Estuary). Regarding the EA influence on river discharge, significant correlations were found for all lags (r>0.46) with a maximum (r=0.54) when 1-month lag is considered. This result is in the line of that obtained by deCastro et al. (2006) for the Minho River (Figure 3.1). They found smaller correlation coefficients between the Minho River discharge and EA index with 0 and 1-month lag (close to 0.40). Significant correlation coefficients were observed between EA index and $nLw555$ for all lags with a maximum for a 1-month lag (r=0.51). The influence of EA index could be related to the prevalence of southerly winds at shelf, which tend to maximize the turbid signal near the river mouth (Chapter 2; deCastro et al. (2006) and Mendes et al. (2014)).

The correlation coefficient between river flow and the NAO index reaches its maximum value of -0.50 for a time lag of 1 month. This result is in the line to those obtained by Trigo et al. (2004) for Atlantic Iberian rivers, including the Douro River. Nevertheless, it is smaller than the one found by these authors from 1978 to 1998 (r=-0.76) and smaller than the one obtained for the Minho River by deCastro et al. (2006) (r=-0.54) from 1970 to 2005. This contrasts with the tendency for correlations to diminish from south to north over the region (Trigo et al., 2004; deCastro et al., 2006). However, deCastro et al. (2006) also found that correlation for the Minho River decreases in time, reaching values below –0.4 for periods from 1980 to 2005. The correlation coefficients found between precipitation anomaly and NAO index show a similar pattern to that described for the river. Maximum correlation is found at 1-month lag (r=-0.48) and drops to insignificant values for subsequent lags (Figure 3.7).

The correlation between $nLw555$ time series anomaly and NAO index presents unexpected results (Figure 3.7). A significant maximum correlation of -0.42 is reached for a time lag of 3 months, corresponding to early spring months (MAM). Several physical and biogeochemical processes can change ocean water turbidity, turning the relation between $nLw555$ and atmospheric patterns more difficult to evaluate. This correlation could be explained in terms of biological influence (i.e. coastal blooms) during spring upwelling events (3-month lags).

$nLw555$ composites (March and April) after a positive and negative winter phase

of NAO are depicted in Figures 3.8a and 3.8b, respectively. Under a positive DJF NAO (Figure 3.8a), turbid values during the subsequent spring are lower than after a negative DJF NAO (Figure 3.8b). The main differences were found along the coast, near the river mouth. Medium turbid values (0.6-1 mW $cm^{-2}\mu m^{-1}$ sr^{-1}) are confined to a short coastal band of about 10 km after a positive DJF NAO (Figure 3.8a) and until 30 km off coast after a negative one (Figure 3.8b). Phytoplankton blooms are usually a source of medium turbid values (0.6-1 mW $cm^{-2}\mu m^{-1}$ sr^{-1}) on coastal waters, but significantly smaller compared with the turbidity induced by the river outflow (Saldías et al., 2012).

The positive phase of the NAO (JFM) is characterized by colder, drier winters and by stronger northerly winds, which favour the winter upwelling events in the Douro coastal region (Lorenzo and Taboada, 2005; deCastro et al., 2006, 2008). Northerly winds increase, together with a decrease of the sea surface temperature and atmospheric conditions, inhibited water-column stratification and, combined with lower nutrient availability, appears to limit the phytoplankton development (Barton et al., 2003). Thus, it is reasonable to assume that this higher correlation between NAO and $nLw555$ at 3-month lag is due to the upwelling

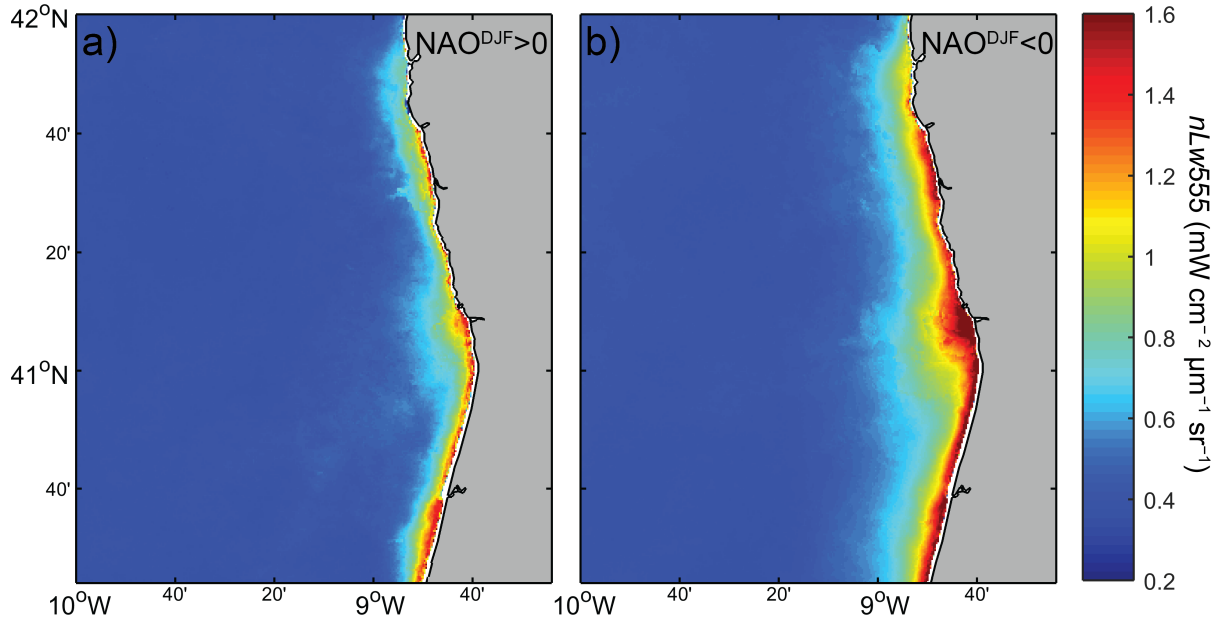

Figure 3.8: $nLw555$ spring composites (March and April) after a (a) positive and (b) negative NAO winter phases (DJF).

season shift towards winter, which can affect the magnitude and the timing of coastal spring blooms off the Douro River region.

3.3.5 The anomalous 2004 event

An anomalous turbid patch (values above 3-4 mW $cm^{-2}\mu m^{-1}$ sr^{-1}) was observed during 2004 autumn by means of monthly $nLw555$ images (Figure 3.3a and Figure 3.4a). The evolution of this anomalous event can be observed in daily images of Figure 3.9a. These images show a patch with very high $nLw555$ values unconnected with the Douro River discharge. The turbid feature development starts south of Douro Estuary (between the Douro Estuary mouth and the Ria de Aveiro) at about 15 km offshore on 25 September (Figure 3.9a), presenting several ramifications but none suggesting a fluvial origin (26 and 27 September, Figure 3.9a). The bloom increases rapidly both in area and in magnitude after 28 September, when $nLw555$ reaches values of about 4 mW $cm^{-2}\mu m^{-1}$ sr^{-1}.

Well-developed patterns related to freshwater plume turbidity are unexpected when river discharge is below 500 m^3 s^{-1} (Chapter 2; Teodoro et al. (2009) and Mendes et al. (2014)). The daily river discharge between the end of September and the beginning of October is low ($\sim$300 m^3 s^{-1}), although over September/October average (Figure 3.3a and 3.3b).

Two spectra of **nLw!** (**nLw!**) taken from the bloom core (28 September and 12 October) are depicted in Figure 3.9b. In 28 September, after 15 days of upwelling-favourable winds, maxima turbid values are observed in bands near 550 nm ($nLw547$=3.9 mW $cm^{-2}\mu m^{-1}$ sr^{-1}; $nLw555$=3.8 mW $cm^{-2}\mu m^{-1}$ sr^{-1}, Figure 3.9a). After that, those turbid features merged into a larger and brighter bloom (12 October, Figure 3.9a) with $nLw555$ values near to 4 mW $cm^{-2}\mu m^{-1}$ sr^{-1}. In this case, the bloom core spectrum is characterized by a peak at 488 nm (5.3 mW $cm^{-2}\mu m^{-1}$ sr^{-1}, Figure 3.9b) with higher reflectance in the blue region, but with a $nLw555$ value higher for the first case (Figure 3.9b).

A biological factor may be responsible or co-responsible for these very high turbid

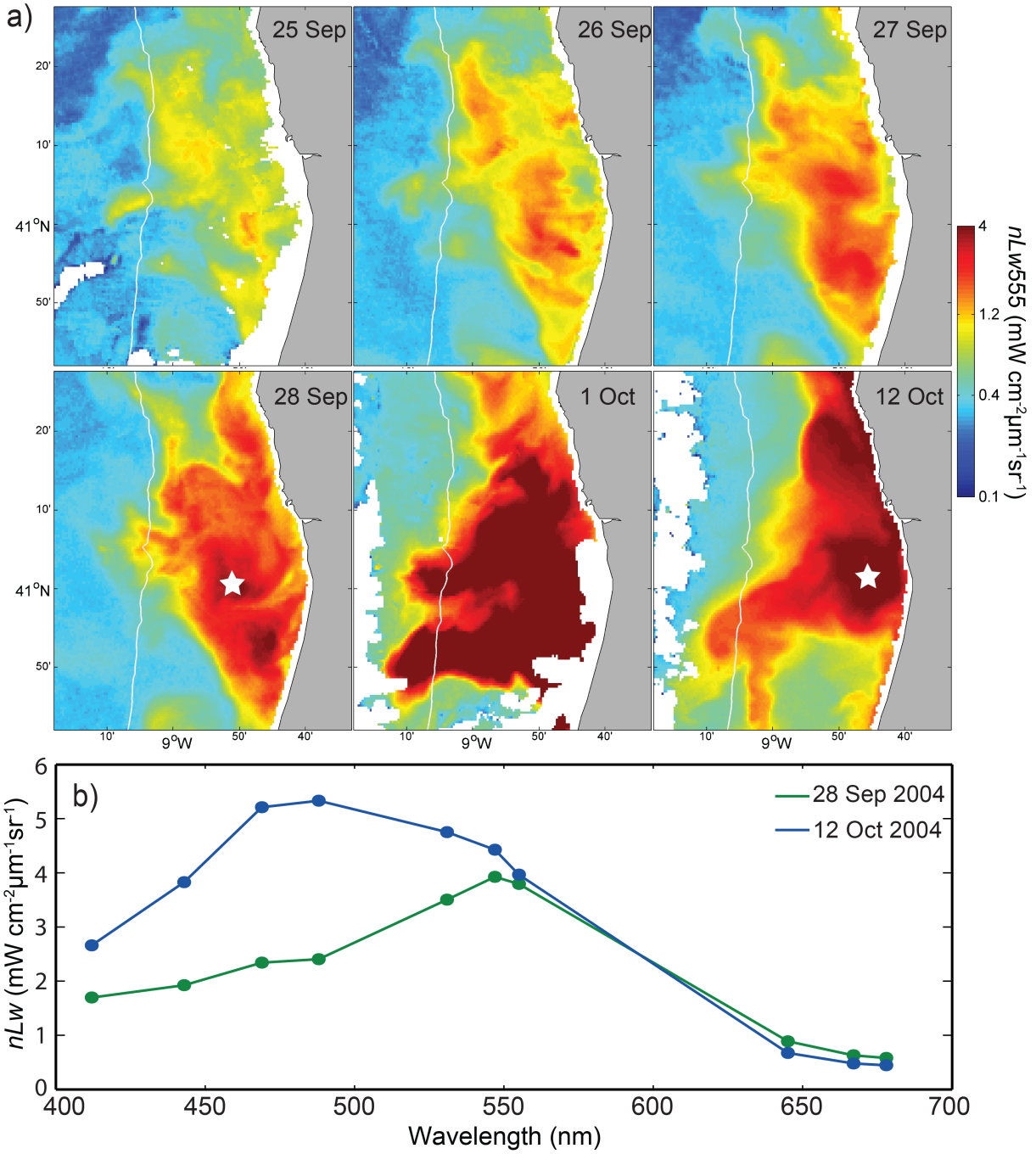

Figure 3.9: (a) $nLw555$ daily images from 26 September to 12 October of 2004. (b) nLw spectra from the pixels marked with a white star on September 28 and October 12.

values. One of the best assumption is a coccolithophore bloom, which usually causes a very bright patch of water with a turquoise colour (Moore et al., 2012; IOCCG, 2014). These

blooms can be visible in ocean-colour images as a result of light scattering by the coccolith plates detached from cells (from death or overproduction) suspended in near-surface waters (Moore et al., 2009). The transitions from upwelling to downwelling (summer-autumn) are often reported to be the most favourable situation for coccolithophore growth (Giraudeau et al., 1993; Ziveri et al., 1995). This transition is typically observed in the Northwestern of Iberian Peninsula during October (Figueiras et al., 2002) and is characterized by intermittent upwelling events, as in 3.9b. These conditions promote the confluence of warmer oceanic waters into colder and nutrient rich coastal upwelled waters (Silva et al., 2009; Moita et al., 2010).

Coccolithosphore blooms and turbid plumes are usually discriminated by the wavelength peak for reflected light, which is around 555 nm for sediment-dominated waters and 490 nm for coccolithospore bloom (Moore et al., 2012; IOCCG, 2014). That is the spectrum shape of October 12, indicating that a coccolithospore bloom (Figure 3.9b) could induce this higher $nLw555$ anomaly (Figure 3.3a). A conclusion from the spectrum analysis of September 28 remains unclear. Nevertheless, the coastal detection of any coccolithosphore bloom will be certainly affected by the background optical properties of the water during the event. For example, the presence of detritus and coloured dissolved matter can attenuate the reflectance in the blue region, causing a peak shift towards 555 nm, as already reported for a bloom event in the English Channel (Smyth et al., 2002; Gordon et al., 2009; Moore et al., 2012).

The real source of these anomalous turbid features during 2004 autumn remains unclear. The detection of coccolithophore blooms apart from other phenomena related to bright water by remote sensing is a challenging task. Even more without available *in situ* data for the period under analysis. However, this phenomenon could give a reasonable explanation of disagreements between the Douro River discharge and $nLw555$ time series for this single case. Despite these limitations, $nLw555$ MODIS imagery can be a useful tool, in combination with other ocean-colour products (Particulate Inorganic Carbon (PIC) concentration among others) to explore other turbid anomalies that can be related to phytoplankton blooms at higher temporal resolution in the Northwestern Iberian Peninsula.

3.4 Conclusion

The seasonal and inter-annual variability of the Douro turbid plume was evaluated taking into account the river discharge, wind, precipitation rates and climate patterns, namely NAO and EA indices. The main conclusions of this Chapter can be summarized as:

- High correlations were obtained between monthly time series of $nLw555$, river discharge and precipitation rates. All peak values of $nLw555$ matched with extreme local forcing. The autumn of 2004 is a remarkable exception.

- Positive $nLw555$ anomalies are often related with south and westerly winds that favours precipitation and, consequently, increases monthly river discharge. Although stronger downwelling winds usually enhances the positive anomaly intensity, it also reduces turbid plume width. Negative anomalies are usually associated with winters with the predominance of upwelling-favourable winds when precipitation and river discharge are minimum.

- The first EOF is representative of large turbid plumes with a strong correlation with anomalies of river discharge (59.7%). The second EOF mode characterizes the zonal Ekman transport (offshore propagation) and the third EOF one is related to northerly and southerly winds variability, representing a smaller part of the total variability (9.4% and 6.1%, respectively).

- The EA pattern plays a key role on precipitation rate in the Douro Estuary region, being directly correlated with all variables and in agreement with previous studies. The correlation between $nLw555$ and DJF EA index presents a peak at 1-month lag (r=0.51), as well as the river discharge (r=0.54).

- The correlation coefficient between DJF NAO index and Douro river discharge is high (-0.50), for a time lag of 1-month. Correlation between $nLw555$ and DJF NAO index present a peak of -0.42 at 3-month lag. The spring correlation (MAM) is possibly affected by upwelling season shifts, affecting biological coastal production.

- An extreme anomalous turbid pattern not related to estuarine outflow was found south of the Douro river mouth during the autumn of 2004. Despite the real source of this event remains uncertain, a coccolithophore bloom could be the most reasonable explanation.

  Although Chapters 2 and 3 were fundamental to detect and observe the mean-state and the inter-annual variability of the Douro estuarine plume, finer-scale temporal and spatial phenomena continue to be unclear.

  Numerical modelling and *in situ* monitoring could possibly fill comprehension gaps that MODIS daily images cannot afford. A numerical model implementation with tidal flow and freshwater variations as inputs is required to assess a better knowledge of Douro estuarine plume both in near and far field regions. The implementation and exploitation of a coastal numerical model is one of the main objectives of this dissertation that will be presented and discussed in Chapters 4, 5, and 6.

Chapter 4

Numerical model: estuarine and coastal implementations

4.1 Introduction

A general overview of the main formulations solved by MOHID is presented in this chapter. The modelling methodology developed and implemented to evaluate the propagation of the Douro estuarine plume (Chapters 5 and 6) is also described.

Two model configurations with three nested coastal levels each were used to evaluate the Douro estuarine plume dynamics and its propagation over shelf. The first level is a 2D barotropic model (L1) that propagates the hydrodynamic solution for high resolution 3D baroclinic models (L2 and L3), where water properties are computed. The main differences between the two configurations are the limits of the higher resolution levels (L2 and L3), which need to comprise two different areas affected by the Douro estuarine plume due to computational limitations. The configuration #1 was already validated by Sousa et al. (2013) and comprises the region north of Douro Estuary. The configuration #2 is focused on the adjacent coast of this estuary, comprising an area between the Ria de Aveiro Lagoon and the mouth of the Minho River, from south to north, respectively. Although the core of these implementations is based on the previous numerical modelling design by Sousa et al.

(2014c,b) and Vaz et al. (2015) for Minho and Tagus estuarine plumes, respectively, small updates were applied. In addition, a proper validation of the new coastal implementation was performed (configuration #2) by comparing computed water properties results and *in situ* observations.

A good validation likewise a satisfactory confidence in the model results are strongly dependent on the boundary conditions imposed, such as land discharges and atmospheric forcings. Therefore, three other models are used and/or developed. The results from two estuarine models that simulate estuarine tidal flows from Douro (novel application) and Minho (Sousa et al., 2013) rivers are used as inputs for coastal model as well as the inputs from small rivers discharging into Rias Baixas. Moreover, an atmospheric application using the Weather Research and Forecasting model (WRF) was also implemented for the coastal region under study in configuration #2 and its predictions were validated through comparison with meteorological *in situ* measurements.

This Chapter is organized as follows: Section 4.2 introduces the numerical model and an outline of its physics background. Section 4.3 presents the main description of the coastal models implementation. In addition, are described the estuarine and atmospheric model applications and presented the results of their validation. The validation of the coastal model (configuration #2) is shown in Section 4.4, while in Section 4.5 a brief conclusion of this Chapter is presented.

4.2 Numerical model - MOHID

4.2.1 Hydrodynamic model

MOHID solves the primitive equations for incompressible flows in 3D Cartesian coordinates. Hydrostatic equilibrium is assumed as well as Boussinesq and Reynolds approximations. A brief summary of the physics solved by the model is presented (a more detailed description can be found in Santos (1995), Martins et al. (2001), Leitão (2002) and Vaz (2007)).

The momentum balance equations for horizontal velocities is described in Cartesian coordinates by:

$$\frac{\partial u}{\partial t} = -u\frac{\partial u}{\partial x} - u\frac{\partial v}{\partial y} - u\frac{\partial w}{\partial z} + fv - \frac{1}{\rho_0}\frac{\partial p}{\partial x} + \frac{\partial}{\partial x}\left(A_h\frac{\partial u}{\partial x}\right) + \frac{\partial}{\partial y}\left(A_h\frac{\partial u}{\partial y}\right) + \frac{\partial}{\partial z}\left(A_z\frac{\partial u}{\partial z}\right) \tag{4.1}$$

$$\frac{\partial v}{\partial t} = -v\frac{\partial u}{\partial x} - v\frac{\partial v}{\partial y} - v\frac{\partial w}{\partial z} - fu - \frac{1}{\rho_0}\frac{\partial p}{\partial y} + \frac{\partial}{\partial x}\left(A_h\frac{\partial u}{\partial x}\right) + \frac{\partial}{\partial y}\left(A_h\frac{\partial u}{\partial y}\right) + \frac{\partial}{\partial z}\left(A_z\frac{\partial u}{\partial z}\right) \tag{4.2}$$

where u, v and w are the velocity vector components in x, y and z directions, respectively, f the Coriolis parameter, A_h and A_z the turbulent viscosities in the horizontal and vertical directions and p is pressure. The temporal evolution of velocities is given by the balance between advective transports, Coriolis force, pressure gradient and turbulent diffusion.

The hydrostatic approximation is assumed with:

$$\frac{\partial p}{\partial z} - \rho g = 0 \tag{4.3}$$

where g is gravity and ρ is density. If the atmospheric pressure (p_{atm}) is subtracted from p, and density is divided into a constant reference density (ρ_0) and a deviation (ρ') from that reference density, the pressure in any depth is obtained integrating between z and free surface η:

$$p(z) = p_{atm} + g\rho_0(\eta - z) + g\int_z^\eta \rho' \tag{4.4}$$

Equation 4.4 relates pressure at any depth with atmospheric pressure at free surface, sea level and density anomaly integrated between the level and surface. Deriving this equation in the horizontal directions is obtained the pressure gradient to be used in

Equations 4.1 and 4.2:

$$\frac{\partial p}{\partial x} = \frac{\partial p_{atm}}{\partial x} - g\rho_0 \frac{\partial \eta}{\partial x} - g\frac{\partial}{\partial x}\int_z^\eta \rho' dz \tag{4.5}$$

$$\frac{\partial p}{\partial y} = \frac{\partial p_{atm}}{\partial y} - g\rho_0 \frac{\partial \eta}{\partial y} - g\frac{\partial}{\partial y}\int_z^\eta \rho' dz \tag{4.6}$$

The total pressure gradient is the sum of the gradients of atmospheric pressure, of the sea surface elevation (barotropic pressure gradient) and the density distribution (baroclinic pressure gradient). This decomposition is then introduced in Equations 4.1 and 4.2 assuming the Boussinesq approximation ($\rho' \ll \rho_0$) resulting in:

$$\begin{aligned}\frac{\partial u}{\partial t} + \frac{u\partial u}{\partial x} + \frac{u\partial v}{\partial y} + \frac{u\partial w}{\partial z} = &+fv - \frac{1}{\rho_0}\frac{\partial p_{atm}}{\partial x} - g\frac{\partial \eta}{\partial x} - \frac{g}{\rho_0}\int_z^\eta \frac{\partial \rho'}{\partial x} dz \\ &+\frac{\partial}{\partial x}\left(A_h \frac{\partial u}{\partial x}\right) + \frac{\partial}{\partial y}\left(A_h \frac{\partial u}{\partial y}\right) + \frac{\partial}{\partial z}\left(A_z \frac{\partial u}{\partial z}\right)\end{aligned} \tag{4.7}$$

$$\begin{aligned}\frac{\partial v}{\partial t} + \frac{v\partial u}{\partial x} + \frac{v\partial v}{\partial y} + \frac{v\partial w}{\partial z} = &-fu - \frac{1}{\rho_0}\frac{\partial p_{atm}}{\partial y} - g\frac{\partial \eta}{\partial y} - \frac{g}{\rho_0}\int_z^\eta \frac{\partial \rho'}{\partial y} dz \\ &+\frac{\partial}{\partial x}\left(A_h \frac{\partial u}{\partial x}\right) + \frac{\partial}{\partial y}\left(A_h \frac{\partial u}{\partial y}\right) + \frac{\partial}{\partial z}\left(A_z \frac{\partial u}{\partial z}\right)\end{aligned} \tag{4.8}$$

The vertical velocity is calculated from the incompressible continuity equation (mass balance equation):

$$\frac{\partial u}{\partial x} + \frac{\partial v}{\partial y} + \frac{\partial w}{\partial z} = 0 \tag{4.9}$$

by integrating between the bottom and the depth z:

$$w(z) - w(-h) = -\frac{\partial}{\partial x}\left(\int_{-h}^z u dz\right) - \frac{\partial}{\partial y}\left(\int_{-h}^z v dz\right) \tag{4.10}$$

where $w(-h)$ is assumed null.

The free surface equation is obtained by integrating the continuity equation over the

water column, between the bottom ($z = -h$) and the free surface elevation ($z = \eta$):

$$\frac{\partial \eta}{\partial t} = -\frac{\partial}{\partial x}\int_{-h}^{\eta} u dz - \frac{\partial}{\partial y}\int_{-h}^{\eta} v dz \tag{4.11}$$

MOHID also solves a transport equation for salinity, water temperature or any other tracer:

$$\begin{aligned}\frac{\partial \alpha}{\partial t} + \frac{\partial (u\alpha)}{\partial x} + \frac{\partial (v\alpha)}{\partial y} + \frac{\partial (w\alpha)}{\partial z} = \frac{\partial}{\partial x}\left(K_H \frac{\partial \alpha}{\partial x}\right) + \frac{\partial}{\partial y}\left(K_H \frac{\partial \alpha}{\partial y}\right) \\ + \frac{\partial}{\partial z}\left(K_V \frac{\partial \alpha}{\partial z}\right) + FP\end{aligned} \tag{4.12}$$

where α is the property which is transported, K_H and K_V are the horizontal and vertical diffusion coefficients, respectively, and FP is a source or sink term.

Finally, the density ρ is calculated as function of water temperature and salinity by the United Nations Educational, Scientific and Cultural Organization (UNESCO) equation of state (Fofonoff and Millard, 1983).

4.2.2 Lagrangian model

The Lagrangian particle-tracking model is a subset of MOHID modelling system and has been used specially to study pollutant dispersion (Gómez-Gesteira et al., 1999; Braunschweig et al., 2003). This type of model uses the passive tracer's concept, which is characterized by their spatial coordinates. The Lagrangian module uses hydrodynamic information, updating the calculations without need to solve all variables at the same time. Model assumes that velocity of each particle (u_P) can be split into a large scale organized flow, characterized by a mean velocity (u_M), provided by the hydrodynamic model, and a smaller scale random fluctuation (u_F), so that $u_P = u_M + u_F$. Particle tracking model solves the following equation:

$$\frac{\partial x_i}{\partial t} = u_P(x_i, t) \tag{4.13}$$

where x_i is the particle position. Equation 4.13 is solved using an explicit method:

$$x_i^{t+\Delta t} = x_i^t + \Delta t u_p^t \tag{4.14}$$

The random movement is calculated following the Allen (1982) procedure, based on the mixing length and the standard deviation of the turbulent velocity provided by the hydrodynamic model. Particles retained velocity for long enough to perform the random movement, which is dependent on the local turbulent mixing length.

In this study, every particle is taken to be a water parcel whose paths are computed as it moves through the surface layer.

4.2.3 Equations discretization

MOHID uses a finite volume approach to perform the spatial discretization of the equations, which is fully described in Martins et al. (1998, 2001) and Leitão (2002). In the horizontal direction an Arakawa C staggered grid is adopted (Arakawa and Lamb, 1977). The temporal discretization is carried out using a semi-implicit algorithm: the Alternate Direction Implicit (ADI) described in Abbott and Basco (1989) that computes sea level evolution with two time levels per iteration, following the method proposed by Leendertse (1967). This algorithm calculates alternatively one component of the horizontal velocity implicitly while the other is calculated explicitly, avoiding the calculation of internal and external modes with different time steps (Leitão, 2002).

For the baroclinic force, MOHID uses a z-level approach for any type of vertical coordinates (Kliem and Pietrzak, 1999). The horizontal density gradient is always integrated into the Cartesian space. Advection and diffusion of tracer properties, i.e. water temperature and salinity, are computed explicity in horizontal and implicity in vertical, using a Total Variation Diminishing (TVD) Superbee method (Pietrzak, 1998). The vertical mixing is solved using a laplacian diffusion equation, where the turbulent viscosity is computed using the $k - \epsilon$ model. MOHID system is coupled to the General Ocean Turbulence Model (GOTM) (Burchard et al., 1998; Burchard and Bolding, 2001). This is a water column

model, which simply allows a choice between some standard turbulence parameterizations. The parameterization proposed by Canuto et al. (2001) were used in the nested coastal applications.

4.2.4 Initial conditions

In terms of hydrodynamic, initial elevation equal to the mean water level of the study region with null gradient was used as well null velocity for 2D estuarine and 3D nested coastal models.

The initial ocean stratification in levels 2 and 3 of the nested model applications was set by 3D fields of water temperature and salinity from World of Ocean Atlas 2013 (WOA2013) monthly mean climatologies (`https://www.nodc.noaa.gov/OC5/WOD13/docwod13.html` - Zweng et al. (2013) and Locarnini et al. (2013)).

Initial condition of water temperature and salinity for estuarine models are set constant in space with typical values considering the period of simulation.

4.2.5 Boundary conditions

Five different types of boundaries were considered in this work: bottom, surface, lateral closed, lateral opened and moving boundaries.

4.2.5.1 Surface boundary

On the free surface boundary all advective fluxes across the surface are assumed null, which means vertical $Wflux$ is null:

$$Wflux|_{surface} = 0 \tag{4.15}$$

Diffusive flux of momentum is explicitly imposed by means of wind surface stress, $\vec{\tau}_W$:

$$A_z \frac{\partial u}{\partial z}|_{surface} = \tau_{Wx} \tag{4.16}$$

$$A_z \frac{\partial v}{\partial z}|_{surface} = \tau_{Wy} \tag{4.17}$$

The wind stress is computed according to a quadratic friction law:

$$\tau_{Wx} = C_{10}\rho_a W_x |\vec{W}| \tag{4.18}$$

$$\tau_{Wy} = C_{10}\rho_a W_y |\vec{W}| \tag{4.19}$$

where $\vec{W}$ is the wind speed measured 10 m above sea surface and ρ_a is the air density. C_{10} is a drag coefficient, which is a function of wind velocity in each horizontal direction (W_x and W_y).

The sensible and latent heat fluxes are calculated using the Bowen and Dalton laws, respectively (Chapra, 1997).

Surface boundary conditions are computed by the model from meteorological data provided by the user, such as wind intensity and direction, air temperature, atmospheric pressure, relative humidity, solar radiation.

4.2.5.2 Bottom boundary

At the bottom, advective fluxes are imposed null and diffusive flux of momentum is estimated from bottom stress calculated from a quadratic law, which depends on the near-bottom velocity:

$$A_z \frac{\partial u}{\partial z}|_{bottom} = C_D u\sqrt{u^2 + v^2} \tag{4.20}$$

$$A_z \frac{\partial v}{\partial z}|_{bottom} = C_D v\sqrt{u^2 + v^2} \tag{4.21}$$

where C_D is the bottom drag coefficient, which is calculated by:

$$C_D = \left(\frac{k_c}{\log(\frac{z+z_0^b}{z_0^b})} \right)^2 \tag{4.22}$$

where k_c is the von Karman constant and z_0^b is the bottom roughness length. z_0^b was set to 0.0025. Bottom stress must be semi implicitly calculated in the momentum equation for numerical stability reasons. No fluxes of salinity and/or water temperature are considered at the bottom.

4.2.5.3 Lateral closed boundaries

Closed boundaries correspond to land. A free slip condition is used to resolve this lateral boundary, assuming a zero normal component of mass and momentum diffusive fluxes at cell faces in contact with land.

4.2.5.4 Lateral open boundaries

Two different types of lateral open boundaries are considered in the coastal and estuarine model implementations: the ocean and landward boundary conditions.

Considering the 3D nested model applications, amplitude and phase of the main tidal constituents from a product based on a global hydrodynamic model (Finite Element Solutions of 2004 or 2012) are imposed in the 2D barotropic model at first level. The tidal reference solution generated by this model is then propagated to the subsequent 3D baroclinic levels applying the Flather (1976) radiation scheme. External solutions of salinity and water temperature provided by monthly climatologies from WOA2013 database are also imposed at baroclinic models in level 2. All ocean boundary conditions at level 3 are supplied by hydrodynamic and water properties solutions from level 2. A Flow Relaxation Scheme (Martinsen and Engedahl, 1987) is applied to water level, velocity components, water temperature and salinity in baroclinic models. This scheme also adds small corrections to model predictions by diminishing deviations from the reference solution.

As landward boundary condition, estuarine discharges are imposed only in level 3 with related water temperature and salinity properties from outflows predicted offline from 2D estuarine numerical models. Small rivers that discharging into Rias Baixas are also imposed at this level.

Regarding the estuarine 2D model applications, tidal forcing and daily river discharges are imposed in lateral ocean and landward boundaries, respectively. Water temperature and salinity are considered constant at ocean and river boundaries, with typical values considering the period of simulation. Only for validation purposes, the water temperature of rivers discharge was set dependent on predicted daily smooth air temperature for the estuarine region.

4.2.5.5 Moving boundaries

Moving boundaries are closed boundaries that change position in time. If there are intertidal zones in the domain, some model cells can be alternatively covered or uncovered depending on tidal elevation. These type of boundaries are especially useful in this study for estuarine model applications. A stable algorithm is required for modelling these zones and their effect on hydrodynamics of estuaries. A detailed explanation of the algorithms used by MOHID can be found in Martins et al. (2001) and Leitão (2002).

4.3 Coastal model implementation

The implementation of the coastal model to the region of influence of the Douro estuarine plume follows a downscaling methodology similar to that used to simulate the Algarve coastal circulation (Leitão et al., 2005) and the Tagus estuarine plume propagation (Vaz et al., 2009a). Moreover, this method was recently validated for the Northwest coast of the Iberian Peninsula in a study about the Minho estuarine plume propagation and its influence on Rias Baixas circulation (Sousa, 2013; Sousa et al., 2014c,b). Coastal numerical applications with identical implementations to that used by Sousa (2013) was applied, with few updates that will be described in next subsections.

In the last years, downscaling techniques have been successfully applied in the field of coastal oceanography to simulate hydrodynamics and water quality, and to solve common management questions on the local scale (Leitão et al., 2005; Kenov et al., 2012; Mateus et al., 2012). Downscaling techniques are used to transfer information from large-scale (regional/global) to small-scale models (local), enabling a comprehensive description of dynamics processes and the properties within water. These techniques are often used as well to extend operational forecasts from global and regional scales to local coastal and estuarine systems (Franz et al., 2014).

A domain included inside the domain of another model is named as nested domain, or sub-domain. The boundary conditions are then provided from a domain to its sub-domains. Thus, larger and coarse resolution domains (*father* models) provide boundary conditions for finer nested domains (*son* models). *Son* models are used to represent regions where a higher spatial resolution is needed.

In addition to the 3D nested coastal model implementation, 2D estuarine implementation for the Douro and Minho estuaries are included in order to simulate the estuarine-coastal exchange. These applications run offline, computing the estuarine outflows, which serve as landward boundaries for 3D coastal models.

Atmospheric boundary conditions to the estuarine and coastal models are provided from WRF model predictions for the study region.

4.3.1 Configurations

The region of Douro estuarine plume influence is very large, especially during extreme conditions of river discharge. Due to computational constraints, two 3D configurations need to be implemented to represent this region, with three nested coastal levels each, comprising the region between the Ria de Aveiro Lagoon and the Minho River, and between the Douro River and Rias Baixas. 2D models applications for the Douro and Minho estuaries were used to accurately simulate the Douro estuarine plume propagation and its interaction with Minho estuarine plume and Rias Baixas.

The nested model configuration adopted for both cases is systematized in Figure 4.1. The first and larger level is used to simulate the barotropic tide (L1). The second and third levels are baroclinic models (L2 and L3). The third level comprises a smaller region with higher horizontal resolution to compute plume propagation. The downscaling from second to third level is made to smooth the transition of resolution from the first level.

The first level (L1) is equal for both configurations (Figure 4.2), ranging from 13.5°W to 1°E and 33.5°N to 50°N, with a variable horizontal resolution of 0.06°(∼6 km) offshore and was constructed based on the ETOPO1 global database. This level is a 2D barotropic model using the fully revised tidal solution from a global hydrodynamic model (Finite Element Solution 2012 (FES2012)) as boundary condition (Carrère et al., 2012). This constitute an update to the Sousa (2013) coastal application, which used an older version of this global product as tidal forcing in the L1 domain (FES2004).

As stated before, two configurations with different high-resolution levels (L2 and L3) were adopted in this work. To study the interaction between Douro and Minho estuarine plumes and their impact on the Rias Baixas adjacent circulation, the same L2 and L3 levels of Sousa (2013) were used, with a small southward extension of L3 in order to include the Douro River mouth (configuration #1 - Table 4.1). This configuration was already

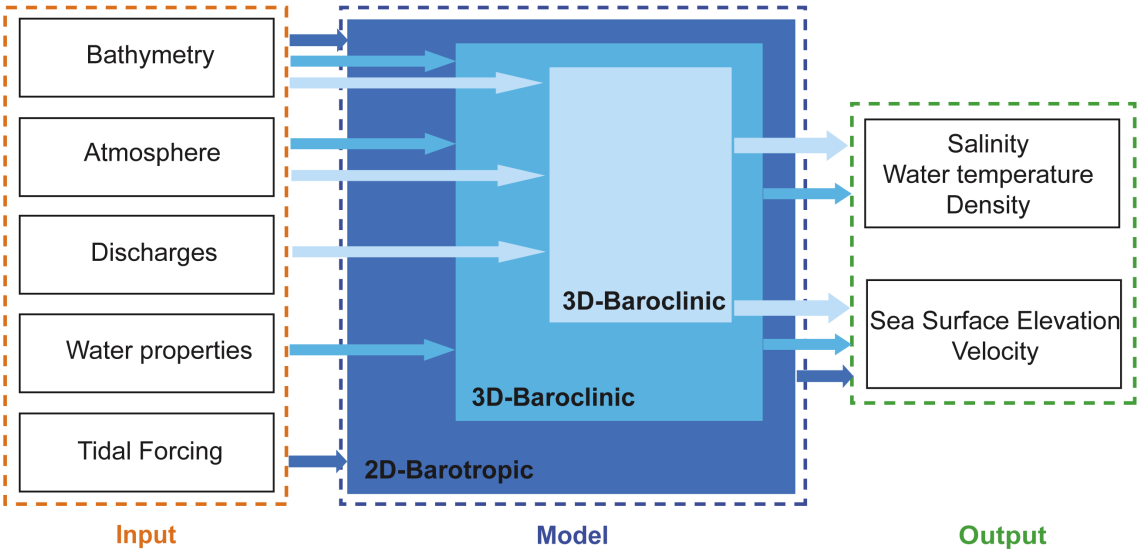

Figure 4.1: Schematic diagram of the MOHID (Sousa, 2013).

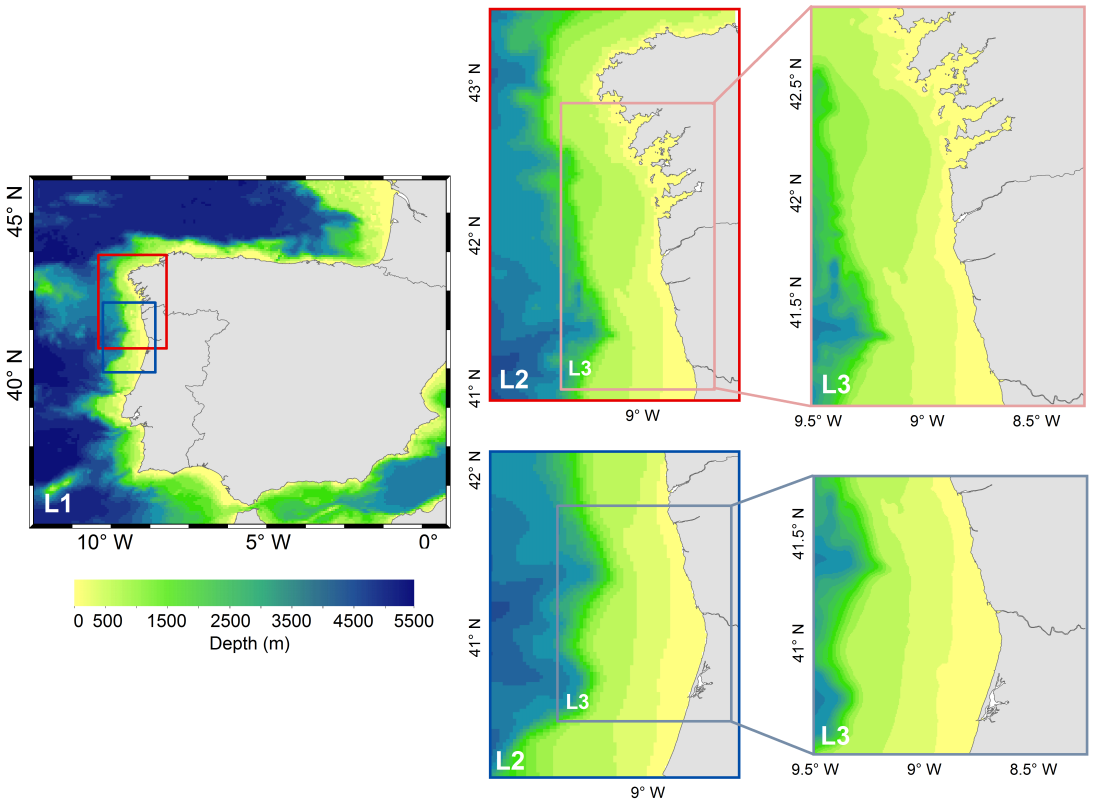

Figure 4.2: The MOHID nesting applications for configurations #1 (red-upper panel) and #2 (blue-lower panel).

validated by Sousa (2013).

L2 and L3 levels were created comprising a region further south and focused in the Douro Estuary (configuration #2 - Table 4.2) to study a southward possible larger range of plume propagation along the coastal region in response to wind forcing from north conditions.

Both L2 and L3 bathymetries were built based on GEBCO (Becker et al., 2009). A z-level vertical discretization using Cartesian coordinates was adopted. Sigma coordinates were applied on the first 10 m, considering the surface behaviour of estuarine plumes and the importance of the baroclinic processes on their dispersion (Tables 4.1 and 4.2).

The initial conditions of water temperature and salinity in L2 and L3 set by 3D fields from WOA2013 and the open boundary conditions at level 2 are forced from the same external solution representing an additional improvement of the Sousa et al. (2013)

Table 4.1: Summary of configuration #1. Dimensions and characteristics.

Domain	D1	D2	D3
Grid Corners	Lon; -13.50 / 1.00° Lat: 33.48 / 49.90°	Lon; -10.08 / -8.40° Lat: 40.91 / 43.50°	Lon; -9.52 / -8.60° Lat: 40.99 / 42.86°
Dimensions	273 × 241	129 × 24	372 × 184
# cells	65793	10836	68448
Δx (km)	6	2	0.5
Δt (s)	180	60	15
z Discretization	———	7 Sigma + 39 Cartesian	7 Sigma + 35 Cartesian
Tide	FES2012	D1	D2
Water Properties	———	WOA2013	D2
Atmosphere	———	WRF	WRF
Discharge	———	———	Estuarine Model

model configuration, which used an older version of this database (World of Ocean Atlas 2009 (WOA2009)).

In L2 a time step of 60 s is used and the turbulent horizontal eddy viscosity is set to 20 $m^2\ s^{-1}$. The time step and turbulent horizontal eddy viscosity in the L3 are set to 60 s and 5 $m^2\ s^{-1}$, respectively. Following Sousa (2013), the baroclinic forcing is slowly activated over 10 inertial periods. The 3D momentum, heat and salt balance equations are computed implicitly in the vertical direction and explicitly in the horizontal direction.

As landward boundary condition (only in L3 grids), a point discharge representing the Douro outflow is considered (configurations #1 and #2). In addition, the Minho estuary outflow as well as small inputs from rivers discharging in Rias Baixas are considered in configuration #1. Oitabén-Verdugo, Lérez, Umia and Ulla River discharges were obtained from estimations presented by Otero et al. (2010) and Douro and Minho outflows are computed by estuarine models (see Section 4.3.2.2), and directly imposed as momentum, water and mass discharge to coastal models (L3).

Table 4.2: Summary of configuration #2. Dimensions and characteristics.

Domain	D1	D2	D3
Grid Corners	Lon; -13.50 / 1.00° Lat: 33.48 / 49.90°	Lon; -9.94/ -8.40° Lat: 40.16 / 42.10°	Lon; -9.52 / -8.60° Lat: 40.50 / 41.75°
Dimensions	273 × 241	97 × 68	251 × 184
# cells	65793	6596	46184
Δx (km)	6	2	0.5
Δt (s)	180	60	15
z Discretization	———	7 Sigma + 39 Cartesian	7 Sigma + 36 Cartesian
Tide	FES2012	D1	D2
Water Properties	———	WOA2013	D2
Atmosphere	———	WRF	WRF
Discharge	———	———	Estuarine Model

Surface boundary conditions are imposed using predictions of the WRF model with a spatial resolution of 4 km. Meteorological data predictions for configuration #1 were obtained from MeteoGalicia (`www.meteogalicia.es`) as in Sousa et al. (2013) coastal model application, while for configuration #2 a new implementation of this atmospheric model was required since those data does not totally covered the region. This application will be fully described in Section 4.3.3. WRF output spatial fields were then hourly interpolated for L2 and L3 levels using a triangulation method in space and a linear method in time.

All simulations were carried out using a multi-core approach (4 cores) through Open Multi-Processing (OpenMP) parallel programming tool adding up another improvement to the MOHID configuration of Sousa et al. (2013) that run in single mode. OpenMP Application Programming Interface (API) was used to reduce the computational time, following the shared memory paradigm in order to improve model performance (Mateus and Neves, 2013).

4.3.2 Landward boundary - Estuarine models

4.3.2.1 Douro Estuary

The Douro estuarine model was implemented in a 2D mode (depth integrated) to reproduce outflow and respective water properties at the mouth, under different discharge conditions (Figure 4.3).

The numerical grid for the Douro Estuary was built from bathymetric data provided by the *Instituto Hidrográfico* (IH), updated with topographic data from an available Digital Terrain Model (DTM) for adjacent offshore area. The numerical bathymetry has 233 and 527 cells in North-South and West-East directions, respectively, with 40 m spatial resolution.

The tidal forcing is imposed on the ocean open boundary. The tide is determined from fifty harmonic constituents calculated from a Sea Surface Elevation (SSE) dataset measured at the tide gauge located near the Leixões harbour during 2007 (see Figures 2.1 and 2.2 in Chapter 2). A phase and amplitude correction factor was imposed in way that model accurately reproduces the SSE at the tidal gauge (Vaz et al., 2005; Mendes, 2010).

Daily mean Douro River discharge data was obtained from the SNIRH database

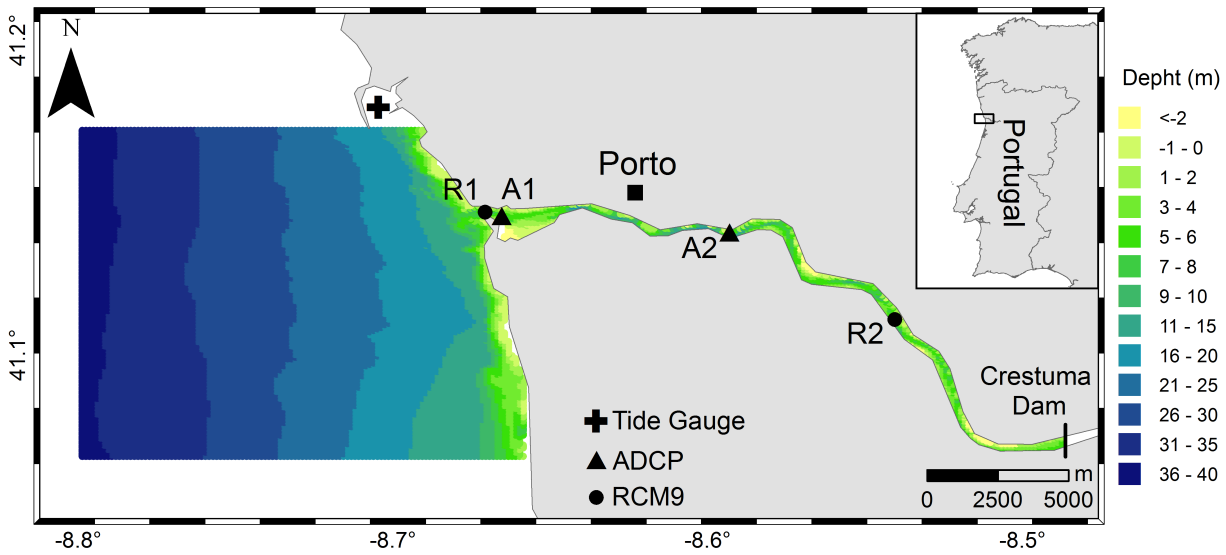

Figure 4.3: The numerical bathymetry of the Douro Estuary with reference to the location of the stations used on the model calibration and validation.

(`www.snirh.pt`) at the Crestuma dam and was imposed in the model as land boundary.

The initial and the ocean boundary conditions were fixed with typical values for the simulation period based on WOA2013 climatologies. After performing several experiences, a time step of 6 s and a horizontal eddy viscosity of 5 m^2s^{-1} were adopted.

The model configuration was calibrated and validated using the methodologies proposed by Dias and Lopes (2006a,b) and Dias et al. (2009). As a first approach, a qualitative comparison of the temporal evolution between model predictions and SSE data measured is performed for September 2005, using data from the IH project Estuarine COntributions to Inner Shelf dynamics (ECOIS) at several locations (Figure 4.3). The validation procedure was performed using independent data sets, which include observations of current velocities and SSE values (February/March 2006 data). The model's accuracy was evaluated through determination of the $RMSE$ (Equation 4.23) and $SKILL$ parameter (Equation 4.24)(Willmott, 1981; Warner et al., 2005), and also through the comparison between amplitude and phase of the main tidal constituents determined from harmonic analysis (Dias and Lopes, 2006a,b; Dias et al., 2009). It should be noted that the low frequency signal was removed from the observation data, considering a cut-off frequency of 30 h.

$RMSE$ is given by:

$$RMSE = \left\{ \frac{1}{N} \sum_{i=1}^{N} [X_{i_{obs}} - X_{i_{model}}]^2 \right\}^{\frac{1}{2}} \tag{4.23}$$

where N corresponds to the number of records and X_{obs} and X_{model} represent observed and predicted data, respectively. For local comparison of SSE, values between 5 and 10% of the local amplitude should be considered very good (Dias et al., 2009).

The $SKILL$ parameter is calculated by:

$$SKILL = 1 - \frac{\sum |X_{model} - X_{obs}|^2}{\sum \left(\left| X_{model} - \overline{X}_{obs} \right| + \left| X_{obs} - \overline{X}_{obs} \right| \right)^2} \tag{4.24}$$

where values close to 1 correspond to a perfect adjustment, while small values (near 0)

indicates a complete disagreement between predictions and observations. Values higher than 0.95 should be considered excellent (Dias et al., 2009).

It is well known that the water column depth, the estuary geometry and the bottom friction strongly influence the propagation of the tidal wave. The first two factors depends on estuarine and coastal characteristics. Therefore, calibration was performed by tuning the bottom friction coefficient for the entire estuary. In this study, the best overall adjustment between model results and field observations was achieved using a bottom rugosity of 0.0025, which was the same adopted for a previous MOHID implementation in the Minho estuary (Sousa et al., 2013).

Figure 4.4 shows the comparison between predictions and observed SSE values for all stations (Figure 4.3) and Table 4.3 presents the model accuracy parameters calculated between both time series.

$RMSE$ results range between 2 and 3% of local tidal amplitude and, according to the

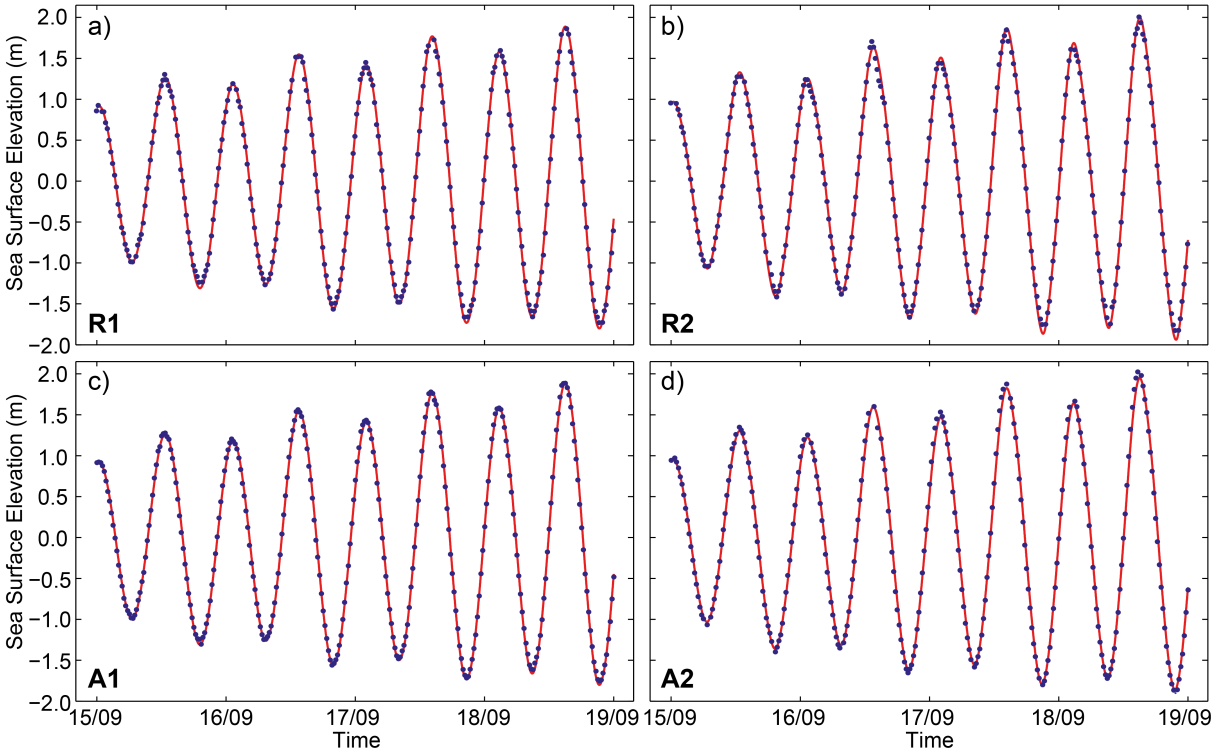

Figure 4.4: Comparison between predicted (red) and measured (blue) SSE for R1 (a), R2 (b), A1 (c) and A2 (d) stations.

Table 4.3: $RMSE$ and $SKILL$ parameters and percentage of error (relative to the amplitude range) for SSE.

	SSE (m)		
Station	$RMSE$	$SKILL$	Error (%)
R1	0.06	0.99	2.9
R2	0.05	0.99	2.3
A1	0.05	0.99	2.0
A2	0.07	0.99	2.0

criterion proposed by Dias et al. (2009), these values are considered excellent (Table 4.3). Regarding the $SKILL$, values are higher than 0.998 in all calibration stations, showing an excellent agreement between predictions and observations (Table 4.3).

The comparison between harmonic constituents (Pawlowicz et al., 2002) determined from predictions and *in situ* SSE data also attest the excellent adjustment obtained in the calibration procedure (Table 4.4). According to results, amplitude and phase agreement is excellent. The higher difference in the amplitude of the main local constituent (principal lunar semi-diurnal - M_2) was found at R2 station ($\sim$4 cm), while the phase differences for this constituent are lower than 4 minutes for all stations. The mean amplitude difference for the principal solar semi-diurnal constituent (S_2) is $\sim$2 cm, whereas the mean phase lag is $\sim$8 minutes. The amplitude differences of the lunar diurnal constituents, K_1 and O_1, are about 2 cm, while the phase lags are 18 and 30 minutes, respectively.

The SSE amplitude is similar at mouth and inner estuary. Furthermore, the amplitude of tidal constituents also present similar values for all stations (Table 4.4). This is not a typical behaviour in estuaries, where tidal wave propagating along estuary usually conducts to a tidal amplitude attenuation towards the estuary head duet to the bottom friction. Here, the tidal wave is reflected at the head (Crestuma dam) interfering with initial wave, creating conditions for a standing wave generation and consequent resonance as pointed out by Vieira and Bordalo (2000).

Table 4.4: Phase (Pha) and amplitude (Amp) of main tidal constituents determined from predictions (Mod) and observations (Obs) of SSE

Station		A1		A2		R1		R2	
		Obs	Mod	Obs	Mod	Obs	Mod	Obs	Mod
M_2	Amp (m)	1.109	1.084	1.137	1.153	1.109	1.071	1.161	1.116
	Pha (°)	80.5	81.8	83.6	85.4	81.9	81.8	87.1	87.2
S_2	Amp (m)	0.501	0.482	0.509	0.505	0.501	0.476	0.535	0.501
	Pha (°)	109.3	113.6	113.3	118.1	110.8	113.6	117.1	120.7
K_1	Amp (m)	0.048	0.062	0.051	0.072	0.048	0.058	0.050	0.067
	Pha (°)	77.8	74.1	76.5	73.5	78.2	73.9	78.3	69.5
O_1	Amp (m)	0.067	0.052	0.064	0.053	0.067	0.051	0.067	0.047
	Pha (°)	311.9	319.5	316.8	324.2	312.6	319.4	321.4	326.0

Regarding the model validation, predictions and observations of SSE and current velocity were compared for independent periods to those analysed in the model calibration, keeping all the model parameters previously defined. Figure 4.5 shows SSE and current velocity time series from *in situ* measurements and model predictions in R1 and R2 stations. $RMSE$ values for SSE have the same order of magnitude of those determined in the calibration (Table 4.3), but relative errors are higher, especially in R1 station. The $SKILL$ values are higher than 0.997 for all stations (Table 4.5). Both parameters indicate an excellent fit between predictions and observations, showing that the model is properly validated.

Concerning the current velocity (Figures 4.5c and 4.5d), and its intrinsic differences between predictions and observations, a higher disagreement is expected for both stations (Table 4.5). Although the velocity amplitude agreement is good for R1 station ($RMSE$ of 18.9%), higher differences are found for R2 station ($RMSE$ of 29.6%)(Table 4.5). This may be explained by the station proximity to Crestuma dam, which can induce high frequency variations in the current velocity due to freshwater discharge (higher velocity of current in

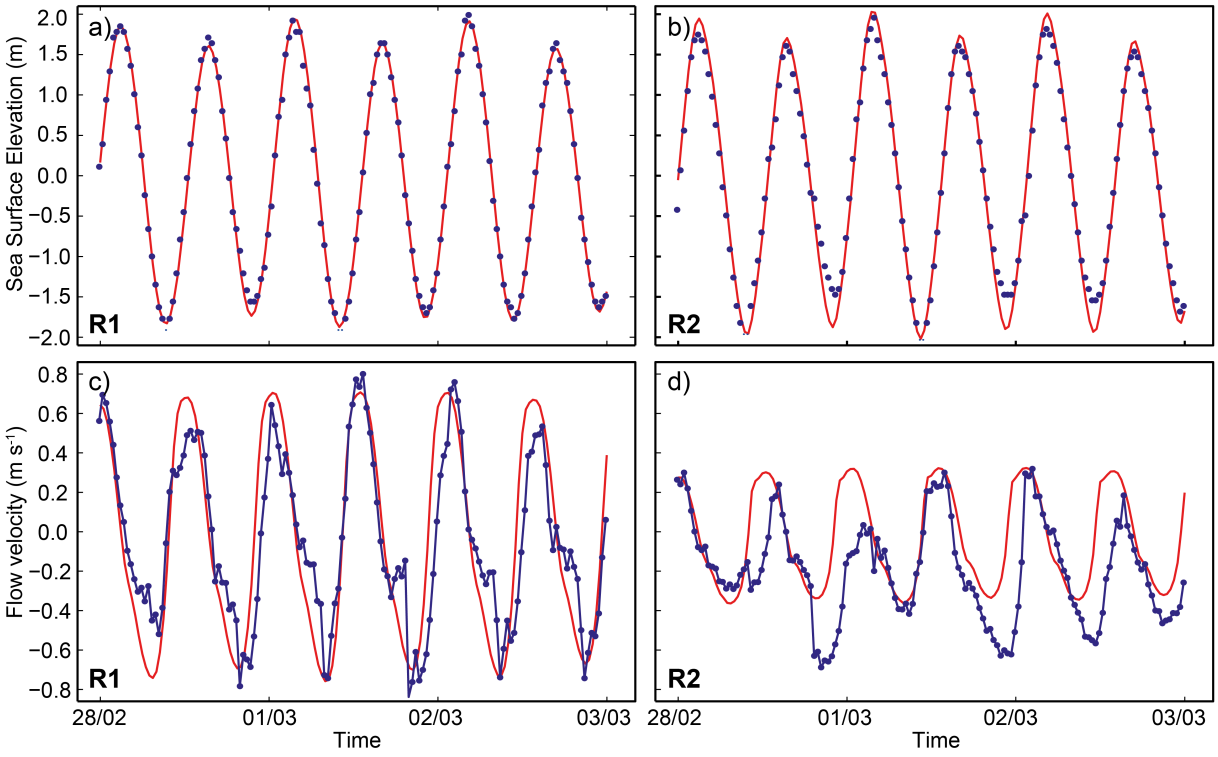

Figure 4.5: Comparison between predicted (red) and measured (blue) SSE and current velocity (along the flow direction) for R1 (a,c) and R2 (b,d) stations.

observations during ebb).

According to these results, it may be considered that estuarine model accurately reproduces the SSE and current velocity data under different and independent conditions. Consequently, this numerical model implementation is considered validated for the Douro Estuary.

Table 4.5: $RMSE$ and $SKILL$ parameters and percentage of error (relative to the amplitude range) for SSE and current velocity comparison.

	SSE (m)			Current velocity (m s^{-1})		
	$RMSE$	$SKILL$	Error (%)	$RMSE$	$SKILL$	Error (%)
R1	0.20	0.99	5.0	0.26	0.92	18.9
R2	0.11	0.99	2.8	0.30	0.68	29.6

4.3.2.2 Minho estuary

The Minho outflow is computed with an estuarine model already implemented, calibrated and validated in previous works (Sousa, 2013; Sousa et al., 2014c)(Figure 4.6). In the following, a brief description is given:

The numerical grid has 119 × 100 cells, with a variable spatial step between 100 m, in inner part of the estuary, and 650 m (300 m in the west-east direction) at the ocean boundary. The numerical bathymetry was generated from data measured by IH in 1978/1989/1999. Tidal forcing from a global tidal model (Le Provost et al., 1998) is imposed at the open boundary and the Minho River discharge supplied by the *Confederación Hidrográfico del Miño-Sil* is imposed at the upstream end of the estuary. Meteorological data were obtained from MeteoGalicia (`www.meteogalicia.es`). The time step is 10 s, the horizontal eddy viscosity is 10 m^2 s^{-1}, and a constant value of 0.0025 is assumed for bottom rugosity.

The calibration/validation results obtained by Sousa et al. (2013) for this model implementations reveal averages of $RMSE$ and $Skill$ calculated from SSE observations and predictions of 0.16 m and 0.96, respectively. The results for the semi-diurnal constituents

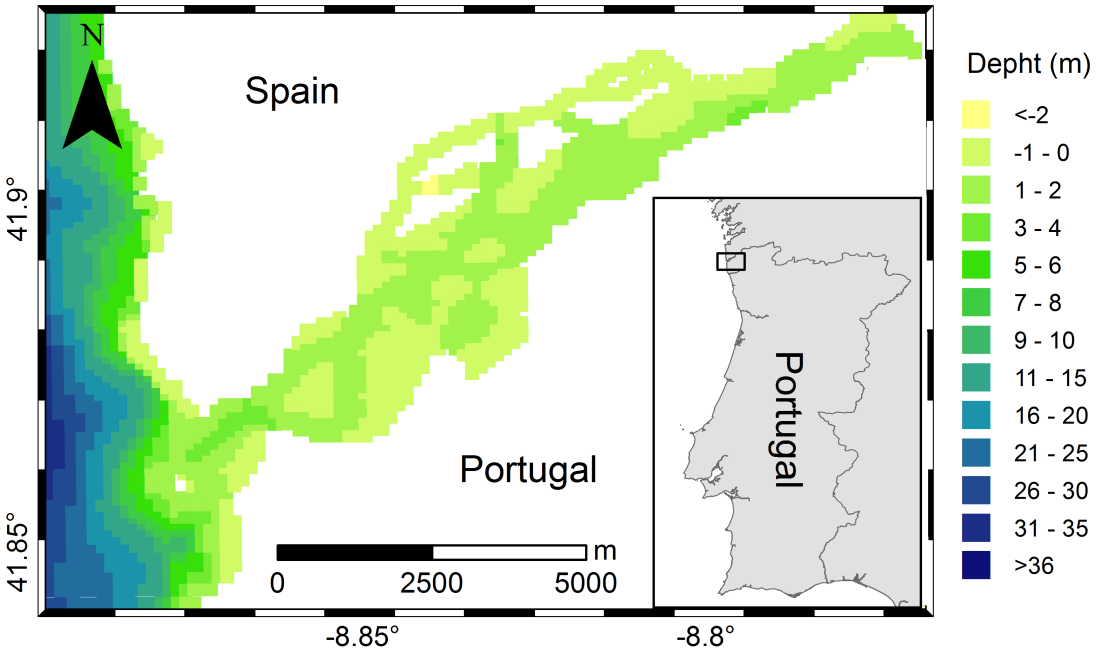

Figure 4.6: Numerical grid of the Minho Estuary.

(M_2 and S_2) presented an excellent agreement between model predictions and observations at the mouth of the estuary, with amplitude errors of 0.06 m for both constituents. The differences in terms of phase were 4.09° and 7.58° for M_2 and S_2, respectively. The diurnal constituents also revealed a good agreement between model predictions and observations, with average amplitude (phase) errors of about 10% (11.5°) and 17% (10.6°) for the constituents K_1 and O_1, respectively.

4.3.3 Surface boundary - Atmospheric input

In order to supply the coastal model (configuration #2) with proper atmospheric data, an implementation of the WRF version 3.6.1 (Skamarock et al., 2008) was performed for the whole area under study, comprising both configurations. This model has being widely used, not only for researchers, but also by national meteorological institutes (Pereira et al., 2013).

The implementation here developed uses three two-way nested domains (Figure 4.7).

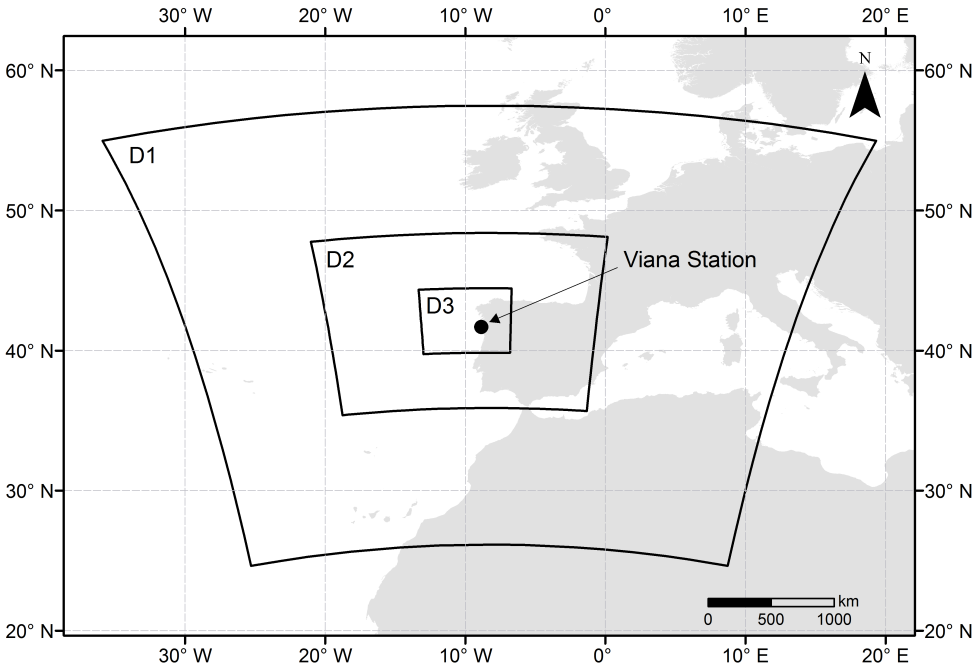

Figure 4.7: WRF domains.

The downscaling methodology follows a domain ratio of 1/3, with the *father* domain (D1) covering most of the Europe with a spatial resolution of 36 km. The two other domains (D2 and D3) present 12 and 4 km of resolution, respectively. The higher resolution domain (4 km) allows reproducing in detail small-scale features, especially coastal wind variations, which are crucial to define the plume propagation and fate. The vertical discretization was composed by 28 unequal spaced layers in each domain.

The atmospheric model boundary condition was forced, every 6 hours, with data from the Global Forecast System (GFS) model (NCEP, 2003) with 1° spatial resolution.

Model predictions of air temperature, meridional and zonal wind components, solar radiation and relative humidity were compared with *in situ* measurements acquired for Northwest Iberian Coastal Current (NICC) project (`http://www.hidrografico.pt/nicc.php`) at Viana do Castelo coastal station (41.706°N -8.860°W; Figure 4.7) during 2006 and 2007 in order to validate WRF model outputs.

The visual assessment of model results revealed an accurate reproduction of the general data variability (Figures 4.8, 4.9, 4.10, 4.11, and 4.12). A quantitative evaluation was also performed comparing model predictions and the Viana's observations, calculating

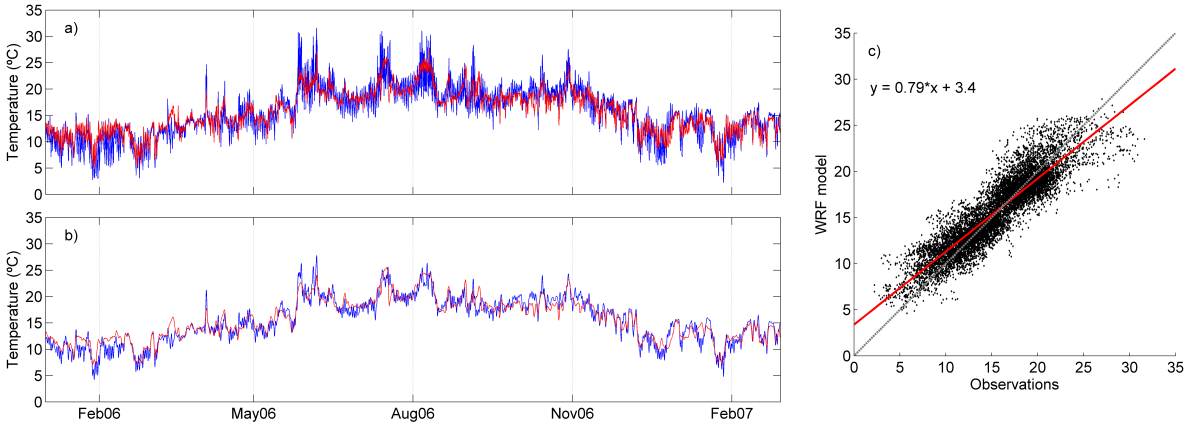

Figure 4.8: Original (a) and 24 h smoothed (b) time series of WRF predictions (red) and *in situ* observation (blue) of air temperature at Viana station. Scatter plot with fitted regression line (c). Optimal and best fit is represented by dashed grey and solid red line, respectively.

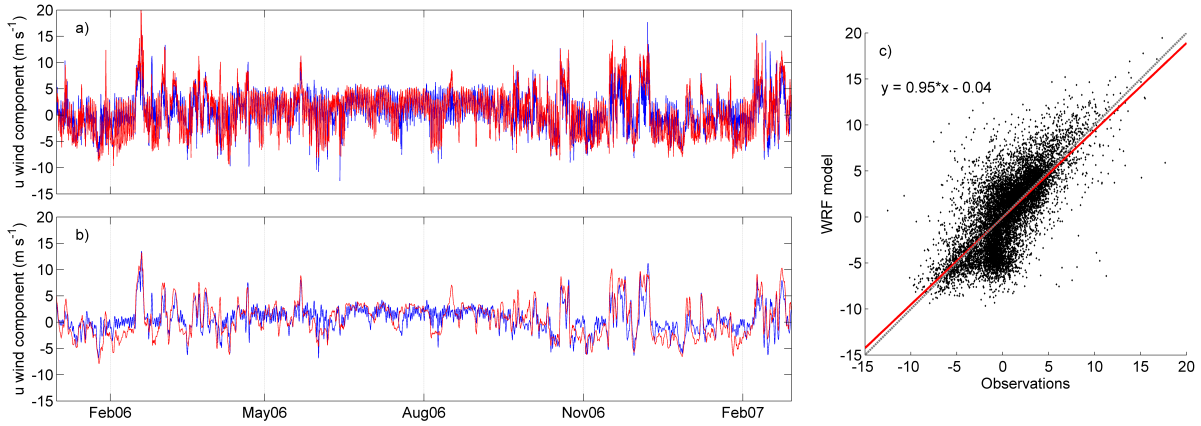

Figure 4.9: Original (a) and 24 h smoothed (b) time series of WRF predictions (red) and *in situ* observation (blue) of zonal wind component at Viana station. Scatter plot with fitted regression line (c). Optimal and best fit is represented by dashed grey and solid red line, respectively.

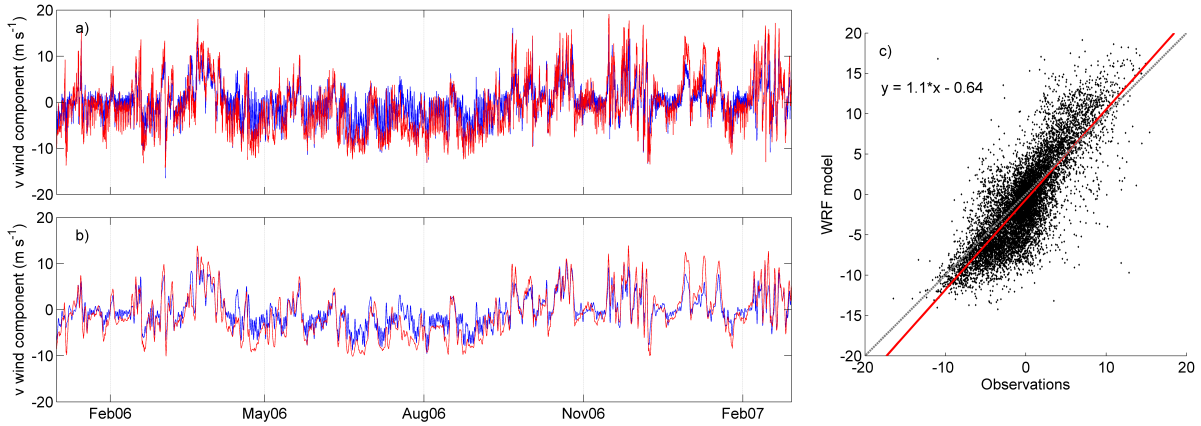

Figure 4.10: Original (a) and 24 h smoothed (b) time series of WRF predictions (red) and *in situ* observation (blue) of meridional wind component at Viana station. Scatter plot with fitted regression line (c). Optimal and best fit is represented by dashed grey and solid red line, respectively.

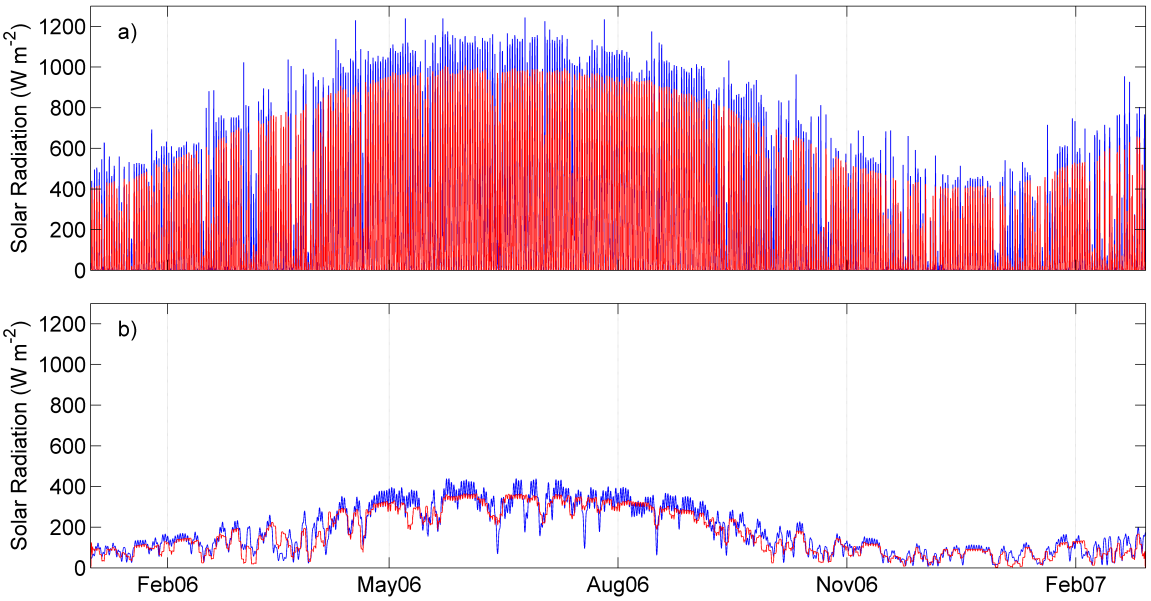

Figure 4.11: Original (a) and 24 h smoothed (b) time series of WRF predictions (red) and *in situ* observation (blue) of solar radiation at Viana station.

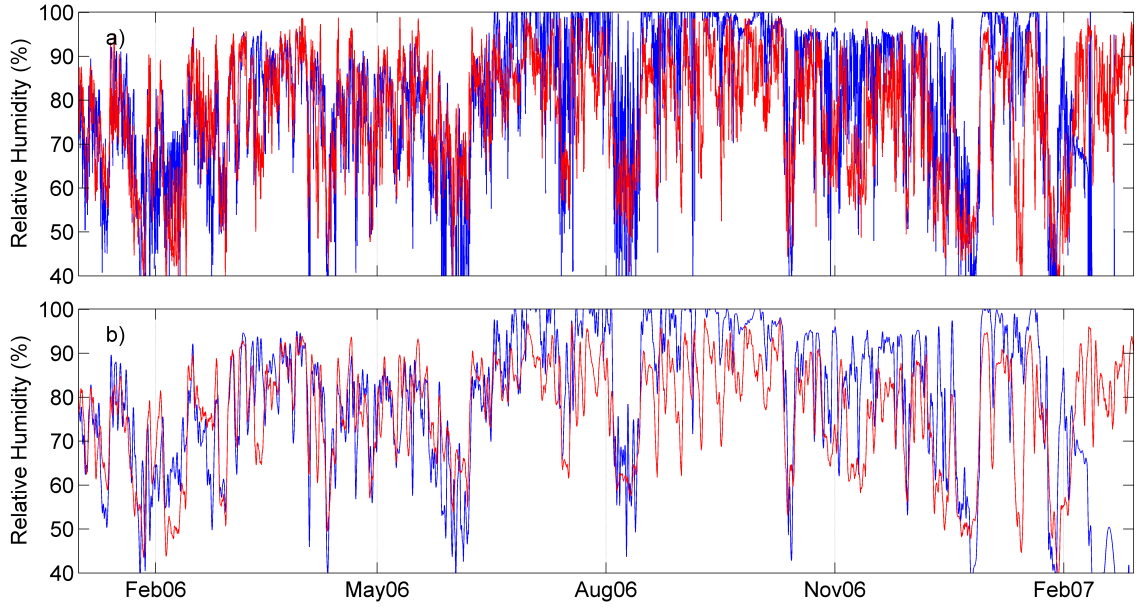

Figure 4.12: Original (a) and 24 h smoothed (b) time series of WRF predictions (red) and *in situ* observation (blue) of relative humidity at Viana station.

Table 4.6: Quantitative assessment of WRF model predictions with Viana station observations of air temperature (T_{air}), zonal wind component (W_x), meridional wind component (W_y), solar radiation (SR), and relative humidity (RH) from January 2006 to March 2007.

	T_{air} (°C)	W_x (m s^{-1})	W_y (m s^{-1})	SR (W m^{-2})	RH (%)
$RMSE$	1.94	2.93	3.33	119	14.5
$SKILL$	0.95	0.83	0.87	0.95	0.95

$RMSE$ (Equation 4.23) and $SKILL$ parameter (Equation 4.24).

Predicted air temperature presents a good agreement with observations (Figure 4.8), with $RMSE$ values lower than 2°C (Table 4.6) and a $SKILL$ of 0.95. The daily variation of temperature is underestimated by the model (Figure 4.8a and c), but presents a very good agreement concerning 24 hours smoothed time series.

Concerning zonal and meridional wind components, the model reproduces very well the observations (Figures 4.9 and 4.10). The meridional component is better predicted with $RMSE$ values of 3.33 (about 16% of the meridional wind amplitude) and a $SKILL$ of 0.87, while the zonal component comparisons show an $RMSE$ value of 2.93 (about 29% of the local amplitude) and a $SKILL$ of 0.83 (Table 4.6).

Regarding solar radiation, a very good correlation between predictions and observations was found, with $SKILL$ of 0.97. On the other hand, relative humidity presents only a reasonable agreement ($SKILL$=0.75). This variable presents a higher dispersion between predicted and observed values, but with a good overall correlation (Figure 4.12). In the end of simulation, during February 2007, a strong disagreement is detected. As it was not observed for other variables, an error on data acquisition may be responsible for this discrepancy.

Wind is the most important atmospheric variable concerning studies of plume propagation over the ocean. Thus, a very good WRF model performance is required for efficient coastal numerical modelling applications. For that purpose, in addition to the zonal and meridional wind components comparisons, wind rose diagrams were computed

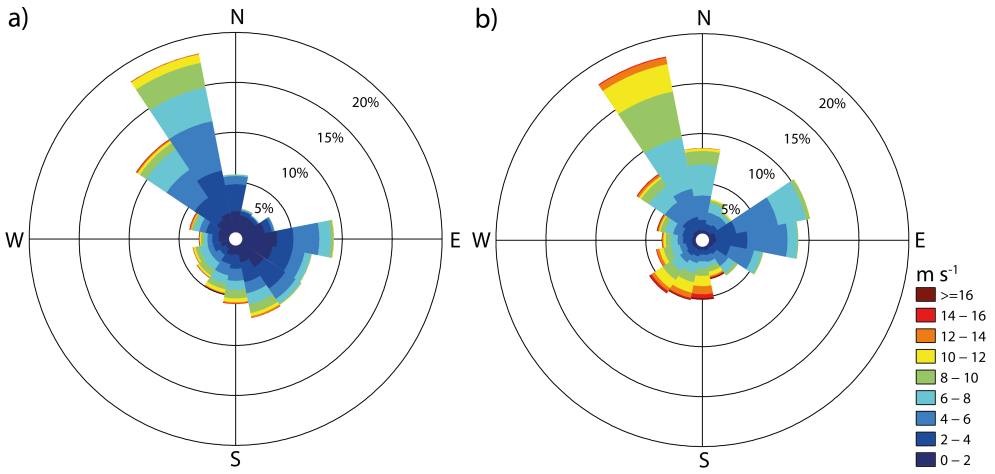

Figure 4.13: Wind rose diagrams from *in situ* observations (a) and from WRF model predictions (b).

for both *in situ* data and predictions (Figure 4.13).

Northwesterly winds are prevalent during the comparison period in both datasets. The wind intensity tends to be higher in WRF predictions. Westerly winds are the second predominant for both datasets, but with higher intensity for model predictions. Southerly winds that usually correspond to stormy winter conditions, are well represented by the model, but with less predominance and intensity than *in situ* data.

Results depicted in Figure 4.13 show that WRF reproduces very well wind variability in the Douro Estuary region and in the adjacent coastal area.

The atmospheric model implementation was considered successfully validated for the study region. Results show that the model is able to reproduce accurately the main atmospheric features of this region, being able to produce accurate boundary conditions for the coastal model.

4.4 Coastal model validation - Configuration #2

The validation of the nesting numerical modelling application (configuration #2) developed to characterize the impact of the Douro estuarine plume in the adjacent coast will be described in this section. The model's accuracy to reproduce the plume dispersion

in coastal ocean is analysed for the winter of 2007. CTD and Acoustic Doppler Current Profiler (ADCP) data collected during NICC project by IH are described and then compared with model predictions. The spatial assessment of the model in terms of salinity and water temperature are evaluated through the comparison of model predictions and remote sensing imagery. Predictions from L1 barotropic domain (Figure 4.2), which is the same for both configurations, were also compared to tidal constituents derived from observation (IH) taking into account the FES2012 solution as ocean boundary condition. The model predictions using the Finite Element Solution 2004 (FES2004) as tidal forcing were also included in this analysis to evaluate the gain of performance when using the newer version of this external solution.

Two sets of simulations were performed to validate the coastal model application using the initial and boundary conditions described in previous sections (configuration #2). The first was dedicated to evaluate the accuracy of the L1 barotropic domain and the other to evaluate the coastal model accuracy in prediction the Douro estuarine plume dispersion under winter conditions.

The barotropic simulation comprises the year of 2013, but only for the L1 domain. The other simulation is carried out for all domains from 20 January to 28 February of 2007, excluding the spin-up period (6-months). Due to the lack of information in the SNIRH database, the water temperature of the freshwater inflow in the estuarine model was set based on the daily smooth air temperature provided by WRF model predictions in the Douro Estuary region. The salinity was set to 0.

A comparison between the amplitudes and phases of the main solar (K_1 and O_1) and lunar (M_2 and S_2) constituents calculated from predicted and observed data provided by IH for 2013 (`websig.hidrografico.pt/content/produtos/tabelasmare/`) was performed to validate the L1 domain. Five stations were analysed: Leixões, Aveiro, Cascais, Sines and Faro (Figure 4.14). First, a harmonic analysis of the predicted SSE time series for each station was performed using the software T_TIDE (Pawlowicz et al., 2002). After are compared the predicted tidal constituents with those available from *in situ* measurements.

L3 validation is performed for January/February of 2007. The dataset includes profile

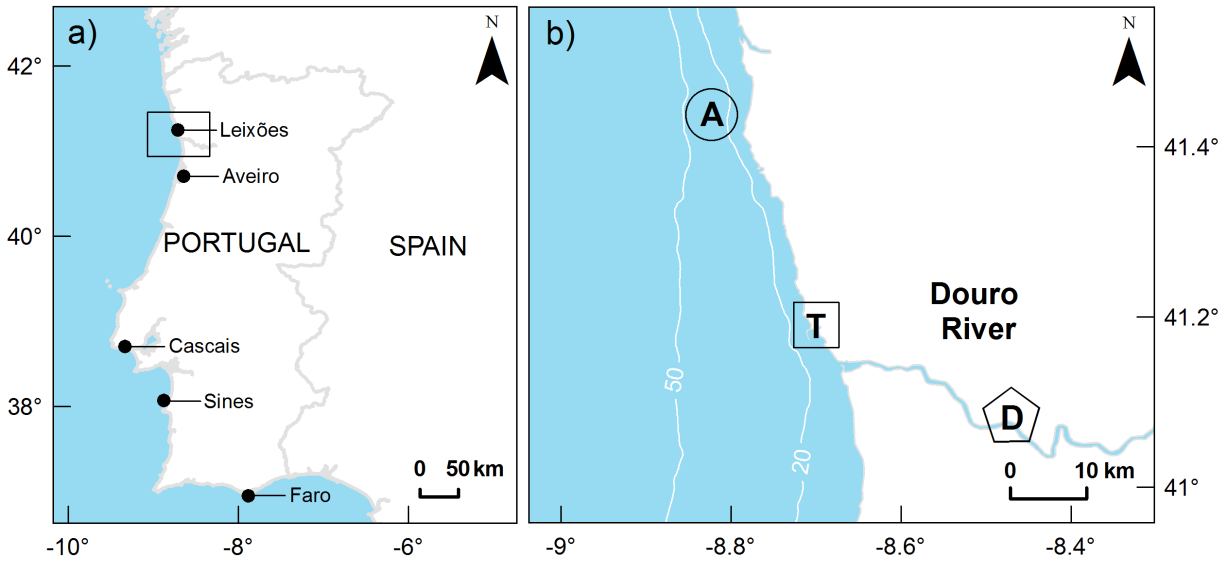

Figure 4.14: Location of the study area with the tide gauges used to validate tidal propagation in L1 domain (a). The Douro Estuary and the coastal adjacent ocean (b). The dam and the tide gauge at Leixões harbour are marked with a black pentagon (D) and square (T), respectively. The ADCP is marked by a circle (A). The bathymetry, from GEBCO, is shown with white lines (contours in meters).

current measurements from an ADCP installed at ∼40 km north of the Douro Estuary mouth (Figure 4.14) and hydrographic surveys performed using Conductivity, Temperature, and Depth (CTD) sensors carried on aboard of *NRP Auriga* (2007), which cover the shelf area off the Douro River. Figure 4.15 shows the location of sampling stations used in this study. The adjustment between model predictions and observed data was evaluated by means of the $RMSE$ (Equation 4.23) and $Bias$ computation:

$$Bias = \frac{1}{N}\sum_{i=1}^{N}(X_{i_{obs}} - X_{i_{model}}) \tag{4.25}$$

The spatial model ability to reproduce water temperature patterns in the continental shelf is also analysed, comparing SST horizontal predicted fields with daily infrared remote sensing images obtained from MODIS sensor onboard of Aqua satellite. SST products were obtained by applying an algorithm that uses the MODIS 31 and 32 bands at 11 μm and 12 μm. In each image, a quality evaluation of remote sensed data was performed. A quality flag of 0 indicates best quality, while 4 indicates complete failure. All pixels with quality

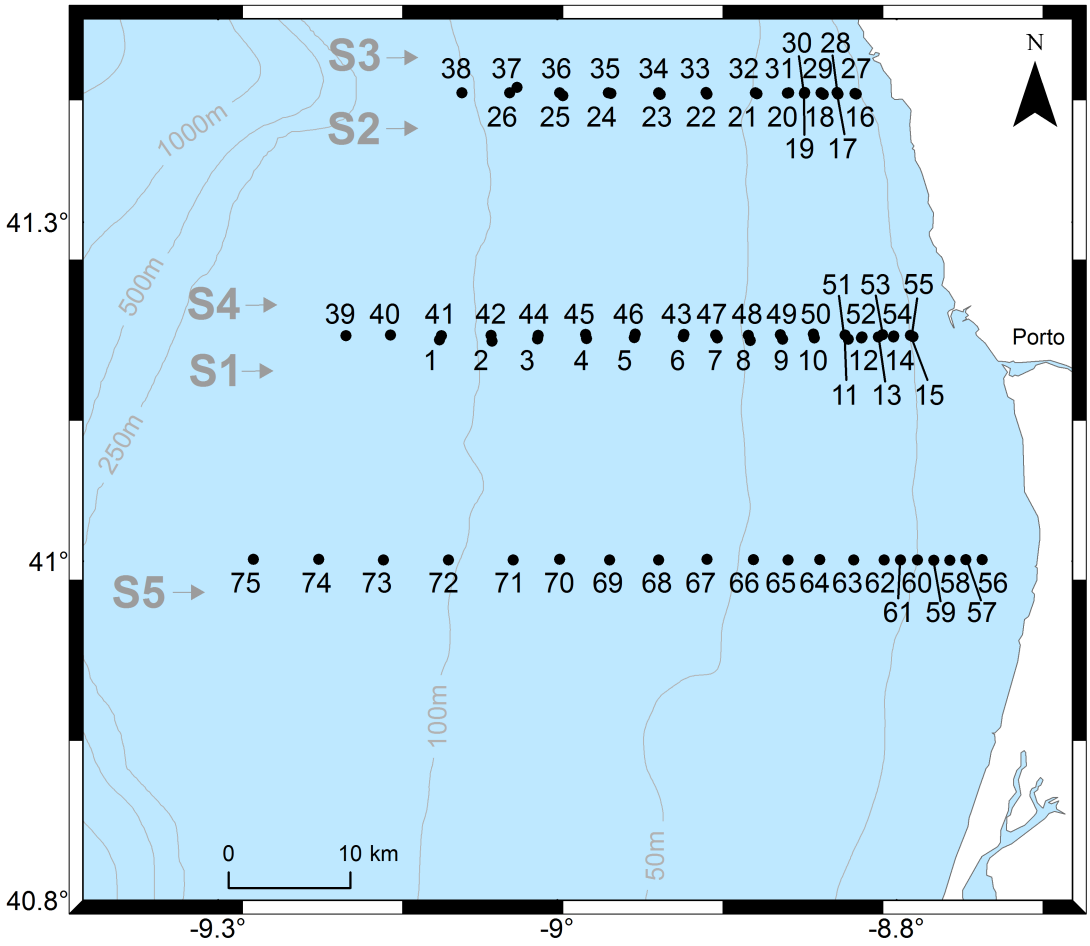

Figure 4.15: Sampling stations location during the 2007 survey.

flags higher than 1 were removed from the images. This threshold was used since a quality flag of 1 can be representative of below average SST values associated with upwelling events, river plumes or even clouds (NASA, 2015). L2 ocean-colour images of $nLw555$ were used as plume tracers, considering that high turbid regions are associated with low salinity patches created by freshwater sources (Nezlin and DiGiacomo, 2005; Nezlin et al., 2005; Saldías et al., 2012). Images were processed following the methodology presented in Chapter 2.

4.4.1 Tidal propagation

Table 4.7 summarizes the results from comparison of the main tidal constituents between the implementations using the FES2004 (old version) as tidal forcing and the

Table 4.7: Harmonic analysis results of observed data from (IH) and predicted SSE results using FES2004 and FES2012 databases during 2013 for Leixões, Aveiro, Cascais, Sines, and Faro (Amplitude (Amp) and phase (Pha) of M_2, S_2, O_1, and K_1 constituents).

		M_2		S_2		O_1		K_1	
		Amp (m)	Pha (°)	Amp (m)	Pha (°)	Amp (m)	Pha (°)	Amp (m)	Pha (°)
Leixões	FES2004	1.081	74.45	0.370	102.47	0.061	320.07	0.076	60.16
	FES2012	1.073	74.42	0.373	102.72	0.064	319.79	0.073	61.26
	IH	1.044	76.10	0.366	104.40	0.062	319.40	0.070	60.20
Aveiro	FES2004	1.079	72.94	0.370	100.74	0.065	319.01	0.075	60.93
	FES2012	1.072	72.92	0.373	101.00	0.074	318.80	0.072	62.01
	IH	0.968	78.80	0.334	106.90	0.056	318.70	0.590	61.60
Cascais	FES2004	1.016	63.30	0.352	89.70	0.058	316.70	0.069	53.69
	FES2012	1.007	63.27	0.356	90.01	0.058	312.27	0.067	57.52
	IH	0.988	64.20	0.350	90.60	0.060	314.50	0.070	54.10
Sines	FES2004	1.021	62.20	0.354	88.44	0.059	314.66	0.071	53.28
	FES2012	1.010	62.15	0.357	88.75	0.061	307.38	0.067	56.82
	IH	0.985	63.30	0.347	89.40	0.062	312.70	0.070	54.50
Faro	FES2004	1.026	55.87	0.360	81.45	0.059	310.80	0.067	47.62
	FES2012	1.001	56.27	0.359	82.34	0.056	302.78	0.064	55.17
	IH	0.982	66.00	0.345	94.80	0.059	318.50	0.065	56.9

FES2012 (new version) and also with data provided by IH for several tidal gauges along Portuguese coast.

The overall distribution of the observed and predicted amplitude and phase is similar. The semi-diurnal contributions (M_2 and S_2) are responsible for the majority of the tidal energy (∼90%), in agreement with results from Marta-Almeida et al. (2002). The FES2004 and FES2012 presents very similar results, with a slight improvement found for the new database. Larger differences are detected in the M_2 amplitude for all stations, with a maximum of 3 cm for the Faro tidal gauge. From these results is demonstrated that the model implementation with the new forcing at the open ocean boundary from FES2012 (in the L1 domain) presents better results in this validation. Comparing with observations,

the maximum error in terms of amplitude is detected for Aveiro station for all constituents (0.11 cm for M_2, -0.04 cm for S_2, -0.02 cm for O_1, and -0.01 cm for K_1). The larger phase lag is observed in Faro station (about 19 minutes for M_2). Regarding the station near Douro Estuary (Leixões), the comparison presents the better results. For the semi-diurnal constituents, the amplitude differences are -0.03 cm and 0.007 cm for M_2 and S_2, respectively. The phase lag is about 1.68° for both constituents corresponding to about 3 minutes in the arrival of the tidal wave. For the diurnal tidal constituents the amplitude difference is minimal: -0.002 cm (O_1) and -0.002 cm (K_1). Phase differences are -0.39° (∼1.6 minutes) and 1.06° (∼6 minutes) for O_1 and K_1, respectively.

In summary, the harmonic analysis results show that the amplitude and phase of major tidal constituents are well reproduced by the 2D barotropic model (L1 domain), with better results when using the FES2012 database as open boundary condition.

4.4.2 Plume propagation

River discharge and wind forcing affect the propagation of estuarine plumes, influencing its fate and mixing over shelf waters (Choi and Wilkin, 2007). It is important to evaluate the model accuracy to reproduce the Douro estuarine plume under different conditions of wind and river discharge. Therefore, a fully comparison between *in situ* observations, remote sensing data and model predictions is carried out to guarantee the confidence in this nested coastal model implementation.

During the winter of 2007, CTD data were acquired on 24^{th} (stations 1-15) and 26^{th} of January (stations 16-26) and 6^{th} of February (stations 27-75)(Figure 4.15).

Five days before 24 January, the Douro freshwater input was very low (ranging from 168 to 348 $m^3\ s^{-1}$) and wind was weak (< 3 m s^{-1}) and variable. This situation remains until 10^{th} February, in terms of discharge, which makes difficult to clearly detect low salinity features in coastal ocean. In 26^{th} of January, moderate southerly winds are observed, remaining with the same direction until 5^{th} of February.

4.4.2.1 Salinity

Five representative vertical profiles for each section were individually analysed in order to avoid figures overload. *In situ* and predicted salinity values (Figure 4.16) reveal low salinity features in all sections, being section 2 an exception. Although the plume spreading is well simulated, the model tends to overestimate the stratification, which is an expected feature in front of the Douro Estuary mouth. The plume depth is about ∼15-20 m while the model generates a thinner less dense water layer (∼5-10 m), but with a similar offshore dispersion. Similar disagreements are observed in sections 4 and 5 profiles on a smaller magnitude (differences lower than 5 m) (Figure 4.16). These deviations may be possible related with short-time variations in the river discharge inflow, which are not imposed in this model application. Moreover, the wind-wave contribution, which is not implemented in this model configuration, may enhance the vertical mixing in surface layers (1-2 meters).

A quantitative comparison of the visual differences detected in the vertical profiles between model predictions and observation were evaluated by $RMSE$ and $Bias$ parameters. $RMSE$ values range from 0.01 (DV16 station) to 1.05 (DV55 station) in profiles presented in Figure 4.16. $Bias$ are negative for all stations, except for DV39 and DV73 stations, indicating that model underestimate the plume signal. The values vary from -0.54 (DV55 station) to 0.08 (DV28 station).

Vertical salinity structures along five cross-shore sections are depicted in Figure 4.17. The model predictions reproduce well the impact of the estuarine buoyant water in the coast, where water masses with low salinity are expected to be found. However, as stated above, vertical mixing is underestimated by the model, retaining the riverine waters near surface (section 1 in Figure 4.17).

Data from sections 1 and 2 were obtained under northeast and northerly wind forcing, which tends to increase the offshore and southward transport as reported in Chapter 2 (from ocean-colour observations). This is corroborated by both *in situ* data and model predictions. The maximum plume extent is observed in section 1, located in front of the river's mouth, and no plume signal is detected in the northward section of the estuary.

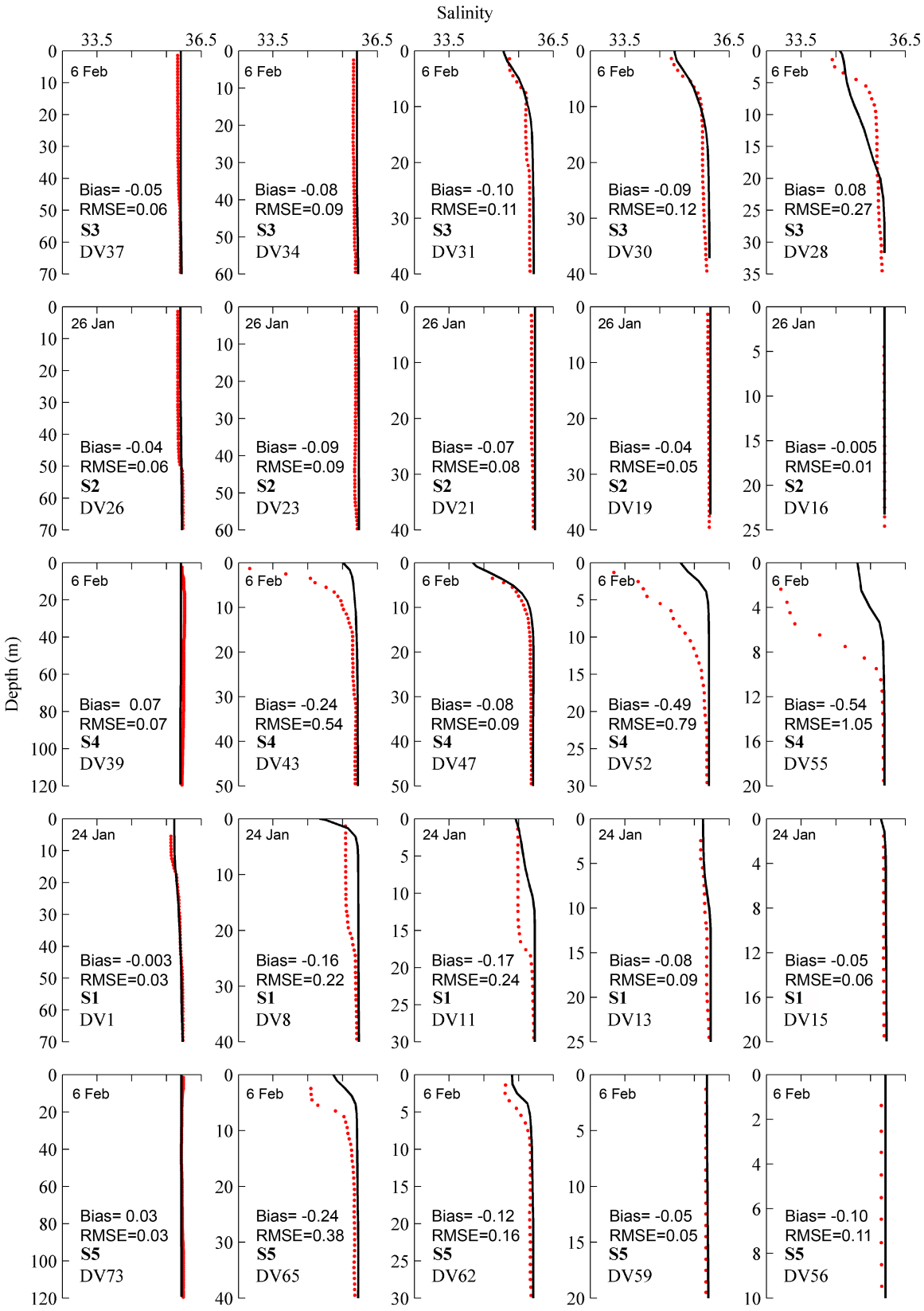

Figure 4.16: Observed (red dots) and predicted (black line) salinity vertical profiles during the 2007 survey - Figure 4.15.

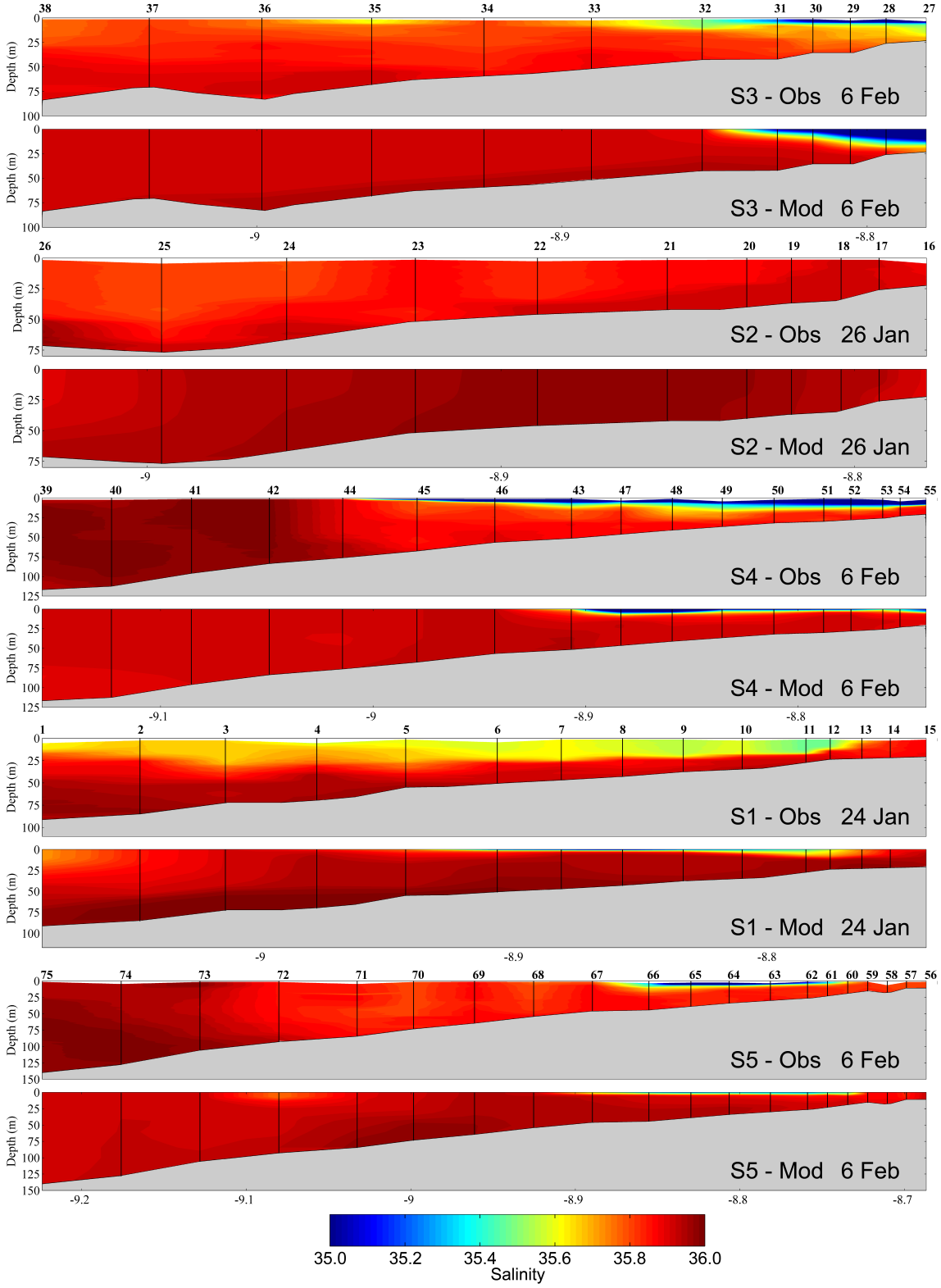

Figure 4.17: Observed and predicted salinity along cross-shore sections 1, 2, 3, 4, and 5 during the 2007 survey - Figure 4.15.

Data from sections 3, 4 and 5 were collected before the region started to be affected by cold fronts, associated with successive low-pressure systems. Most of the results show a transition moment from northerly to southerly wind regimes with low freshwater inflow. The plume detachment from the coast (section 5) is well reproduced by the model, revealing that the plume jet is aligned with the NE-SW direction as expected in a transition from upwelling to downwelling-favourable winds. In contrast to section 1 results, the model predictions reproduce very well the halocline in section 4 (same location - Figure 4.15), but disagrees in terms of plume extension.

The large errors found for sections closer to the river mouth can be attributed to the high temporal variability of river inflow from Crestuma dam. Daily average water volume discharged by the dam is imposed as land boundary in the 2D estuarine model. However, the volume can vary from 0 to 1000 m^3 in a small period of time (few hours), depending on the hydroelectric power demand or other constrains (Azevedo et al., 2010). The data used as landward boundary condition in the estuarine model was not available at this finer temporal scale.

Section 3 results depicts the excellent model accuracy in predicting the Douro River plume behaviour under downwelling-favourable winds.

Figure 4.18 presents the comparison between the turbid signal $nLw555$ and the predicted surface salinity patterns off the Douro Estuary. Despite the restricted available images for this period, these 4 snapshots corroborates the results from the vertical salinity structure (Figure 4.17).

In general, the spatial pattern from model predictions and observations is similar north of the Douro Estuary. All images represent the plume propagation under southerly winds, when it was confined to the coast, creating a turbid coastal band north of the estuary mouth. The model can reproduce very well the bulge extension in front of the estuary mouth (Figures 4.18a and 4.18e). After 10^{th} of February (Figures 4.18b, 4.18c, 4.18d, 4.18f, 4.18g, and 4.18h), the river discharge increases from low to moderate-high regimes (1200-1400 $m^3\ s^{-1}$). Besides the intermittent wind regime, a northward coastal band is well identified in both predictions (low salinity) and satellite observations (high turbidity). Some

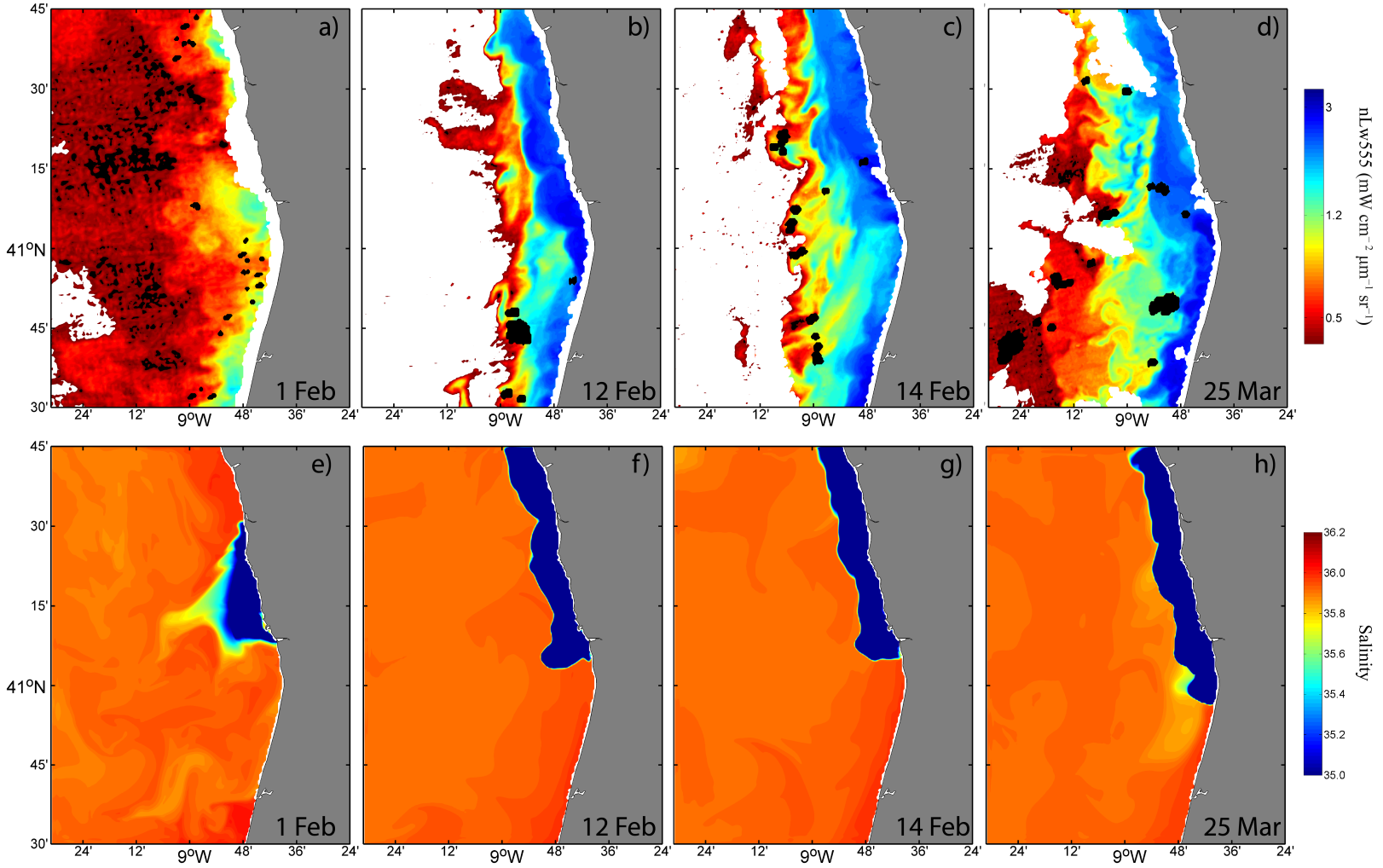

Figure 4.18: Comparison between the turbid signal from MODIS sensor (upper panel) and predicted surface salinity (bottom panel) for 1 (a,e), 12(b,f), 14 (c,g) and 25 February(d,h) of 2007.

high turbid features that are detected in the ocean-colour images southwards the Douro River mouth, are not observed in model results as low salinity values. As shown in section 2.4, the coastal region between Aveiro and Porto is shallower than the area located north of the Douro Estuary and, consequently, it is more susceptible to sediment resuspension caused by wind-wave forcing(Coelho and Veloso-Gomes, 2006). This may resulted in high values of $nLw555$ associated with turbidity, but not related with Douro estuarine outflow.

4.4.2.2 Water temperature

The comparison between observed and predicted vertical structures of water temperature is depicted in Figure 4.19 for the same profiles that were analysed for salinity. Since water temperature has higher variability and is more dependent from the open ocean and atmospheric boundary conditions, it is expected a lower agreement than for salinity results. Nevertheless, cold water temperature associated with the Douro estuarine discharge during winter helps to identify the plume signal in warmer coastal waters (Peliz et al., 2002).

As for salinity profiles a quantitative assessment of the model accuracy using $RMSE$ and $Bias$ parameters were perfomed for water temperature profiles. $RMSE$ ranges from 0.16°C (DV34 station) to 1.07°C (DV16 station), with an average of 0.58°C considering all stations. $Bias$ is positive for all profiles, even for those not shown in Figure 4.19, indicating that the model tends to underestimate observed water temperature. $Bias$ range from 0.08°C (DV37 station) to 0.90°C (DV16 station).

Figure 4.20 shows the vertical structure of water temperature along the five sections depicted in Figure 4.19. Besides the good representation of the plume and the low $RMSE$ and $Bias$ values, model predictions diverge from observations in sections 1 and 2 (deviation of about ~ 1°C). In section 2, where no low salinity water masses are observed, the disagreement may be generated by a ineffective setting of the ocean boundary condition. Although WOA2013 climatology shows to be useful to study hypothetical numerical scenarios or typical winter events, may not be an accurate choice to evaluate cases under anomalous

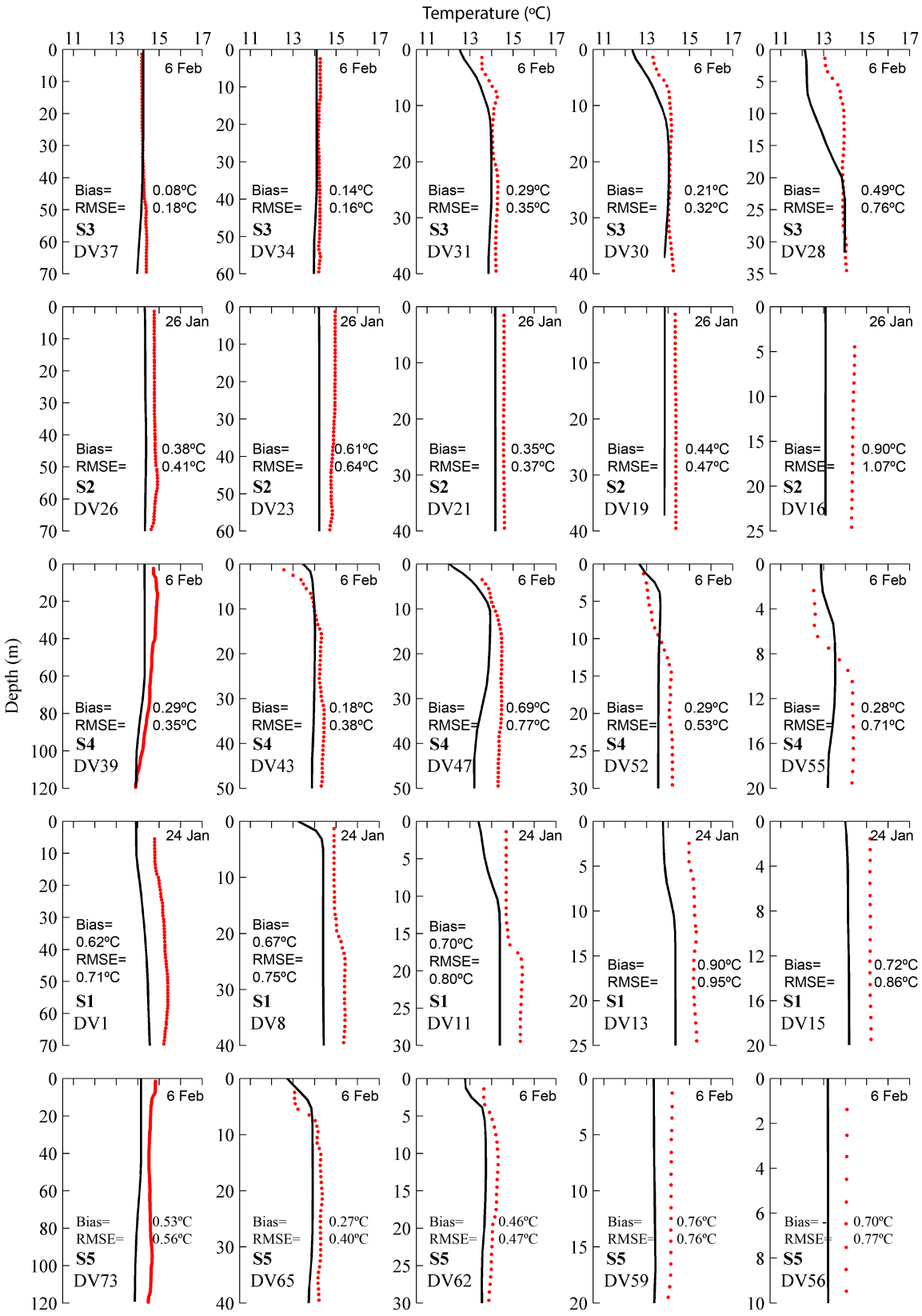

Figure 4.19: Observed (red dots) and predicted (black line) water temperature vertical profiles during the 2007 survey - Figure 4.15.

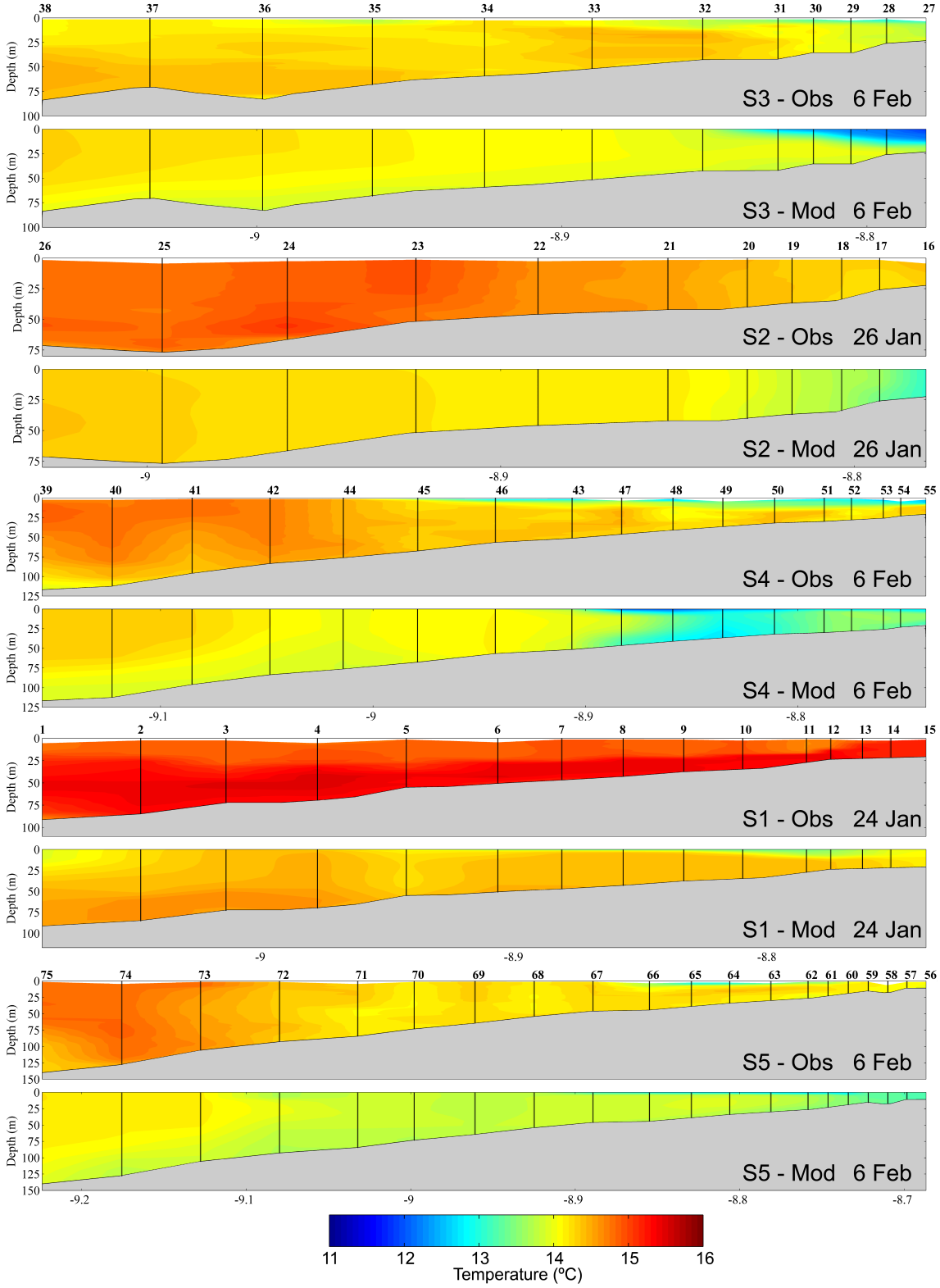

Figure 4.20: Observed and predicted temperature along cross-shore sections 1, 2, 3, 4, and 5 during the 2006 survey - Figure 4.15.

seasonal conditions. Nonetheless, the deviation range (∼1°C) is low and very similar to that obtained by Sousa (2013) in the numerical predictions for the coastal ocean near the Minho River and Rias Baixas.

Figure 4.21 shows SST patterns obtained from predictions and satellite data on 26^{th} (Figures 4.21a and 4.21e) and 27^{th}(Figures 4.21b and 4.21f) of January and on 1^{st}(Figures 4.21c 4.21g) and 25^{th}(Figures 4.21d and 4.21) of February 2007. The last snapshot shows an event of moderate-to-high river discharge (1423 m^3 s^{-1}) and downwelling-favourable winds, while the others represent low discharge regimes under weak and intermittent northerly winds. The plume propagation over the ocean is fairly predicted by the model. A weak plume jet is observed in the southwest direction in both satellite and predicted images at the end of January (Figures 4.21a, 4.21b, 4.21e, and 4.21f), but the model underestimates the estuarine outflow.

Tidal influence in estuarine flux increases under low regimes of river discharge. Thus, the isolated colder patches in the jet plume direction, observed in predicted and *in situ* data from 26^{th} and 27^{th} of January are possible related with that influence. Tidal plume pattern suggests the generation of internal waves (Nash and Moum, 2005) by the Douro River plume. Images from February 1 represent a weak wind event, where a perfect circular bulge is observed in the satellite image (Figure 4.21b). Besides the shape is not well predicted by the model, water temperature within the plume is similar to the observations (∼12.5°C). An upwelling phenomenon, which is not directly related with the plume propagation, is observed in model predictions between the Ria de Aveiro Lagoon and the Douro River mouth, where colder waters emerge from deeper layers of the ocean (Figure 4.21g). This feature is also observed in MODIS images, with small offshore extension and lower magnitude. Here, water temperature presents a deviation from the model of about 2-2.5°C. The comparison between Figures 4.21d and 4.21h shows that model predicts very well the propagation of Douro estuarine plume under southerly winds events, when a coastal band with lower water temperatures is visible north of estuary mouth. The prediction of plume shape is excellent and the SST deviation in the northward coastal band does not exceed 1°C.

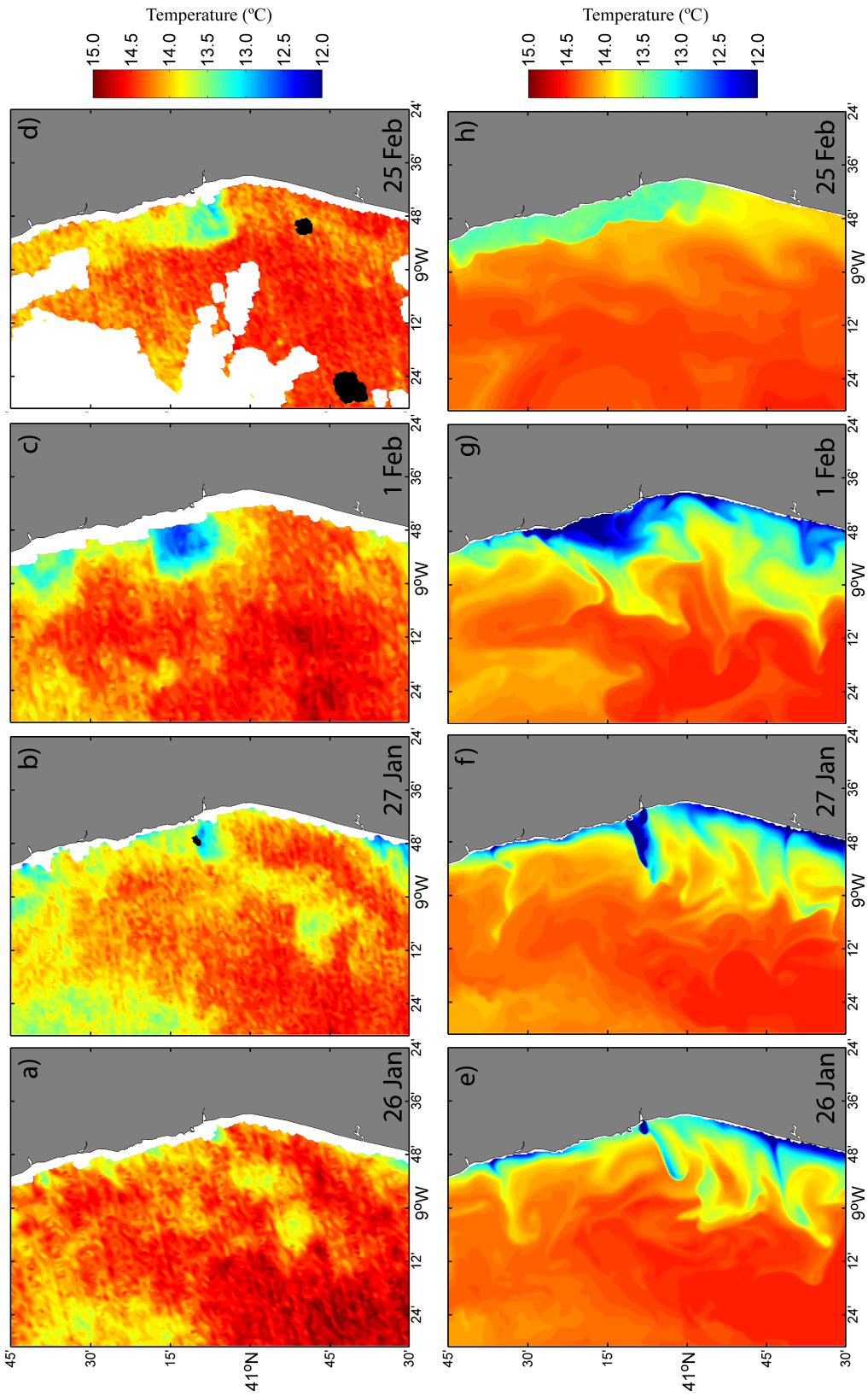

Figure 4.21: Comparison between SST from MODIS sensor (upper panel) and model predictions (bottom panel) for for 26 (a,e), 27(b,f) January, 1(c,g) and 25 February (d,h) of 2007.

4.4.2.3 Coastal circulation

The effect of the Douro River discharge in the generation of a northward coastal current in the inner shelf was researched in some recent works (Marta-Almeida et al., 2002; Ruiz Villarreal et al., 2005; Otero et al., 2013). These are essential numerical modelling studies, but proved that a high Douro river discharge combined with strong southerly winds can generate a northward surface coastal current with velocities of about 1 m s^{-1}. Thus, the characterization of surface velocity and its vertical structure with measurements from an ADCP is very relevant in the context of this dissertation. In addition, observations help to validate the coastal hydrodynamic model, contributing to fill the knowledge gaps about the impact of the Douro River plume in the adjacent coastal circulation.

Current velocity profile observations from a ADCP placed north of estuary mouth (Figure 4.14) were used to validate the model predictions in terms of circulation in the coastal region off Douro Estuary. This dataset records zonal and meridional current components during more than 1 month, representing important and reliable information to characterize the Douro plume propagation. Figure 4.22 shows the temporal evolution of zonal and meridional components of ADCP *in situ* data velocity and model predictions at the same location (Figure 4.14). Data was recorded from 16^{th} of January to 26^{th} of February 2007. Observed and predicted fields were filtered with a 33-h low pass filter (*pl33tn* - Flagg et al. (1976))to remove high-frequency variability from the series. The wind regime (WRF model) and the Douro River discharge during the survey period are depicted in Figures 4.22a and 4.22b, respectively.

In general, the model accuracy to predict the current magnitude and direction in coastal ocean is satisfactory. The observations recorded by the ADCP during this event presents very peculiar characteristics, with different river discharge regimes, ranging from low (300 m^3 s^{-1}) to high (1500 m^3 s^{-1}), and high variability of wind direction and magnitude, mainly after February 10 (Figure 4.22). The observed zonal component of current presents some spurious values in surface layers, with strong negative values (offshore direction) during several days. The model does not reproduce some of these patterns, but the analysis

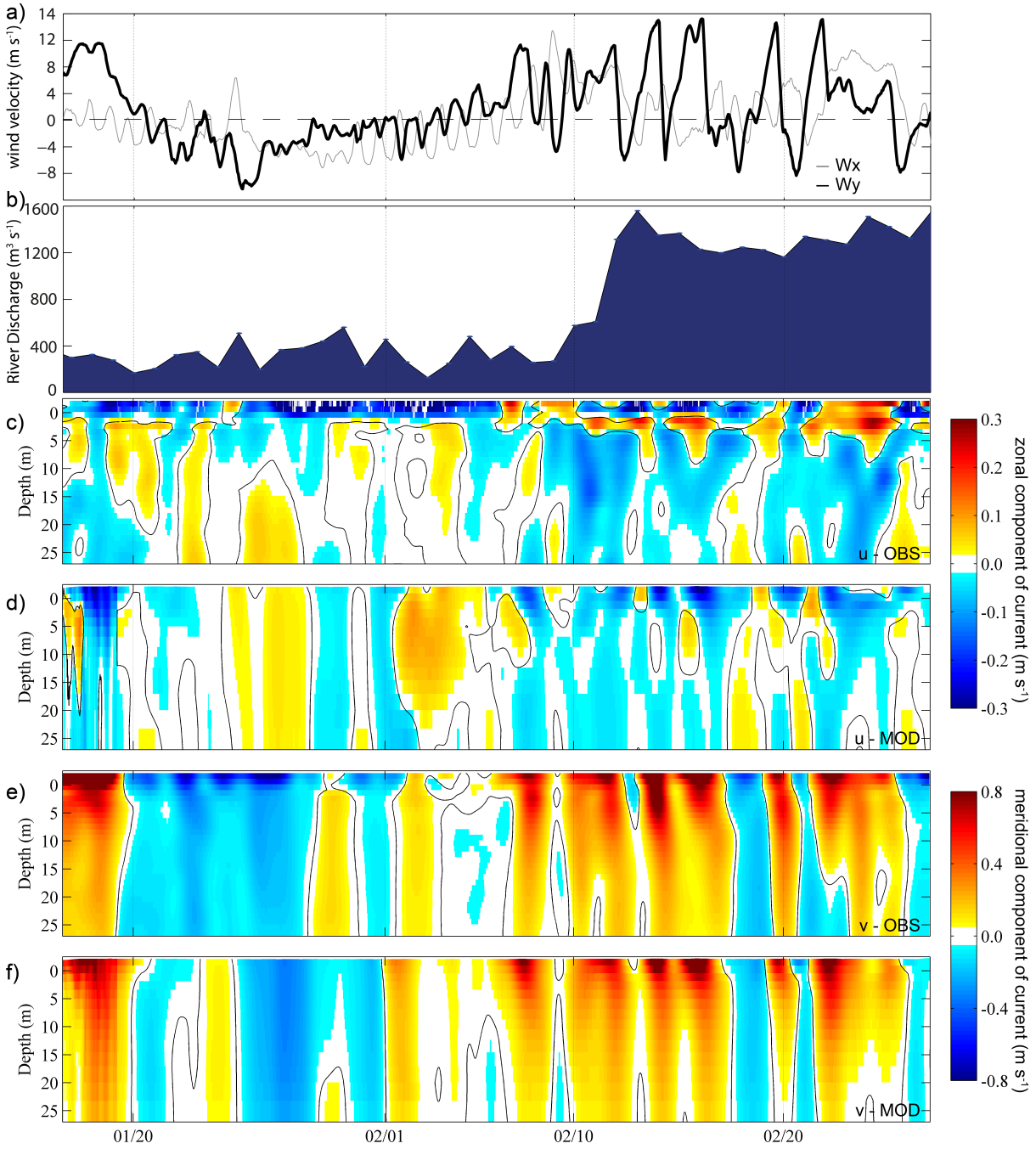

Figure 4.22: (a) Meridional wind component at ADCP location. (b) Douro River discharge at Crestuma dam. (c,d) Time series of observed and predicted cross-shore component of current.(e,f) Time series of observed and predicted along-shore component of current during 2007 survey.

needs to be cautious. Model predictions fairly agree with observations and the offshore transport after the downwelling to upwelling-favourable conditions is clearly represented in both fields. Regarding the meridional component, the agreement is excellent. Periods of higher velocity magnitude in both negative and positive components are very well predicted by the model, even under high wind variability, which confirms again the reliability of WRF atmospheric model outputs. Disagreement was only found during weak and variable wind and low discharge regimes from January 20 to February 1 of 2007, where the model underestimates the southward current, especially in surface layers. Around January 25 model predictions disagree also in direction, with a weak northward current. In a period of significant wind oscillations and moderate-to-high river discharges, surface velocity is very high, reaching values of about 1-1.2 m s^{-1} under stronger downwelling winds (10-12 m s^{-1}).

Figure 4.23 shows the time evolution of zonal (Figure 4.23a) and meridional (Figure 4.23b) current results for the profile previously analysed, but from an idealized model simulation without the Douro estuarine discharge. In general, results are very similar to the *real* simulation (Figure 4.22), revealing the crucial importance of wind regime in the inner-shelf circulation and, therefore, in the plume propagation (Lentz and Fewings, 2012). Nevertheless, the northward current magnitude is significantly lower, with values ranging from 0.3 to 0.6 m s^{-1}. The deviation is larger the higher is the river discharge. Peaks of low

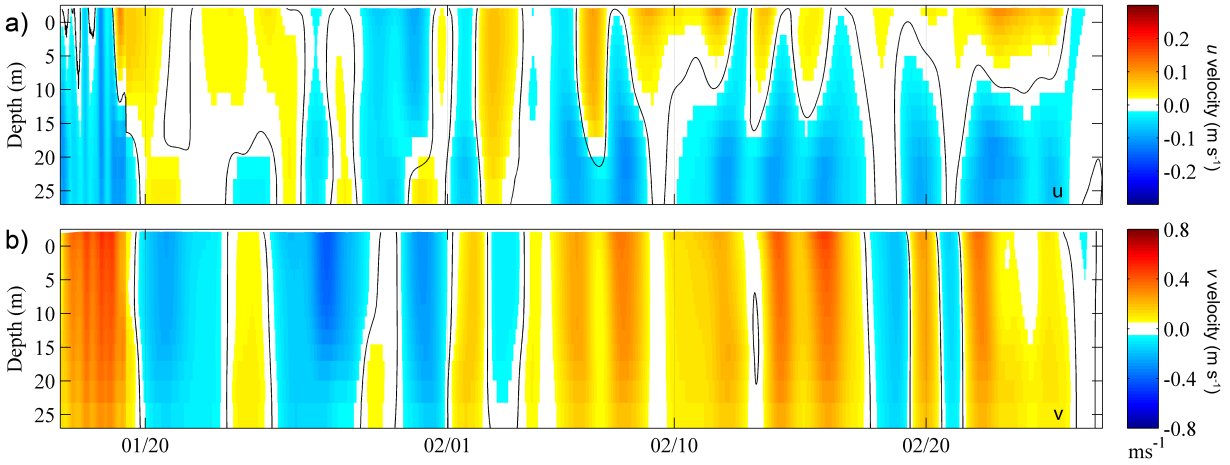

Figure 4.23: Profile time series of cross-shore (a) and along-shore (b) component of current during 2007 survey without Douro River discharge.

salinity and water temperature near surface correlate very well with the northward current (Figure 4.24). There is an exception observed in January 22 that represents a transitional moment from downwelling (northward transport) to upwelling-favourable winds (southward and offshore transport). In this moment, the reminiscent volume of freshwater is carried out offshore and southwards (salinity ∼35) after had been transported northward forced by southerly winds in the first instant (salinity ∼33)(Figure 4.24a).

To evaluate how quickly coastal currents respond to wind variations, time series of meridional current at 2 m depth are depicted in Figure 4.25for simulations with and without river discharge. This figure also includes the meridional wind component for comparison with current time series. Douro estuarine plume contributes to reinforce the northward coastal current, which is generated by strong downwelling favourable winds, even in a moderate flux regime. The plume presence can double or triple the current magnitude. The real simulation, with the estuarine outflow imposed in the coastal domain, presents a lag of few hours (3-12 hours) between northward current and southerly winds (wind ahead current). On another hand, if coastal waters are not affected by the buoyant plume, the average time lag is larger (∼7 hours), indicating that currents respond slowly to wind forcing. It is observed that the spring-neap tidal cycle may influence this delay, when coastal water is affected by the buoyant plume. Around the neap tide peak, current tends to

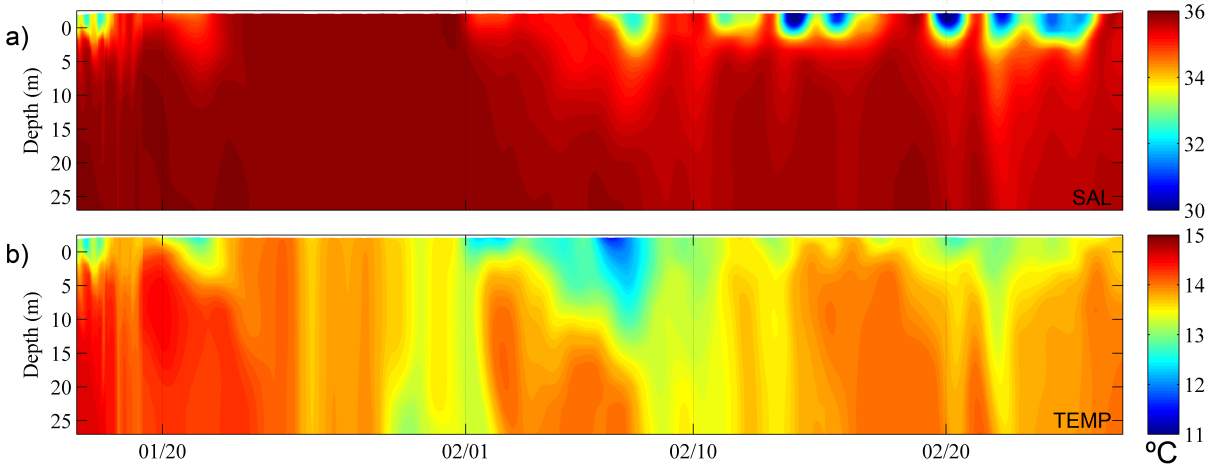

Figure 4.24: Time series of salinity (a) and water temperature (b) during 2007 survey.

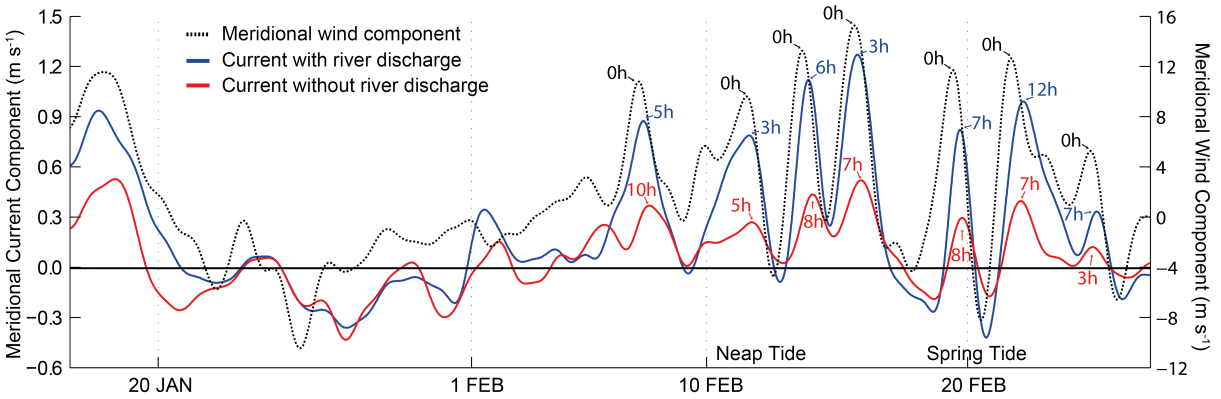

Figure 4.25: Time series of meridional wind component (black dashed line) and along-shore component of current for a simulation with (blue) and without (red) the Douro River discharge during 2007.

respond faster to wind variations (∼4.25 hours) than in spring tide situations (∼8.6 hours). In the simulation without the Douro estuarine outflow the delay is approximately the same for both tidal moments. These results reveal some fortnightly tidal cycle influence in the plume propagation, even during high-river discharge. As stated in Chapter 2, the ebb-flood cycle impact would be more evident in the near-field region, close to the river mouth.

4.5 Conclusion

In this Chapter, several numerical model applications were designed, implemented, calibrated and successfully validated for the coastal region under influence of the Douro estuarine plume.

Two different coastal numerical model configurations, both based on the nested domains technique, were applied to study the Douro estuarine propagation through the coastal ocean using the MOHID model. The configurations #1 and #2 diverge essentially in the geographical limits of the regions under scope in the high-resolutions sub-domains (L2 and L3). While configuration #1 (including the Minho River and Rias Baixas) will be only used to study the Douro estuarine plume interaction with northern coastal regions (Chapter 6), configuration #2 will be applied to evaluate in detail the propagation of the

Douro plume under different river discharges and wind scenarios (Chapter 5).

Landward and atmospheric boundary conditions in both coastal configurations are supplied by data from estuarine and atmospheric model applications totally or partially implemented and validated in this work. A 2D estuarine model was implemented and validated with success for the Douro Estuary. In this way, estuarine water fluxes and properties with respective tidal fluctuations are satisfactory imposed in the L3 coastal domains in configurations #1 and #2, better describing the reality of estuary-coast dynamics. The outflows from Minho Estuary are calculated from a previously validated model (Sousa et al., 2013) and will only be imposed in L3 domain of configuration #1 (Chapter 6). Regarding the atmospheric input, the implementation of the atmospheric WRF for the region under study revealed a good agreement between model predictions and *in situ* measurements, namely with air temperature, zonal and meridional wind components, relative humidity and solar radiation. These atmospheric parameters are essential to a proper prediction of the Douro estuarine plume propagation using this coastal model application.

Comparisons between observations and predictions of phase and amplitude of major tidal harmonic constituents in several locations along the portuguese coast revealed that model accurately reproduces the tidal propagation in the large barotropic domain (L1). Moreover, the use of a new global tidal solution (FES2012) for boundary condition in this domain revealed a higher model accuracy than when using the older version (FES2004). Salinity and water temperature surface fields from L3 domain (3D) were evaluated against remote sensing products (SST and turbid composites). In addition, model predictions were compared with field observations of ocean vertical structure (water temperature, salinity and current) from CTD casts and ADCP measurements. Model predicts horizontal and vertical local structures of water temperature and salinity accurately, considering both qualitative and quantitative comparisons with observations.

Both predictions and observations of current velocity revealed a rapid response of the plume to wind variations and notable influence of the riverine water in the reinforcing of the northward coastal current.

Although errors are not negligible, the validation procedure shows that the model developed in this study adequately reproduces the hydrodynamic and water properties of Douro region and its adjacent coastal ocean. Therefore, this nested model implementation is a useful and suitable tool to study the propagation and fate of Douro estuarine plume in the Northwest of the Iberian Peninsula.

In next chapters, the nesting numerical model using configuration #2 validated here will be applied to characterize and study the propagation of the Douro estuarine plume. In addition, the implementation based on configuration #1 will be applied to assess the interaction between the Douro and Minho estuarine plumes.

Chapter 5

Characterization of the Douro estuarine plume

5.1 Introduction

As stated in Chapter 1, the classic pattern of propagation of a estuarine plume in the coastal ocean consist in the formation of a jet-like non-steady structure (bulge) in front of the river's mouth, recirculating freshwater that then feeds a coastal buoyant current (Fong and Geyer, 2002; Avicola and Huq, 2003; Dzwonkowski and Yan, 2005; Horner-Devine et al., 2006; Thomas and Weatherbee, 2006).

The river discharge and tides have major influence in the source and near-field regions (Hetland, 2005; Horner-Devine et al., 2015). Here, the balance between the inertial momentum and buoyancy determines the plume dynamics. The wind starts to dominate the plume dispersion (far-field), when the discharge decreases its influence (mid-field). Usually, downwelling-favourable winds tend to push the plume against the coast through an Ekman transport response and vertical mixing reduces stratification in the plume. Upwelling-favourable winds have been found to thin the plume and transport the buoyant layer offshore, increasing vertical stratification in the area under the wind's influence (Fong and Geyer, 2001; Lentz, 2004; Lentz and Largier, 2006; Otero et al., 2008; Jurisa and Chant,

2012).

In Chapters 2 and 3, the mean-state and the inter-annual variability of the Douro estuarine plume was evaluated using satellite imagery. This Chapter aims to study the response of the Douro estuarine plume to several idealized wind forcing scenarios under low, moderate and high winter river discharges using the coastal numerical implementations described in Chapter 4. Several scenarios are considered from weak-to-moderate winds from each of the four cardinal directions.

All data used in this Chapter and the methodology followed are described in Section 5.2. Section 5.3 presents the major results from numerical simulations carried out to study the influence of river discharge and wind variability on the plume propagation. General characteristics of the wind driven plume in terms of main patterns and circulation are highlighted in Section 5.3.2.4. A brief summary of this Chapter is presented in Section 5.4.

5.2 Data and methods

5.2.1 Discharge and wind scenarios

A statistical analysis of the maximum annual values of the Douro River discharge was performed to characterize the winter river discharge events. River discharge from SNIRH database measured in Crestuma dam from 1986 to 2014 were used (D in Figure 5.1). Three scenarios were chosen taking into account the 25^{th}, 50^{th} and 75^{th} percentiles of annual maxima of the month with maximum daily mean inflows (January - 1055 $m^3\ s^{-1}$). These percentiles correspond to low (608 $m^3\ s^{-1}$), moderate (1486 $m^3\ s^{-1}$) and high (3299 $m^3\ s^{-1}$) discharge winter scenarios, respectively.

Following the methodology proposed by Sousa (2013), the idealized scenario with high river discharge starts from the mean base value for January (1055 $m^3\ s^{-1}$) and then increases exponentially to 3299 $m^3\ s^{-1}$ (Figure 5.2a, red line). The maximum is about three times the average discharge for January. This ratio was adopted for moderate (Figure 5.2a, black line) and low (Figure 5.2a, blue line) discharge scenarios. Thus, the low and moderate

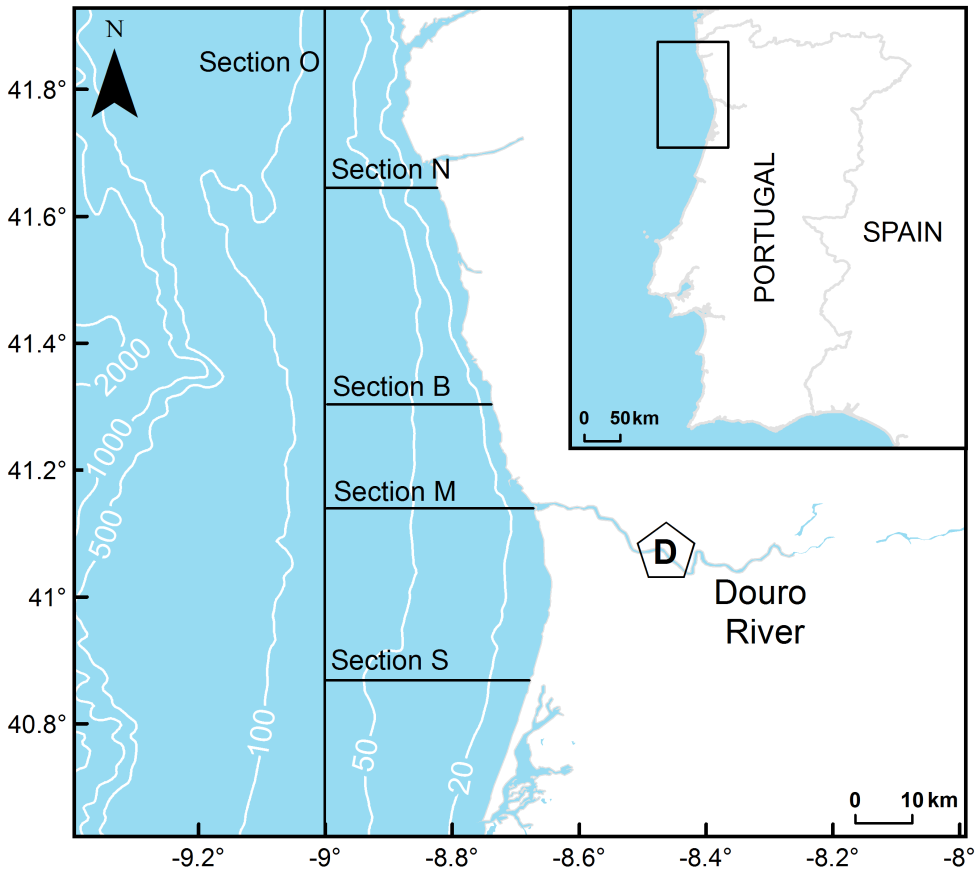

Figure 5.1: Location of the study area. The coastal region adjacent to the Douro Estuary. Dam location marked with a pentagon (D) and cross-sections (O, N, B, M, and S) marked with black lines. The bathymetry, from GEBCO, is shown with white lines (contours in meters).

discharge scenarios initiate with a river input of 192 $m^3\ s^{-1}$ and 475 $m^3\ s^{-1}$, respectively and then, likewise for the high river discharge scenario, increases exponentially during 4 days until reaching the fixed value previously defined for each case. The water temperature and salinity of the Douro River discharge in the estuarine model implementation described in Chapter 4 were set to 8°C and 0, respectively.

The definition of the wind scenarios was based on statistical results by Sousa (2013) from wind data provided by the NCEP-CFSR (`http://rda.ucar.edu/pub/cfsr.html`) at a control station located in the region off the Minho estuary from 1979 to 2010. Considering that wind magnitude variability is almost negligible between the coast off the Douro and

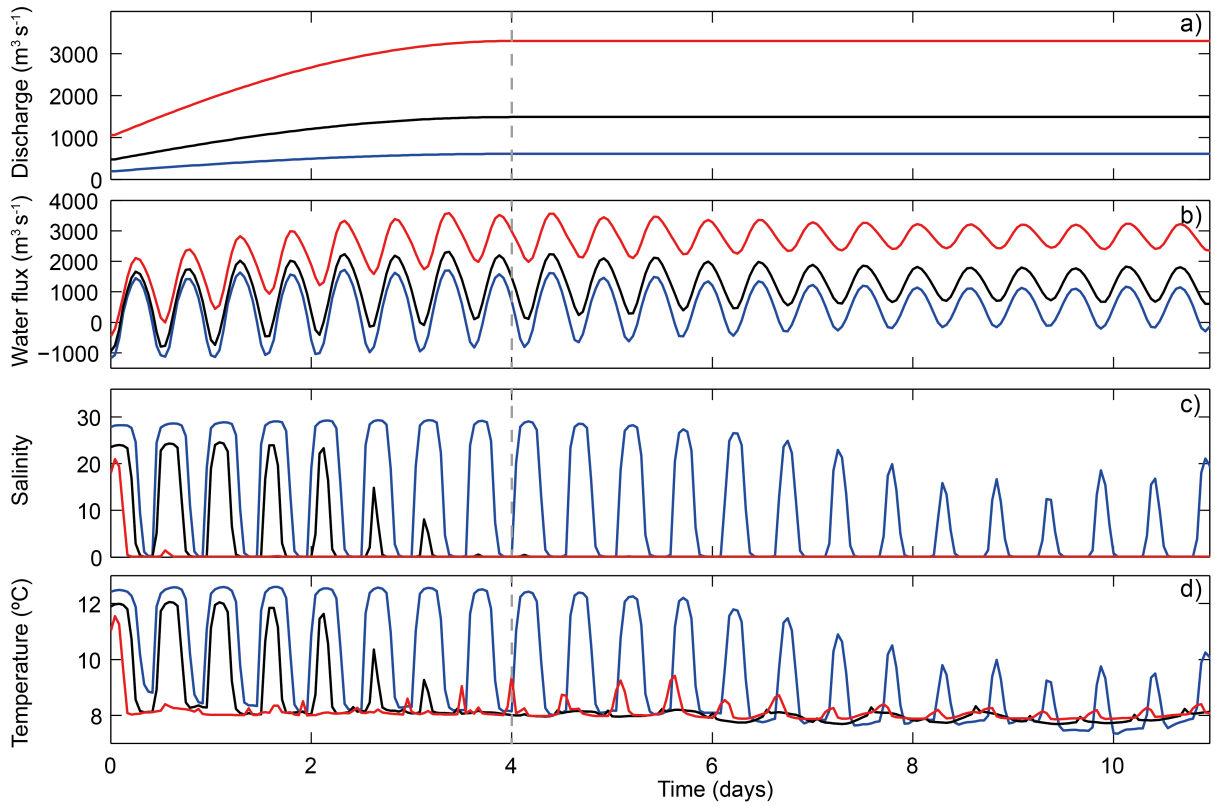

Figure 5.2: The Douro River discharge scenarios (red line: high discharge; black line: moderate discharge; blue line: low discharge) (s). Water flux (b), water temperature (c) and salinity (f) computed in the river mouth from estuarine model simulations for the three scenarios.

Minho estuaries, the results by Sousa (2013) are acceptable for this study. Sousa (2013) revealed that the probability of occurrence of winds with intensity lower than 3 m s^{-1} is 32 %, while the probability of occurrence of moderate winds (between 3 and 6 m s^{-1}) is higher than 46 %. These wind intensities were used as representative of the prevailing wind regime of this region in the simulations.

To study the behaviour of the Douro estuarine plume and its response to external forcing, several numerical experiments were conducted. 27 experiments to test the plume propagation were simulated, including four different wind directions (north, south, west and east), two different wind intensities (3 and 6 m s^{-1}) and three different river discharges (high, moderate and low). Moreover, three simulations were carried out without wind imposition. All simulations run with a six months spin-up period, from July 2009 to February 2010, but

only results for January 2010 are analysed. The defined wind forcing for each scenario starts on 5 January 2010, when the river discharge reached its maximum, and then held steady constant in all scenarios. Although both wind and discharges are idealized, the conditions adopted for 2010 are representative of an average winter in this region (see Chapters 3 and 6).

To evaluate the role of river discharge and wind forcing in the plume propagation a variety of results will be analysed. Several surface and cross-section fields of salinity 5 days after the peak discharge will be depicted considering the main numerical scenarios. At the same time, the equivalent depth of freshwater is determined in order to evaluate the horizontal pattern of plume dispersal:

$$F_w = \int_{-h}^{\eta} \frac{S_a - S(z)}{S_a} dz \tag{5.1}$$

where S_a is a reference or ambient salinity, which represents the limit of the buoyant plume. Following Peliz et al. (2002) and Otero et al. (2008), 35.6 was used as the reference salinity. $S(z)$ is the water column salinity.

The freshwater transport was also evaluated in five sections (Figure 5.1) to identify its temporal and spatial variability and to study the effect of wind and discharge on plume dispersal. Section O (Offshore) is the only alongshore section, and was selected to study the offshore plume propagation. It is located at 9° of longitude between 50 and 100 isobaths. Section N (North) was defined in the far-field region of the Douro plume, to evaluate the northward coastal transport and the alongshore velocities promoted by the buoyant current. Section B (Bulge) was defined in the region where the re-circulating bulge will be likely observed. Section M (Mouth) represents the region near the mouth of the river. It was chosen to evaluate the role of cross-shore current velocities and vertical salinity fields in the near-field region. Section S (South) was defined in the region between the Douro River mouth and the Ria de Aveiro Lagoon to assess the possibility that plume generates a southward current and Douro riverine waters affect this region.

The freshwater transport, relative to the reference salinity, S_a, is determined as the

integral of freshwater fraction:

$$V_{F_w} = \iint_{-h}^{\eta} \frac{S_a - S(z)}{S_a} u_s dz dx_s \tag{5.2}$$

where u_s is the horizontal velocity normal and x_s is the horizontal distance across each section (Choi and Wilkin, 2007).

5.2.2 Plume parameters

River plumes may be characterized and classified based on a number of parameters and criteria that will be determined and analysed. In this study, it was considered the numbers related to estuarine, outflow and plume properties. A brief description of each is given below.

Estuarine processes govern the initial momentum and buoyancy of a river plume when enters in the coastal ocean (Horner-Devine et al., 2015). To evaluate how estuarine dynamics affects the spreading and properties of the estuarine plume, Nash et al. (2009) adopted the estuary Richardson number, Ri_E, as defined by Fischer (1972). The formulation evaluates how the tidal velocity (u_{tidal}) is important and competes with the freshwater inflow (Q_f) in influencing the plume propagation in over shelf, assuming that advection scales with Q_f and turbulence scales with u_{tidal}. This number is defined as:

$$Ri_E = \frac{g_r^{'} Q_f}{W_E u_{tidal}^3} \tag{5.3}$$

where $g_r^{'} = g(\rho_{amb} - \rho_r)/\rho_r$ represents the reduced gravity, where g is the gravitational acceleration, ρ_{amb} is the ambient ocean density and ρ_r is the river input density. Q_f is the freshwater inflow rate, u_{tidal} the root-mean-squared velocity due to tide-generated currents (Llebot et al., 2014), and W_E is the width of the estuary.

High values of Ri_E ($Ri_E^{-1} \rightarrow 0$) indicate no mixing and a purely fresh plume with salinity 0. When $Ri_E^{-1} \rightarrow \infty$ (low values of Ri_E) there are no river inflow into the estuary (Nash et al., 2009). Following Fischer et al. (1979), the transition between well-mixed and

stratified estuaries occurs in the range $0.8 > Ri_E > 0.08$ and this limit will be considered in this study to establish the tide influence on the plume.

Several non-dimensional parameters applied by Yankovsky and Chapman (1997) to predict the plume propagation based only on the properties of the buoyant inflow at the source (here the estuarine outflow at the mouth) were used to characterized and identify the type of the Douro estuarine plume in the absence of ambient shelf circulation. Moreover, the length predictions by Yankovsky and Chapman (1997) will be also compared with model predictions.

The Rossby number is a dynamic parameter commonly used to estimate the relative strength of inertial and rotational processes. Here, the Rossby number associated with the velocity and length scale of the river inflow into the coastal ocean (Horner-Devine et al., 2006), R_i, was computed by:

$$R_i = \frac{U_i}{f R_{Di}} \tag{5.4}$$

U_i and R_{Di} are the mean velocity and the baroclinic Rossby radius of the estuarine outflow, respectively, calculated by:

$$U_i = \frac{Q_E}{W_m h_i} \tag{5.5}$$

$$R_{Di} = \frac{\sqrt{g_e^{'} h_i}}{f} \tag{5.6}$$

where Q_E is the estuarine outflow, here computed from the estuarine model simulations (Figure 5.2 b), $g_e^{'}$ is the mean reduced gravity considering the estuarine outflow density and h_i is the average bottom depth at the mouth of the Douro Estuary.

The Burger number, B_i, was calculated to evaluate the buoyancy of the estuarine outflow. High values of B_i often indicate a plume with surface-advected behaviour (depending on the value of R_i) in the classification stated by Yankovsky and Chapman (1997).

$$B_i = \frac{(g_e^{'} h_i)^{1/2}}{f W_m} \tag{5.7}$$

To examine whether a flow tends to be governed by baroclinic or inertial processes, the inflow Froude number will be calculated, Fr_i (Chao, 1988b):

$$Fr_i = \frac{U_i}{\sqrt{g_e^{'} h_i}} = \frac{R_i}{S_i} \tag{5.8}$$

When Froude number is greater than one ($Fr_i \gg 1$), the flow is characterized as supercritical, and inertial processes are dominant. Lower values ($Fr_i \leq 1$) represent a subcritical flow in which stratification is more important.

The next parameters are dependent from the ocean properties and therefore some results from numerical simulations are required to perform these computations. Thus, these numbers will be determined not only for the river discharge scenarios, but also for all scenarios tested.

The bulk Kelvin number (Garvine, 1995), K_b, describes the importance of rotational processes in the plume propagation, and also offers a classification of its scale:

$$K_b = \frac{W_p}{R_{Dh}} \tag{5.9}$$

where W_p is the extent of the plume across-shelf and R_{Dh} is the internal Rossby radius of the plume, which is expressed by:

$$R_{Dh} = \frac{\sqrt{g_p^{'} h_p}}{f} \tag{5.10}$$

where h_p is the thickness of the plume and $g_p^{'}$ is the reduced gravity in the plume layer. In the mouth $g_p^{'}$ is equivalent to $g_e^{'}$. *Large (small)-scale* plume behaviour is identified by large (small) Kelvin numbers, $K_b \gg 1$ ($K_b \ll 1$). Large-scale plumes tend to be more affected by the Earth's rotation than by inertial dynamics. Small-scale plumes are governed by inertial dynamics and tend to form freshwater bulges that radiate in all directions from the source (Garvine, 1995).

While the K_b is largely a geometric parameter that explores length scales of the plume,

the plume Rossby number, Rp, is used to estimate the relative strength of inertial and rotational processes on the plume. Here, the terms in balance are relative to the plume itself. Rp will be computed by:

$$R_p = \frac{u_{plu}}{f R_{Dh}} \tag{5.11}$$

where u_{plu} is the velocity of the flow in the surface layers (in the plume). High Rossby numbers ($R_p \gg 1$) indicate that the plume is dominated by inertial processes. When the Rossby number is low ($R_p \ll 1$), the rotational processes are dominant.

The mouth Kelvin number, K_m, requires a different length scale from K_b (here the W_m) (Garvine, 1995; Huq, 2009; Horner-Devine et al., 2015):

$$K_m = \frac{W_m}{R_{Dh}} \tag{5.12}$$

The K_m is used to characterize and classify the plumes in terms of the bulge formation around the river mouth, taking into account the ratio of estuary width (W_m) at the mouth to the internal Rossby radius (R_{Dh}) of the plume.

The Ekman number, E_{kp}, will also be calculated to estimate the relative strengths of frictional and rotational processes within the plume (Cushman-Roisin, 1994; Tilburg et al., 2011). This number is expressed by:

$$E_{kp} = \frac{A_z}{f h_p^2} \tag{5.13}$$

High values ($E_{kp} \gg 1$) represent a friction-dominated flow, while low values ($E_{kp} \ll 1$) indicate a rotational-dominated one.

As R_p, the Froude number can be calculated throughout the plume to examine how dynamics change within plume (Tilburg et al., 2011; Horner-Devine et al., 2015):

$$Fr_1 = \frac{u_p lu}{\sqrt{g_p' h_p}} \tag{5.14}$$

In this study, the upper-layer Froude number will be calculated in the mouth, Fr_{1m},

and within the plume, Fr_{1p}, at a distance of $W_p/2$.

The Reynolds number will be calculated, to compare the mechanisms of advection and mixing within the plume:

$$Re_p = \frac{R_p}{E_{kp}} \tag{5.15}$$

High values for the Reynolds number ($Re_p \gg 1$) indicate that advection is dominant over mixing processes. Low values ($Re_p \ll 1$) indicate a flow governed by frictional or mixing processes (Tilburg et al., 2011).

To assess the wind impact in the plume shape, the wind strength index introduced by Whitney and Garvine (2005) will also be computed. This index (W_S) is defined as:

$$W_S = \frac{u_{wind}}{u_{dis}} \tag{5.16}$$

where

$$u_{wind} = \sqrt{\frac{\rho_a}{\rho_{amb}} \frac{C_{10}}{C_{Da}}} W_{10} \tag{5.17}$$

$$u_{dis} = \frac{1}{K_b} (2g' Q_E f)^{\frac{1}{4}} \tag{5.18}$$

where W_{10} is the wind velocity component at 10 m height (3 or 6 m s^{-1}), C_{10} (1.2×10^{-3}) is the surface drag coefficient, C_{Da} (1.3×10^{-3}) is the depth averaged drag coefficient and Q_E is the estuarine outflow. When $|W_S|$ >1, the flow is heavily influenced by the wind, and when $|W_S|$ <1, the flow is dominated by the buoyant forcing. The u_{wind} value is 0.1 and 0.2 for wind scenarios of 3 m s^{-1} and 6 m s^{-1}, respectively.

5.3 Results and discussion

Wind and river discharge play the most important role in the dispersion of the Douro estuarine plume. For this purpose, several numerical modelling scenarios of river discharge and wind forcing were evaluated. The plume parameter numbers as well as the freshwater

transport were computed in order to obtain a full characterization of the plume propagation and fate in the coastal ocean.

5.3.1 River discharge influence

5.3.1.1 Patterns of propagation

The plume dispersion is analysed in terms of salinity and equivalent depth of freshwater for three scenarios considering different river discharges and without wind forcing. The results after 9 days of simulation, 5 days after the river inflow peak, for each scenario are presented in Figure 5.3. The vertical distribution of salinity and the zonal and meridional current along the sections in front of the Douro River mouth (section M), in the area of each mid-field plume, i.e. bulge (section B) and in the north region between the Cávado and Minho Rivers mouths (section N) are shown in Figure 5.4 for the same instant.

All figures share common features, i.e the low salinity waters are advected to the right due to the Coriolis effect and then the plume water extends northward (along the coastline) after establishing geostrophic balance. These are the common features of a prototypal plume (Horner-Devine et al., 2015). A re-circulating bulge in front of the mouth, a southward filament from the main bulge, and a northward coastal current following the coastline, which generates small-scale eddies promoted by the bathymetry and morphology constrains, are other shared particularities for the three freshwater discharge scenarios (Figures 5.3a, 5.3b and 5.3c). However, spatial length scales, salinity and equivalent depths of freshwater values (Figure 5.3d, 5.3e and 5.3f) are considerable different.

The offshore extension of the plume under low river discharge is about 18 km (in the latitude of the river mouth), the northward current is weak (0.2-0.3 m s^{-1}) (Figure 5.4g), and the plume front is hard to detect reaching the Cávado River mouth (Figure 5.3a). A re-circulating bulge in the near-field region is detectable, slightly tilted northward with an approximately diameter of about 17 km. The maximum equivalent freshwater depth (about 1.2 m) is observed in the centre of the bulge.

Under moderate river discharge, the Douro estuarine plume presents an offshore

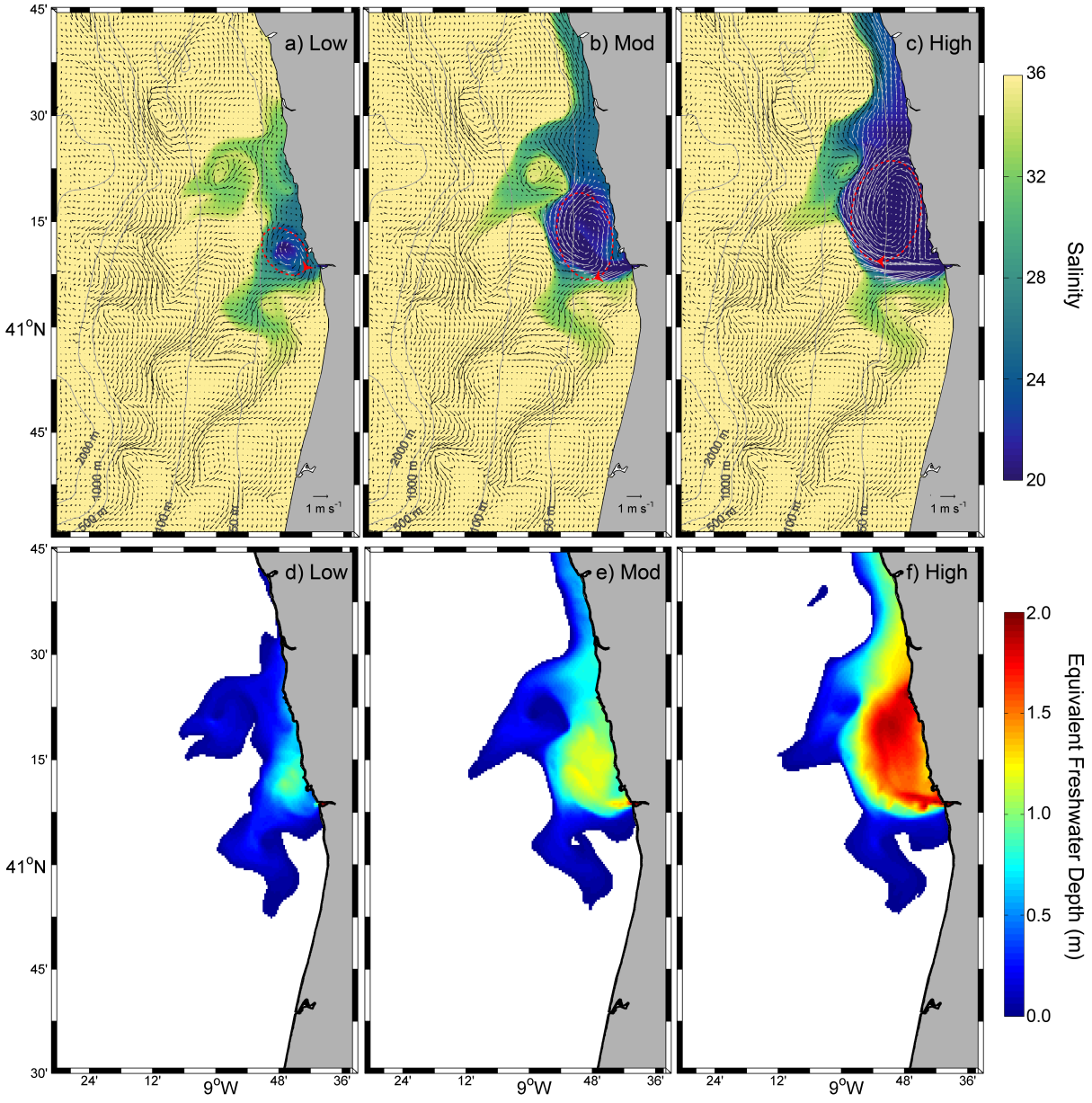

Figure 5.3: Surface currents and salinity (top) and equivalent depth of freshwater (bottom) 5 days after the peak discharge (day 9) under low (a,d), moderate (b,e), and high (c,f) river discharges with no wind forcing.

extension of about 22 km with a clear re-circulating bulge (∼25 km of diameter) northward tilted and partially detached from the coast (Figure 5.3b). The plume thickness is about 4 m, excluding the lift-off point near the freshwater source (Figure 5.4b). The maximum equivalent depth is ∼1.5 m (Figure 5.3b). The vertical structure within the bulge shows

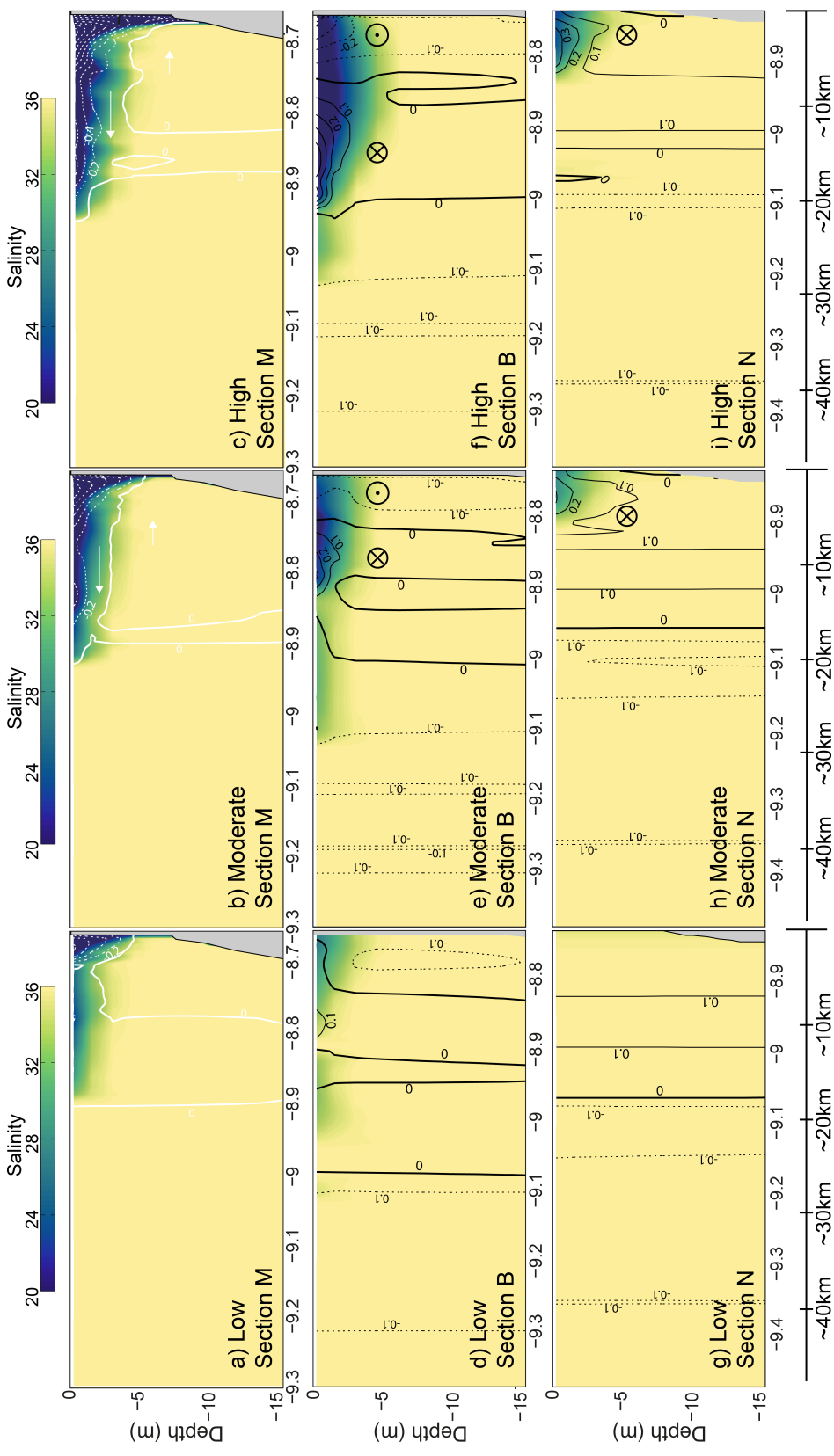

Figure 5.4: Salinity and cross-shore velocity (white contours) along section M (top panel) and salinity and alongshore velocity (black contours) along section B (middle panel) and section N (bottom panel) 5 days after the peak discharge under low (a,d,g), moderate (b,e,h) and high (c,f,i) river discharges.

weak and negative zonal velocities (<0.1 m s^{-1} - southward direction) close to the coast and positive values of about 0.3 m s^{-1} located 10 km from the coastline (Figure 5.4e). A northward nearshore surface current is observed, reaching the Minho River mouth and flowing out the domain (Figure 5.3 b). The buoyant current has 7-8 m thickness, about 8 km width and presents salinity of 32. In near surface layers, the zonal velocity is about 0.3 m s^{-1} (Figure 5.4h).

Salinity surface patterns present very similar features under high river discharge, but with an increase of the equivalent freshwater depth (close to 2 m), mainly in the bulge region (Figure 5.3c). The longitudinal extension of the plume is also similar (∼23 km), but the bulge is larger (∼ 35 km in the major axis of the ellipse). A larger accumulation of freshwater in the bulge is observed, feeding the northward coastal current (with a surface velocity of about 0.4 m s^{-1})(Figure 5.4i).

5.3.1.2 Riverine water transport

Figure 5.5 shows the freshwater transport over sections O (Offshore), N (North), and S (South) (Figure 5.1) for the three simulations with low (blue line), moderate (black line), and high river discharges (red line). As stated before, the growth of plume extension does not increase linearly with river inflow. That is also visible in the freshwater transport over section O (Figure 5.5a), where differences among the discharge scenarios are not

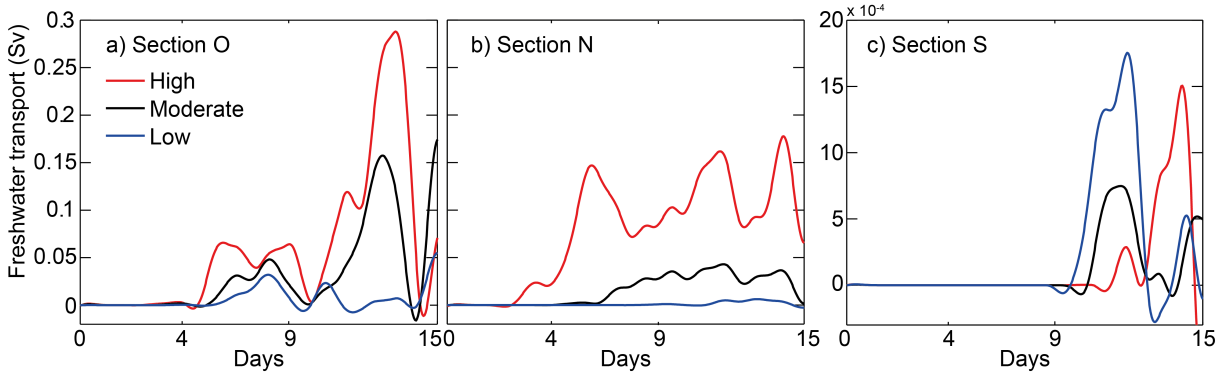

Figure 5.5: Freshwater transport in sections O (a), N (b), and S (e)(Figure 5.1) under low (blue), moderate (black), and high (red) river discharges.

proportional to river inflow. The total sum of the freshwater volume transported between 1 and 10 days after peak discharge is about 2.12×10^6 m^3, 10.56×10^6 m^3, and 19.82×10^6 m^3, for low, moderate, and high river discharge, respectively. Under moderate discharge, the transport is about 5 times larger than under low discharge. Under high river discharge, transport is about the double than for the moderate discharge (Table 5.1), following a logarithmic trend.

However, this trend is not noticeable in the freshwater transport over section N (Figure 5.5b). Under low river discharge, the total volume of freshwater passing through this section is lower than 1×10^6 m^3 (0.33×10^6 m^3). For moderate and high river discharge scenarios are found values of 5.35×10^6 m^3 and 24.55×10^6 m^3, respectively (Table 5.1). In this case, the northward freshwater transport seems to follow a temporal linear trend with

Table 5.1: Total volume of freshwater transported over sections O, N, and S (5.1) between 1 and 10 days after peak discharge for all combined wind and river discharge scenarios.

	Section O ($\times10^6$ m^3)			Section N ($\times10^6$ m^3)			Section S ($\times10^6$ m^3)		
	Low	Moderate	High	Low	Moderate	High	Low	Moderate	High
No Wind	2.12	10.56	19.82	0.33	5.35	24.55	0.07	0.04	0.04
East 3 m s^{-1}	1.02	2.56	8.99	4.78	15.57	37.74	0.00	0.00	0.00
East 6 m s^{-1}	0.48	5.31	17.53	3.93	17.82	42.96	0.00	0.00	0.00
West 3 m s^{-1}	0.28	7.93	45.75	0.00	0.03	9.43	4.76	11.98	4.62
West 6 m s^{-1}	0.00	0.00	0.34	0.00	0.06	0.00	2.53	9.89	36.76
North 3 m s^{-1}	18.71	52.12	127.15	0.00	0.00	0.50	0.00	0.00	0.00
North 6 m s^{-1}	18.79	57.85	138.90	0.00	0.00	0.03	0.00	0.00	0.00
South 3 m s^{-1}	0.04	0.01	0.19	8.70	23.37	48.55	0.00	0.00	0.00
South 6 m s^{-1}	0.00	0.00	0.00	8.93	26.86	61.23	0.00	0.00	0.00

the river discharge, but more simulations with different values of freshwater inflow need to be performed to confirm this relationship ($V_{F_w}(SecN) = 0.0051Q_f + 1.14Days - 9.5$).

Regarding the southward freshwater transport, the volume is negligible in all cases: 0.07×10^6 m^3, 0.04×10^6 m^3, and 0.04×10^6 m^3 for low, moderate and high river discharge scenarios (Figure 5.5c - Table 5.1). This confirms that in the absence of significant wind or under null wind forcing the southward plume dispersion is unlikely.

5.3.1.3 Parameters and criteria

The averaged parameters determined between 1 and 10 days after the peak discharge for estuarine outflow and plume properties are presented in Tables 5.2 and 5.3, respectively.

In order to evaluate the tidal influence on the estuarine outflow, the Estuarine Richardson number, Ri_E, was computed for neap (u_{tidal}=0.28 m s^{-1}), spring (u_{tidal}=1.12 m s^{-1}) and mean tide (u_{tidal}=0.75 m s^{-1}) conditions (Table 5.2). Under low river discharge, the induced tidal mixing is very important even during a mean and spring-tides ($Ri_{E-Neap} < 0.8$). The tide decreases its influence under moderate and high river discharge scenarios. During a neap-tidal periods, the estuary is also well mixed ($Ri_{E-Neap} >> 0.8$) in moderate and high river discharge scenarios. Nevertheless, the currents associated with spring-tides are important under moderate river discharges. Although the $Ri_{E-Spring}$ under high river discharges indicate a well-mixed estuary, the value is close to the limit, showing that the spring currents can influenced the near-field plume.

Table 5.2: Estuary Richardson number, Ri_E, during neap (Ri_{E-Neap}), mean (Ri_{E-Mean}), and spring-tides ($Ri_{E-Spring}$). Outflows baroclinic Rossby radius (R_{Di}), Rossby number (R_i), Burger number (B_i) and Froude number (Fr_i) under low, moderate, and high river discharges.

	Ri_{E-Neap}	Ri_{E-Mean}	$Ri_{E-Spring}$	R_{Di} (km)	R_i	S_i	Fr_i
Low	9.09	0.47	0.14	16.42	1.70	32.83	0.05
Mod	29.02	1.51	0.45	18.64	4.21	37.28	0.11
High	64.77	3.37	1.01	18.67	9.38	37.33	0.25

Table 5.3: Key parameters for the Douro estuarine plume under all wind and river discharge scenarios in study.

		W_p (km)	R_{Dh} (km)	K_m	K_b	R_p	Fr_{1m}	Fr_{1p}	Ek_p	Re_p	u_{dis} (m s^{-1})	u_{wind} (m s^{-1})	W_S
No Wind	Low	20.86	7.30	0.07	2.86	0.31	0.90	0.45	0.32	0.91	0.13	0.00	0.00
	Mod	28.54	9.10	0.05	3.14	0.49	1.28	0.73	0.26	2.10	0.16	0.00	0.00
	High	28.73	11.53	0.04	2.49	0.62	1.45	0.96	0.18	6.87	0.24	0.00	0.00
East 3 m s^{-1}	Low	11.34	6.73	0.07	1.68	0.60	1.04	0.93	0.45	1.27	0.22	0.10	0.45
	Mod	15.18	8.75	0.06	1.73	0.73	1.35	1.18	0.38	2.66	0.29	0.10	0.35
	High	20.55	11.33	0.04	1.81	0.75	1.49	1.23	0.18	7.69	0.33	0.10	0.30
East 6 m s^{-1}	Low	6.94	6.64	0.08	1.05	0.92	1.14	1.68	0.76	1.84	0.35	0.20	0.56
	Mod	11.40	8.75	0.06	1.30	0.82	1.38	1.47	0.44	3.00	0.38	0.20	0.52
	High	16.68	11.58	0.04	1.44	0.80	1.47	1.52	0.24	8.94	0.42	0.20	0.47
West 3 m s^{-1}	Low	15.56	7.43	0.07	2.09	0.25	0.86	0.32	0.23	0.80	0.18	0.10	0.56
	Mod	27.50	9.48	0.05	2.90	0.20	1.22	0.30	0.14	1.00	0.17	0.10	0.58
	High	38.56	11.48	0.04	3.36	0.24	1.46	0.33	0.11	2.59	0.18	0.10	0.55
West 6 m s^{-1}	Low	8.73	8.97	0.06	0.97	0.34	0.64	0.45	0.18	2.27	0.38	0.20	0.52
	Mod	14.47	10.89	0.05	1.33	0.32	0.97	0.45	0.15	2.83	0.37	0.20	0.53
	High	23.73	12.19	0.04	1.95	0.22	1.34	0.29	0.06	3.11	0.31	0.20	0.64
North 3 m s^{-1}	Low	30.26	7.20	0.07	4.20	0.21	0.94	0.43	0.49	0.57	0.09	0.10	1.13
	Mod	54.08	9.51	0.05	5.69	0.24	1.23	0.53	0.37	1.21	0.09	0.10	1.14
	High	62.27	11.72	0.04	5.31	0.37	1.43	0.76	0.27	4.39	0.11	0.10	0.87
North 6 m s^{-1}	Low	6.62	6.53	0.08	1.02	0.75	1.06	1.16	0.49	1.40	0.37	0.20	0.54
	Mod	17.52	8.95	0.06	1.96	0.54	1.31	1.01	0.34	2.17	0.25	0.20	0.78
	High	56.91	11.76	0.04	4.84	0.21	1.43	0.55	0.19	2.57	0.13	0.20	1.59
South 3 m s^{-1}	Low	8.70	7.20	0.07	1.21	0.58	0.95	0.91	0.42	1.62	0.31	0.10	0.32
	Mod	12.99	8.85	0.06	1.47	0.73	1.33	1.18	0.43	2.79	0.34	0.10	0.29
	High	21.74	11.07	0.05	1.96	0.75	1.53	1.25	0.26	7.04	0.31	0.10	0.32
South 6 m s^{-1}	Low	3.82	7.25	0.07	0.53	0.85	0.97	1.32	0.45	2.80	0.71	0.20	0.28
	Mod	6.57	8.55	0.06	0.77	0.99	1.40	1.78	0.87	4.66	0.65	0.20	0.31
	High	10.46	10.67	0.05	0.98	0.96	1.60	2.35	1.27	12.94	0.62	0.20	0.32

The outflow parameters used to predict the plume propagation defined by Yankovsky and Chapman (1997) are also presented in Table 5.2.

The Rossby radius of deformation, R_{Di}, is equivalent to the longitudinal extension of the plume: it is low under low river discharge, and higher, with similar values, under moderate and high estuarine outflows, reaching a steady distance at some point. R_i shows that inertial dominate over the rotational processes, even under low discharge. This is a expected conclusion since the Douro River mouth is very narrow and the water flux is unidirectional along the outflow section. In combination with higher Burger values, B_i, the results suggest that the Douro plume is a surface-advected plume. Here B_i values ranged from 32.83 (low discharge) to 37.33 (high discharge). From Yankovsky and Chapman (1997) theory, a plume can be considered as surface advected when $B_i = \sqrt{2R_i}$. This is true for all discharges scenarios in this study. Bottom-advected plumes are possible only for a relatively weak density difference between the ambient flow and buoyant discharge (small B_i), which is unlikely to be found in Douro Estuary under winter regimes.

The higher density differences found in Douro estuarine discharge yields to an outflow Froude number, Fr_i, bellow 1 in all situations, which is an expected result for surface-advected plume. As $Fr_i < 1$ in all situations of the estuarine outflow, the dilution and mixing processes starts in the estuary (Horner-Devine et al., 2015), revealing the importance accurately resolving the variable water fluxes between the estuary and coastal ocean to study the plume propagation. Following Yankovsky and Chapman (1997) formulations, the surface-advected plume spreads a minimum of more than four outflow Rossby radii offshore ($W_p =\sim 4.22R_{Di}$). This means that in the low, moderate and high river discharge scenarios the predicted offshore extension would be ∼69.3 km, ∼78.7 km and ∼78.8 km, respectively.

From Table 5.3 may be analysed the plume numbers and criteria calculated based on the numerical model results for all discharge and wind scenarios.

R_{Dh} is about 1/3 of the plume width, W_p, and this ratio tends to increase with the estuarine discharge (Table 5.3). This disagrees with the offshore extension predicted by Yankovsky and Chapman (1997). The model results indicate W_p values of 20.86 km, 28.54 km and 28.73 km under low, moderate and high river discharge scenarios. The predicted values from Yankovsky and Chapman (1997) are ∼50 km greater than the observed in the simulations. According to Yankovsky and Chapman (1997), this difference is not surprising

considering that the theory neglects the strong winds and tidal forcing. Here, the tidal forcing associated with both shelf currents and variable estuarine outflow is a key factor in the stabilization of the bulge growing (Isobe, 2005). The tidal forcing tends to tilt the plume northwards, creating a partially detached bulge as observed in Figure 5.3 and in line with results of numerical simulations of Yankovsky et al. (2001). The tidal currents in the inner shelf also demonstrated to be important in the enhancement of the freshwater transport northward, changing in time the relation between the bulge growth and the estuarine outflow, until the moment when this transport equals the river discharge (Isobe, 2005).

The Kelvin bulk number, K_b, is higher than 1 for the three different discharge scenarios, which indicate that the Douro estuarine plume can be classified as a large scale plume (Garvine, 1995) without the wind forcing influence.

The very low values for the Kelvin mouth parameter, K_m, show the importance of the inertial processes in the generation of the plume. The existence of a re-circulating bulge, which is clear in Figures 5.3b and 5.3c, is also supported by the low values of K_m (Table 5.3). If the river mouth width is much smaller than the internal Rossby radius, R_{Dh}, a re-circulating bulge within the plume (without other external forcing) will be observed (Garvine, 1995; Huq, 2009; Horner-Devine et al., 2015).

Froude mouth numbers, Fr_{1m} are supercritical ($Fr_{1m} > 1$) for moderate and high river discharge scenarios (Table 5.3). In these cases, a near-field region is well defined until the conditions are reduced to subcritical at some distance from the river mouth (Horner-Devine et al., 2015). At a distance of $W_p/2$, the subcritical condition was almost achieved for the moderate discharge simulation, $Fr_{1p} < 1$, while for high river discharges the condition is critical, $Fr_{1p} \sim 1$. This marks the transition between the near and the mid-field plume region ($\sim$14 km) (Horner-Devine et al., 2015). In the low discharge scenario Fr_{1m} is lower than 1 and the plume tends to be strongly influenced by rotation (Horner-Devine et al., 2015). In addition, the plume Rossby number (R_p) corroborates this result, indicating that rotational processes dominate within plume. R_p is lower than 1 in all cases, which is consistent with the Ekman number results ($E_{kp} << 1$) where rotation processes also

dominate over frictional ones (Table 5.3).

Plume Reynolds numbers, Re_p, are greater than 1 under moderate and high river discharges, indicating that inertial processes are very important and the flow within the plume is not governed by frictional processes in these cases (Table 5.3).

According to the results, the Douro estuarine plume can be classified as a surface-advected and large-scale plume and can be dynamically characterized as a prototypal plume (Figure 1.3a - Chapter 1), comprising all dynamical regions. It has a relatively high discharge and a narrow mouth and its dynamic is modified by Earth's rotation (Horner-Devine et al., 2015). The Douro estuarine plume shares this type of morphology with other important river plumes in the world, such as the Columbia River (Hickey et al., 1998; Thomas and Weatherbee, 2006; Horner-Devine, 2009; Hickey et al., 2010; Kilcher and Nash, 2010), the Merrimack River (MacDonald et al., 2007; Kakoulaki et al., 2014), the Niagara River (Masse and Murthy, 1992; Horner-Devine et al., 2008) and the Hudson River (Chant et al., 2008b).

5.3.2 Wind-driven plume dispersion

5.3.2.1 Patterns of propagation

Surface salinity and equivalent depth of freshwater fields, under the wind scenarios previously defined and moderate river discharge (5 days after peak discharge - Figure 5.2), are depicted in Figure 5.6. The vertical distribution of salinity and current is shown in Figures 5.7, 5.8, and 5.9 for sections M (cross-shore current), N (alongshore current) and S (alongshore current), respectively.

For the sake of simplicity, equivalent depth of freshwater and vertical structure of salinity and velocity are not shown under low and high river discharges. As stated before, independently from discharges, the Douro estuarine plume presents a similar mean state, varying only in terms of length scale and volume of freshwater. Nevertheless, the plume parameters and freshwater transport over the sections were calculated and presented for all combinations of river discharge and wind scenarios.

The maxima distance of offshore plume spreading is observed under upwelling-

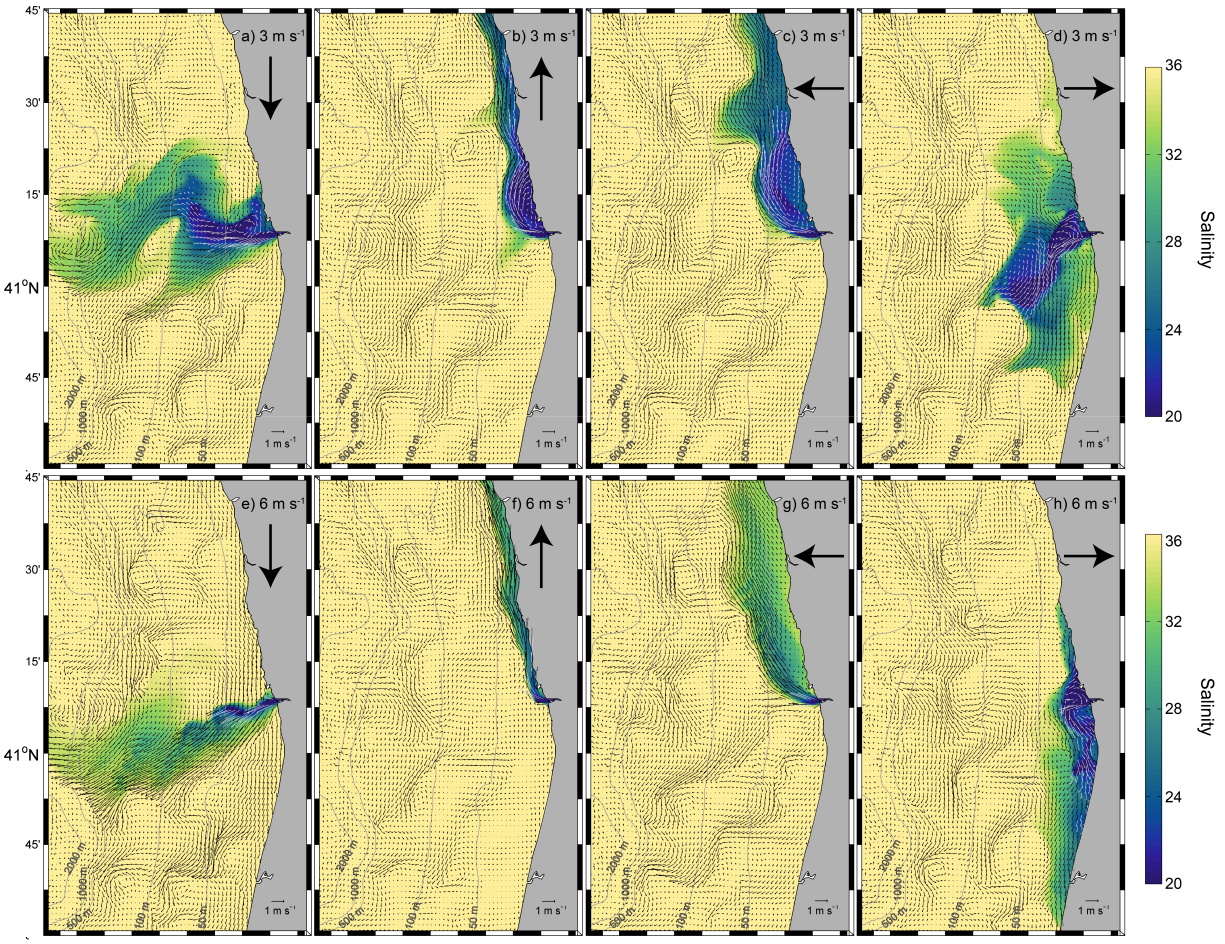

Figure 5.6: Surface currents and salinity 5 days after peak discharge under moderate river discharge and moderate and strong northerly (a, e), southerly (b, f), easterly (c, g), and westerly wind forcing (d, h).

favourable winds (Figures 5.6a and 5.6e). In this case, the inclination observed between the main direction of the plume propagation and the river's mouth is influenced by an equilibrium between the river discharge and wind intensity. The higher the discharge, further from the coast the plume starts to be affected by wind, i.e. the near-field region is larger when the discharge is higher and the transition from supercritical to subcritical flow (far-field) occurs further away from the river mouth (Hetland, 2005; Horner-Devine et al., 2015). No re-circulating bulge is detectable and the offshore propagation of the plume exceeds the western boundary of the domain under moderate and high river discharges. The plume in this location is much diluted, but yet may impacts ocean waters in the continental

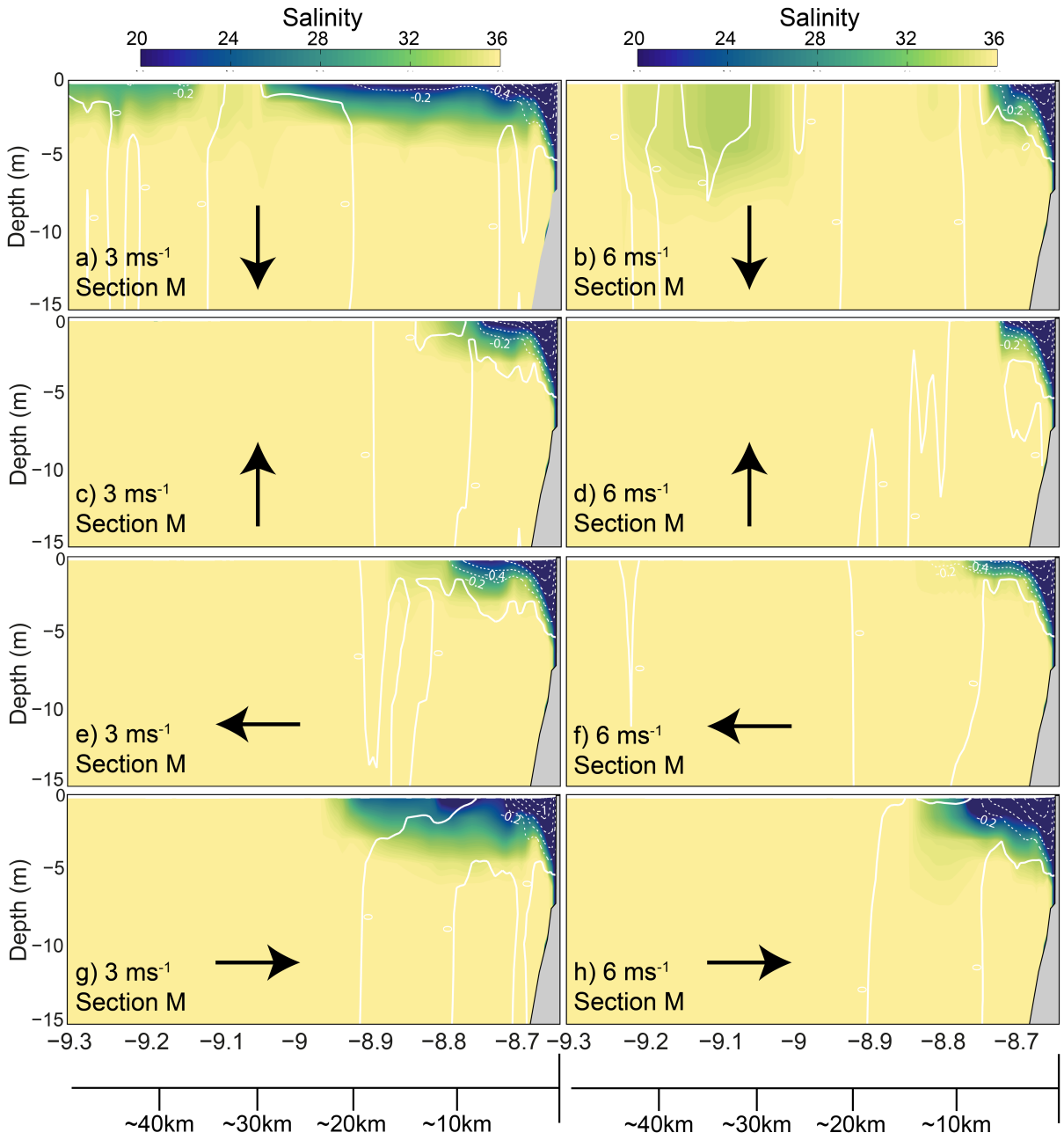

Figure 5.7: Salinity and cross-shore velocity (white contours) along section M under moderate and strong northerly (a, b), southerly (c, d), easterly (e, f), and westerly wind forcing (g, h) 5 days after peak discharge under moderate river discharges.

margin. In this condition, its spreading will be probably influenced by the main regional ocean circulation, which is not implemented in this coastal numerical model application.

The vertical salinity dispersion in section M shows a well-stratified and thinner plume

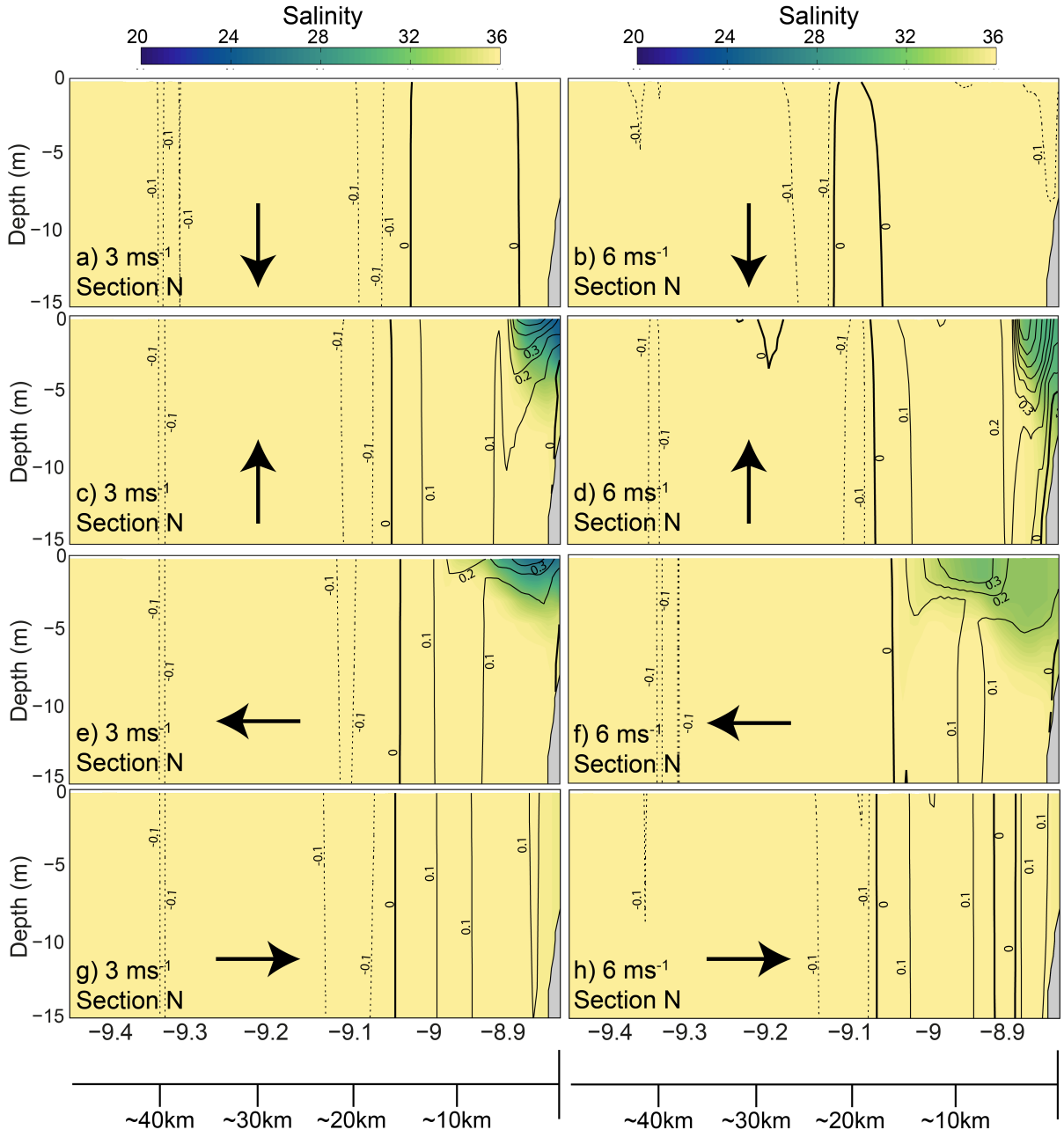

Figure 5.8: Salinity and alongshore velocity (black contours) along section N under moderate and strong northerly (a, b), southerly (c, d), easterly (e, f), and westerly wind forcing (g, h) 5 days after peak discharge under moderate river discharges.

structure with the freshwater confined to 2-3 m depth in the far-field region (Figure 5.7a). The analysis of the salinity vertical structure under strong winds is challenging due to the plume dispersion toward southwest. For example, low salinity patches located offshore

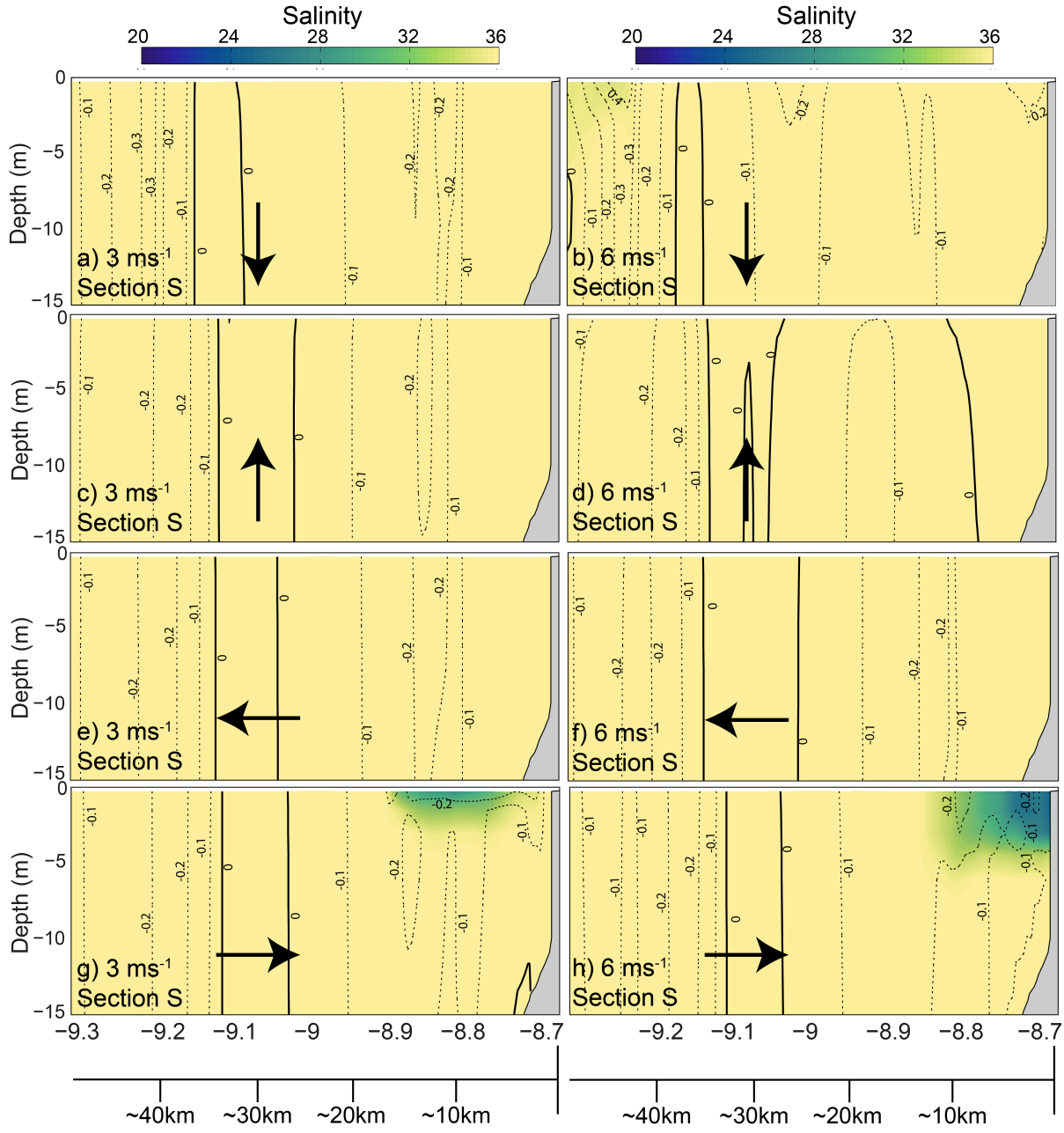

Figure 5.9: Salinity and alongshore velocity (black contours) along section S under moderate and strong northerly (a, b), southerly (c, d), easterly (e, f), and westerly wind forcing (g, h) 5 days after peak discharge under moderate river discharges.

(Figure 5.7b) in section M derives from a well-mixed plume filament, which is visible in Figure 5.6e. This preferential direction of propagation generates a plume signal that is observed in the vertical structure of the section S (Figure 5.9), where alongshore current is

higher than 0.4 m s^{-1}.

Isolated patches of low salinity waters caused by the tidal variation in the estuarine outflow (tidal-plume, Nash and Moum (2005)) are well identified (Figure 5.6e). The stratification level, the supercritical behaviour of the flow in the source, and the observation of tidal salinity pulses/bands along the plume jet are characteristics already observed in the Columbia River plume (Nash and Moum, 2005; Stashchuk and Vlasenko, 2009; Kilcher and Nash, 2010), constituting a well known source of internal waves in the Oregon coast, USA. Likewise, the possibility that the Douro estuarine plume generates circular internal waves seawards increases under upwelling-favourable wind conditions and moderate and high river discharge.

The analysis of the horizontal and vertical salinity fields shows a confinement of the estuarine plume in the coastal region under southerly winds (northwards) (Figures 5.6c and 5.6f). Comparing with moderate river discharge without wind forcing, the downwelling-favourable winds shrink the bulge in front of the river mouth, enhancing the northward current and the vertical mixing (Figures 5.7c, 5.7d, 5.8c and 5.8d).

The offshore extension of the plume in front of the river mouth does not exceed ∼10 km and ∼6 km under moderate and strong southerly winds, respectively (Figures 5.7c and 5.7d). The numerical results corroborate the plume patches and coastal band scales identified in the turbid MODIS composites (Chapter 2) and in previous numerical modelling studies (Otero et al., 2008).

Two main differences are found between the results under moderate (3 m s^{-1}) and strong (6 m s^{-1}) southerly winds:

1 - the re-circulating bulge is only detected under moderate wind, where a weak southward current is observed (∼0.1-0.2 m s^{-1})(Figure 5.6c). The bulge is much distorted northwards, comparing with the simulation without wind (Figure 5.3b).

2 - the alongshore current in surface layers is about 1.7 (∼0.5 m s^{-1}) and 2.7 (∼0.8 m s^{-1}) times higher under moderate and strong winds, respectively, comparing with results for moderate river discharge without wind forcing (∼0.3 m s^{-1}).

In easterly wind simulation, the results are similar to those found for the southerly

wind scenario, but with the plume core detached from the coast (Chao, 1988b) and a weaker northward current ($\sim$ 0.3 m s^{-1})(Figures 5.6c and 5.6g). The plume detachment is especially noticeable under strong wind events, which push the plume offshore in opposition to the pressure gradient force, stopping the water re-circulation near coast (Figure 5.6g) and enhancing stratification. The plume width near the mouth is larger under moderate ($\sim$15 km) than under strong winds ($\sim$11 km), which can be explained by the reminiscent freshwater from the re-circulating bulge, which increases the plume width in front of the river mouth (Figures 5.7e and 5.7f). However, the buoyant coastal plume width is larger ($\sim$15 km) under strong than under moderate wind intensities ($\sim$10 km)(Figures 5.8e and 5.8f).

The westerly wind simulation results are very consistent with the turbid composites presented in Chapter 2. The plume is squeezed landward, accumulating freshwater along the coast (Figures 5.6d and 5.6h). That accumulation of water is observed in terms of plume depth in the vertical salinity structure in section M (Figures 5.7g and 5.7h). The plume thickness is about 5-6 m, excluding the estuary mouth region, where the equivalent depth of freshwater surpass 2 m (not shown). The offshore extension of the plume in section M, under moderate wind intensity (3 m s^{-1}) is equivalent (about 22 km) to results from the simulation without wind (Figure 5.4b). This extension decreases to $\sim$15 km under strong westerly winds (6 m s^{-1}).

Both simulations with moderate and strong westerly wind show that the plume does not generate a buoyant northward coastal current. Nevertheless, these are the only idealized scenarios where the riverine water from the Douro flows southward along the shelf, reaching the Ria de Aveiro Lagoon (Figure 5.6h). This turns very plausible the hypothesis that Douro estuarine plume propagates into the Ria de Aveiro Lagoon (tidal forced estuary, Dias et al. (2000)) or, at least, mixes with the lagoon waters in the region close to the mouth.

Figures 5.9g and 5.9h show a southward coastal current of about 0.2 m s^{-1} where low salinity waters (28-30) are identified. The plume is slightly detached from the coast, with a thickness of about 3 m under moderate westerly winds (Figure 5.9g). When the wind intensity is stronger (6 m s^{-1}) the plume flows ($\sim$-0.2 m s^{-1}) confined to the coast with a

width and thickness of about 12 km and 6 m, respectively.

5.3.2.2 Riverine water transport

Figure 5.10 shows the time evolution of the freshwater transport over sections O (Figure 5.10a), N (Figure 5.10b), and S (Figure 5.10c), under moderate river discharge and for all wind scenarios with stronger intensities (6 m s^{-1}) (Northerly - red line; Southerly - blue line; Easterly - green line; Westerly - black line). To assess an easy comparison to the simulation without wind forcing, the results under moderate discharge in this situation are also depicted (brown line).

Results confirm the visual evaluation of the horizontal and vertical salinity fields. The offshore transport is mainly promoted by northerly winds (Figure 5.10a). The total freshwater volume transported between 1 and 10 days after peak discharge is about 18.79, 57.85, and 138.90×10^6 m^3 under low, moderate and high river discharge, respectively. (Table 5.1). Similar values are found for the simulation with moderate wind intensities. The total volume of freshwater discharged from the Douro Estuary is dispersed offshore under northerly winds, independently from their magnitude. The transport is equivalent under strong easterly wind events and without wind forcing (0.48, 5.31, and 17.53×10^6 m^3 under low, moderate, high river discharge, respectively - Table 5.1).

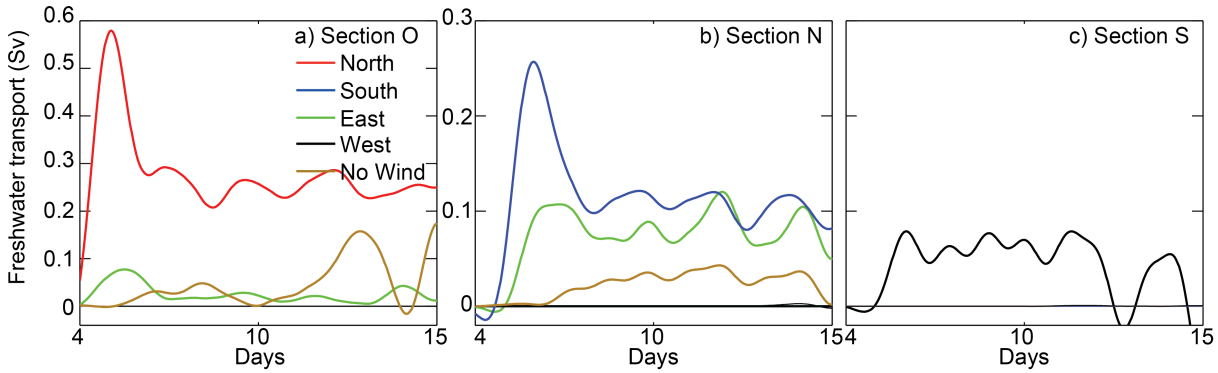

Figure 5.10: Freshwater transport in sections O (a), N (b), and S (e)(5.1) under northerly (red line), southerly (blue line), easterly (green line), and westerly winds (black line) and without wind forcing (brown line) with moderate river discharge.

Offshore transport is null under strong westerly winds in low and moderate discharge simulations and residual (0.34×10^6 m^3) for the higher case (Table 5.1). However, this trend is not observed under moderate westerly winds (Table 5.1). The wind forcing does not stop cross-shore transport promoted by the inertial processes in front of the river mouth. The freshwater is retained in the bulge, increasing the offshore transport through section O (Figure 5.7d). The competition between inertial and wind stress forces is expressed by the total volume of freshwater which is propagated offshore under low, moderate, and high river discharge. Under low and moderate river discharge the offshore transport is considerable lower (0.28 and 7.93×10^6 m^3, respectively) than in scenario without wind forcing (wind stress is efficient enough to confine the bulge near the coast). The offshore freshwater transport in the high river discharge scenario is more than the double (45.75×10^6 m^3) under moderate westerly winds (wind stress stops northward transport, but is not efficient to decrease the bulge growth)(Table 5.1).

The total volume of freshwater propagated offshore under downwelling-favourable winds is negligible and null for moderate and strong wind intensities, respectively (Figure 5.10a - Table 5.1).

Easterly, southerly and no wind scenarios are idealized cases in which the northward freshwater transport is noticeable (Figure 5.10b). Both easterly and southerly wind events increase the northward transport about 3 (15.57×10^6 m^3 for 3 m s^{-1} and 17.82×10^6 m^3 for 6 m s^{-1}) and 5 times (23.37×10^6 m^3 for 3 m s^{-1} and 26.86×10^6 m^3 for 6 m s^{-1}), respectively, in comparison to the scenario without wind forcing under moderate river discharges (5.35×10^6 m^3) (Table 5.1). In high river discharge and moderate westerly wind scenario, the total volume of freshwater flowing northward is not negligible (9.43×10^6 m^3). In this case, wind stress is not strong enough to deflect the plume southward, in the opposite direction of the Kelvin wave propagation. Northward freshwater transport in the remaining cases is small or even null (Figure 5.10b - Table 5.1).

5.3.2.3 Parameters and criteria

The key parameters calculated for each scenario summarize very well the results discussed above for all simulations (Table 5.3). The internal Rossby radius values (R_{Dh}) are very similar between each scenario, as expected. The main differences are identified when the plume is impacted by westerly winds, where the accumulation of freshwater into the coast increases the plume thickness near the mouth and, consequently, the R_{Dh} value (see Equation 5.10). The maximum (12.19 km) is found for the high river discharge scenario under strong westerly winds.

The W_P values are higher than R_{Dh} and the K_b values are above 1 in the majority of situations. Some remarkable exceptions are found under strong downwelling-favourable winds, when the plume is confined to the coast and the length scales of both coastal band and bulge are equivalent (3.82-10.46 km / 7.25-10.67 km) (Table 5.3). In this situation, the plume propagation is closer to the small-scale plume according to the classification proposed by Garvine (1995), where rotational processes have minor impact and the plume propagates only as northward coastal buoyant current.

The R_p values for all wind scenarios are similar to the case without wind forcing, indicating that rotational processes dominate within plume, especially under wind scenarios, which do not favour the northward current (northerly and westerly winds). R_p values under strong easterly winds are close to 1, showing major importance of inertial processes influenced by the higher upper layer current velocity within the plume (Table 5.3).

In the same way, E_{kP} values are consistent with Rossby numbers, showing that rotational processes dominate over friction in all scenarios, except under strong southerly wind with high river discharges ($> h_p$)(Table 5.3).

Plume Reynolds numbers, Re_p, are greater than 1 for most combinations of wind and river discharge scenarios. Higher values are found under southerly winds, when the confinement of the plume near the coast induces higher surface current velocities (Table 5.3). Under northerly wind, the plume propagations is limited near surface and the mixing by frictional processes from wind forcing increases, leading to low Re_p values.

The Fr_{1m} numbers for all wind scenarios are similar to that for the case without wind, being the westerly winds simulation the only case where the wind stress, opposed to estuarine outflow, can decrease the momentum near the mouth. However, the flow maintains supercritical under strong westerly winds at the mouth (Fr_{1p}) in higher river discharge scenario (Table 5.3). Under easterly and southerly winds this supercritical behaviour is maintained or even amplified within the plume (Fr_{1p}). In these situations, wind enhances the plume velocity, especially under downwelling-favourable winds (Table 5.3).

W_S shows how the flow in the plume under different wind and river discharge scenarios is influenced by the wind. The larger and stratified is the plume, more efficient is the control of the plume fate by wind stress. All values indicate the inertial dominance over wind stress, except for upwelling-favourable winds (Table 5.3). Due to the jet inclination under strong northerly winds, values below 1 are uncertain since W_p, which influences K_b, was calculated taking into account only the plume extension at the river mouth latitude.

5.3.2.4 General features

A summary of the influence of the wind forcing in the Douro estuarine plume propagation in the western portuguese coast is schematically depicted in Figure 5.11.

The Douro estuarine plume is confined to the coast under downwelling-favourable winds (Figure 5.11 - blue), generating a narrow and strong northward current. Southerly winds increase the meridional surface velocity and the vertical mixing. The coastal current width varies between 4 and 22 km, depending on both wind intensity and estuarine freshwater volume. Easterly winds (Figure 5.11 - green) tend to detach the plume core from the coast, stopping the water re-circulation (bulge), and creating a wider and weaker northward coastal current, in comparison with plume shape under southerly winds. The wind stress tend to thin the plume, increasing the offshore dilution and dispersion in the boarder. The region influenced by the estuarine plume under northerly winds is very large (Figure 5.11 - red), with an offshore freshwater exportation through surface layers (higher stratification). The plume propagates preferentially in southwest direction, but the angle with the river's

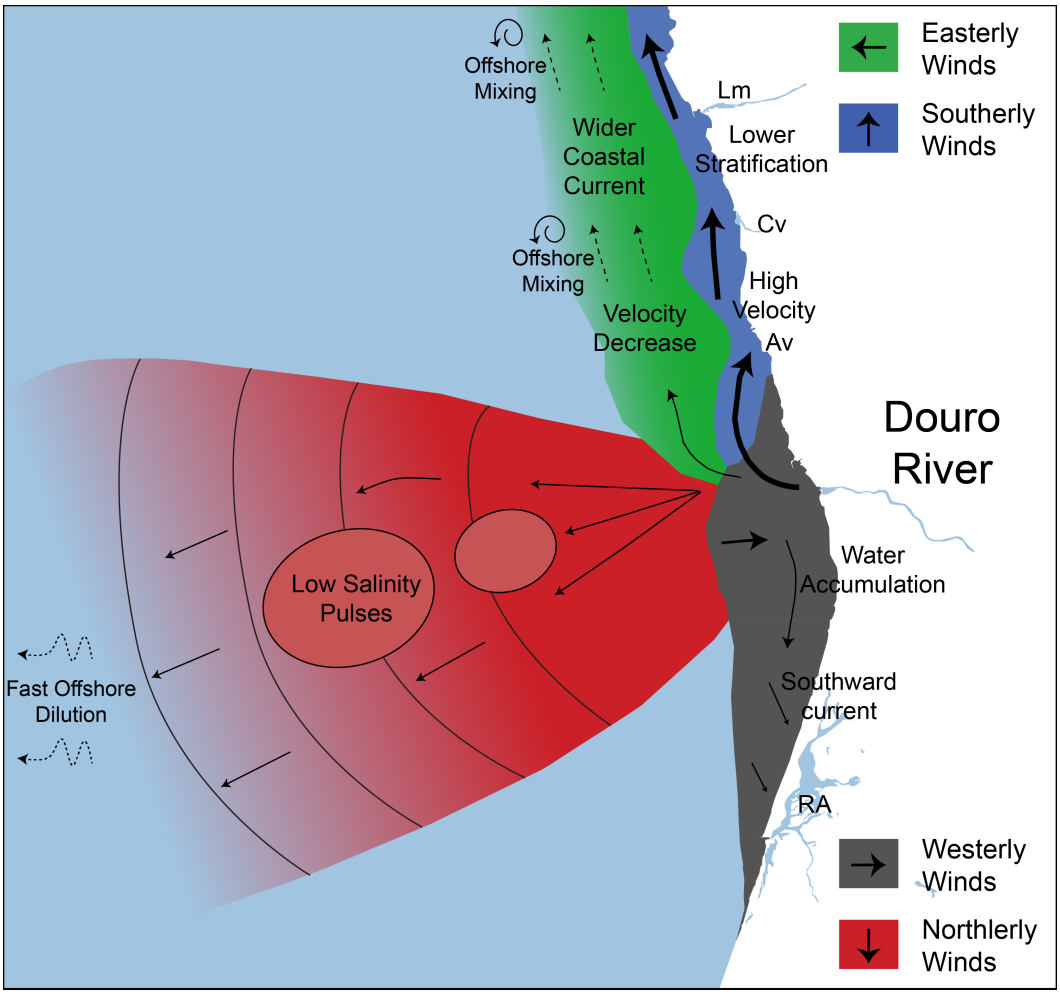

Figure 5.11: Schematic representation of the Douro estuarine plume under influence of northerly (red), southerly (dark blue), easterly (green) and westerly winds (grey). The location of secondary freshwater outflows are also marked (Lm-Lima River; Cv-Cávado River; Av - Ave River; RA - Ria de Aveiro Lagoon).

mouth latitude is strongly influenced by the competition between the wind intensity and the estuarine outflow. Isolated patches of low salinity (tidal pulses) are observed in this wind scenario. Westerly winds (Figure 5.11 - grey) force a freshwater accumulation in the near-field region, toward both north and south of the river mouth, increasing the vertical mixing and decreasing the stratification. This accumulation also generates a southward coastal current, promoting a freshwater transport until the region of influence of the Ria de Aveiro Lagoon.

5.4 Conclusion

The main objectives of this chapter were to characterize the Douro estuarine plume in terms of its dynamics, scale and fate. Several numerical experiments were conducted to test scenarios under different river discharges, wind directions and intensities.

The results obtained from this analysis suggest the following:

- Without wind forcing, the plume expands offshore, creating a re-circulating bulge (partial detached) in front of the river mouth. The low salinity waters are advected to the right due to the Coriolis force and after the establishment of the geostrophic balance, the plume water flows northward. Both validation procedure (with ADCP observations - Chapter 4) and numerical idealized scenarios demonstrated that the buoyancy generated by the Douro estuarine plume under moderate-to-high river discharges is able to generate, without wind forcing, a northward coastal current of 0.2-0.3 m s^{-1} with a width lower than 10 km.

- The Douro estuarine plume (without wind forcing) is classified as a surface-advected large-scale plume and can be characterized as a prototypal plume, comprising a near-field region (supercritical flow at the source), a tidal plume (isolated low salinity patches generated by the ebb-tidal cycle), a mid-field region (a re-circulating bulge in front of the river mouth) and a far-field region (where a coastal current is created).

- Among several river plumes with identical characteristics, the Columbia River plume seems to be that with higher similitude, despite the higher mean river discharge and different spatial scales. The Columbia River mouth is located in the same range of latitude, in an area with a relatively straight and meridional oriented coastline, with narrow shelf, and strong semi-diurnal tidal activity. Considering this fact, the possibility of the Douro estuarine plume sharing more particularities with the Columbia River plume, such as the generation of internal tidal waves (Nash and Moum, 2005; Nash et al., 2009), is a reasonable hypothesis.

- The response of the Douro estuarine plume to wind forcing takes less than 1 day, generating plume propagation main features that can be summarized as follows:

  1) Easterly winds form a similar feature to the case without wind forcing. However, the low salinity band in this case is detached from the coast and a small increase of the northward current is found.

  2) Westerly winds tend to accumulate freshwater into the coast. A southward coastal current is identified with strong winds and moderate and high river discharge. This is the only wind scenario where the Douro estuarine plume may reach the Ria de Aveiro Lagoon.

  3) Northerly winds generates an offshore extension of the plume with an inclination towards southwest. The stratification increases in this case and isolated low salinity bands propagating offshore were detected in the numerical results.

  4) Southerly winds confine the plume to the coast, enhancing the northward current velocity.

- Combined with moderate-to-high river discharge, downwelling-favourable winds forcing increases the possibility of the Douro estuarine plume to merge with estuarine sources located north of the Douro Estuary mouth, such as Minho estuarine plume. In addition, the combined effect of these plumes can affect the dynamics of the Rias Baixas, located $\sim$100 km north of the Douro River mouth. This possibility will be addressed and analysed in the following Chapter.

Chapter 6

Interaction between the Douro and Minho estuarine plumes under winter conditions

6.1 Introduction

Previous Chapters reveal that Douro estuarine plume can propagate far from its source and that wind regime plays a crucial role in the definition of the plume fate.

Southerly wind regimes, generally associated with rainfall episodes, which mostly occur during the fall and winter seasons (Trigo and DaCamara, 2000; Lorenzo et al., 2008), tend to confine the Douro estuarine plume against coast, feeding a northward buoyant coastal current. In this case, the probability of that Douro riverine water interacts with Minho estuarine plume increases as well as the possibility to influence the Rias Baixas circulation.

Taking advantage of available *in situ* data, the dynamics of the Minho river plume and its influence on the Rias Baixas was analysed by Sousa et al. (2014c,b,a) during an upwelling-downwelling event in May 1998 . These authors found that the plume responds rapidly to wind variations, being both wind and river discharge the most important forcings

that influence its size and shape in coastal waters. They emphasized that the Minho river plume may reverse the normal circulation and the vertical density structure inside the Rias Baixas and that downwelling-favourable winds are crucial for this occurrence (Sousa et al., 2014c).

Recently, Sousa et al. (2014a) reviewed the event of May 1998 in more detail, confirming the importance of the Minho plume in the circulation inversion inside the Rias de Vigo and Pontevedra. This work revealed the significant influence that the mouth morphology of the Rias has on this process and the lesser effect of rivers discharging into this system. None of these numerical modelling studies included the Douro estuarine outflow in their simulations, given its low discharge compared to the Minho during the period under analysis. Although the Douro River outflow is located approximately 80 km south of the Minho River mouth, its influence on the Galician coast should be taken into account under certain circumstances, as it represents the most important freshwater input in this region. One of the most evident examples of this influence was the February/March 2001 event, when a maximum Douro River mean daily discharge of over 8000 m^3 s^{-1} was observed.

The winter event of 2010 was choosed to study the interaction between Douro and Minho estuarine plumes and by two main reasons: 1- wind patterns are typical of winter conditions and comparable to those of the May 1998 event studied by Sousa et al. (2014c,b,a): upwelling-favourable winds are followed by strong southerly winds. This situation favours the influence of external sources of lower surface saline waters on Rias Baixas circulation, in this case from both the Minho and Douro plumes; 2 - Unlike May 1998, the two major rivers have discharges close to their winter averages and consequently with exceptional conditions to detect the plumes propagation through satellite imagery.

Otero et al. (2013) presented a full description of shelf circulation and WIBP behaviour during winter 2009/2010. However, they focused on the period of extreme discharges of this winter (from December 2009 to January 2010), when the Douro and Minho peak discharges were 3-4 times higher than the typical winter values. As dam regulation can generate substantial differences in the river runoff over a typical winter, there is a good reason to find out more about the role of each river and its direct and indirect impact on the WIBP

and shelf circulation under such conditions.

The main goal of this Chapter is to perform an integrated analysis of the dispersion of the Douro and Minho estuarine plumes and assess their individual influence on the already well-studied WIBP behaviour during the 2010 winter (typical winter conditions). The description of this event was based on numerical modelling and remote sensing imagery. Moreover, two additional scenarios were simulated under hypothetical conditions: turning off each one of the estuary discharges for each case. Thus, the relative importance of each plume in WIBP circulation and its direct/indirect influence on Rias Baixas circulation is studied and compared with the results of Sousa et al. (2014c,b,a). Lagrangian floating particles were also released at the estuary mouths of the Minho and Douro Rivers, to assess the main differences in particle trajectories and the water exchange with the Rias Baixas. It is also worth noting that, although the estuarine mouths are close to each other, the river basins are mainly located in quite different regions and are strongly regulated by dams. Although the seasonal variations are identical, substantial differences are often found in the daily volumes of freshwater. Thus, a study of these hypothetical scenarios would be an essential part of any accurate analysis of the influence of Douro and Minho Rivers on circulation patterns on the shelf and Rias Baixas.

This Chapter is organized as follows. The description of the study area is presented in Section 6.2. A general overview of data, plume parameters, numerical model and numerical experimental design is given in Section 6.3. The results and the discussion are presented in Section 6.4. Finally, the main conclusions are drawn in Section 6.5.

6.2 Study area

The study area is the northwestern coast of the Iberian Peninsula, the region mainly affected by the WIBP propagation (Figure 6.1). This region includes four coastal systems (Rias de Vigo, Pontevedra, Arousa and Muros) called Rias Baixas and the estuaries of the major rivers flowing off this coast (Minho and Douro) further south (Figure 6.1). This area is located on the northernmost limit of the Eastern North Atlantic Upwelling System

Figure 6.1: Study Area with the three model domains (L1, L2, and L3). Cross-sections (I, II, III, IV, and V) are marked with black lines. Stars indicate river runoff stations location. The wind data station is marked with a black triangle.

(Wooster et al., 1976), where alongshore winds interact with coastal topography to generate upwelling-downwelling processes. The river plumes propagation, mostly from the Douro and Minho estuaries, dominates surface layer dynamics.

The Douro River is the most important freshwater contributor to the Atlantic Ocean in the study region and more information about its characteristics and properties can be

found in Section 1.3.1 (Chapter 1).

The Minho River outflow is located ∼80 km north of the Douro and flows southwestward from the interior of Galicia until it reaches the Atlantic Ocean, at the northern border between Portugal and Spain. The river has a length of 300 km with a catchment area of 17080 km^2. The annual average discharge is 405 m^3 s^{-1} (Table 6.1) and the monthly average discharge oscillates between 100 m^3 s^{-1} in August and 800 m^3 s^{-1} in February (Río-Barja and Rodriguez-Lestegás, 1992). More than 50 dams, mainly for power generation, control the river flow. The Frieira dam, situated 80 km from the mouth and with a capacity of 44 Hm^3, is the main artificial barrier before the estuary. The estuary presents a semidiurnal, high-mesotidal regime and the range of the astronomical tide varies between 2 m and 4 m during neap and spring tides, respectively (IH, 2006; Sousa et al., 2013).

There are three other freshwater sources between the Douro and Minho estuaries, all with insignificant freshwater discharges: Ave, Cávado, and Lima Rivers (Figure 6.1, Table

Table 6.1: Mean discharges of major rivers in the region under scope. $^{(a)}$ data from `http://www.ospar.org`. $^{(b)}$ data from Río-Barja and Rodriguez-Lestegás (1992).

	Mean River Flow (m^3 s^{-1})
Tambre $^{(b)}$	51.3
Ulla $^{(b)}$	64.5
Umia $^{(b)}$	9.0
Lérez $^{(b)}$	14.4
Verdugo $^{(b)}$	10.6
Minho $^{(a)}$	405
Lima $^{(a)}$	92
Cávado $^{(a)}$	73
Ave $^{(a)}$	32
Douro $^{(a)}$	708

6.1).

The Rias Baixas are four flooded tectonic valleys (from south to north: Ria de Vigo, Ria de Pontevedra, Ria de Arousa, and Ria de Muros) located 30 km north of the mouth of the Minho River (Figure 6.1). They behave as partially mixed estuaries, with a two-layered residual circulation pattern, with water flowing seaward through the upper layers and landward through the lower ones (Álvarez et al., 2006; deCastro et al., 2006; Sousa et al., 2014c). This particular type of circulation is enhanced by coastal upwelling (Fraga, 1981), which introduces colder and nutrient-rich water into the estuaries (Wooster et al., 1976; Fiúza et al., 1998). Freshwater contributions come from rivers that are relatively small, compared to the Douro and Minho Rivers: Verdugo River at the head of the Ria de Vigo, Lérez River at the Ria de Pontevedra, Umia and Ulla Rivers at the Ria de Arousa and Tambre at the Ria de Muros (Figure 6.1, Table 6.1).

6.3 Data and methods

6.3.1 Data

Wind data, provided by the NCEP CFSR (`http://rda.ucar.edu/pub/cfsr.html`) at a control station located near the mouth of the Minho River (9.0°W; 42.0°N – Figure 6.1), with a temporal resolution of 6 h was used to characterize the wind speed over the study area. During the simulation period, the wind was characterized by two interchanging patterns: downwelling (until 25 January and from 1 to 10 February) and upwelling (from 25 January to 1 February and after 10 February) favourable winds (Figure 6.2a). 6-hourly averaged winds range between 3 and 6 m s^{-1}, reaching peaks of 6 m s^{-1}. This intensity range is representative of the prevailing wind regime for this region (Sousa et al., 2014b).

The daily discharge for the Minho River was provided by the Confederación Hidrográfica del Miño-Sil, while daily mean Douro River outflow data were obtained from the SNIRH database (`www.snirh.pt`) at the Crestuma dam. Both rivers present coincident patterns over this winter (Figure 6.2b). In general, the Minho freshwater input

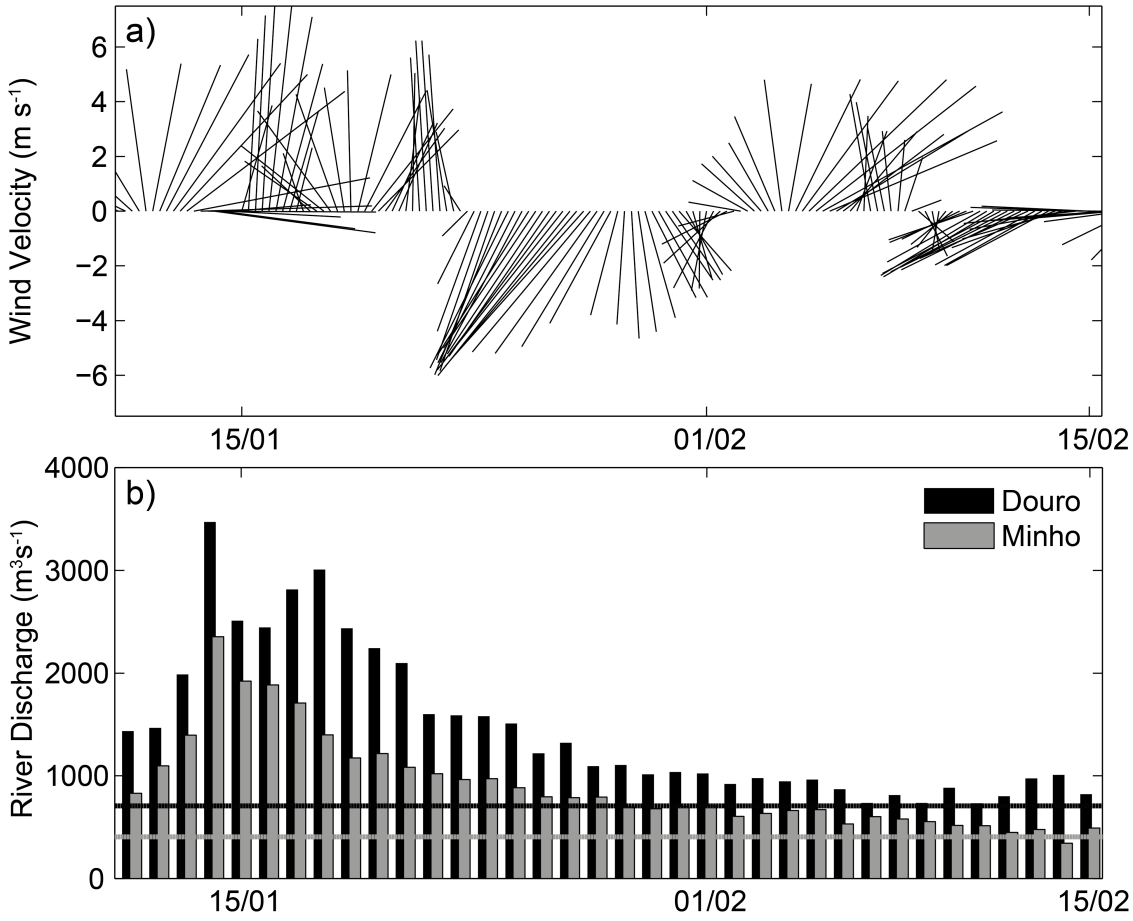

Figure 6.2: (a) Wind pattern (m s^{-1}) and (b) Minho and Douro rivers discharges (m^3 s^{-1}) over the period under study (January/February 2010). Black and grey lines represent the climatological river discharge trend.

is two thirds that of the Douro River. During the first southerly wind period, there is a high discharge peak (Douro: $>$ 3000 m^3 s^{-1}; Minho: $>$ 2000 m^3 s^{-1}), and after that a slow decrease down to the winter averages - Douro: 1000 m^3 s^{-1} (Chapter 2); Minho: 700 m^3 s^{-1} (Sousa et al., 2014b).

Estimations from Otero et al. (2010) show that the rivers discharge at an approximately constant rate into the Rias Baixas during the winter period, with values significantly lower than those from the Minho and Douro discharges. The Ulla River discharge is about 150 m^3 s^{-1} and the Lérez, Umia and Verdugo rivers discharges are about 50 m^3 s^{-1}.

The period of January/February 2010 can be considered representative of local winter

conditions for two main reasons: Wind patterns are typical of winter conditions and the two major rivers have discharges similar to their winter averages (Figure 6.2b), in particular in the event ending.

6.3.2 Plume parameters

River plumes are characterized and classified based on parameters and criteria that are determined or applied in this chapter.

The bulk Kelvin number, K_b (Equation 5.9), the internal Rossby radius, R_{Dh} (Equation 5.10), the outflow Rossby number, R_i (Equation 5.4), the plume Rossby number, R_p (Equation 5.11), the plume Ekman number, E_{kp} (Equation 5.13), the upper-layer Froude numbers at the mouth and within plume, Fr_1 (Equation 5.14), the Kelvin mouth number, K_m (Equation 5.12), and the Reynolds number Re_p (Equation 5.15) are calculated for the Douro and Minho estuarine plumes.

In addition, the Richardson number is computed (Tilburg et al., 2011), for the purpose of comparing mixing and stratification:

$$Rich = \frac{g' \Delta z}{(\Delta u_c)^2} \tag{6.1}$$

where Δu_c is the absolute difference between velocities at two different depths (Δz). An $Rich$ lower than 0.25 commonly indicates that the kinetic energy of the flow can nullify the vertical stratification by mixing the plume (Smyth and Moum, 2000; Sanders and Garvine, 2001).

6.3.3 Model

The hydrodynamic model MOHID (`www.mohid.com`) had been previously implemented and validated by Sousa et al. (2014c,b) for the area under research. The implementation consists in the Configuration #1 described in Section 4.4 (Figure 6.1).

Freshwater inputs from the Rias Baixas, Minho and Douro estuarine outflows are

considered landward boundary conditions in the L3 domain (Figure 6.1). Small rivers that flow into the Rias Baixas, are considered inputs in the Rias de Arousa, Pontevedra and Vigo in the L3 domain. Sousa et al. (2014b) showed that the influence of the Minho estuarine plume on the Ria de Muros is insignificant and may only be relevant in extreme cases of river discharges and northward wind intensity. The Minho and Douro outflows had been computed previously, using estuarine models developed for the inner part of each estuary (Mendes et al., 2013; Sousa et al., 2014c) as it was described in Sections 4.3.2.2 and 4.3.2.1, respectively. Both outflows are then imposed offline in the coastal model. The Ave, Cávado and Lima Rivers are not considered in this study, due to their small river flow, which is considered irrelevant for the purposes of coastal circulation (Table 6.1).

A particle-tracking model was coupled to the L3 domain in order to evaluate the trajectories of passive tracers. This module is described in Section 4.2.2.

The model was run from July 2009 to February 2010 (the first six-months were a spin-up period), with the aim of covering a typical winter event, from January to February 2010.

6.3.4 Numerical experimental design

The interaction between the Minho and Douro estuarine plumes is assessed by performing simulations under three scenarios. In the first scenario, the real conditions corresponding to the period under analysis are simulated, including both the Minho and Douro River discharges (called the reference scenario, hereafter). In the second simulation, only the Minho River discharge is considered for the whole simulation (called the Minho scenario, hereafter). In the third scenario, only the Douro freshwater input is considered (called the Douro scenario, hereafter). All scenarios take into account the small rivers input in the Rias Baixas.

The results from the reference scenario simulations were first analysed and compared with ocean-colour imagery. The salinity and equivalent depth of freshwater fields were computed, following the procedure of Sousa et al. (2014b), and qualitatively compared with

$nLw555$ from MODIS sensor on both the Aqua and Terra satellites (Chapter 2). Average daily images during upwelling and downwelling-favourable wind conditions were obtained.

The equivalent depth of freshwater is calculated by Equation 5.1.

The interaction between the two estuarine plumes and the water exchange with the Rias Baixas was assessed following continuously released passive particles (simulation time step - 15 s) at the Minho and Douro River mouths. Particles release began on 1^{st} and ended on 10^{th} of February, 2010. The location of these particles was recorded half-hourly over 10 days of downwelling-favourable winds. Maps of the spatial density of the particles were calculated during the Lagrangian simulations, as a way of studying the dispersion of both plumes. Thus, the number of particles in each cell is summed, to represent the fate of the plumes. The longitudinal maximum for particle densities was also computed at each latitude step from the river mouths to Ria de Arousa, under each scenario, in order to define the main plume trajectories.

The offshore dispersion of the Minho plume for the reference and Minho scenarios was evaluated through of the ratio between the number of particles and the number of grid cells calculated under both scenarios. This procedure allows the analysis of the influence of both plumes on the generation of small-scale eddies in the coastal region between the Minho River mouth and the Ria de Arousa entrance. The generation of eddies was tracked using the Okubo-Weiss method (Okubo, 1970; Weiss, 1991). This method provides information about the relative dominance of strain and vorticity. Eddies are defined as regions of concentrated vorticity, where there is a dominance of vorticity over strain. The Okubo-Weiss parameter, OW, is defined as:

$$OW = s_n^2 + s_s^2 \omega_r^2 \tag{6.2}$$

where s_n and s_s are the normal and shear components of strain and ω_r is the relative

vorticity:

$$s_n = \frac{\partial u}{\partial x} - \frac{\partial v}{\partial y}$$

$$s_s = \frac{\partial v}{\partial x} + \frac{\partial u}{\partial y} \tag{6.3}$$

$$\omega_r = \frac{\partial v}{\partial x} - \frac{\partial u}{\partial y}$$

The Okubo–Weiss parameter serves as a basis for defining a vortex identification criterion for a region with negative OW. This work followed the Isern-Fontanet et al. (2006) and Chang and Oey (2014) conditions to define the vortex region. OW needs to be smaller than a threshold, $OW_0 = 0.2\sigma_{OW}$, where σ_{OW} is the spatial standard deviation of OW. Although the Okubo-Weiss parameter has been widely used to analyse numerical simulations (Elhmaïdi et al., 1993; Mcwilliams, 1984, among others), the validity of the criterion may be inaccurate (Basdevant and Philipovitch, 1994). However, it is still valid to characterize vortex core regions or saddle points (Isern-Fontanet et al., 2006).

The freshwater transport was evaluated in several sections (Figure 6.1) to identify the temporal and spatial variability of freshwater transport and to study plume interaction. The freshwater transport, relative to the reference salinity, S_a, is defined by Equation 5.2.

6.4 Results and discussion

6.4.1 Reference scenario on winter 2010

The behaviour of the Douro and Minho estuarine plumes is shown in Figure 6.3 under upwelling (upper panel) and downwelling (lower panel) favourable winds.

The salinity and equivalent depth of freshwater snapshots at 1 pm on February 1^{st} (end of northerly winds period, Figure 6.2a) show an offshore dispersion of both plumes in a southwestern direction (Figure 6.3a and 6.3b). There is a typical bulge around the mouth of

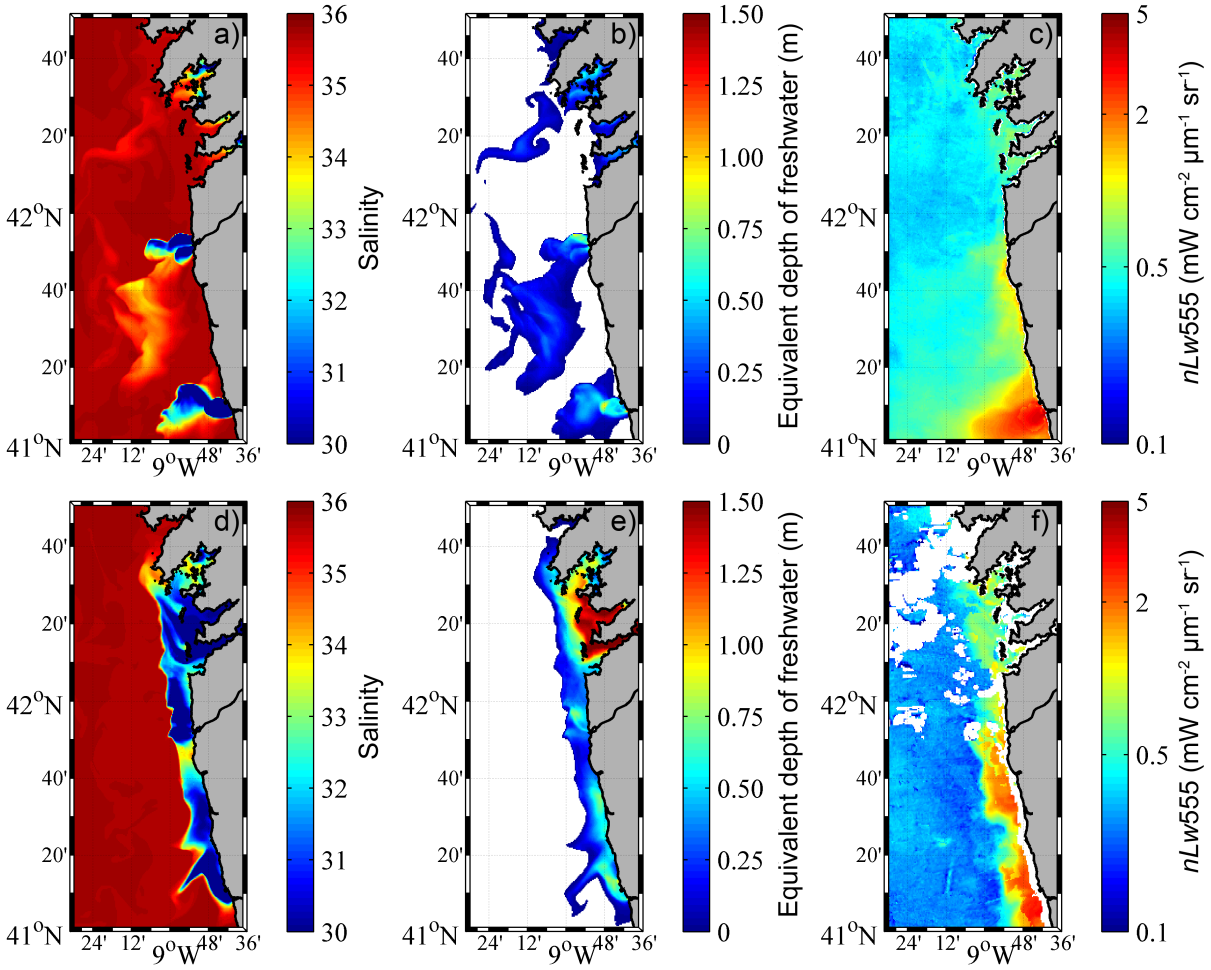

Figure 6.3: Model snapshots of salinity and equivalent depth of freshwater (m) on February 1 (a and b, respectively) and on February 9 (d and e, respectively). Average $nLw555$ (mW cm^{-2} μ m^{-1}sr^{-1}) from MODIS observations during upwelling (25/1 – 01/02) (c) and downwelling-favourable winds (01/02 – 10/02) (f).

each estuary (Otero et al., 2013; Mendes et al., 2014). This offshore expansion leads to higher stratification and mixing/dilution (Lentz, 2004; Lentz and Largier, 2006), which decreases the probability of any interaction between the plumes. The fast dilution of the freshwater from the Minho River prevents a more explicit contact between the two plumes. Thus, direct interaction is extremely unlikely during upwelling events. During the downwelling period, there is a confinement of both plumes against the coast, creating a continuous along-shore freshwater feature ∼10 km wide (Figure 6.3d and 6.3e). Stratification decreases compared with the upwelling event and both plumes tend to be aligned northward, in a

coherent structure with surface velocities of about 1 m s^{-1}, in line with the results obtained by Otero et al. (2013) and observed in previous Chapter. The salinity and equivalent depth of freshwater snapshots at the end of the downwelling event show an accumulation of freshwater against the coast. Since the discharges from small rivers are almost constant over time, the Douro and Minho plume intrusion in the Rias de Vigo, Pontevedra, and Arousa was unequivocal in this situation (Figure 6.3e). As expected, the plume influence on the Ria de Muros is very small, when compared with the southern Rias. This concurs with Sousa et al. (2014c).

MODIS turbid composites show similar patterns during the offshore expansion and confinement of both plumes (Figure 6.3c and 6.3f). Both composites attest the ability of this model configuration to simulate river plume features (length and width) and variability.

Values for several parameters that describe general plume characteristics were calculated for the Minho and Douro Rivers (Garvine, 1995; Tilburg et al., 2011; Horner-Devine et al., 2015) for all scenarios during upwelling and downwelling periods (Table 6.2).

The results for the Douro scenario (not shown) are similar to the reference scenario. For the other scenarios, the Douro and Minho River plumes share some characteristics; however, they also show some differences.

The Douro plume width, W_p, is about twice that of the Minho for downwelling periods and that difference is lower under upwelling events (Table 6.2). On the other hand, the Rossby radius of deformation, R_{Dh}, is similar for both plumes, but higher for Minho River ($\sim$1/6 of distance between Minho and Douro River mouths). In the majority of situations of upwelling-favourable winds, when R_{Dh} is smaller than W_p , the K_b is above or near 1, indicating an important influence of rotational processes . Under downwelling winds, when the plume is confined to the coast, inertial processes are more important ($K_b < 1$; $R_{Dh} > W_p$). Low values for the Kelvin mouth parameter, K_m, suggest that regions near the river mouths are more affected by inertial than by rotational processes and, as both mouth widths are narrow comparing with each internal Rossby radius, river discharges are likely to form a bulge, even under northward winds (Garvine, 1995; Huq, 2009; Horner-Devine

Table 6.2: Key parameters of the Minho (Minho and Reference scenarios) and Douro estuarine plumes (Reference scenario) under upwelling and downwelling-favourable winds.

	Minho plume Minho Scenario		Minho plume Reference Scenario		Douro plume Reference Scenario	
	Upwelling	Downwelling	Upwelling	Downwelling	Upwelling	Downwelling
R_{Dh} (km)	8.82	16.40	12.55	16.67	9.45	12.82
W_p (km)	10.25	3.84	10.05	3.43	16.45	7.56
K_b	1.16	0.23	0.80	0.21	1.74	0.59
K_m	0.06	0.03	0.04	0.03	0.05	0.04
R_p	0.57	0.32	0.41	0.36	0.52	0.42
R_i	2.08	1.74	2.08	1.74	3.69	2.76
E_{kp}	0.20	0.02	0.06	0.01	0.15	0.05
Re_p	3.50	25.78	10.21	30.83	3.26	8.39
Fr_{1p}	1.11	0.54	0.82	0.50	0.82	0.58
Fr_{1m}	0.94	0.43	0.66	0.43	1.05	0.64

et al., 2015).

Froude numbers within the plumes, Fr_{1p}, and at the estuary mouths, Fr_{1m}, show that stratification is more important than inertial processes, except for the Minho estuarine plume in the Minho scenario (Table 6.2). Fr_{1p} is always larger than Fr_{1m} for all situations in Minho plume, showing that the near-field region is larger than $W_p/2$ for this estuarine plume (Hetland, 2005; Horner-Devine et al., 2015).

The outflow Rossby values (R_i) indicate that inertial processes dominate at the mouth of the estuaries in line with K_m results (Table 6.2). Rotational influence within plume is evident for both rivers in all cases, R_p. This is also consistent with the values for the Ekman number, ($E_{kp} \ll 1$), where rotational processes also dominate over frictional ones, even during upwelling periods. Plume Reynolds numbers, Re_p, are greater than 1 for all situations, indicating that inertial processes are more important than frictional

mixing-related processes within the plume (Table 6.2). However, the results show that this dominance is more evident during downwelling periods. Frictional processes tend to be more relevant under northerly winds, when the plume is thinner.

Differences between the values found in the Minho and reference scenarios show the significant influence that the Douro discharge can have on the Minho plume. However, the increase of freshwater in the Minho region, from the Douro River, does not change the Minho plume average width during upwelling or downwelling periods where a slightly decrease is found (10.25-10.05 km and 3.84-3.43 km, respectively, Table 6.2).

6.4.2 Interaction between the Douro and Minho estuarine plumes under southerly winds

The interaction between the Douro and Minho estuarine plumes, and their consequent intrusion in the Rias Baixas, is enhanced during downwelling-favourable winds. Thus, the Lagrangian model was set from 1^{st} to 10^{th} February, when the discharges from both rivers are close to the climatological winter average.

For the comparison between the Reference scenario and the Douro scenario, particles are released at the Douro river mouth. The Minho River plume dynamic is taken into account in the reference scenario, but not in the Douro scenario (the Minho River is *switched off*). No particles are released at the Minho river mouth in any of these scenarios. Similarly, in the comparison between the reference scenario and the Minho scenario, particles are released at the Minho river mouth and the Douro River dynamic is taken into account in the reference scenario, but not in the Minho one (the Douro River is *switched off*). In this case, no particles are released at the Douro river mouth, in any of those scenarios. The spatial particle density during the Lagrangian simulations for the Douro and Minho rivers is depicted in Figures 6.4 and 6.5, respectively. In general, concerning the release of particles at the Douro estuary mouth, the Douro (Figure 6.4a) and reference (Figure 6.4b) scenarios do not show great differences regarding the release of particles at the Douro estuary mouth. In both simulations, the particles tend to turn right after the release point

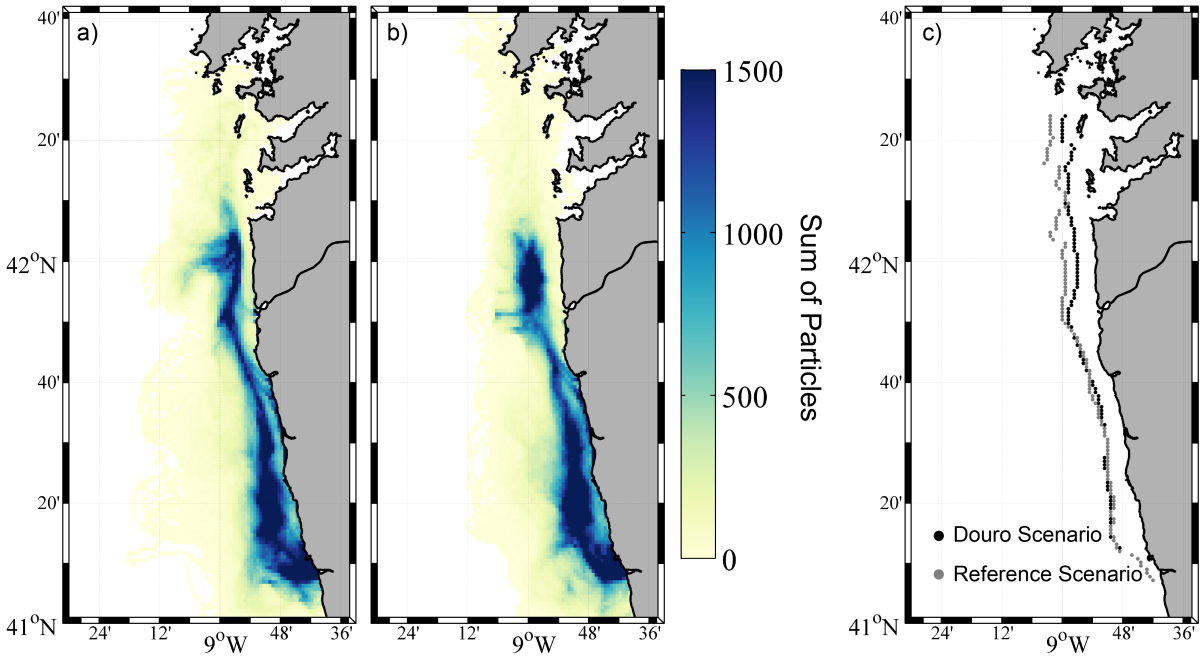

Figure 6.4: Sum of Lagrangian particles released from Douro River mouth over the downwelling period (01/02 – 10/02) for the Douro (a) and the Reference (b) scenario. Main trajectories for two scenarios (c).

and then continue northward, maintaining their distance from the coast.

After the Minho River mouth, there are some changes in the main trajectories (Figure 6.4c). Though particles in the Douro scenario follow a preferential pathway closer to the coastline, their offshore dispersion seems to be larger and with more branches in that direction (Figure 6.4c, black points). Considering the small number of particles in the Rias Baixas region, plume intrusion remains unclear.

Under the Minho (Figure 6.5a) and reference (Figure 6.5b) scenarios, there are major differences in the density map for the particles released at the Minho River mouth. In the Minho scenario, particles near the Minho River mouth are aligned with the plume jet toward the southwest (Figure 6.5a). In the reference scenario (Figure 6.5b), the buoyant coastal current produced by the Douro estuarine plume limits the Minho plume expansion in that direction, pushing more particles northwards.

In two-river systems, like the Douro-Minho, the coastal current due to the upstream river flow (Douro) acts like a variable ambient current to the downstream plume (Minho)

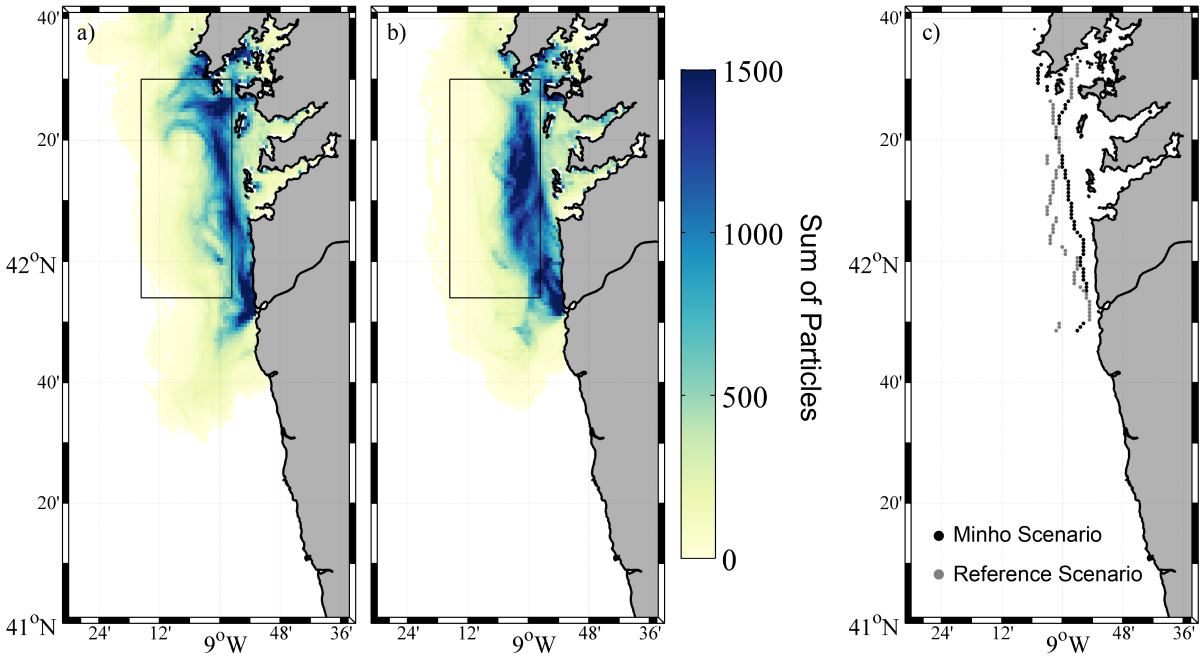

Figure 6.5: Sum of Lagrangian particles released from Minho River mouth over the downwelling period (01/02 – 10/02) for the Minho (a) and the Reference (b) scenario. Main trajectories for two scenarios (c). The offshore eddies generation (Okubo-Weiss parameter) is calculated for the area represented by the black rectangle (a,b).

(Yuan et al., 2011). Moreover, in the presence of an alongshore ambient current, Fong and Geyer (2002) demonstrated that bulge growth, from the freshwater source (here the Minho River), ceases. Similarly, when particles are released at the Douro River, there is a smaller dispersion of particles offshore in the reference scenario (Figure 6.5a and 6.5b). The main trajectory of particles is closer to the coast in the Minho scenario (Figure 6.5c, black points).

Regarding the dispersion of particles over the shelf and in the Rias Baixas, a higher number of branches and a larger dispersion in the offshore direction are evident in the Minho scenario (Figure 6.5a). On the other hand, the reference scenario (Figure 6.5b) shows a greater concentration of particles in a smaller area. This is an interesting feature of this particular region, and is similar to the patterns obtained in laboratory experiments by Yuan et al. (2011). They observed that the upstream plume (here the Douro plume) wrapped the downstream plume (here the Minho plume) to form a large re-circulating bulge

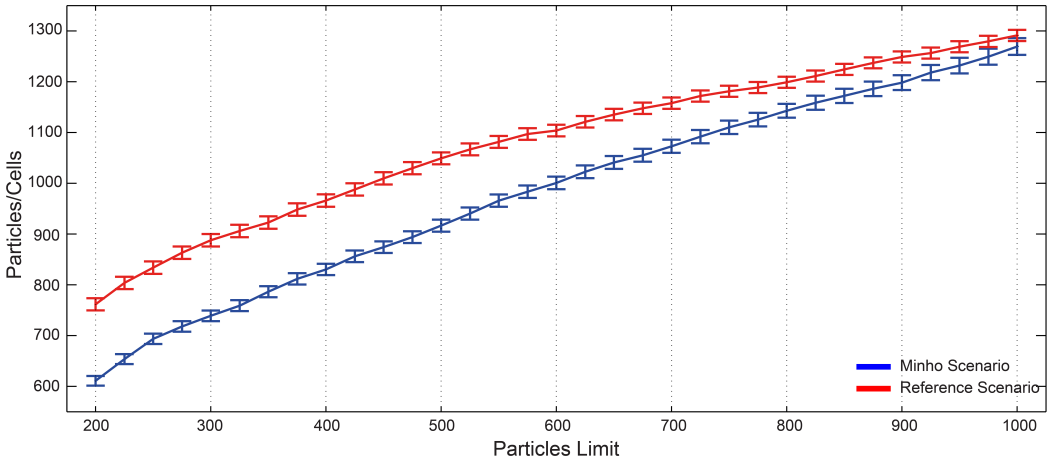

Figure 6.6: Number of particles per cell for the reference scenario (red line) and the Minho scenario (blue line). Error bars represent the standard deviation divided by the square root of the total number of particles.

system. Such plume *wrapping* can be identified by the difference between the main particle trajectories in the Douro and Minho scenarios and in the reference scenario (Figures 6.4 and 6.5). The bulge re-circulation enhancement could cause the high density of particles in the Minho-Rias Baixas region in the reference scenario. To confirm this visual analysis, the ratio of particles per cell for the reference and Minho scenarios was calculated (Figure 6.6). Various thresholds for the minimum number of particles in each cell (particle limit, Figure 6.6) were considered, in order to determine if both scenario trends remain the same in higher particle density regions (larger particle threshold). In the reference scenario, more particles per cell were found than in the Minho scenario (Figure 6.6). This result indicates that particles from the Minho River cover a large area in the latter scenario than in the reference scenario, even in areas greatly influenced by the Minho discharge (larger particle limit).

6.4.3 Douro estuarine plume effect on freshwater fate and on the generation of small-scale instabilities

The offshore freshwater export, over the shelf, from the low-salinity band, will be different in the regions marked in Figure 6.5a and 6.5b with a rectangle. The Okubo-Weiss

parameter, OW, was calculated for the reference and Minho scenarios, to evaluate the dispersion of plume and the generation of eddies. The sum of grid points, A_{eddy}, was analysed where the condition for a vortex creation is fulfilled: $OW \leq OW_0$ (Isern-Fontanet et al., 2006; Chang and Oey, 2014).

Figure 6.7a shows A_{eddy} time series for simulations under both scenarios. Time series were also compared with hourly meridional wind component in the coastal region (Figure 6.7b) and Minho and Douro rivers discharges (Figure 6.7c). Figure 6.7b shows a clear relation between wind pattern and the generation of small-scale eddies. On the other hand, changes in river input seem to be irrelevant for the generation of instabilities over the shelf (Figure 6.7c).

The A_{eddy} is higher after the change of wind from downwelling to upwelling (moment 1 and 3) and smaller under downwelling-favourable winds. During southerly winds, the

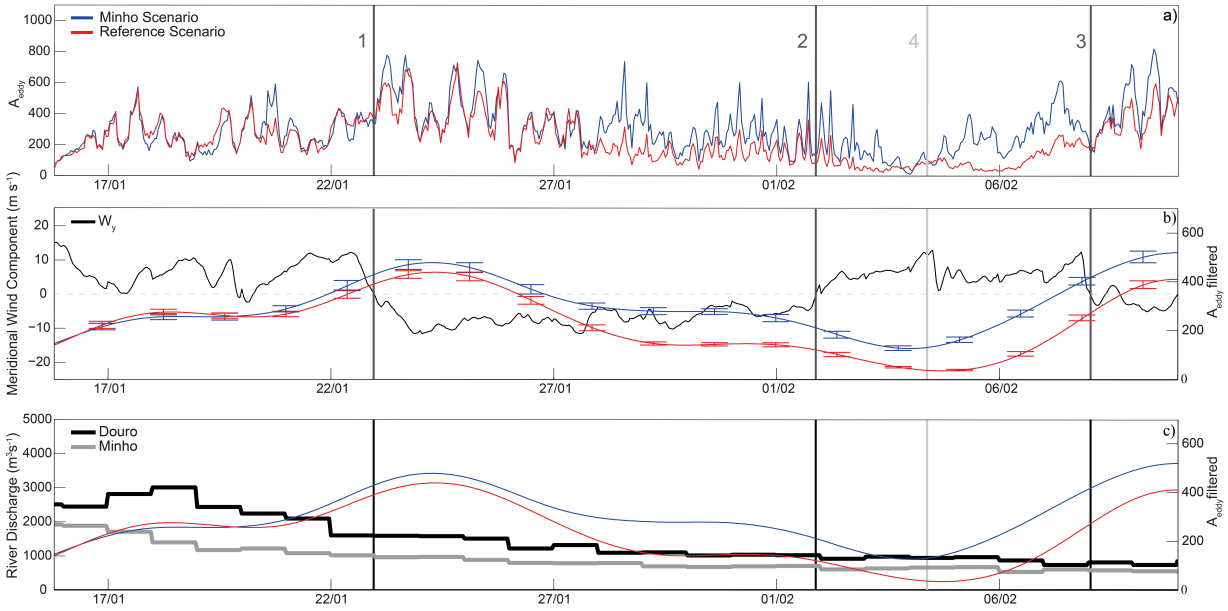

Figure 6.7: (a) A_{eddy} where $OW < 0.2\sigma_{OW}$ for Reference (red) and Minho (blue) scenarios. (b) Hourly meridional wind component near coast off Douro and Minho rivers and (c) daily freshwater inflow of Minho and Douro rivers. Red (Reference) and blue (Minho) lines in figures (b) and (c) represents the A_{eddy} filtered with a 132-h low pass. Vertical lines 1, 2, and 3 represent upwelling/downwelling wind favourable transitions and line 4 represents the instant when Douro river plume reaches the Minho River coastal area. Error bars represent the A_{eddy} standard deviation divided by the square root of A_{eddy} size.

freshwater is retained in a less stratified band attached to the coast and, when wind direction reverses, the riverine water tends to expand offshore (Hetland, 2005; Lentz and Largier, 2006), creating instabilities when the plume front collides with ocean waters. The decreasing trend of A_{eddy} is not greatly altered when the wind reverses from northerly (upwelling-favourable) to southerly (downwelling-favourable) (moment 2). This shows that the plume transition from a very stratified and expanded structure over the shelf (upwelling) to a vertical mixed and confined coastal band (downwelling) is not the cause of more small-scale instabilities. The behaviour of the Mississippi-Atchafalaya plume in the numerical simulations of Marta-Almeida et al. (2013) presents some similarities. These authors also noticed that, during upwelling winds, the river plume front is more susceptible to instabilities than under downwelling winds. Considering the difference in A_{eddy} in the reference and Minho scenarios from moment 2 to 3, the plume behaviour is related to the generation of small-scale eddies. More small-scale eddies were generated under the Minho than under the reference scenario (coherent with Figure 6.5, black box). During a constant wind regime, the differences in the buoyant coastal feature caused by the influence of the Douro plume (line 4, Figure 6.7) is sufficient to generate more small-scale eddies over the shelf and, consequently to favour effective freshwater exportation and the offshore entrainment of the plume, as low salinity bands.

Thus, in order to analyse the Douro effect on the Minho plume, the temporal evolution of the Richardson number (Figure 6.8a) was calculated at ∼5 m depth in a region near the coast (Figure 6.1, section IV). After 4^{th} of February, when the Douro plume reached the Minho region, the Richardson number is smaller in the reference scenario than in the Minho scenario. Although values are over 0.25 in both scenarios, indicating that the flow cannot overturn the vertical stratification, the influence of freshwater from the Douro River plays an important role in increasing the vertical mixing in this region. This is clear in the snapshots of vertical salinity structure along section IV (Figure 6.8b and 6.8c). In the reference scenario, vertical salinity fields show the influence of freshwater until ∼20 m, especially close to the coast (Figure 6.8b). On the other hand, in the Minho scenario (Figure 6.8c), the plume is restricted to the first 5-8 m.

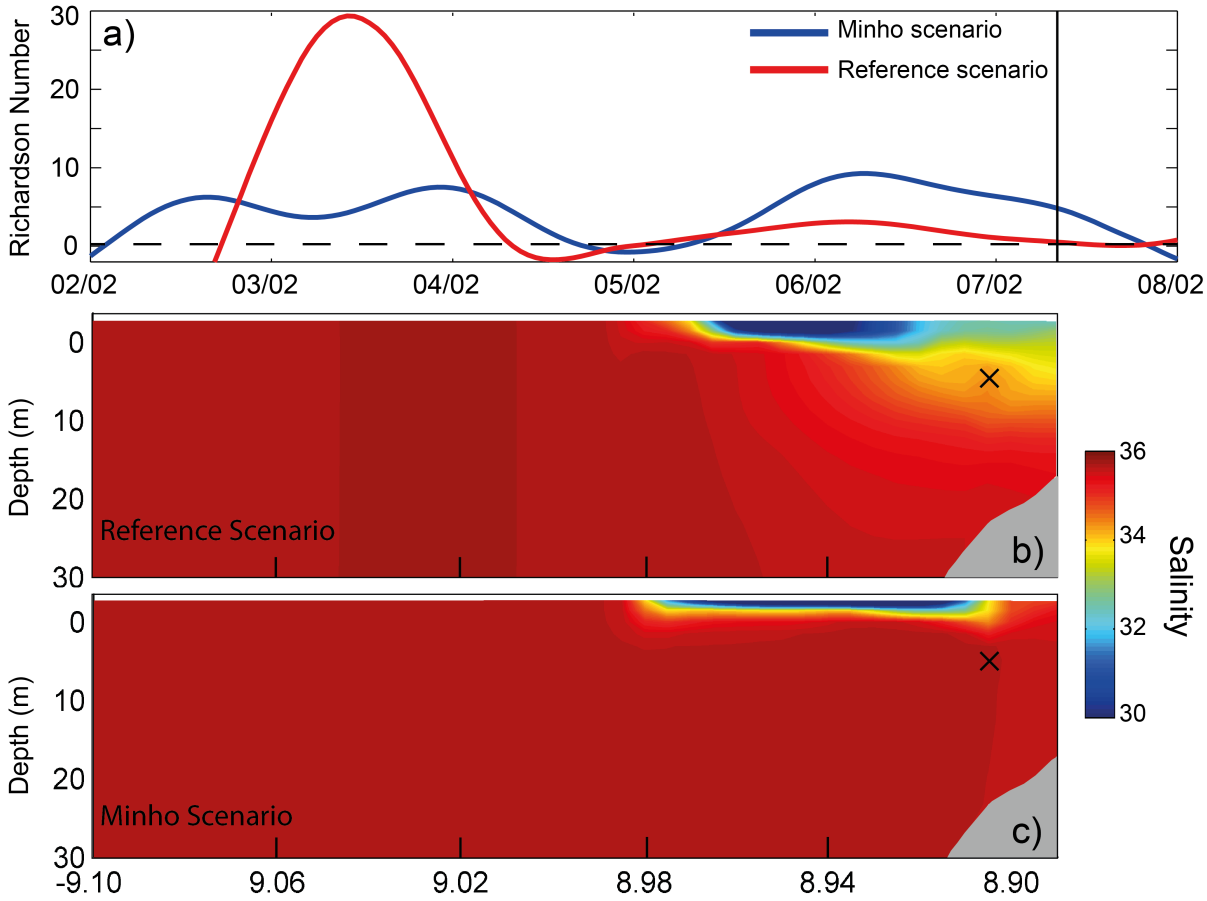

Figure 6.8: (a) Time series of Richardson number calculated in the location marked by a cross in lower panels. Snapshots of salinity vertical structure in cross-section IV (Figure 1) for Reference (b) and Minho (c) scenarios. Vertical line in upper panel represents the snapshots instant.

Results obtained under the reference scenario present some similar patterns to those found in laboratory experiments (Cenedese and Lerczak, 2007; Yuan et al., 2011). The Douro plume has a higher chance of mixing with ocean waters and, when it reaches the Minho plume (less dense surface water), tends to flow underneath the Minho outflow (Figure 6.8b). In this way, the two-river plume system is aligned more vertically (in agreement with Cenedese and Lerczak (2007) and Yuan et al. (2011) results), limiting the well-known surface-advected plume behaviour of the Minho plume (Sousa et al., 2014b).

The freshwater transport offshore and northward was calculated (Figures 6.9e and 6.9d). The results are in line with the hypothesis proposed above. The freshwater transport

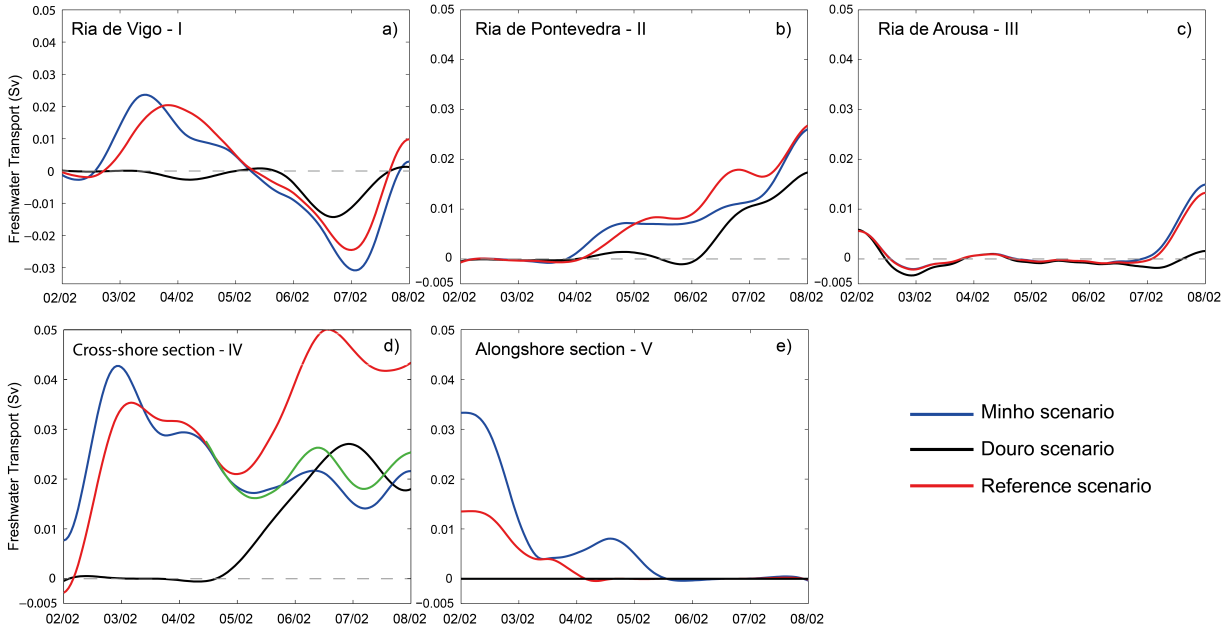

Figure 6.9: Freshwater transport in sections I (a), II (b), III (c), IV (d), and V (e) (Figure 6.1) for Reference (red), Minho (blue), and Douro (black) scenarios. Green line in subplot (d) represents the difference in freshwater transport at section IV between Reference and Douro scenarios.

in section IV (Figure 6.9d) shows that when the Douro plume starts to interact with the Minho one, there is an increase in the freshwater volume (+37%) that flows northward in the Rias Baixas direction. The difference between the freshwater transport in the reference and Douro scenarios is also larger (+11%), compared to the Minho scenario after 4th February (Figure 6.9d, green line). The presence of an ambient flow (here the Douro river plume) makes the northward transport of freshwater more efficient (Fong and Geyer, 2002).

For freshwater transport through section V (Figure 6.9e), V_{F_w} is positive (to the coast) before 4^{th} of February, because the wind rotates from south to north on 1^{st} of February, and pushes freshwater from offshore into the coast. After 4^{th} of February, when the Douro plume reaches the Minho region, the offshore transport (negative) is very small (∼0.004 Sv and ∼0.006 Sv for reference and Minho scenarios, respectively). Nevertheless, the difference suggests, once again, that the Douro plume prevents offshore freshwater transport in the region of plume interaction (-34%).

The results presented in this section suggest that, despite its small contribution to

surface salinity changes in the Minho-Rias Baixas region, the Douro plume has an important influence on plume stratification. The isopycnals tend to be more vertical in presence of the Douro plume (even during a downwelling event), preventing the generation of small-scale eddies and the consequent offshore transport of freshwater.

6.4.4 The influence of the Douro plume on the intrusion of less dense water into the Rias Baixas

The Minho plume intrusion into the Rias Baixas during events of moderate-to-high river discharge combined with southerly winds has been well documented in previous studies (Sousa et al., 2014b). This intrusion of less dense water at the surface produces an unusual salinity gradient, which is able to generate an inversion of normal estuarine circulation (Sousa et al., 2014a). The impact of the Douro plume on the intrusion of less dense water in the Rias Baixas was also explored taking advantage of the Lagrangian particles tracking model. For this purpose, the sum and the temporal average of particles released at Minho and Douro rivers that cross the section defined at each Ria mouth (Table 6.3; sections I, II, and III shown in Figure 6.1) were analysed and the fraction of particles, P, inside each Ria was compared to the total of particles at each region of influence:

$$P = \frac{P_i}{P_i + P_m} \times 100 \tag{6.4}$$

where P_i is the number of particles inside each Ria and P_m represents the number of particles in the adjacent area of each mouth. Moreover, the freshwater transport was calculated over the same sections between 2 and 8 February.

As stated in Section 6.4.2, the small number of particles derived from the Douro River in the Rias Baixas region show that, during this winter event of average river inflows, the direct effect of the Douro plume on the Rias Baixas is irrelevant (Figure 6.4, Table 6.3). The same conclusions may be obtained from the freshwater transport results under the Douro scenario (Figure 6.9). In this scenario a null freshwater transport into the Ria de

Table 6.3: Sum (S) and average (A) of the particles, released at Minho and Douro river mouths, recorded, over time, inside the Rias Baixas in the downwelling period (01/02 - 10/02) for Reference, Douro and Minho scenarios. Average of particles fraction, P, is calculated between particles inside each Ria, P_i, and the total of particles inside each region of influence (P_i+P_m).

River	Scenario	Ria de Vigo			Ria de Pontevedra			Ria de Arousa		
		P (%)	S	A	P (%)	S	A	P (%)	S	A
Douro	Reference	0.2 ±0.02	41	0.1	0 ±0	0	0	10.9 ±0.7	318	0.7
	Douro	0.7 ±0.09	414	1	1.2 ±0.08	422	1	6.6 ±0.6	158	0.4
Minho	Reference	13.8 ±0.9	96228	221.7	24.1 ±0.9	134396	309.7	22.5 ±1.0	125762	289.8
	Minho	9.8 ±0.6	53846	124.1	23.7 ±1.2	116195	267.7	30.9 ±0.7	180557	416

Vigo (positive values) was found (Figure 6.9a). The freshwater intrusion into the Rias de Pontevedra and Arousa after 6^{th} and 7^{th} of February, respectively, is not related with the Douro River discharge (Figures 6.9b and 6.9c). Rather, this originates from small rivers that flow into the Ria de Vigo and then enter the Ria de Pontevedra. This confirms the interconnectivity of the Rias Baixas in terms of water exchange, as previous verified by Sousa et al. (2014b). An analogous process is observed between the Rias de Pontevedra and Arousa, but with a lower water volume exchange.

The direct influence of the Douro plume on the Rias Baixas could not be negligible during extreme discharges peaks, as has been presented by Marta-Almeida et al. (2002) and Otero et al. (2013). However, there is an indirect influence of the riverine waters from the Douro (Figures 6.8 and 6.9) that can change the fate of lighter water (mainly from the Minho Estuary), which definitely affects the intrusion pattern inside the Rias Baixas. In the Minho scenario, the number of particles released at the Minho estuary mouth (sum

and average) that cross the Ria de Vigo and Pontevedra entrances is lower than in the reference scenario (Table 6.3). On the contrary, the number of particles that cross the Ria de Arousa mouth section is lower in the reference scenario. The results from the fraction of the particles that penetrate each Ria, P, are identical (Table 6.3). The fraction of particles inside the Rias de Vigo and Pontevedra is larger for the reference scenario, while for the Ria de Arousa it is larger for the Minho scenario. Although the main trajectory of particles off the Rias Baixas, in the reference scenario, is far from the coast, it seems that the volume of freshwater that reaches the mouths of the Rias de Vigo and Pontevedra is more important (enhancing the horizontal density difference between inside and outside) for the intrusion of particles. In addition, the lower number of small-scale instabilities (Figure 6.7) and the resulting lower dispersion of freshwater offshore also leads to an important confinement of the plume against the coast and, consequently, to an higher intrusion efficiency into the Rias de Vigo and Pontevedra. The results for the Ria de Arousa have a different interpretation as regards coastline orientation (Sousa et al., 2014b). This ria's mouth is located along the main plume trajectory for both scenarios, acting as a *fishing net* for the particles that flow northward. The freshwater fate results from the number of particles released at the Minho river mouth that reach each Ria in the reference and Minho scenarios.

The results from the freshwater transport computed over sections I, II, and III (Figures 6.9a, 6.9b, and 6.9c) corroborates the outcomes from the Lagrangian particle simulations (Table 6.3) previous described. The Douro river plume transports a slightly higher volume of lighter water (+1.6%) into the Ria de Vigo from 2^{th} to 5^{th} of February and then contributes to its retention inside this Ria (+25% retention) (Figure 6.9a). In the Ria de Pontevedra, freshwater intrusion is 14% more effective in the reference scenario than in the Minho one (Figure 6.9b). Conversely, a lower volume of freshwater enters the Ria de Arousa (Figure 6.9c) during the reference scenario than in the Minho scenario (-13%), showing agreement, once again, with Lagrangian particle results.

It is worth mentioning the significant impact that this high freshwater intrusion could have on the ecology of the Rias de Pontevedra and Vigo. The possible enhancing of negative circulation inside these estuaries (Álvarez et al., 2006; Sousa et al., 2014c), caused by the

increased supply of freshwater, tends to stop the water exchange between the Ria de Vigo and the shelf, thus increasing residence time and consequently affecting water quality (Sousa et al., 2014c). This freshwater intrusion acts as a selective force on the phytoplankton assemblage. For example, diatoms are unable to counteract under these conditions and are therefore removed from the water column (Pitcher et al., 2010). On other hand, the extra supply of nutrients from the plume could fertilize the outer part of the estuary, resulting in an extra feeding source for the main shellfish in the area (deCastro et al., 2006).

A summary of the new results, bearing in mind the main known features of the Minho estuarine plume and the influence of the Douro plume, was drawn up and schematically depicted in Figure 6.10. Figure 6.10a shows the well-documented behaviour of the Minho plume and its influence on the Rias Baixas under southerly winds and moderate river discharges. When the wind blows northwards, part of the plume tends to turn southwest but most of it is confined against the coast. The export of freshwater offshore is intensified through small-scale eddies. Moreover, there is Minho plume intrusion into the Rias Baixas, through surface layers, when the density in the inner part of estuaries is higher than in the outer part.

The indirect influence of the Douro plume on the Minho plume is summarized in the diagram presented in Figure 6.10b. In both Minho and reference scenarios downwelling-favourable winds push both plumes against the coast, generating the WIBP (Peliz et al., 2002). North of the Minho Estuary, waters from the Douro River merge with the Minho plume to change its preferential trajectory. The main trajectory of particles released at the Minho River is slightly displaced westward. In addition, the Douro plume prevents the dispersion of freshwater and its consequent transport to the open ocean through small-scale eddies. The increase in freshwater in the outer part of the Rias de Vigo and Pontevedra increases the density gradient between water inside and outside the estuaries, enhancing the water exchange. The results for the Ria de Arousa have a different interpretation, as regards its coastline orientation (Sousa et al., 2014b).

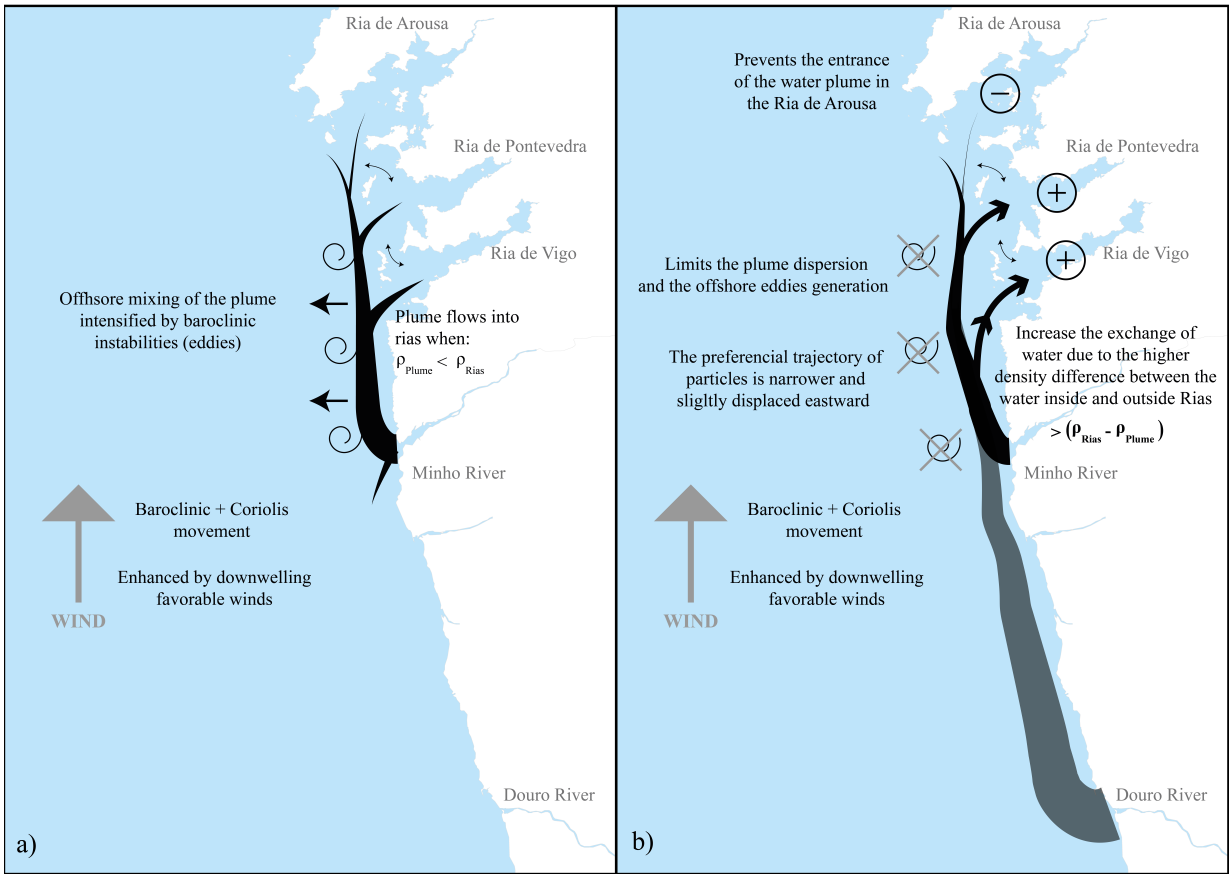

Figure 6.10: (a) Schematic representation of Minho River plume behaviour and its influence on Rias Baixas (Sousa et al., 2014c,b,a) and (b) schematic representation of Minho River plume behaviour and its influence on Rias Baixas under the influence of Douro River plume during downwelling favourable winds.

6.5 Conclusion

The results present in this Chapter contribute to the definition and understanding of the western Iberian Peninsula circulation patterns, highlighting the importance of the interaction between the Douro and Minho estuarine plumes in the propagation of WIBP. Representative winter conditions were analysed, taking into account the estuarine inflow from the Douro and Minho Rivers under different river discharge conditions. Comparisons with remote sensing images attest the accuracy of this model configuration to simulate both estuarine plume features along the inner shelf.

Interaction between the Douro and Minho plumes is unlikely during upwelling events. The Ekman transport leads to an offshore dispersion of plumes and the fast dilution of freshwater from the Minho plume prevents any explicit contact with the Douro plume.

Under southerly winds, both plumes tend to be confined against the coast. A well-mixed ∼10 km wide freshwater band (WIBP) is formed with strong northward surface currents (∼1 m s^{-1}). The probability of interaction between the Douro and Minho plumes increases, as does their intrusion into the Rias Baixas.

Lagrangian simulations showed that the direct influence of the Douro plume on the Rias Baixas is small, when compared to the Minho plume. However, the Douro estuarine plume has an important indirect influence on both plumes' fate over the shelf. The freshwater contribution from the Douro Estuary leads to a WIBP current stabilization, preventing offshore freshwater export (by means of the generation of small-scale eddies), enhancing water exchange with the Rias de Vigo and Pontevedra, and contributing to reverse circulation inside these. As the Rias Baixas are important production sites for marine species, minor changes to the local salinity field, estuarine circulation or input of nutrients can significantly affect the local economy.

Further research into other implications inside the Rias Baixas would be helpful. The implementation of a higher resolution model in this particular area would offer a clearer image of the influence of both the Douro and Minho plumes. Moreover, the consequences for southward estuarine systems and coastal regions from the Douro freshwater input during upwelling events should be addressed in future studies, as its daily discharge peaks can be much higher those from the Minho.

Chapter 7

Final conclusions and future work

Whereas summary conclusions were presented at the end of each Chapter, an overview of the main outcomes as well as some suggestions for future research are given in this section.

Ocean-colour images from MODIS were fundamental to characterize the temporal and spatial scale of the Douro estuarine plume, showing the utility of remote sensing imagery to monitor estuarine plumes like the Douro. The $nLw555$ data showed to be the best proxy to detect the turbid signal of riverine waters in the coastal zone adjacent to the Douro Estuary mouth, presenting the best compromise amongh the percentage of available pixels and the correlation values between river discharge and $nLw555$. The turbid plume is well observed in $nLw555$ composites when the river discharge exceeds 500 m^3 s^{-1}. River discharge and wind act as primary forcing in the plume propagation and fate. Near coast, the variability of the turbid signal intensity responds very well to the river discharge in Crestuma. Wind modulates the plume propagation and fate over the ocean, generating different turbid plume mean-states, which strongly depend on wind direction and magnitude. Turbid composites show the secondary influence of the tide on the Douro estuarine plume dispersion. Major influence was observed in the near-field region, related to the tidal variation of estuarine outflow (flood-ebb cycle). No significant differences between low and high tide turbid composites were found in offshore regions.

The temporal variability of the Douro estuarine plume was evaluated taking into account long-term data from river input, precipitation and climate patterns, namely NAO and EA indices. Large turbid river plumes occurred in the winters of 2000/01, 2002/03, and 2013/14 with high correlations obtained between monthly time series of $nLw555$, river inflow and rainfall rates. Turbid time series showed a high correlation (r=0.51) with EA winter patterns (DJF), presented a maximum peak at 1-month lag (EA ahead $nLw555$ signal). The NAO index shows a secondary role in the extension and magnitude of the Douro turbid plume. Although NAO winter pattern are well correlated with the Douro river discharge, it is not observed for $nLw555$ time series with same time lag (1-month). However, a high correlation was observed between $nLw555$ and winter NAO at 3-month lag. This unexpected spring correlation can be related with an upwelling season shift from spring to winter. The spring biological production is affected and, consequently, coastal turbid patterns are changed in a range of low-to-medium $nLw555$ values. An anomalous turbid pattern was found in the autumn of 2004 without any direct relation with Douro estuarine outflow. Despite the real source of this event remains uncertain, a coccolithophore bloom rises as a reasonable.

The numerical modelling tasks were performed by setting-up two configurations to study the Douro estuarine plume propagation (Chapter 4). These coastal configurations (configurations #1 and #2) are based on the numerical model MOHID, where three levels one-way nested grids and two estuarine models (Minho and Douro estuaries) are included. An improved configuration #1 and Minho estuarine model, previously validated by Sousa et al. (2013), were used to study the impact of the Douro estuarine plume water in the Minho and Rias Baixas regions. Computational limitations prevent the study of the whole area of interest in a single L3 domain (from Ria de Aveiro to cape Finisterra) without reducing the spatial resolution. Thus, configuration #2, based on a previous implementation (Sousa et al., 2013) was developed with focus in the Douro Estuary and both northward and southward adjacent coastal regions. This configuration, as well as the Douro estuarine 2D model application, were validated by comparing model predictions and observations from a large variety of datasets. The results reveal that this coastal nested model implementation

accurately reproduces local hydrodynamics and thermohaline patterns over the Northwestern Portuguese coast, allowing the proper study of the Douro estuarine plume propagation.

The characterization of the Douro estuarine plume in terms of its dynamics, scale and propagation over the continental shelf was addressed in Chapter 5 using the numerical model implementation validated in Chapter 4 (configuration #2). For this purpose, several scenarios with different river discharges (low, moderate and high), wind directions (north, south, west and east) and intensities (3 and 6 m s^{-1}) were defined.

In the absence of significant wind or under null wind forcing, the plume presents typical characteristics of a prototypal plume (Horner-Devine et al., 2015). It comprises a near-field region, a re-circulating bulge in front of the river mouth and a northward coastal current in the far-field region. Moreover, the Douro estuarine plume can be classified as a surface-advected and large-scale plume according to classifications of Yankovsky and Chapman (1997) and Garvine (1995), respectively. The results also demonstrate that a moderate-to-high river discharge is enough to create, without southerly wind component, a northward near surface coastal current of 0.2-0.3 m s^{-1} (about 10 km width).

Simulations considering wind forcing reveal low salinity patterns similar to those found for turbid composites generated in Chapter 2, confirming $nLw555$ as a good proxy for the Douro estuarine plume signal. From the analysis of model predictions, a schematic representation of the main plume propagation and circulation patterns under different wind forcing scenarios were proposed. Under easterly winds, a plume shape similar to that predicted in the simulations without wind forcing is revealed. However, a slight detachment from the coast is observed with a small increase in current velocity. Westerly winds tend to accumulate freshwater near the coast, being the only wind scenario where a southward coastal current is generated. Under northerly winds, the plume main feature is an offshore extension with an inclination towards southwest, while southerly winds tend to confine the plume to the coast, enhancing the velocity within the plume, with values higher than 0.8 m s^{-1} under high river discharge.

A particular characteristic of the plume propagation under downwelling-favourable winds and moderate-to-high river discharge is the generation of a strong northward coastal

current, which transport about five times more riverine water from Douro than in the absence of wind forcing. In these wind conditions, the Douro and Minho estuarine plumes starts to interact. The interaction between these estuarine plumes is addressed in Chapter 6, where the influence of the merging process in the WIBP propagation is highlighted. A representative winter event was simulated and analysed (2010 winter), including the Douro and Minho estuarine outflows, by using an improved version of the coastal model application previously validated by Sousa et al. (2013) (configuration #1) and a particle tracking model implementation. A schematic representation of the direct and indirect influence of the Douro estuarine water in the coast off Minho Estuary and in Rias Baixas was proposed. Lagrangian simulations revealed that the Douro plume has a small direct influence on Rias Baixas dynamics. However, it has an important indirect influence on merged plumes' fate, leading to the WIBP current stabilization, preventing the offshore freshwater export and enhancing water exchange with the southern Rias (Vigo and Pontevedra). As Rias Baixas are recognized as an important production area for marine species, minor changes in their hydrography can significantly affect the local economy.

More work can be addressed in future using remote sensing products for the region of influence of the Douro discharge. The current lack of long-term *in situ* data such as salinity, water temperature, Coloured Dissolved Organic Material (CDOM), chlorophyll, remote sensing reflectances, among other properties is a fundamental limitation to fully understand the relation between turbidity (used in this work as a Douro estuarine plume proxy) and low salinity waters. The development of consistent monitoring programs dedicating to measure high volumes of data would generate conditions to create feasible satellite derived salinity fields. This can be performed based on linear and multi-linear relationships (Ahn et al., 2008; Palacios et al., 2009), or more complex, using neural networks to pair *in situ* salinity values with satellite data along with other environmental variables such as tides, bathymetry, SST, chlorophyll-a, river discharge, etc., generating links between these variables (Geiger et al., 2013). A large number of *in situ* measurements would also contribute to create and tune regional algorithms, properly validating remote sensing products for this coastal region. This can be done for past (SeaWiFS, MERIS, etc.), current and future satellite missions

(MODIS from NASA and Sentinel from ESA) devoted to ocean observations

Considering short-term possibilities, the examination of further anomalous turbid features under low discharge regimes deserves more attention. If the relation between these patterns and cocolithosphore blooms can be verified, new opportunities will be open to create an easy and practicable method to detect and evaluate bloom events.

From the analysis of numerical simulation results performed in Chapters 5 and 6, two future topics arises, justifying a more in-depth analysis in a short-term period:

1) Is it possible that the Douro riverine water propagates into the Ria de Aveiro Lagoon, changing substantially the local hydrography under strong westerly wind events?

2) What are the main patterns of the Douro plume propagation under a punctual event of moderate-to-high river runoff during late spring and summer seasons?

A methodology similar to that followed in Chapter 6 should be implemented to study the first question, using a more realistic estuarine-coast system (two-way) in the numerical simulation. In this way, both estuarine systems can be computed integrated in the coastal domain, giving conditions to perform an important analysis of the water mixing within this tidal-driven coastal lagoon.

Configuration #2 should be validated under summer conditions to assure conditions to accurately answer the second question, when the typical differences between water temperatures in ocean and in estuary are usually opposite to those found during winter. Then, a methodology similar to that followed in Chapter 5 should be adopted, including a prior statistical analysis of wind and river discharge in summer conditions.

Despite different discharge regimes and length scales, the Douro estuarine plume can be compared with other river plumes. One example is the Columbia River plume (U.S.A), which shares some particularities with the Douro plume. Consequently, some investigations similar to that performed off Oregon coast can be tested in the Douro region in the future. For example, the possibility that Douro Estuary acts as a generator of internal waves seems to be a reasonable hypothesis and need to be verified, since internal waves can potentially increase nutrients supply to euphotic zone, enhancing the near-surface chlorophyll, which is often visible in ocean-colour images (da Silva, 2002). This task should be addressed by

combining resources such as remote sensing, field observations and numerical modelling: 1) using Synthetic Aperture Radar (SAR) images that often indicate regions of enhanced surface roughness associated with internal wave velocity convergences (Nash and Moum, 2005), 2) performing front tracking experiments as documented by Kilcher and Nash (2010) and Hickey et al. (2010) (see Figure 4 of Kilcher and Nash (2010)) to observe tidal plume fronts, 3) implementing numerical coastal models (preferably a two-way coupled estuary-coast system) with higher vertical and horizontal resolution in the tidal plume region.

The Douro re-circulating bulge structure is clear in majority of the numerical simulations (Chapter 5). However, this structure was never observed *in situ* and modelling results need to be verified. To observe this anticyclonic circulation north of the Douro River mouth, a field work based on CTD transects (cross and along shore) and/or gliders observations (Saldías et al., 2016) as well as a deployment of more than one ADCP would be required to characterize its horizontal and vertical structure (Horner-Devine et al., 2009). Another solution would be the implementation of a High Frequency (HF)-Radar system, allowing to the long-term measurement of the surface velocity horizontal fields near the river mouth (Chant et al., 2008b).

References

Abbott M.B. and Basco D.R. (1989). *Computational fluid dynamics: an introduction for engineers*. Longman Scientific & Technical, Harlow, Essex, England, 425 pp.

Ahn Y.H., Shanmugam P., Moon J.E. and Ryu J.H. (2008). Satellite remote sensing of a low-salinity water plume in the East China Sea. *Annales Geophysicae*, 26(7):2019–35.

Allen C.M. (1982). Numerical simulation of contaminant dispersion in estuary flows. In *Proceedings of the Royal Society A: Mathematical, Physical and Engineering Sciences*, Vol. 381, 179–94.

Álvarez I., deCastro M., Gomez-Gesteira M. and Prego R. (2006). Hydrographic behavior of the Galician Rias Baixas (NW Spain) under the spring intrusion of the Miño River. *Journal of Marine Systems*, 60(1-2):144–52.

Álvarez I., Gómez-Gesteira M., deCastro M. and Carvalho D. (2014). Comparison of different wind products and buoy wind data with seasonality and interannual climate variability in the southern Bay of Biscay (2000–2009). *Deep Sea Research Part II: Topical Studies in Oceanography*, 106:38–48.

Álvarez I., Gómez-Gesteira M., deCastro M., Gómez-Gesteira J.L. and Dias J.M. (2010). Summer upwelling frequency along the western Cantabrian coast from 1967 to 2007. *Journal of Marine Systems*, 79(1-2):218–26.

Álvarez I., Gómez-Gesteira M., deCastro M., Lorenzo M.N., Crespo A.J.C. and Dias J.M.

(2011). Comparative analysis of upwelling influence between the western and northern coast of the Iberian Peninsula. *Continental Shelf Research*, 31(5):388–99.

Álvarez I., Gómez-Gesteira M., deCastro M. and Novoa E. (2008). Ekman transport along the Galician Coast (NW, Spain) calculated from QuikSCAT winds. *Journal of Marine Systems*, 72(1-4):101–15.

Álvarez I., Ospina-Álvarez N., Pazos Y., deCastro M., Bernardez P., Campos M., Gómez-Gesteira J., Alvarez-Ossorio M., Varela M., Gómez-Gesteira M. and Prego R. (2009). A winter upwelling event in the Northern Galician Rias: frequency and oceanographic implications. *Estuarine, Coastal and Shelf Science*, 82(4):573–82.

Arakawa A. and Lamb V.R. (1977). Computational design of the basic dynamical processes of the UCLA general circulation model. In *Methods in computational physics* (Chang J., ed.). Academic Press, Inc., New York. USA, 173–265 pp.

Arnau P., Liquete C. and Canals M. (2004). River mouth plume events and their dispersal in the Northwestern Mediterranean Sea. *Oceanography*, 17(3):22–31.

Arnoux-Chiavassa S., Rey V. and Fraunié P. (2003). Modeling 3D Rhône river plume using a higher order advection scheme. *Oceanologica Acta*, 26(4):299–309.

ASTM-International (2003). D1889-00 standard test method for turbidity of water. In *Annual Book of ASTM Standards, Water and Environmental Technology 11.01* (ASTM International, ed.). American Society for Testing and Materials International, West Conshohocken, Pennsylvania, 6.

Aurin D., Mannino A. and Franz B. (2013). Spatially resolving ocean color and sediment dispersion in river plumes, coastal systems, and continental shelf waters. *Remote Sensing of Environment*, 137:212–25.

Avicola G. and Huq P. (2003). The characteristics of the recirculating bulge region in coastal buoyant outflows. *Journal of Marine Research*, 61(4):435–63.

Azevedo I.C., Bordalo A.A. and Duarte P.M. (2010). Influence of river discharge patterns on the hydrodynamics and potential contaminant dispersion in the Douro estuary (Portugal). *Water Research*, 44(10):3133–46.

Azevedo I.C., Duarte P.M. and Bordalo A.A. (2008). Understanding spatial and temporal dynamics of key environmental characteristics in a mesotidal Atlantic estuary (Douro, NW Portugal). *Estuarine, Coastal and Shelf Science*, 76(3):620–33.

Bailey S.W., Franz B.A. and Jeremy Werdell P. (2010). Estimation of near-infrared water-leaving reflectance for satellite ocean color data processing. *Optics Express*, 18(7):7521–7.

Baith K., Lindsay R., Fu G. and McClain C.R. (2001). Data analysis system developed for ocean color satellite sensors. *Eos, Transactions American Geophysical Union*, 82(18):202–.

Bakun A. (1973). *Coastal upwelling indices, west coast of North America, 1946-71.* Tech. Rep., NOAA - NMFS SSRF-671, U.S. Dep. Commer., 103 pp.

Barton A., Greene C., Monger B. and Pershing A. (2003). The continuous plankton recorder survey and the North Atlantic Oscillation: interannual to multidecadal-scale patterns of phytoplankton variability in the North Atlantic Ocean. *Progress in Oceanography*, 58(2-4):337–58.

Basdevant C. and Philipovitch T. (1994). On the validity of the "Weiss criterion" in two-dimensional turbulence. *Physica D: Nonlinear Phenomena*, 73(1-2):17–30.

Becker J.J., Sandwell D.T., Smith W.H.F., Braud J., Binder B., Depner J., Fabre D., Factor J., Ingalls S., Kim S.H., Ladner R., Marks K., Nelson S., Pharaoh A., Trimmer R., Von Rosenberg J., Wallace G. and Weatherall P. (2009). Global bathymetry and elevation data at 30 arc seconds resolution: SRTM30_PLUS. *Marine Geodesy*, 32(4):355–71.

Bernardes B.D.L. (2007). *Hydrodynamical and ecological modelling of the North Sea.* MSc Thesis, Technical University of Lisbon, Lisboa, Portugal, 81 pp.

Bordalo A.A., Teixeira R. and Wiebe W.J. (2006). A water quality index applied to an international shared river basin: the case of the Douro River. *Environmental Management*, 38(6):910–20.

Braunschweig F., Martins F., Chambel P. and Neves R. (2003). A methodology to estimate renewal time scales in estuaries: the Tagus Estuary case. *Ocean Dynamics*, 53(3):137–45.

Brodie J., Schroeder T., Rohde K., Faithful J., Masters B., Dekker A., Brando V. and Maughan M. (2010). Dispersal of suspended sediments and nutrients in the Great Barrier Reef lagoon during river-discharge events: conclusions from satellite remote sensing and concurrent flood-plume sampling. *Marine and Freshwater Research*, 61(6):651–64.

Bruland K.W., Lohan M.C., Aguilar-Islas A.M., Smith G.J., Sohst B. and Baptista A. (2008). Factors influencing the chemistry of the near-field Columbia River plume: nitrate, silicic acid, dissolved Fe, and dissolved Mn. *Journal of Geophysical Research*, 113:C00B02.

Burchard H. and Bolding K. (2001). Comparative analysis of four second-moment turbulence closure models for the oceanic mixed layer. *Journal of Physical Oceanography*, 31(8):1943–68.

Burchard H., Petersen O. and Rippeth T.P. (1998). Comparing the performance of the Mellor-Yamada and the κ-ϵ two-equation turbulence models. *Journal of Geophysical Research: Oceans*, 103(C5):10543–54.

Canuto V.M., Howard A., Cheng Y. and Dubovikov M.S. (2001). Ocean turbulence. Part I: one-point closure model—momentum and heat vertical diffusivities. *Journal of Physical Oceanography*, 31(6):1413–26.

Carrère L., Lyard F., Cancet M., Guillot A. and Roblou L. (2012). FES2012: a new global tidal model taking advantage of nearly twenty years of altimetry. In *Proceedings of*

the 20 Years of Progress in Radar Altimetry Symposium (Ouwehand L., ed.), ESA Communications, Venice, Italy, 1–20 pp.

Carvalho A.N., Vaz A.S.L., Sérgio T.I.B. and dos Santos P.J.T. (2013). Sustainability of bait fishing harvesting in estuarine ecosystems – case study in the local natural reserve of Douro Estuary, Portugal. *Revista de Gestão Costeira Integrada*, 13(2):157–68.

Cenedese C. and Lerczak J.A. (2007). Understanding the dynamics of the interaction between two river plumes. In *Proceedings of Fifth international symposium on environmental hydraulics* (Boyer D.L., ed.), IAHR, Tempe, Arizona, USA, 1–6 pp.

Chang Y.L. and Oey L.Y. (2014). Analysis of STCC eddies using the Okubo–Weiss parameter on model and satellite data. *Ocean Dynamics*, 64(2):259–71.

Chant R., Wilkin J., Zhang W., Choi B.J., Hunter E., Castelao R., Glenn S., Jurisa J., Schofield O., Houghton R., Kohut J., Frazer T. and Moline M. (2008a). Dispersal of the Hudson River plume in the New York Bight: synthesis of observational and numerical studies during LaTTE. *Oceanography*, 21(4):148–61.

Chant R.J., Glenn S.M., Hunter E., Kohut J., Chen R.F., Houghton R.W., Bosch J. and Schofield O. (2008b). Bulge formation of a buoyant river outflow. *Journal of Geophysical Research: Oceans*, 113(1):C01017.

Chao S.Y. (1988a). River-forced estuarine plumes. *Journal of Physical Oceanography*, 18(1):72–88.

Chao S.Y. (1988b). Wind-driven motion of estuarine plumes. *Journal of Physical Oceanography*, 18(8):1144–66.

Chao S.Y. and Boicourt W.C. (1986). Onset of estuarine plumes. *Journal of Physical Oceanography*, 16(12):2137–49.

Chapra S.C. (1997). *Surface water-quality modeling*. Waveland press, Inc., Long Grove, Illinois, USA, 844 pp.

Chícharo M.A., Esteves E., Santos A.M.P., Dos Santos A., Peliz Á. and Ré P. (2003). Are sardine larvae caught off northern portugal in winter starving? An approach examining nutritional conditions. *Marine Ecology Progress Series*, 257:303–9.

Choi B.J. and Wilkin J.L. (2007). The effect of wind on the dispersal of the Hudson River plume. *Journal of Physical Oceanography*, 37(7):1878–97.

Coelho C. and Veloso-Gomes F. (2006). Crosshore beach profile models - application to Aveiro coast. *Journal of Coastal Research*, SI39(39):345–50.

Coelho H.S., Neves R.J.J., White M., Leitão P.C. and Santos A.J. (2002). A model for ocean circulation on the Iberian coast. *Journal of Marine Systems*, 32(1-3):153–79.

Costoya X., Fernández-Nóvoa D., deCastro M., Santos F., Lazure P. and Gómez-Gesteira M. (2015). Modulation of sea surface temperature warming in the Bay of Biscay by Loire and Gironde Rivers. *Journal of Geophysical Research: Oceans*, 120.

Cushman-Roisin B. (1994). *Introduction to geophysical fluid dynamics*. Prentice Hall College Div., Englewood Cliff, New Jersey, USA, 320 pp.

da Silva J.C.B. (2002). On the observability of internal tidal waves in remotely-sensed ocean colour data. *Geophysical Research Letters*, 29(12):1569.

Davies-Colley R.J. and Smith D.G. (2001). Turbidity, suspended sediment, and water clarity: a review. *Journal of the American Water Resources Association*, 37(5):1085–101.

de Kok J.M. (1996). A two-layer model of the Rhine plume. *Journal of Marine Systems*, 8(3-4):269–84.

de Kok J.M. (1997). Baroclinic eddy formation in a Rhine plume model. *Journal of Marine Systems*, 12(1-4):35–52.

de Kok J.M., de Valk C., van Kester J.H.T.M., de Goede E. and Uittenbogaard R.E. (2001). Salinity and temperature stratification in the Rhine plume. *Estuarine, Coastal and Shelf Science*, 53(4):467–75.

de Ruijter W.P.M., Visser A.W. and Bos W.G. (1997). The Rhine outflow: a prototypical pulsed discharge plume in a high energy shallow sea. *Journal of Marine Systems*, 12(1-4):263–76.

deCastro M., Álvarez I., Varela M., Prego R. and Gómez-Gesteira M. (2006). Miño River dams discharge on neighbor Galician Rias Baixas (NW Iberian Peninsula): hydrological, chemical and biological changes in water column. *Estuarine, Coastal and Shelf Science*, 70(1-2):52–62.

deCastro M., Gómez-Gesteira M., Alvarez I., Lorenzo M., Cabanas J., Prego R. and Crespo A. (2008). Characterization of fall–winter upwelling recurrence along the Galician western coast (NW Spain) from 2000 to 2005: dependence on atmospheric forcing. *Journal of Marine Systems*, 72(1-4):145–58.

deCastro M., Gómez-Gesteira M., Prego R. and Álvarez I. (2004). Ria-ocean exchange driven by tides in the Ria of Ferrol (NW Spain). *Estuarine, Coastal and Shelf Science*, 61(1):15–24.

Demaster D.J. and Pope R.H. (1996). Nutrient dynamics in Amazon shelf waters: results from AMASSEDS. *Continental Shelf Research*, 16(3):263–89.

Dias J.M. and Lopes J. (2006a). Implementation and assessment of hydrodynamic, salt and heat transport models: the case of Ria de Aveiro Lagoon (Portugal). *Environmental Modelling & Software*, 21(1):1–15.

Dias J.M. and Lopes J.F. (2006b). Calibration and validation of hydrodynamic, salt and heat transport models for Ria de Aveiro Lagoon (Portugal). *Journal of Coastal Research*, (39):1680–4.

Dias J.M., Lopes J.F. and Dekeyser I. (2000). Tidal propagation in Ria de Aveiro lagoon, Portugal. *Physics and Chemistry of the Earth, Part B: Hydrology, Oceans and Atmosphere*, 25(4):369–74.

Dias J.M., Sousa M.C., Bertin X., Fortunato a.B. and Oliveira a. (2009). Numerical modeling of the impact of the Ancão Inlet relocation (Ria Formosa, Portugal). *Environmental Modelling and Software*, 24(6):711–25.

Dias J.M.A. (1987). *Dinâmica sedimentar e evolução recente da plataforma continental portuguesa setentrional*. PhD Thesis, University of Lisbon, Lisbon, Portugal, 150 pp.

Dias J.M.A. (1990). A evolução actual do litoral português. *Geonovas*, 11:15–28.

Dias J.M.A., Jouanneau J., Gonzalez R., Araújo M.F., Drago T., Garcia C., Oliveira A., Rodrigues A., Vitorino J. and Weber O. (2002). Present day sedimentary processes on the northern Iberian shelf. *Progress in Oceanography*, 52(2-4):249–59.

Dogliotti A.I., Ruddick K., Nechad B., Lasta C. and Mercado A. (2011). Calibration and validation of an algorithm for remote sensing of turbidity over La Plata River Estuary, Argentina. *EARSeL eProceedings*, 10(2):119–30.

Doxaran D., Froidefond J.M., Castaing P. and Babin M. (2009). Dynamics of the turbidity maximum zone in a macrotidal estuary (the Gironde, France): observations from field and MODIS satellite data. *Estuarine, Coastal and Shelf Science*, 81(3):321–32.

Dzwonkowski B. and Yan X.H. (2005). Tracking of a Chesapeake Bay estuarine outflow plume with satellite-based ocean color data. *Continental Shelf Research*, 25(16):1942–58.

Elhmaïdi D., Provenzale A. and Babiano A. (1993). Elementary topology of two-dimensional turbulence from a Lagrangian viewpoint and single-particle dispersion. *Journal of Fluid Mechanics*, 257:533.

Esteban-Parra M.J., Rodrigo F.S. and Castro-Diez Y. (1998). Spatial and temporal patterns of precipitation in Spain for the period 1880–1992. *International Journal of Climatology*, 18(14):1557–74.

Fernández-Nóvoa D., Mendes R., deCastro M., Dias J.M., Sánchez-Arcilla A. and Gómez-Gesteira M. (2015). Analysis of the influence of river discharge and wind on the Ebro

turbid plume using MODIS-Aqua and MODIS-Terra data. *Journal of Marine Systems*, 142:40–6.

Ferreira J.G., Simas T., Nobre A., Silva M.C., Shifferegger K. and Lencart-Silva J. (2003). *Identification of sensitive areas and vulnerable zones in transitional and coastal portuguese systems: application of the united states national estuarine eutrophication assessment to the Minho, Lima, Douro, Ria de Aveiro, Mondego, Tagus, Sado, Mira, Ria.* Instituto da Água, Institute of Marine Research, Lisboa, Portugal, 151 pp.

Figueiras F., Labarta U. and Fernández Reiriz M. (2002). Coastal upwelling, primary production and mussel growth in the rías baixas of galicia. *Hydrobiologia*, 484(1):121–31.

Fischer H.B. (1972). Mass transport mechanisms in partially stratified estuaries. *Journal of Fluid Mechanics*, 53(4):671.

Fischer H.B., List E.J., Koh R.C.Y., Imberger J. and Brooks N.H. (1979). *Mixing in inland and coastal waters.* Academic Press Inc., San Diego, California, USA, 483 pp.

Fiúza A.F.G., Hamann M., Ambar I., Díaz Del Río G., González N. and Cabanas J.M. (1998). Water masses and their circulation off western Iberia during May 1993. *Deep-Sea Research Part I: Oceanographic Research Papers*, 45(7):1127–60.

Flagg C.N., Vennersch J.A. and Beardsley R.C. (1976). 1974 MIT New England shelf dynamics experiment (March, 1974), Part II: the moored array: M.I.T. report 76-1.

Flather R. (1976). {A tidal model of the northwest European continental shelf}. *Memoires de la Societe Royale de Sciences de Liege*, 10(6):141–64.

Fofonoff N.P. and Millard R.C. (1983). Algorithms for computation of fundamental properties of seawater. *UNESCO Technical papers in marine science*, 44:53.

Fong D.A. and Geyer W.R. (2001). Response of a river plume during an upwelling favorable wind event. *Journal of Geophysical Research: Oceans*, 106(C1):1067–84.

Fong D.A. and Geyer W.R. (2002). The alongshore transport of freshwater in a surface-trapped river plume*. *Journal of Physical Oceanography*, 32(3):957–72.

Font J., Camps A., Borges A., Martin-Neira M., Boutin J., Reul N., Kerr Y.H., Hahne A. and Mecklenburg S. (2010). SMOS: the challenging sea surface salinity measurement from space. In *Proceedings of the IEEE*, Vol. 98, 649–65.

Fraga F. (1981). Upwelling off the Galacian Coast, northwest Spain. In *Coastal Upwelling* (Richardson F., ed.). American geophysical union, washington d.c., usa ed., 176–182 pp.

Franz B.A., Kwiatkowska E.J., Meister G. and McClain C.R. (2007). Utility of MODIS-Terra of ocean color applications. In *Proceeding of SPIE 6677, Earth Observing Systems XII, 66770Q* (Butler J.J. and Xiong J., eds.), Vol. 6677, 66770Q–14.

Franz B.A., Werdell P.J., Meister G., Kwiatkowska E.J., Bailey S.W., Ahmad Z. and Mcclain C.R. (2006). MODIS land bands for ocean remote sensing applications. In *Proceedings of Ocean Optics XVIII*, 10, Montreal, Canada.

Franz G., Pinto L., Ascione I. and Fernandes R. (2014). *Implementation of the Tagus Estuary hydrodynamic model*. Tech. Rep., ISDAMP Project (Grant Agreement No. 638516/2012/ECHO/A5/SUB), 12 pp.

García Berdeal I., Hickey B.M. and Kawase M. (2002). Influence of wind stress and ambient flow on a high discharge river plume. *Journal of Geophysical Research*, 107(C9):3130.

Garvine R.W. (1974). Dynamics of small-scale oceanic fronts. *Journal of Physical Oceanography*, 4(4):557–69.

Garvine R.W. (1982). A steady state model for buoyant surface plume hydrodynamics in coastal waters. *Tellus*, 34(3):293–306.

Garvine R.W. (1995). A dynamical system for classifying buoyant coastal discharges. *Continental Shelf Research*, 15(13):1585–96.

Garvine R.W. (2001). The impact of model configuration in studies of buoyant coastal discharge. *Journal of Marine Research*, 59(2):193–225.

Geiger E.F., Grossi M.D., Trembanis A.C., Kohut J.T. and Oliver M.J. (2013). Satellite-derived coastal ocean and estuarine salinity in the Mid-Atlantic. *Continental Shelf Research*, 63:S235–42.

Geyer W., Hill P., Milligan T. and Traykovski P. (2000). The structure of the Eel River plume during floods. *Continental Shelf Research*, 20(16):2067–93.

Geyer W.R., Beardsley R.C., Candela J., Castro Filho B.M., Legeckis R.V., Lentz S.J., Limebuerner R., Miranda L.B. and Trowbridge J.H. (1991). The physical oceanography of the Amazon outflow. *Oceanography*, 4(1):8–14.

Giraudeau J., Monteiro P.M. and Nikodemus K. (1993). Distribution and malformation of living coccolithophores in the northern Benguela upwelling system off Namibia. *Marine Micropaleontology*, 22(1-2):93–110.

Gómez-Gesteira M., Montero P., Prego R., Taboada J.J., Leitao P., Ruiz-Villarreal M., Neves R. and Perez-Villar V. (1999). A two-dimensional particle tracking model for pollution dispersion in A Coruna and Vigo Rias (NW Spain). *Oceanologica Acta*, 22(2):167–77.

Gómez-Gesteira M., Moreira C., Álvarez I. and deCastro M. (2006). Ekman transport along the Galician coast (northwest Spain) calculated from forecasted winds. *Journal of Geophysical Research: Oceans*, 111(C10):C10005.

Gonçalves H., Teodoro A.C. and Almeida H. (2012). Identification, characterization and analysis of the Douro river plume from MERIS data. *IEEE Journal of Selected Topics in Applied Earth Observations and Remote Sensing*, 5(5):1553–63.

Gordon H.R. and Morel A.Y. (1983). *remote assessment of ocean color for interpretation of satellite visible Imagery: a review.* Lecture Notes on Coastal and Estuarine Studies, Springer-Verlag New York Inc., New York, USA, 113 pp.

Gordon H.R., Smyth T.J., Balch W.M., Boynton G.C. and Tarran G.A. (2009). Light scattering by coccoliths detached from Emiliania huxleyi. *Applied Optics*, 48(31):6059–73.

Gordon H.R. and Voss K.J. (1999). *MODIS Normalized Water-leaving Radiance, Algorithm Theoretical Basis Document (MOD 18), version 4*. Tech. Rep., NASA, Contract Number NAS503163, 100 pp.

Gordon H.R. and Wang M. (1992). Surface-roughness considerations for atmospheric correction of ocean color sensors 1: The Rayleigh-scattering component. *Applied Optics*, 31(21):4247.

Guo X. and Valle-Levinson A. (2007). Tidal effects on estuarine circulation and outflow plume in the Chesapeake Bay. *Continental Shelf Research*, 27(1):20–42.

Güttler F.N., Niculescu S. and Gohin F. (2013). Turbidity retrieval and monitoring of Danube Delta waters using multi-sensor optical remote sensing data: an integrated view from the delta plain lakes to the western–northwestern Black Sea coastal zone. *Remote Sensing of Environment*, 132:86–101.

Hessner K., Rubino A., Brandt P. and Alpers W. (2001). The Rhine outflow plume studied by the analysis of synthetic aperture radar data and numerical simulations. *Journal of Physical Oceanography*, 31(10):3030–44.

Hetland R.D. (2005). Relating river plume structure to vertical mixing. *Journal of Physical Oceanography*, 35(9):1667–88.

Hetland R.D. (2010). The effects of mixing and spreading on density in near-field river plumes. *Dynamics of Atmospheres and Oceans*, 49(1):37–53.

Hetland R.D. and MacDonald D.G. (2008). Spreading in the near-field Merrimack River plume. *Ocean Modelling*, 21(1-2):12–21.

Hickey B.M., Kudela R.M., Nash J.D., Bruland K.W., Peterson W.T., MacCready P., Lessard E.J., Jay D.a., Banas N.S., Baptista a.M., Dever E.P., Kosro P.M., Kilcher L.K., Horner-Devine a.R., Zaron E.D., McCabe R.M., Peterson J.O., Orton P.M., Pan J. and Lohan M.C. (2010). River influences on shelf ecosystems: introduction and synthesis. *Journal of Geophysical Research: Oceans*, 115(2):1–26.

Hickey B.M., Pietrafesa L.J., Jay D.A. and Boicourt W.C. (1998). The Columbia River plume study: subtidal variability in the velocity and salinity fields. *Journal of Geophysical Research: Oceans*, 103(C5):10339–68.

Hopkins J., Lucas M., Dufau C., Sutton M., Stum J., Lauret O. and Channelliere C. (2013). Detection and variability of the Congo River plume from satellite derived sea surface temperature, salinity, ocean colour and sea level. *Remote Sensing of Environment*, 139:365–85.

Horner-Devine A.R. (2009). The bulge circulation in the Columbia River plume. *Continental Shelf Research*, 29(1):234–51.

Horner-Devine A.R., Fong D.A. and Monismith S.G. (2008). Evidence for the inherent unsteadiness of a river plume: Satellite observations of the Niagara River discharge. *Limnology and Oceanography*, 53(6):2731–7.

Horner-Devine A.R., Fong D.A., Monismith S.G. and Maxworthy T. (2006). Laboratory experiments simulating a coastal river inflow. *Journal of Fluid Mechanics*, 555:203.

Horner-Devine A.R., Hetland R.D. and MacDonald D.G. (2015). Mixing and transport in coastal river plumes. *Annual Review of Fluid Mechanics*, 47(1):569–94.

Horner-Devine A.R., Jay D.A., Orton P.M. and Spahn E.Y. (2009). A conceptual model of the strongly tidal Columbia River plume. *Journal of Marine Systems*, 78(3):460–75.

Houghton R.W., Tilburg C.E., Garvine R.W. and Fong A. (2004). Delaware River plume response to a strong upwelling-favorable wind event. *Geophysical Research Letters*, 31(7).

Huq P. (2009). The role of Kelvin number on bulge formation from estuarine buoyant outflows. *Estuaries and Coasts*, 32(4):709–19.

IH (2006). *Tabela de Marés*. Instituto Hidrográfico, Portugal, 192 pp.

IOCCG (2011). *Bio-optical sensors on Argo floats*. 11, Reports of the International Ocean-Colour Coordinating Group, Dartmouth, Canada., 89 pp.

IOCCG (2014). *Phytoplankton functional NOOPNOOPtypes from Space.* 15, Reports of the International Ocean-Colour Coordinating Group, Dartmouth, Canada., 156 pp.

Isern-Fontanet J., García-Ladona E. and Font J. (2006). Vortices of the Mediterranean Sea: an altimetric perspective. *Journal of Physical Oceanography*, 36(1):87–103.

Isobe A. (2005). Ballooning of river-plume bulge and its stabilization by tidal currents. *Journal of Physical Oceanography*, 35(12):2337–51.

Jiang L., Yan X. and Klemas V. (2009). Remote sensing for the identification of coastal plumes: case studies of Delaware Bay. *International Journal of Remote Sensing*, 30(8):2033–48.

Jurisa J.T. and Chant R. (2012). The coupled Hudson River estuarine-plume response to variable wind and river forcings. *Ocean Dynamics*, 62(5):771–84.

Kakoulaki G., MacDonald D. and Horner-Devine A.R. (2014). The role of wind in the near field and midfield of a river plume. *Geophysical Research Letters*, 41(14):5132–8.

Kao T.W. (1981). The dynamics of oceanic fronts. Part II: shelf water structure due to freshwater discharge. *Journal of Physical Oceanography*, 11(9):1215–23.

Kenov I.A., Garcia A.C. and Neves R. (2012). Residence time of water in the Mondego Estuary (Portugal). *Estuarine, Coastal and Shelf Science*, 106:13–22.

Kilcher L.F. and Nash J.D. (2010). Structure and dynamics of the Columbia River tidal plume front. *Journal of Geophysical Research: Oceans*, 115(5):C05S90.

Kilcher L.F., Nash J.D. and Moum J.N. (2012). The role of turbulence stress divergence in decelerating a river plume. *Journal of Geophysical Research: Oceans*, 117(5):C05032.

Kilham N.E. and Roberts D. (2011). Amazon River time series of surface sediment concentration from MODIS. *International Journal of Remote Sensing*, 32(10):2659–79.

Kirk J.T.O. (1994). *Light and photosynthesis in aquatic ecosystems*. Cambridge University Press, Cambridge, United Kingdom, 2 ed., 509 pp.

Kliem N. and Pietrzak J.D. (1999). On the pressure gradient error in sigma coordinate ocean models: A comparison with a laboratory experiment. *Journal of Geophysical Research: Oceans*, 104(C12):29781–99.

Kohut J., Roarty H., Glenn S. and Chant R. (2005). Surface current response of Hudson River plume to wind forcing. In *Proceedings of OCEANS 2005 MTS/IEEE*, IEEE, Washington D. C., USA, Vol. 3, 2540–2.

Korosov A., Counillon F. and Johannessen J.A. (2015). Monitoring the spreading of the Amazon freshwater plume by MODIS, SMOS, Aquarius, and TOPAZ. *Journal of Geophysical Research: Oceans*, 120(1):268–83.

Kourafalou V.H., Oey L.Y., Wang J.D. and Lee T.N. (1996). The fate of river discharge on the continental shelf: 1. Modeling the river plume and the inner shelf coastal current. *Journal of Geophysical Research: Oceans*, 101(C2):3415–34.

Lahet F. and Stramski D. (2010). MODIS imagery of turbid plumes in San Diego coastal waters during rainstorm events. *Remote Sensing of Environment*, 114(2):332–44.

Le Pape O., Chauvet F., Désaunay Y. and Guérault D. (2003). Relationship between interannual variations of the river plume and the extent of nursery grounds for the common sole (Solea solea, L.) in Vilaine Bay. Effects on recruitment variability. *Journal of Sea Research*, 50(2-3):177–85.

Le Provost C., Lyard F., Molines J.M., Genco M.L. and Rabilloud F. (1998). A hydrodynamic ocean tide model improved by assimilating a satellite altimeter-derived data set. *Journal of Geophysical Research: Oceans*, 103:5513.

Le Vine D.M., Lagerloef G.S.E., Colomb F.R., Yueh S.H. and Pellerano F.A. (2007). Aquarius: An instrument to monitor sea surface salinity from space. *IEEE Transactions on Geoscience and Remote Sensing*, 45(7):2040–50.

Leendertse J.J. (1967). *Aspects of a computational model for long-period water wave propagation*. The Rand Corporation, Santa Monica, California, 165 pp.

Leitão P. (2002). *Integração de escalas e processos na modelação do ambiente marinho*. PhD Thesis, Instituto Superior Técnico, Lisboa, 466 pp.

Leitão P., Coelho H., Santos A. and Neves R. (2005). Modelling the main features of the Algarve coastal circulation during July 2004: a downscaling approach. *Journal of Atmospheric & Ocean Science*, 10(4):421–62.

Lentz S. (2004). The response of buoyant coastal plumes to upwelling-favorable Winds*. *Journal of Physical Oceanography*, 34(11):2458–69.

Lentz S. and Largier J. (2006). The Influence of Wind Forcing on the Chesapeake Bay Buoyant Coastal Current*. *Journal of Physical Oceanography*, 36(7):1305–16.

Lentz S.J. and Fewings M.R. (2012). The wind and wave-driven inner-shelf circulation. *Annual Review of Marine Science*, 4(1):317–43.

Lentz S.J. and Limeburner R. (1995). The Amazon River plume during AMASSEDS: spatial characteristics and salinity variability. *Journal of Geophysical Research: Oceans*, 100(C2):2355–75.

Lihan T., Saitoh S.I., Iida T., Hirawake T. and Iida K. (2008). Satellite-measured temporal and spatial variability of the Tokachi River plume. *Estuarine, Coastal and Shelf Science*, 78(2):237–49.

Liu J.T., Chao S.Y. and Hsu R.T. (2002). Numerical modeling study of sediment dispersal by a river plume. *Continental Shelf Research*, 22(11-13):1745–73.

Llebot C., Rueda F.J., Solé J., Artigas M.L. and Estrada M. (2014). Hydrodynamic states in a wind-driven microtidal estuary (Alfacs Bay). *Journal of Sea Research*, 85:263–76.

Locarnini R.A., Mishonov A.V., Antonov J.I., Boyer T.P., Garcia H.E., Baranova O.K., Zweng M.M., Paver C.R., Reagan J.R., Johnson D.R., Hamilton M. and Seidov D. (2013). World ocean atlas 2013. Vol. 1: Temperature. *NOAA Atlas NESDIS 73*, 40 pp.

Loisel H. and Morel A. (1998). Light scattering and chlorophyll concentration in case 1 waters: a reexamination. *Limnology and Oceanography*, 43(5):847–58.

Loisel H., Vantrepotte V., Jamet C. and Ngoc Dat D. (2013). Challenges and new advances in ocean color remote sensing of coastal waters. In *Topics in Oceanography* (Zambianchi E., ed.). InTech.

Lorenzo M.N. and Taboada J.J. (2005). Influences of atmospheric variability on freshwater input in Galician Rías in winter. *Journal of Atmospheric & Ocean Science*, 10(4):377–87.

Lorenzo M.N., Taboada J.J. and Gimeno L. (2008). Links between circulation weather NOOPtypes and teleconnection patterns and their influence on precipitation patterns in Galicia (NW Spain). *International Journal of Climatology*, 28(11):1493–505.

Lu L.F. and Shi J.Z. (2007). The dispersal processes within the tide-modulated Changjiang River plume, China. *International Journal for Numerical Methods in Fluids*, 55(12):1143–55.

MacCready P., Banas N.S., Hickey B.M., Dever E.P. and Liu Y. (2009). A model study of tide and wind-induced mixing in the Columbia River Estuary and plume. *Continental Shelf Research*, 29(1):278–91.

MacDonald D.G., Goodman L. and Hetland R.D. (2007). Turbulent dissipation in a near-field river plume: a comparison of control volume and microstructure observations with a numerical model. *Journal of Geophysical Research: Oceans*, 112(7):1–13.

Malhadas M., Silva A., Leitao P. and Neves R. (2009). Effect of the bathymetric changes on the hydrodynamic and residence time in Óbidos Lagoon (Portugal). *Journal of Coastal Research*, SI56:549–53.

Marmorino G.O., Donato T.F., Sletten M.A. and Trump C.L. (2000). Observations of an inshore front associated with the Chesapeake Bay outflow plume. *Continental Shelf Research*, 20(6):665–84.

Marta-Almeida M. and Dubert J. (2006). The structure of tides in the Western Iberian region. *Continental Shelf Research*, 26(3):385–400.

Marta-Almeida M., Dubert J. and Peliz Á. (2002). Simulations of extreme shelf current along the North-Western Iberian Shelf forced by wind and river runoff. In *3rd Iberian meeting on Geophysics and Geodesy*, Valencia, Spain, 1555–9.

Marta-Almeida M., Hetland R.D. and Zhang X. (2013). Evaluation of model nesting performance on the Texas-Louisiana continental shelf. *Journal of Geophysical Research: Oceans*, 118(5):2476–91.

Martins F., Leitão P., Silva A. and Neves R. (2001). 3D modelling in the Sado estuary using a new generic vertical discretization approach. *Oceanologica Acta*, 24:51–62.

Martins F., Neves R. and Leitão P. (1998). A three-dimensional hydrodynamic model with generic vertical coordinate. In *Hydro-informatics 98*, 1403–10.

Martinsen E.A. and Engedahl H. (1987). Implementation and testing of a lateral boundary scheme as an open boundary condition in a barotropic ocean model. *Coastal Engineering*, 11(5-6):603–27.

Masse A. and Murthy C. (1992). Analysis of the Niagara River plume dynamics. *Journal of Geophysical Research: Oceans*, 97:2403–20.

Mateus M. and Neves R. (2013). *Ocean modelling for coastal management - case studies with MOHID*. IST Press, Lisboa, Portugal, 265 pp.

Mateus M., Riflet G., Chambel P., Fernandes L., Fernandes R., Juliano M., Campuzano F., de Pablo H. and Neves R. (2012). An operational model for the West Iberian coast: products and services. *Ocean Science*, 8(4):713–32.

Mcwilliams J.C. (1984). The emergence of isolated coherent vortices in turbulent flow. *Journal of Fluid Mechanics*, 146:21–43.

Mendes R. (2010). *Numerical modeling of the Ria de Aveiro plume: a preliminary study*. MSc Thesis, Universidade de Aveiro, 50 pp.

Mendes R., Sousa M.C., deCastro M., Gómez-Gesteira M. and Dias J.M. (2016). New insights into the Western Iberian Buoyant Plume: interaction between the Douro and Minho River plumes under winter conditions. *Progress in Oceanography*, 141:30–43.

Mendes R., Vaz N., Fernández-Nóvoa D., da Silva J., deCastro M., Gómez-Gesteira M. and Dias J. (2014). Observation of a turbid plume using MODIS imagery: the case of Douro estuary (Portugal). *Remote Sensing of Environment*, 154:127–38.

Mendes R., Vaz N. and João M.D. (2013). Potential impacts of the mean sea level rise on the hydrodynamics of the Douro river estuary. *Journal of Coastal Research*, SI65:1951–6.

Miller R.L. and McKee B.A. (2004). Using MODIS Terra 250 m imagery to map concentrations of total suspended matter in coastal waters. *Remote Sensing of Environment*, 93(1-2):259–66.

Moita M., Silva A., Palma S. and Vilarinho M. (2010). The coccolithophore summer-autumn assemblage in the upwelling waters of Portugal: Patterns of mesoscale distribution (1985–2005). *Estuarine, Coastal and Shelf Science*, 87(3):411–9.

Molleri G.S.F., Novo E.M.L.D.M. and Kampel M. (2010). Space-time variability of the Amazon River plume based on satellite ocean color. *Continental Shelf Research*, 30(3-4):342–52.

Montero P. and Pérez-Villar V. (1999). *Estudio de la hidrodinámica de la Ría de Vigo mediante un modelo de volumenes finitos*. PhD Thesis, Universidad de Santiago de Compostela, Spain, 178 pp.

Moore T.S., Campbell J.W. and Dowell M.D. (2009). A class-based approach to characterizing and mapping the uncertainty of the MODIS ocean chlorophyll product. *Remote Sensing of Environment*, 113(11):2424–30.

Moore T.S., Dowell M.D. and Franz B.a. (2012). Detection of coccolithophore blooms in ocean color satellite imagery: a generalized approach for use with multiple sensors. *Remote Sensing of Environment*, 117:249–63.

Morris A., Allen J., Howland R. and Wood R. (1995). The estuary plume zone: source or sink for land-derived nutrient discharges? *Estuarine, Coastal and Shelf Science*, 40(4):387–402.

Mourato P. (2008). Hidromar-Boletim do Instituto Hidrográfico. *nº103, II Série, Novembro*, 31 pp.

NASA (2015). SST quality flags. Available in: http://oceancolor.gsfc.nasa.gov/cms/atbd/sst/doc/html/flag.html [Consulted in 2015-11-13].

Nash J.D., Kilcher L.F. and Moum J.N. (2009). Structure and composition of a strongly stratified, tidally pulsed river plume. *Journal of Geophysical Research: Oceans*, 114(8):C00B12.

Nash J.D. and Moum J.N. (2005). River plumes as a source of large-amplitude internal waves in the coastal ocean. *Nature*, 437(7057):400–3.

Navarro G. and Ruiz J. (2006). Spatial and temporal variability of phytoplankton in the Gulf of Cádiz through remote sensing images. *Deep Sea Research Part II: Topical Studies in Oceanography*, 53(11-13):1241–60.

NCEP (2003). *The GFS atmospheric model*. Tech. Rep., NCEP Office Note 442. Global Climate and Weather Modeling Branch, EMC, Camp Springs, Maryland, 14 pp.

Nezlin N.P. and DiGiacomo P.M. (2005). Satellite ocean color observations of stormwater runoff plumes along the San Pedro Shelf (southern California) during 1997-2003. *Continental Shelf Research*, 25(14):1692–711.

Nezlin N.P., DiGiacomo P.M., Diehl D.W., Jones B.H., Johnson S.C., Mengel M.J., Reifel K.M., Warrick J.A. and Wang M. (2008). Stormwater plume detection by MODIS imagery in the southern California coastal ocean. *Estuarine, Coastal and Shelf Science*, 80(1):141–52.

Nezlin N.P., DiGiacomo P.M., Stein E.D. and Ackerman D. (2005). Stormwater runoff plumes observed by SeaWiFS radiometer in the Southern California Bight. *Remote Sensing of Environment*, 98(4):494–510.

Nezlin N.P., Weisberg S.B. and Diehl D.W. (2007). Relative availability of satellite imagery and ship-based sampling for assessment of stormwater runoff plumes in coastal southern California. *Estuarine, Coastal and Shelf Science*, 71(1-2):250–8.

Nykjær L. and van Camp L. (1994). Seasonal and interannual variability of coastal upwelling along nothwest Africa and Portugal from 1981 to 1991. *Journal of Geophysical Research: Oceans*, 99(C7):14197–14.

Okubo A. (1970). Horizontal dispersion of floatable particles in the vicinity of velocity singularities such as convergences. *Deep Sea Research and Oceanographic Abstracts*, 17(3):445–54.

Oliveira I.M., Valle A. and Miranda F. (1982). Littoral problems in the portuguese west coast. In *18th International Conference on Coastal Engineering* (Edge B.L., ed.), American Society of Civil Engineers, Cape Town, South Africa, Vol. 3, 1950–69.

O'Reilly J.E., Maritorena S., Mitchell B.G., Siegel D.A., Carder K.L., Garver S.A., Kahru M. and McClain C. (1998). Ocean color chlorophyll algorithms for SeaWiFS. *Journal of Geophysical Research: Oceans*, 103(C11):24937–53.

O'Reilly J.E., Maritorena S., O'Brien M.C., Siegel D.A., Toole D., Menzies D., Smith R.C., Mueller J.L., Mitchell B.G., Kahru M., Chavez F.P., Strutton P., Cota G.F., Hooker S.B., Mcclain C.R., Carder K.L., Müller-Karger F.E., Harding L., Magnuson A., Phinney D., Moore G.F., Aiken J., Arrigo K.R., Letelier R. and Culver M. (2000). SeaWiFS postlaunch calibration and validation analyses, Part 3. In *SeaWiFS Postlaunch Technical Report Series*, Vol. 11. 51 pp.

Otero M.P. and Siegel D.A. (2004). Spatial and temporal characteristics of sediment plumes and phytoplankton blooms in the Santa Barbara Channel. *Deep Sea Research Part II: Topical Studies in Oceanography*, 51(10–11):1129–49.

Otero P., Ruiz-Villarreal M., García-García L., González-Nuevo G. and Cabanas J.M. (2013). Coastal dynamics off Northwest Iberia during a stormy winter period. *Ocean Dynamics*, 63(1):115–29.

Otero P., Ruiz-Villarreal M. and Peliz Á.. (2009). River plume fronts off NW Iberia from satellite observations and model data. *ICES Journal of Marine Science*, 66(9):1853–64.

Otero P., Ruiz-Villarreal M. and Peliz Á. (2008). Variability of river plumes off Northwest Iberia in response to wind events. *Journal of Marine Systems*, 72(1-4):238–55.

Otero P., Ruiz-Villarreal M., Peliz Á. and Cabanas J.M. (2010). Climatology and reconstruction of runoff time series in northwest Iberia: influence in the shelf buoyancy budget off Ría de Vigo. *Scientia Marina*, 74(2):247–66.

Palacios S.L., Peterson T.D. and Kudela R.M. (2009). Development of synthetic salinity from remote sensing for the Columbia River plume. *Journal of Geophysical Research: Oceans*, 114(4):C00B05.

Palmer M.R. and Polton J.A. (2011). A strain-induced freshwater pump in the Liverpool Bay ROFI. *Ocean Dynamics*, 61(11):1905–15.

Park K. (1966). Columbia River plume identification by specific alkalinity. *Limnology and Oceanography*, 11(1):118–20.

Pawlowicz R., Beardsley B. and Lentz S. (2002). Classical tidal harmonic analysis including error estimates in MATLAB using T_TIDE. *Computers and Geosciences*, 28(8):929–37.

Peel M.C., Finlayson B.L. and McMahon T.A. (2007). Updated world map of the Köppen-Geiger climate classification. *Hydrology and Earth System Sciences Discussions*, 4(2):439–73.

Peliz Á., Rosa T.L., Santos A.P. and Pissarra J.L. (2002). Fronts, jets, and counter-flows in the Western Iberian upwelling system. *Journal of Marine Systems*, 35(1-2):61–77.

Pereira S.C., Carvalho A.C., Ferreira J., Nunes J.P., Keizer J.J. and Rocha A. (2013). Simulation of a persistent medium-term precipitation event over the western Iberian Peninsula. *Hydrology and Earth System Sciences*, 17(10):3741–58.

Petus C., Chust G., Gohin F., Doxaran D., Froidefond J.M. and Sagarminaga Y. (2010). Estimating turbidity and total suspended matter in the Adour River plume (South Bay of Biscay) using MODIS 250-m imagery. *Continental Shelf Research*, 30(5):379–92.

Petus C., Marieu V., Novoa S., Chust G., Bruneau N. and Froidefond J.M. (2014). Monitoring spatio-temporal variability of the Adour River turbid plume (Bay of Biscay, France) with MODIS 250-m imagery. *Continental Shelf Research*, 74:35–49.

Picado A., Alvarez I., Vaz N., Varela R., Gómez-Gesteira M. and Dias J. (2014). Assessment of chlorophyll variability along the northwestern coast of Iberian Peninsula. *Journal of Sea Research*, 93:2–11.

Pietrzak J. (1998). The use of TVD limiters for forward-in-time upstream-biased advection schemes in ocean modeling. *Monthly Weather Review*, 126(3):812–30.

Pitcher G.C., Figueiras F.G., Hickey B.M. and Moita M.T. (2010). The physical oceanography of upwelling systems and the development of harmful algal blooms. *Progress in Oceanography*, 85(1-2):5–32.

Prego R., Guzmán-Zuñiga D., Varela M., deCastro M. and Gómez-Gesteira M. (2007). Consequences of winter upwelling events on biogeochemical and phytoplankton patterns in a western Galician ria (NW Iberian peninsula). *Estuarine, Coastal and Shelf Science*, 73(3-4):409–22.

Pritchard M. and Huntley D.A. (2006). A simplified energy and mixing budget for a small river plume discharge. *Journal of Geophysical Research: Oceans*, 111(August 2005):1–11.

Qiao L., Bao X., Wu D. and Wang X. (2008). Numerical study of generation of the tidal shear front off the Yellow River mouth. *Continental Shelf Research*, 28(14):1782–90.

Reis A., Parker A., Alencoão A.M.P. and Oliveira A.S. (2012). Dynamics of sediment-associated nutrients if mountainous rivers: a case study in northern Portugal. In *Para conhecer a Terra: memórias e notícias de Geociências no espaço lusófono*. Imprensa da Universidade de Coimbra, Coimbra, 389–98.

Relvas P., Barton E., Dubert J., Oliveira P.B., Peliz Á., da Silva J. and Santos A.M.P. (2007). Physical oceanography of the western Iberia ecosystem: latest views and challenges. *Progress in Oceanography*, 74(2-3):149–73.

Ribeiro A.C., Peliz Á. and Santos A.M.P. (2005). A study of the response of chlorophyll-a biomass to a winter upwelling event off Western Iberia using SeaWiFS and in situ data. *Journal of Marine Systems*, 53(1-4):87–107.

Río-Barja F.J. and Rodriguez-Lestegás F. (1992). *Os ríos galegos. Morfoloxía e réxime.* Consello da cultura galega, Santiago de Compostela, Spain, 2ª ed., 331 pp.

Robinson I.S. (2004). *Measuring the oceans from space: the principles and methods of satellite oceanography.* Spring-Praxis, Chichester, UK, 669 pp.

Robinson I.S. (2010). *Discovering the Ocean from Space: the unique applications of satellite oceanography.* Springer Berlin Heidelberg, Berlin, Heidelberg, 638 pp.

Rodriguez-Puebla C., Encinas A.H., Nieto S. and Garmendia J. (1998). Spatial and temporal patterns of annual precipitation variability over the Iberian Peninsula. *International Journal of Climatology*, 18(3):299–316.

Rong Z. and Li M. (2012). Tidal effects on the bulge region of Changjiang River plume. *Estuarine, Coastal and Shelf Science*, 97:149–60.

Royer L. and Emery W. (1982). Variations of the Fraser River plume and their relationship to forcing by tide, wind and discharge. *Atmosphere-Ocean*, 20(4):357–72.

Ruddick K.G., Deleersnijder E., Luyten P.J. and Ozer J. (1995). Haline stratification in the Rhine-Meuse freshwater plume: a three-dimensional model sensitivity analysis. *Continental Shelf Research*, 15(13):1597–630.

Ruddick K.G., Deleersnijder E., Mulder T.D.E. and Luyten P.J. (1994). A model study of the Rhine discharge front and downwelling circulation. *Tellus A*, 46(2):149–59.

Ruddick K.G., Ovidio F. and Rijkeboer M. (2000). Atmospheric correction of SeaWiFS imagery for turbid coastal and inland waters. *Applied Optics*, 39(6):897–912.

Ruiz Villarreal M., Bolding K., Burchard H. and Demirov E. (2005). Coupling of the GOTM turbulence module to some three-dimensional ocean. In *Marine Turbulence: theories, observations, and models - Results of the CARTUM Project* (Helmut Z. Baumert, John H. Simpson J.S., ed.). Cambrigde University Press, Cambridge, UK, 225–237 pp.

Ruiz-Villarreal M., Montero P., Taboada J.J., Prego R., Leitão P.C. and Perez-Villar V. (2002). Hydrodynamic model study of the Ria de Pontevedra under estuarine conditions. *Estuarine, Coastal and Shelf Science*, 54(1):101–13.

Rusu E. and Lisboa D. (2007). Avaliações da agitação marítima e deriva litoral junto à costa portuguesa. In *5ª Jornadas Portuguesas de Engenharia Costeira e Portuária*, PIANC, Lisboa, Portugal.

Rusu E. and Soares C. (2013). Coastal impact induced by a Pelamis wave farm operating in the Portuguese nearshore. *Renewable Energy*, 58:34–49.

Saha S., Moorthi S., Pan H.L., Wu X., Wang J., Nadiga S., Tripp P., Kistler R., Woollen J., Behringer D., Liu H., Stokes D., Grumbine R., Gayno G., Wang J., Hou Y.T., Chuang H.Y., Juang H.M.H., Sela J., Iredell M., Treadon R., Kleist D., Van Delst P., Keyser D., Derber J., Ek M., Meng J., Wei H., Yang R., Lord S., Van Den Dool H., Kumar A., Wang W., Long C., Chelliah M., Xue Y., Huang B., Schemm J.K., Ebisuzaki W., Lin R., Xie P., Chen M., Zhou S., Higgins W., Zou C.Z., Liu Q., Chen Y., Han Y., Cucurull L., Reynolds R.W., Rutledge G. and Goldberg M. (2010). The NCEP climate forecast system reanalysis. *Bulletin of the American Meteorological Society*, 91(8):1015–57.

Saldías G.S., Shearman R.K., Barth J.A. and Tufillaro N. (2016). Optics of the offshore columbia river plume from glider observations and satellite imagery. *Journal of Geophysical Research: Oceans*.

Saldías G.S., Sobarzo M., Largier J., Moffat C. and Letelier R. (2012). Seasonal variability of turbid river plumes off central Chile based on high-resolution MODIS imagery. *Remote Sensing of Environment*, 123:220–33.

Sanders T.M. and Garvine R.W. (2001). Fresh water delivery to the continental shelf and subsequent mixing: an observational study. *Journal of Geophysical Research: Oceans*, 106(C11):27087.

Santos A.J. (1995). *Modelo hidrodinâmico tridimensional de circulação oceânica e estuarina*. PhD Thesis, Insituto Superior Técnico, Lisboa, 273 pp.

Santos A.M.P., Peliz Á., Dubert J., Oliveira P.B., Angélico M.M. and Ré P. (2004). Impact of a winter upwelling event on the distribution and transport of sardine (Sardina pilchardus) eggs and larvae off western Iberia: a retention mechanism. *Continental Shelf Research*, 24(2):149–65.

Saraiva S., Pina P., Martins F., Santos M., Braunschweig F. and Neves R. (2007). Modelling the influence of nutrient loads on Portuguese estuaries. *Hydrobiologia*, 587(1):5–18.

Schiller R.V., Kourafalou V.H., Hogan P. and Walker N.D. (2011). The dynamics of the Mississippi River plume: impact of topography, wind and offshore forcing on the fate of plume waters. *Journal of Geophysical Research: Oceans*, 116(6):C06029.

Shi W. and Wang M. (2009a). An assessment of the black ocean pixel assumption for MODIS SWIR bands. *Remote Sensing of Environment*, 113(8):1587–97.

Shi W. and Wang M. (2009b). Satellite observations of flood-driven Mississippi River plume in the spring of 2008. *Geophysical Research Letters*, 36(L07607).

Silva A., Palma S., Oliveira P. and Moita M. (2009). Composition and interannual variability of phytoplankton in a coastal upwelling region (Lisbon Bay, Portugal). *Journal of Sea Research*, 62(4):238–49.

Silva A.J.R. (1996). Implementação de um modelo hidromorfológico para a barra do Douro. Contribuição para a compreensão do sistema. In *3º Congresso da Água* (APRH, ed.), Lisboa, Portugal.

Silva A.J.R., Leitão P.C., Leitão J.C., Braunschweig F. and Neves R. (2002). Ria Formosa 3D Hydrodynamic Model . A Contribution for the Understanding of the Faro-Olhão Inlet Processes. In *Litoral 2002, The Changing Coast, EUROCOAST/EUCC* (EUROCOAST / EUCC, ed.), Porto, Portugal, 197–207 pp.

Skamarock W.C., Klemp J.B., Dudhia J.B., Gill D.O., Barker D.M., Duda M.G., Huang X.Y., Wang W. and Powers J.G. (2008). *A description of the advanced research WRF version 3 - Technical note TN-475+STR*. Tech. Rep., NCAR, 113 pp.

Smith W.O. and Demaster D.J. (1996). Phytoplankton biomass and productivity in the Amazon River plume: correlation with seasonal river discharge. *Continental Shelf Research*, 16(3):291–319.

Smyth T.J., Moore G.F., Groom S.B., Land P.E. and Tyrrell T. (2002). Optical modeling and measurements of a coccolithophore bloom. *Applied Optics*, 41(36):7679–88.

Smyth W.D. and Moum J.N. (2000). Anisotropy of turbulence in stably stratified mixing layers. *Physics of Fluids*, 12(6):1343.

Sousa M.C. (2013). *Modelling the Minho River plume intrusion into the Rias Baixas*. PhD Thesis, Universidade de Aveiro, 136 pp.

Sousa M.C., Álvarez I., Vaz N., Gómez-Gesteira M. and Dias J.M. (2013). Assessment of wind pattern accuracy from the QuikSCAT satellite and the WRF model along the Galician Coast (Northwest Iberian Peninsula). *Monthly Weather Review*, 141(2):742–53.

Sousa M.C., Mendes R., Álvarez I., Vaz N., Gómez-Gesteira M. and Dias J.M. (2014a). Unusual circulation patterns of the Rias Baixas induced by Minho freshwater intrusion (NW of the Iberian Peninsula). *PloS One*, 9(11):e112587.

Sousa M.C., Vaz N., Álvarez I., Gómez-Gesteira M. and Dias J.M. (2014b). Influence of the Minho River plume on the Rias Baixas (NW of the Iberian Peninsula). *Journal of Marine Systems*, 139:248–60.

Sousa M.C., Vaz N., Álvarez I., Gómez-Gesteira M. and Dias J.M. (2014c). Modeling the Minho River plume intrusion into the Rias Baixas (NW Iberian Peninsula). *Continental Shelf Research*, 85:30–41.

Stashchuk N. and Vlasenko V. (2009). Generation of internal waves by a supercritical stratified plume. *Journal of Geophysical Research: Oceans*, 114(C1):C01004.

Stefánsson U. and Richards F.A. (1963). Processes contributing to the nutrient distributions off the Columbia River and Strait of Juan de Fuca. *Limnology and Oceanography*, 8(4):394–410.

Szekielda K.H. and Kupferman S. (1973). Heterogeneities in salinity in a river plume. *Estuarine and Coastal Marine Science*, 1(4):419–24.

Taboada J.J., Prego R., Ruíz-Villarreal M., Gómez-Gesteira M., Montero P., Santos a.P. and Pérez-Villar V. (1998). Evaluation of the seasonal variations in the residual circulation in the Ría of Vigo (NW Spain) by means of a 3D baroclinic model. *Estuarine, Coastal and Shelf Science*, 47(5):661–70.

Takano K. (1954). On the velocity distribution off the mouth of a river. *Journal of Oceanographic Society of Japan*, 10(2):60–4.

Takano K. (1955). A complementary note on the diffusion of the seaward river flow off the mouth. *Journal of Oceanographic Society of Japan*, 11(4):147–9.

Teodoro A.C., Goncalves H., Veloso-Gomes F. and Gonçalves J.A. (2009). Modeling of the douro river plume size, obtained through image segmentation of MERIS data. *IEEE Geoscience and Remote Sensing Letters*, 6(1):87–91.

Thomas A.C. and Weatherbee R.A. (2006). Satellite-measured temporal variability of the Columbia River plume. *Remote Sensing of Environment*, 100(2):167–78.

Thomson R.E. and Emery W.J. (2014). *Data analysis methods in physical oceanography*. Pergamon Elsevier Science, New York, USA, 634 pp.

Tilburg C.E., Gill S.M., Zeeman S.I., Carlson A.E., Arienti T.W., Eickhorst J.A. and Yund P.O. (2011). Characteristics of a shallow river plume: observations from the Saco River Coastal Observing System. *Estuaries and Coasts*, 34(4):785–99.

Torres R. and Barton E.D. (2007). Onset of the Iberian upwelling along the Galician coast. *Continental Shelf Research*, 27(13):1759–78.

Trancoso A.R., Saraiva S., Fernandes L., Pina P., Leitão P. and Neves R. (2005). Modelling macroalgae using a 3D hydrodynamic-ecological model in a shallow, temperate estuary. *Ecological Modelling*, 187(2-3):232–46.

Trigo R.M. and DaCamara C.C. (2000). Circulation weather NOOPtypes and their influence on the precipitation regime in Portugal. *International Journal of Climatology*, 20(13):1559–81.

Trigo R.M., Pozo-Vázquez D., Osborn T.J., Castro-Díez Y., Gámiz-Fortis S. and Esteban-Parra M.J. (2004). North Atlantic oscillation influence on precipitation, river flow and water resources in the Iberian Peninsula. *International Journal of Climatology*, 24(8):925–44.

Valente A.S. and da Silva J.C.B. (2009). On the observability of the fortnightly cycle of the Tagus estuary turbid plume using MODIS ocean colour images. *Journal of Marine Systems*, 75(1-2):131–7.

van Alphen J.S.L.J., Ruijter W.P.M. and Borst J.C. (1988). Outflow and three-dimensional spreading of Rhine river water in the Netherlands coastal zone. In *Physical Processes in Estuaries* (Dronkers J. and Leussen W., eds.). Springer Berlin Heidelberg, Berlin, Heidelberg, 70–92 pp.

Vaz N. (2007). *Study of heat and salt transport processes in the Espinheiro Channel (Ria de Aveiro)*. PhD Thesis, University of Aveiro, Aveiro, Portugal, 151 pp.

Vaz N., Dias J.M., Leitão P. and Martins I. (2005). Horizontal patterns of water temperature and salinity in an estuarine tidal channel: Ria de Aveiro. *Ocean Dynamics*, 55(5-6):416–29.

Vaz N., Fernandes L., Leitão P.C., Dias J.M. and Neves R. (2009a). The Tagus estuarine plume induced by wind and river runoff: Winter 2007 case study II. *Journal of Coastal Research*, SI56:1090–4.

Vaz N., Leitao P.C. and Dias J.M. (2007). Channel-ocean exchange driven by tides and river flow: Espinheiro Channel (Portugal). *Journal of Coastal Research*, SI50:1000–4.

Vaz N., Mateus M. and Dias J.M. (2011). Semidiurnal and spring-neap variations in the Tagus Estuary : application of a process-oriented hydro-biogeochemical model. *Journal of Coastal Research*, SI64:1619–23.

Vaz N., Mateus M., Plecha S., Sousa M., Leitão P., Neves R. and Dias J. (2015). Modeling SST and chlorophyll patterns in a coupled estuary-coastal system of Portugal: the Tagus case study. *Journal of Marine Systems*, 147:123–37.

Vaz N., Miguel Dias J. and Chambel Leitão P. (2009b). Three-dimensional modelling of a tidal channel: The Espinheiro Channel (Portugal). *Continental Shelf Research*, 29(1):29–41.

Veloso-Gomes F., Taveira-Pinto F., das Neves L., Pais Barbosa J. and Coelho C. (2004). Erosion risk levels at the NW Portuguese coast: the Douro mouth - Cape Mondego stretch. *Journal of Coastal Conservation*, 10(1):43.

Verspecht F., Rippeth T.P., Howarth M.J., Souza A.J., Simpson J.H. and Burchard H. (2009). Processes impacting on stratification in a region of freshwater influence: application to Liverpool Bay. *Journal of Geophysical Research: Oceans*, 114(11):1–12.

Vicente-Serrano S.M., Trigo R.M., López-Moreno J.I., Liberato M.L.R., Lorenzo-Lacruz J., Beguería S., Morán-Tejeda E. and El Kenawy A. (2011). Extreme winter precipitation

in the Iberian Peninsula in 2010: Anomalies, driving mechanisms and future projections. *Climate Research*, 46(1):51–65.

Vieira M.E.C. and Bordalo A.A. (2000). The Douro Estuary (Portugal): a mesotidal salt wedge. *Oceanologica Acta*, 23(5):585–94.

Walker N.D. (1996). Satellite assessment of Mississippi River plume variability: causes and predictability. *Remote Sensing of Environment*, 58(1):21–35.

Wang M. and Shi W. (2007). The NIR-SWIR combined atmospheric correction approach for MODIS ocean color data processing. *Optics Express*, 15(24):15722.

Wang M., Son S. and Shi W. (2009). Evaluation of MODIS SWIR and NIR-SWIR atmospheric correction algorithms using SeaBASS data. *Remote Sensing of Environment*, 113(3):635–44.

Warner J.C., Geyer W.R. and Lerczak J.A. (2005). Numerical modeling of an estuary: a comprehensive skill assessment. *Journal of Geophysical Research: Oceans*, 110(5):1–13.

Warrick J.A. (2004). Dispersal scaling from the world's rivers. *Geophysical Research Letters*, 31(4):L04301.

Warrick J.A., DiGiacomo P.M., Weisberg S.B., Nezlin N.P., Mengel M., Jones B.H., Ohlmann J.C., Washburn L., Terrill E.J. and Farnsworth K.L. (2007). River plume patterns and dynamics within the Southern California Bight. *Continental Shelf Research*, 27(19):2427–48.

Weiss J. (1991). The dynamics of enstrophy transfer in two-dimensional hydrodynamics. *Physica D: Nonlinear Phenomena*, 48(2-3):273–94.

Whitney M.M. and Garvine R.W. (2005). Wind influence on a coastal buoyant outflow. *Journal of Geophysical Research: Oceans*, 110(C3):C03014. C03014.

Willmott C.J. (1981). On the validation of models. *Physical Geography*, 2:184–94.

Wooster W., Bakun A. and Mclain D. (1976). Seasonal upwelling cycle along eastern boundary of North-Atlantic. *Journal of Marine Research*, 34(2):131–41.

Wu H., Shen J., Zhu J., Zhang J. and Li L. (2014). Characteristics of the Changjiang plume and its extension along the Jiangsu Coast. *Continental Shelf Research*, 76:108–23.

Xie P. and Arkin P.A. (1997). Global precipitation: a 17-year monthly analysis based on gauge observations, satellite estimates, and numerical model outputs. *Bulletin of the American Meteorological Society*, 78(11):2539–58.

Xing J. and Davies A.M. (1999). The effect of wind direction and mixing upon the spreading of a buoyant plume in a non-tidal regime. *Continental Shelf Research*, 19(11):1437–83.

Yankovsky A.E. (2000). The cyclonic turning and propagation of buoyant coastal discharge along the shelf. *Journal of Marine Research*, 58(4):585–607.

Yankovsky A.E. and Chapman D.C. (1997). A simple theory for the fate of buoyant coastal discharges*. *Journal of Physical Oceanography*, 27(7):1386–401.

Yankovsky A.E., Garvine R.W. and Münchow A. (2000). Mesoscale currents on the inner New Jersey shelf driven by the interaction of buoyancy and wind Forcing. *Journal of Physical Oceanography*, 30(9):2214–30.

Yankovsky A.E., Hickey B.M. and Münchow A.K. (2001). Impact of variable inflow on the dynamics of a coastal buoyant plume. *Journal of Geophysical Research: Oceans*, 106(C9):19809.

Yu Y., Zhang H. and Lemckert C.J. (2011). The response of the river plume to the flooding in Moreton Bay, Australia. *Journal of Coastal Research*, SI64:1214–8.

Yuan Y., Avener M.E. and Horner-Devine A.R. (2011). A two-color optical method for determining layer thickness in two interacting buoyant plumes. *Experiments in Fluids*, 50(5):1235–45.

Ziveri P., Thunell R.C. and Rio D. (1995). Export production of coccolithophores in an upwelling region: results from San Pedro Basin, Southern California Borderlands. *Marine Micropaleontology*, 24(3-4):335–58.

Zorita E., Kharin V. and von Storch H. (1992). The atmospheric circulation and sea surface temperature in the North Atlantic area in winter: their interaction and relevance for Iberian precipitation. *Journal of Climate*, 5(10):1097–108.

Zweng M.M., Reagan J.R., Antonov J.I., Locarnini R.A., Mishonov A.V., Boyer T.P., Garcia H.E., Baranova O.K., Johnson D.R., Seidov D. and Biddle M.M. (2013). World ocean atlas 2013. Vol. 1: Salinity. *NOAA Atlas NESDIS 74*, 40 pp.